In-vitro and In-vivo Effects of Proton-FLASH Irradiation

Sarah Rudigkeit

Vollständiger Abdruck der von der Fakultät für Luft- und Raumfahrttechnik der Universität der Bundeswehr München zur Erlangung des akademischen Grades eines

Doktors der Naturwissenschaften (Dr. rer. nat.)

angenommenen Dissertation.

Gutachter/Gutachterin:

1. Jun.-Prof. Dr. rer. nat. Judith Reindl
2. Prof. Dr. rer. nat. Thomas Schmid

Die Dissertation wurde am 28.09.2023 bei der Universität der Bundeswehr München eingereicht und durch die Fakultät für Luft- und Raumfahrttechnik am 09.02.2024 angenommen. Die mündliche Prüfung fand am 08.03.2024 statt.

Universität der Bundeswehr München
Fakultät für Luft- und Raumfahrttechnik
Institut für angewandte Physik und Messtechnik

Dissertation zur Erlangung des akademischen Grades
Doktor der Naturwissenschaften (Dr. rer. nat.)

In-vitro and In-vivo Effects of Proton-FLASH Irradiation

Sarah Rudigkeit

September 28, 2023

Abstract

Radiotherapy is next to chemotherapy and surgery one of the most important treatment methods in cancer therapy. Its aim is to irradiate the tumor with a lethal dose of ionizing irradiation while keeping the side effects on the healthy tissue at a minimum level. There are several approaches improving radiotherapy and reducing the side effects. A very promising approach is the irradiation with ultra-high dose rates (> 40 Gy/s) known as FLASH. FLASH-radiotherapy provides significant sparing of healthy tissue while maintaining tumor control. This effect has been seen in several animal models and applies for protons, electrons, and x-rays. Although this effect has been highly investigated, the underlying mechanisms are still unclear. Therefore, further investigations are necessary. FLASH radiation therapy with protons has three major advantages over other types of irradiation. Due to their characteristic energy distribution in the tissue, protons often lead to better irradiation results than the frequently used x-rays, existing proton beam facilities can be converted to FLASH, and protons, in contrast to the electrons frequently used in the FLASH experiments, enable the irradiation of deep-seated tumors. In this work, I investigated the proton-FLASH effect using three in-vitro models and an in-vivo mouse ear model. Furthermore, a new method based on longterm live-cell phase-contrast microscopy and artificial intelligence based analysis of the obtained videos to investigate several radiobiological effects in-vitro in one assay was developed and presented here.

The proton-FLASH experiments were conducted on the SNAKE beamline at the tandem accelerator of the Maier-Leibnitz-Laboratorium in Garching near Munich. As in-vitro experiments, a colony forming assay, a Caspase3/7-Sytox assay and a micronuclei test were performed with doses of 4 Gy and at three different dose rates (Conv = 0.06 Gy/s, Flash9 = 9.3 Gy/s and Flash310 = 310 Gy/s). The colony forming assay investigated the cell survival, the Caspase3/7-Sytox assay the cell death and the micronuclei test the genetic damage. Dose rate effects were observed in a reduction of cell death at a dose rate of 310 Gy/s and in reduced genetic damage at dose rates of 310 Gy/s and 9.3 Gy/s. No difference was seen in the cell survival. In the in-vivo mouse ear model, the right ears of Balb/c mice were irradiated at three dose rates (Conv = 0.06 Gy/s, Flash9 = 9.3 Gy/s and Flash930 = 930 Gy/s) for a total dose of 23 Gy or 33 Gy. Desquamation and erythema of the irradiated ear, which were combined into an inflammation score, and the ear thickness were measured for 180 days. The cytokines TGF-β1, TNF-α, IL1α, and IL1β were analyzed in blood samples collected during the first 4 weeks and on the last day of treatment. No differences in inflammatory responses were observed in the 23 Gy group for the different dose rates. In the 33 Gy group, ear swelling and inflammation score were reduced for Flash9 and Flash930 compared to the Conv dose rate. No changes in the cytokines were measured in the blood. However, an estimation of the irradiated blood volume demonstrated, that 100 times more blood is irradiated when using Conv compared to using Flash9 or Flash930. This suggests that the irradiated blood volume may play a role in the underlying mechanisms of the FLASH effect.

In the novel in-vitro method presented in this work, cells were moved directly after irradiation to an inverted phase-contrast microscope equipped with a live-cell set-up that allows recording of living cells for several days. The obtained videos were evaluated by the self-developed artificial intelligence based algorithm CeCILE (Cell Classification and In-vitro Lifecycle Evaluation). CeCILE was trained on a custom dataset I created. To enable the evaluation of the cell cycle, cells in the dataset were assigned to one of four morphological classes, which describe different states in the cell cycle and cell death. The whole development and training process is presented in this thesis. To show CeCILE's potential, my new method was applied to a sample of irradiated cells (3 Gy of x-rays) and a sample of sham irradiated cells. It could be shown that CeCILE sucessfully created cell lineages of every cell in the obtained videos and evaluated the following endpoints: number of cells per frame in the four morphological classes, time points of the first cell divisions of every cell, cell cycle duration, cell cycle abnormalities and proliferation. Therefore, CeCILE is able to accurately assess several important radiobiological endpoints.

In this thesis, new insights into the proton-FLASH effect could be gained and more are expected when the novel method based on CeCILE is applied to proton-FLASH in-vitro experiments in the future.

Zusammenfassung

Die Strahlentherapie ist eine der wichtigsten Behandlungsmethoden in der Krebstherapie neben der Chemotherapie und der Operation. Ziel ist es dabei, den Tumor mit einer tödlichen Dosis ionisierender Strahlung zu bestrahlen und gleichzeitig die Nebenwirkungen im gesunden Gewebe so gering wie möglich zu halten. Es gibt verschiedene Ansätze zur Verbesserung der Strahlentherapie und zur Verringerung der Nebenwirkungen. Ein sehr vielversprechender Ansatz ist dabei die Bestrahlung mit ultrahohen Dosisraten (> 40 Gy/s), bekannt als FLASH (engl. Blitz). Bei der FLASH-Strahlentherapie wird gesundes Gewebe deutlich geschont ohne dass die Tumorkontrolle beeinträchtigt wird. Dieser Effekt konnte in mehreren Tiermodellen nachgewiesen werden und kommt bei Protonen, Kohlenstoff-Ionen, Elektronen und Röntgenstrahlen vor. Obwohl dieser Effekt intensiv untersucht wurde, sind die zugrunde liegenden Mechanismen noch unklar. Daher sind weitere Untersuchungen notwendig. Die FLASH-Strahlentherapie mit Protonen hat dabei drei große Vorteile gegenüber den anderen Bestrahlungsarten. Protonen führen aufgrund ihrer charakteristischen Energieverteilung im Gewebe oft zu besseren Bestrahlungsergebnissen als die häufig verwendeten Röntgenstrahlen, bestehende Protonenstrahlanlagen können auf FLASH umgerüstet werden und Protonen ermöglichen im Gegensatz zu den im FLASH Bereich häufig verwendeten Elektronen die Bestrahlung von tief sitzenden Tumoren. In dieser Arbeit habe ich den Proton-FLASH-Effekt anhand von drei In-vitro-Modellen und einem In-vivo-Mausohrmodell untersucht. Darüber hinaus wurde eine neue Methode entwickelt und vorgestellt, die auf der Langzeit-Phasenkontrastmikroskopie von lebenden Zellen und der Analyse der Videos mittels künstlicher Intelligenz basiert, um mehrere strahlenbiologische Effekte in-vitro in einem Assay zu untersuchen.

Die Proton-FLASH-Experimente wurden an der SNAKE-Beamline am Tandembeschleuniger des Maier-Leibnitz-Laboratoriums in Garching bei München durchgeführt. Als In-vitro-Experimente wurden ein Koloniebildungstest, ein Caspase3/7-Sytox-Assay und ein Mikrokerntest mit einer Dosis von 4 Gy und bei drei verschiedenen Dosisraten (Conv = 0,06 Gy/s, Flash9 = 9,3 Gy/s und Flash310 = 310 Gy/s) durchgeführt. Mit dem Koloniebildungstest wurde das Überleben der Zellen untersucht, mit dem Caspase3/7-Sytox-Test der Zelltod und mit dem Mikrokerntest der genetische Schaden. Dosisrateneffekte wurden in einer Verringerung des Zelltods bei einer Dosisrate von 310 Gy/s und in einer Verringerung der genetischen Schäden bei Dosisraten von 310 Gy/s und 9,3 Gy/s beobachtet. Beim Überleben der Zellen wurde kein Unterschied festgestellt. Im In-vivo-Mausohrmodell wurden die rechten Ohren von Balb/c-Mäusen mit drei Dosisraten (Conv = 0,06 Gy/s, Flash9 = 9,3 Gy/s und Flash930 = 930 Gy/s) mit einer Gesamtdosis von 23 Gy oder 33 Gy bestrahlt. Schuppung und Rö-

tung der bestrahlten Ohren, die zu einem Entzündungsscore zusammengefasst wurden, sowie die Ohrdicke wurden 180 Tage lang gemessen. Die Zytokine TGF-β1, TNF-α, IL1α und IL1β wurden in Blutproben analysiert, die während der ersten vier Wochen und am letzten Tag des Beobachtungszeitraumes entnommen wurden. In der 23-Gy-Gruppe wurden bei den verschiedenen Dosisraten keine Unterschiede in der Entzündungsreaktion festgestellt. In der 33-Gy-Gruppe waren die Ohrschwellung und der Entzündungswert bei Flash9 und Flash930 im Vergleich zur Conv-Dosisrate reduziert. Im Blut wurden keine Veränderungen der Zytokine gemessen. Eine Abschätzung des bestrahlten Blutvolumens zeigte jedoch, dass bei der Verwendung von Conv im Vergleich zu Flash9 oder Flash930 100 Mal mehr Blut bestrahlt wurde. Dies deutet darauf hin, dass das bestrahlte Blutvolumen bei den zugrunde liegenden Mechanismen des FLASH-Effekts eine Rolle spielen könnte.

Bei der in dieser Arbeit vorgestellten neuartigen In-vitro-Methode wurden die Zellen direkt nach der Bestrahlung in ein inverses Phasenkontrastmikroskop gebracht, das mit einem Lebendzell-Aufbau ausgestattet ist und die Aufnahme lebender Zellen über mehrere Tage ermöglicht. Die aufgenommenen Videos wurden mit dem selbstentwickelten, auf künstlicher Intelligenz basierenden Algorithmus CeCILE (englisch: Cell Classification and In-vitro Lifecycle Evaluation, deutsch: Zell-Klassifikation und in-vitro Auswertung des Lebenszyklus) ausgewertet. CeCILE wurde auf einem von mir erstellten Datensatz trainiert. Um die Auswertung des Zellzyklus zu ermöglichen, wurden die Zellen des Datensatzes jeweils einer von vier morphologischen Klassen zugeordnet, die unterschiedliche Zustände während des Zellzyklus und den Zelltod beschreiben. Der gesamte Entwicklungs- und Trainingsprozess wurde in dieser Arbeit vorgestellt. Zur Demonstration des Potentials von CeCILE, habe ich meine neue Methode bei einer Probe bestrahlter Zellen (3 Gy Röntgenstrahlung) und einer Probe unbestrahlter (sham) Zellen angewandt. Es konnte gezeigt werden, dass CeCILE erfolgreich die Zell-Stammbäume jeder Zelle in den erhaltenen Videos erstellen kann und die folgenden Endpunkte ausgewertet werden konnten: Anzahl der Zellen pro Bild in den vier morphologischen Klassen, Zeitpunkte der ersten Zellteilungen jeder Zelle, Zellzyklusdauer, Zellzyklusanomalien und Proliferation. CeCILE ist daher in der Lage, mehrere wichtige radiobiologische Endpunkte akurat auszuwerten.

Mit dieser Arbeit konnten neue Erkenntnisse über den Proton-FLASH-Effekt gewonnen werden, und weitere sind zu erwarten, wenn diese neuartige, auf CeCILE basierende Methode in Zukunft bei Proton-FLASH In-vitro-Experimenten eingesetzt wird.

Contents

Introduction

Every year, 500,000 people in Germany are diagnosed with cancer [1]. In 2021, 22.4 % of deaths were caused by cancer making it the second leading cause of death after diseases of the cardiovascular system, which caused 33.3 % of deaths [2]. These numbers demonstrate that cancer is already a public disease and one of the biggest issues society has to face nowadays. Around 35 % of cancer patients are of working age [1] and are therefore unavailable to the labor market further increasing the shortage of available and qualified workers. Even though the diagnosis of cancer is not necessarily a death sentence as treatments are getting more and more successful, for the most patients, this illness means often years of different treatments and surgeries that cause pain, discomfort and enormous stress. Many cancer survivors suffer from long-term damages that affect their everyday lives [3]. As elderly people are most susceptible to cancer [4] and society is becoming older due to the demographic change, this illness will even be more important in the future. Cancer patients often need medical care, and with the increasing number of patients, medical care is increasingly stretched to its limits, which is also a major issue for society as a whole. Therefore, it is highly important not only for the patients but also for the whole society to find more effective cures with decreased side-effects and long-term damages.

The most commonly used treatments against cancer are surgery, radiotherapy and chemotherapy. Approximately 50 % of all cancer patients receive radiation therapy during their course of illness [5]. In radiotherapy, the aim is to apply high dosis of ionizing radiation in a tumor while sparing the normal tissue. Ionizing radiation of sufficiently high doses causes damage to cell structures such as the sensitive DNA. When a cell receives too much damage, especially to its DNA, it is no longer able to reproduce and eventually dies. If all cells in a tumor received such a high dose, the tumor will no longer be able to grow or might even shrink until the tumor is completely receded. However, in radiotherapy, not only the tumor is irradiated but also the normal tissue receives a partial dose of the lethal tumor dose. Therefore, also the cells in the normal tissue will be damaged leading to different side-effects, like changes in the tissue that impair the tissue functionality and can lead in the worst case to the failure of organs. In radiotherapy, the therapist needs to find a way to achieve the best possible tumor control while keeping the expected side-effects of the normal tissue at the lowest possible level. This challenge is described by the normal tissue complication probability (NTCP) and the tumor control probability (TCP), as shown in Figure 1.

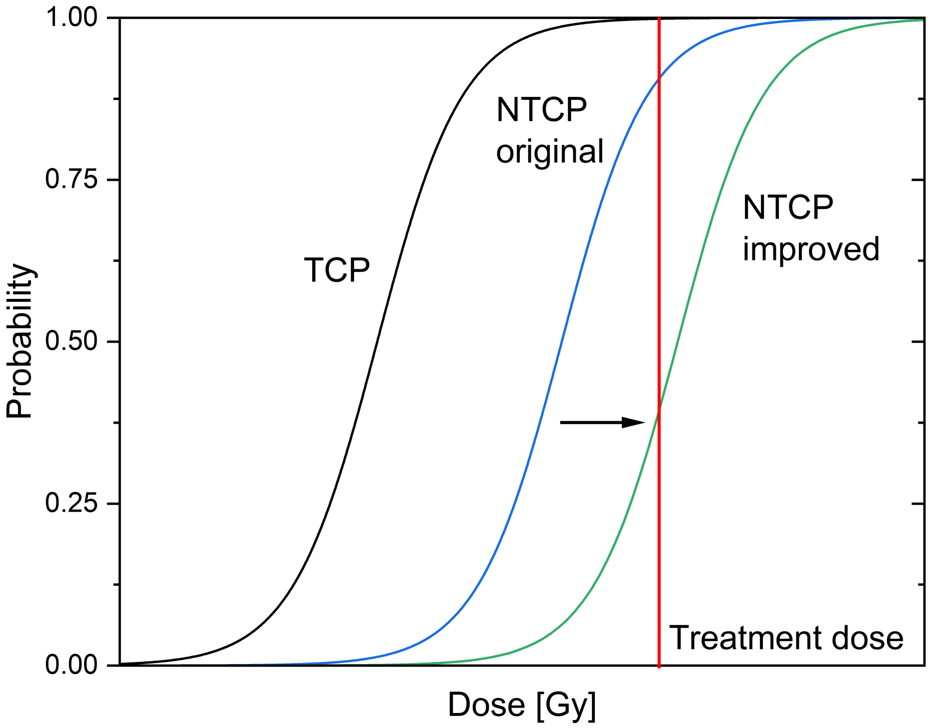

Figure 1: The TCP-NTCP model. The tumor control probability (TCP) is shown by a black curve, the normal tissue complication probability is shown in blue for the original treatment and in green for the improved treatment. The red vertical line indicates the treatment dose. To improve the outcome of radiotherapy, the difference between TCP and NTCP must be increased.

The TCP gives the probability that cells in the tumor are no longer able to reproduce and can no longer increase the tumor or form new tumors. In therapy, it is aimed for a TCP of 1. The NTCP is a measure for the radiation induced side-effects that are highly dependent on the tissues which receive radiation doses. Due to modern irradiation techniques and schedules, normal tissue cells receive less damage and only a part of the dose applied to the tumor cells resulting in a higher TCP than NTCP. Comparing the TCP curve in black with the original NTCP curve in blue, the treatment dose (red vertical line) achieves the aimed TCP of 1, while in this example the NTCP of 0.9 that might be not acceptable for the patient. Therefore, a technique must be find that further increases the difference between TCP and NTCP, shown as a green curve.

One approach is to use protons instead of x-ray photons that are typically used. X-rays have an exponential dose decrease after a build-up region, while protons deposit most of their dose at a certain depth in the tissue known as Bragg-peak. The depth where the Bragg-peak occurs is dependent on the proton energy and is usually planned to be within the tumor. Due to the Bragg-peak, the tumor can be irradiated with high doses while the tissue before and after receives less dose.

In 2014, Favaudon et al. [6] described another approach to further increase the difference between TCP and NTCP. They found that increasing the dose rate, i.e. the dose applied per time interval, to > 40 Gy/s the healthy tissue is spared. In their mouse model, the whole thorax irradiation with such ultra-high doses led to the complete lack of acute and irreversible lesions in the lung, which were observed in 100 % of the control group irradiated with the same dose but with a conventional dose rate (< 1 Gy/s). Furthermore, they observed in two models of mice with implanted tumors that this sparing effect does not apply in tumor tissue. They could show an equal tumor control for high and conventional dose rates. The authors of this study named this effect the FLASH effect, and the dose rate necessary to induce this effect FLASH dose rate. This effect was confirmed by many other studies. It was found in different animal models like mouse [7–9], mini-pig[10], cat [10] and zebrafish [11]. The FLASH effect could be found in various tissues like lung [6, 12], brain [8, 13], gastro-intestinal tract [9] and in skin [10]. Furthermore, the FLASH effect could be induced by electrons [6–8, 14], x-rays [15], protons [16–18] and carbon ions [19]. Although, FLASH is extensively investigated in-vivo and in-vitro, it is widely unknown what the exact requirements are for inducing a FLASH effect and what are the underlying mechanisms of this effect. However, to use FLASH in a clinical setting, knowledge about the requirements and about the mechanisms is urgently needed. Especially, when combining protons with FLASH to profit from the tissue sparing effects of both methods, vast ranges of dose rates have not been tested yet. One problem here is the low availability of irradiation platforms and beam time at proton beamlines. In most of the animal models, large volumes were irradiated like the whole thorax, the abdomen or the brain. In clinical practice, only a small part of the patient's body is irradiated. Therefore, there is a lack of models that mimic such small volume irradiations. To understand the underlying mechanisms, also more in-vitro studies are necessary that are able to cover a wide range of radiobiological endpoints and provide new insights.

In this work, the FLASH radiotherapy on protons (proton-FLASH) was further investigated in an in-vivo and three in-vitro experiments at the ion microprobe SNAKE [1] at the tandem accelerator in Garching near Munich. Completely new proton-FLASH dose rates were tested on a mouse ear model. This model has the advantage that only a small part of the body, similar as in clinical practice was irradiated and the irradiated blood volume could be estimated. To find possible underlying mechanisms, the cell survival, the cell death and the genetic damage was investigated in three in-vitro models. Furthermore, a new method to evaluate several biological endpoints in one study was developed during this thesis. Here, cells were imaged for several days with phase-contrast microscopy. The obtained videos were evaluated on a single cell basis with the artificial intelligence based detection and tracking algorithm CeCILE (Cell Classification and In-vitro Lifecycle Evaluation), which provides detailed information about the cells' behavior, all cell cycle specific endpoints, the evolution of each cell, the relationships between cells and the proliferation.

---

[1] Superconducting Nanoprobe for Applied nuclear (German: Kern-) physics Experiments

In the first chapter of this thesis (Chapter 1), the physical and biological background is discussed. In Chapter 2, the previous findings in the literature regarding the FLASH effect are discussed in Sections 2.1 - 2.4. Then, a new beamline set-up and the dosimetry for proton-FLASH experiments in-vivo and in-vitro are presented in Sections 2.5 and 2.6. The in-vitro experiments are described in Section 2.7 and the in-vitro experiments in Section 2.8 The results of the proton-FLASH experiments are discussed in Section 2.9. In Chapter 3, a novel approach of detecting and tracking cells on a single cell basis by the artificial intelligence based algorithm CeCILE is presented. This chapter starts with a theoretical background of deep learning based object detection in Sections 3.1 - 3.3. In Section 3.4, the creation of the dataset on which CeCILE is trained is described. Sections 3.5 - 3.8 discuss the used methods and the performance of the different parts of the algorithm CeCILE. Section 3.9 presents the results provided by CeCILE of an irradiation experiment and discusses them in Section 3.10. This thesis ends with the conclusion of the experiments and presented methods and gives an outlook of possible future experiments (Chapter 4).

Chapter 1

Effects of ionizing radiation on biological matter

1.1 Physical interaction of ionizing radiation to matter

Ionizing radiation is most commonly used in radiotherapy for the treatment of tumor patients and can consist of photons, electrons, protons or heavier ions. Ionizing radiation is defined as radiation that can ionize electrons in atomic or molecular shells. The ionizations take place when the particles interact with the matter. In this process, it comes to an energy loss of the particles and an energy deposition into the matter. In general, the energy deposition can be described via the physical property dose, which is the amount of energy ΔE that is deposited within a mass element Δm:

$$D = \frac{\Delta E}{\Delta m} \tag{1.1}$$

The unit of dose is Gray: $1\,\mathrm{Gy} = 1\,\mathrm{J/kg}$. Ionizations occur near the particle tracks along which particles traverse matter. Depending on the particle type, 1 Gy of radiation produces different amounts of particle tracks in a certain volume. For example, 1 Gy of 20.5 MeV protons equals approx. 22 tracks in a cell nucleus with an area of 90 $\mu\mathrm{m}^2$ assuming a cell density equal to that of water (997 $\mathrm{kg/m}^3$), while 1 Gy of 55 MeV carbon ions produces approx. 1.5 tracks in a cell nucleus. Due to this large difference, the underlying interactions of the different particle types are addressed individually. In this thesis, x-rays (photons), protons, and carbon ions were used for irradiation. Therefore, these particle types will be described in more detail.

1.1.1 Interaction of x-rays with matter

X-rays are photons produced in an x-ray tube by accelerating electrons (to several keV to MeV) on a target [20]. When electrons hit the target, Bremsstrahlung is generated by the scattering of the electrons near atomic nuclei. The Bremsstrahlung consists of high-energy photons (several keV to MeV) of a continuous spectrum [20]. Additionally, the electrons can generate high energy transitions between the shells of an atom. Thus, photons of characteristic wavelengths are emitted. Both, the continuous spectrum of Bremsstrahlung and the characteristic spectrum form the x-ray spectrum [20], which is shown in Figure 1.1.

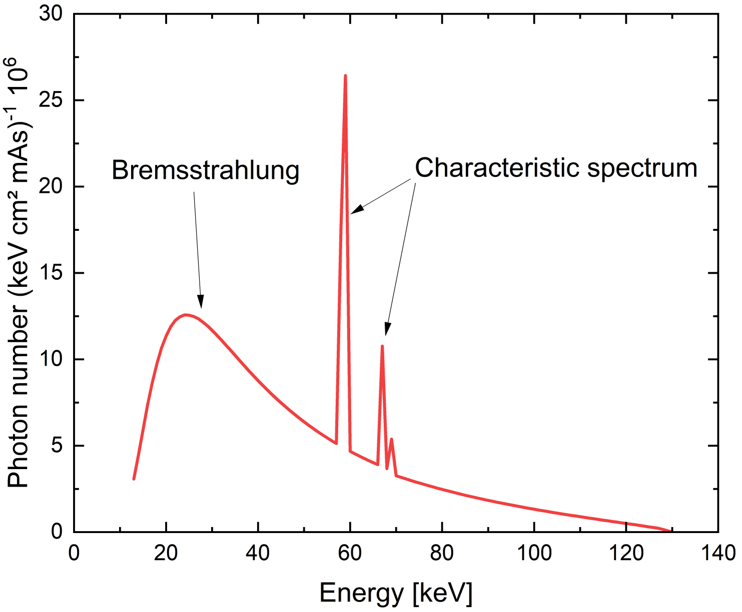

Figure 1.1: The x-ray spectrum of the x-ray cabinet (CellRad, Precision X-ray, US) used in this thesis according to the producer. The x-ray spectrum is calculated for a distance of 1 m to the tube in air by the software SpekCalc [21–23].

When photons interact with matter, it can come to full or partial absorption of the photon energy. In this absorption process, free charged secondary particles are formed like electrons or positrons. These secondary particles interact with their surrounding and ionize and excite the matter. In all these processes, they lose energy. In a photon beam, the amount of photons decreases with the penetration depth as more and more photons are absorbed and secondary particles are formed [24], as shown in Figure 1.2. This process is called attenuation and is described by the attenuation coefficient. This coefficient is dependent on the photon energy, the density and the atomic number of the traversed object. The contributions of these components to the attenuation coefficient vary with the predominant interaction mechanism.

There are three ways for photons to interact with matter. The way of interaction depends on the photon energy. The first interaction is the photoelectric effect: Here, the photon interacts with a tightly bound orbital electron, as shown in Figure 1.3(a). The photon disappears and the electron is ejected from the atom. The kinetic energy of the ejected electron E_K depends on the energy of the incident photon $h\nu$ and the binding energy E_B of the electron.

$$E_K = h\nu - E_B \tag{1.2}$$

When the electron is ejected, an electron vacancy is formed. This vacancy is then filled with an electron from an outer shell. The energy difference of the electron shells is emitted by a photon or an Auger-electron. The probability for an interaction via the photoelectric effect is described by the photoabsorption-coefficient τ. τ depends on the density ρ, the atomic number Z, the mass number A, and the photon energy E_γ. For light atoms, where $\frac{Z}{A} \approx 1/2$, and photon energies < 511 keV the following relation applies [24]:

$$\tau \propto \rho \cdot \frac{Z^{4.5}}{A \cdot E_\gamma^3}. \tag{1.3}$$

In general, the probability for interaction via the photoelectric effect increases with Z and decreases with increasing photon energies [24].

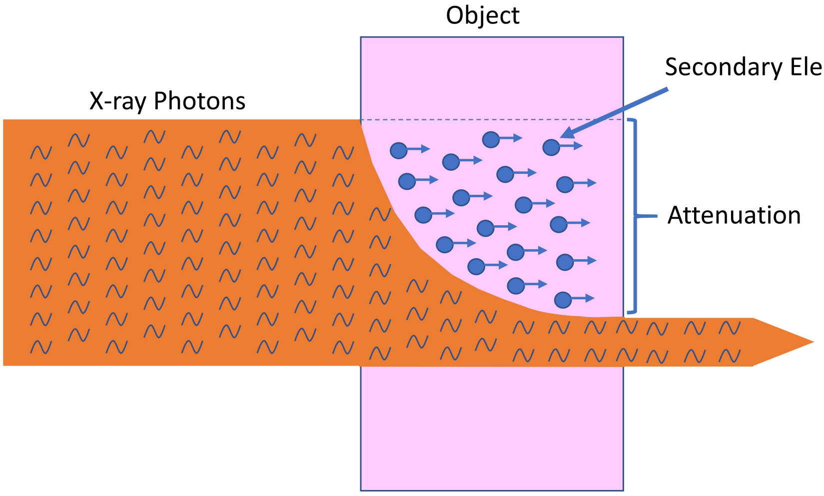

Figure 1.2: Schematic illustration of the photon absorption in matter. As the photons penetrate matter, more and more photons are absorbed and secondary electrons are formed. This process is called attenuation and is characterized by an exponential decay of the photon number and energy.

In the second way of interaction, the Compton effect, the photon interacts via an inelastic collision with a weakly bound orbital electron, as shown in Figure 1.3(b). The energy of the incident photon must be much larger than the binding energy of the orbital electron. During the interaction, the photon loses a part of its energy to the orbital electron and is scattered, i.e. it changes its direction of movement. The angle under which the photon is scattered depends on the proportion of energy which is lost in the collision. For photons with lower energies, the probability for a backscattering is higher, while photons with energies > 1 MeV are scattered at angles $< 45°$ [24]. The collided electron gains enough energy to leave the atomic shell as a recoil electron. The atom left by the electron is ionized. The probability for an interaction via the Compton effect is given by the Compton-interaction coefficient σ_C that can be roughly described as:

$$\sigma_C \propto \rho \cdot \frac{Z}{A} \cdot \frac{1}{E_\gamma}, \tag{1.4}$$

where E_γ is the photon energy [24].

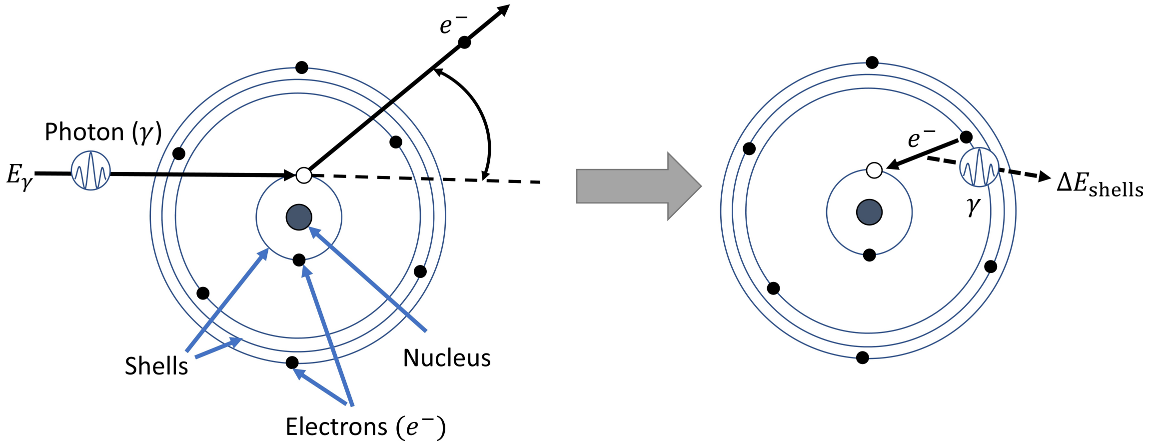

(a) Photoelectric effect

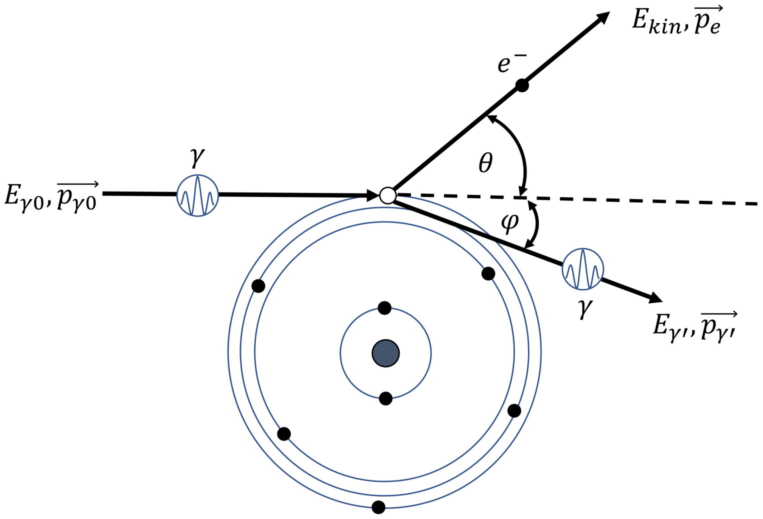

(b) Compton effect

Figure 1.3: In (a) the photoelectric effect is shown. A photon interacts with a tightly bound electron of an inner shell and transfers all its energy to the electron. The electron leaves the atomic shell and leaves behind a vacancy. The vacancy is filled by an electron of an outer shell and a photon is emitted with the energy difference of the shells (ΔE_{shells}). In (b) the Compton effect is shown. Here, a photon with energy $E_{\gamma 0}$ and momentum $\vec{p}_{\gamma 0}$ is scattered at an weakly bound electron of an outer shell. In the collision, the electron gains a part of the photon energy E_{kin} and leaves the atomic shell with a momentum $\vec{p}_e$ under an angle θ. The photon leaves the atomic shell with the remaining energy $E_{\gamma'}$ and a decreased momentum $\vec{p}_{\gamma'}$ under an angle ϕ. Both angles depend on the proportion of the photon energy transferred in the collision.

In the third interaction, the pair production, an electron-positron pair is produced from the incident photon in the Coulomb field of the atomic nuclei. For this effect, a minimum photon energy of $2m_ec^2 = 1.02\,\text{MeV}$ is required. As the x-rays used in this work have a maximal energy of 130 keV, pair production does not occur and only the photoelectric effect and the Compton effect play a role. Via both effects, free electrons and ionized atoms are induced, which can than interact with their surroundings leading to more ionizations. The free electrons can interact with other orbital electrons and thereby cause ejections of these orbital electrons or excitations of atoms. Via Coulomb interactions with the nucleus the free electrons can also produce x-ray photons (Bremsstrahlung) [25]. For low energy x-rays ($<$ 1 MeV), as used in this study, the maximum energy loss ΔE is at the entrance of the tissue and than decreases exponentially with increasing penetration depth d [26, 27]. The energy loss of photon beams is usually described by their intensity

$$I(d) = I_0 \cdot \exp(-\mu d) \tag{1.5}$$

where I_0 is the initial intensity of the photon beam and μ is the attenuation coefficient, which describes the probability of the absorption of a photon, as shown in Figure 1.2.

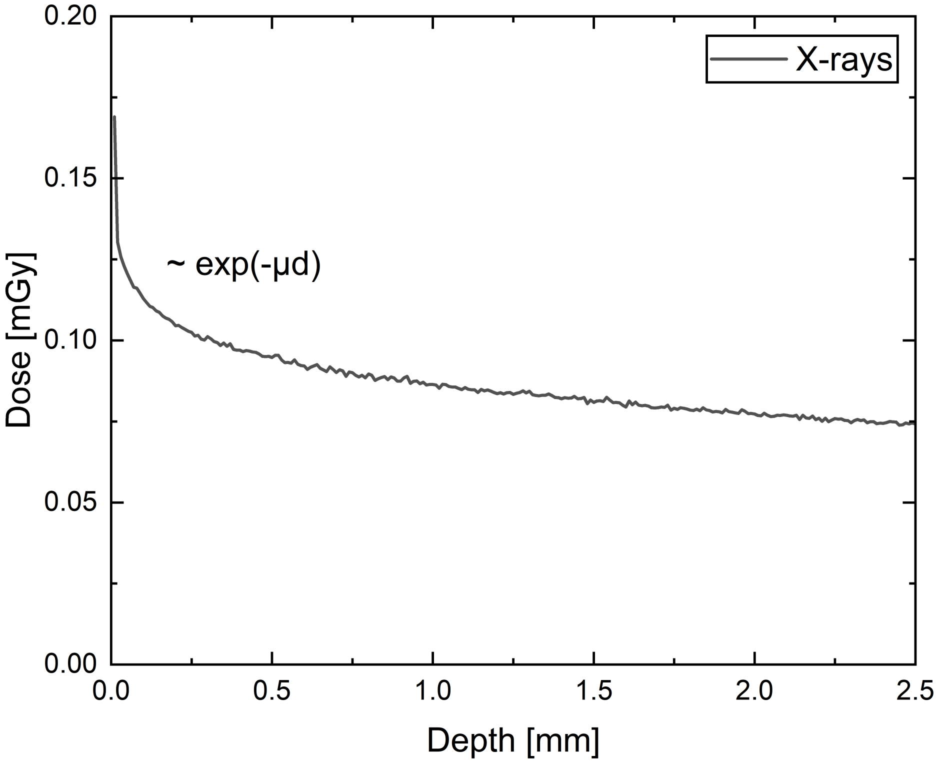

Figure 1.4: The dose deposition of an x-ray beam in water. The dose deposition was simulated with TOPAS (Version 3.8) [28] with $1 \cdot 10^8$ particles of the x-ray spectrum, shown in Figure 1.1. The simulation was performed by Aikaterini Rousseti.

For photon energies used in this work, the attenuation coefficient depends only on the photoelectric interactions and the Compton interactions and is, therefore,

$$\mu = \tau + \sigma_C. \tag{1.6}$$

Dose describes the energy deposition in a certain volume and is therefore the relevant parameter in radiobiology. In Figure 1.4, the dose deposition of an x-ray beam is plotted against the depth of a water phantom. As dose deposition and energy loss are directly correlated, this curve has a similar shape as the intensity with maximum dose deposition at the entrance of the phantom and an exponential decrease in the form of $\exp(-\mu d)$.

1.1.2 Interaction of charged particles with matter

Charged particles are surrounded by an electric field due to their charge. This electric field increases the probability of interaction with atoms close to their tracks compared to uncharged particles like photons to almost 100 % [24]. The energy loss per interaction depends on the particle energy and its mass. Heavy ions lose more energy per interaction than protons resulting in a decreased penetration depth. Therefore, more interactions are necessary to stop a proton than a heavy ion. The interactions of charged particles can be basically divided into two groups: the electronic and the nuclear interactions. The electronic interactions are based on Coulomb forces between the ion and the orbital electrons of atoms in the traversed matter. The detailed interaction mechanisms depend on the distance between the particle and an atom of the traversed matter, the energy of the incoming particle and the size ratio between the collision partners [24]. If the distance of both interaction partners is high, for example due to large atom diameters of both collision partners, the incoming particle can either interact via elastic or inelastic scattering. In elastic scattering, the incoming ion only loses a small part of its energy. The atomic shell of the atom of the traversed matter is transiently deformed. In inelastic scattering, the atom of the traversed matter is ionized or excited by the incoming particle. The incoming particle changes its direction of movement. Freed secondary electrons interact in close vicinity to the interacting atoms due to their low energy. In these both types of interaction, only small amounts of energy (a few eV) are lost and therefore, they are called soft collisions [24]. If the distance of the collision partners is smaller, it can also come to interactions of electrons in the inner atomic shells. These interaction lead to much higher energy losses and are, therefore, called hard collisions [24].

The second group of interactions, the nuclear interactions, occurs when the distances between the collision partners are even smaller. Here, the nuclei of the two collision partners can interact either by elastic scattering in the partially shielded Coulomb potential or by strong interaction in central collisions if their energy is higher than the Coulomb barrier. In the latter, single nucleons can be knocked out or even nuclear fission can be triggered.

In this thesis, ion energies of 20.5 MeV (protons) and 55 MeV (carbon ions) were used. In Figure 1.5, the energy loss induced by electronic (dashed line) and nuclear interactions (dotted line) and the total energy loss in dependency on the energy is shown for protons (black) and carbon ions (red). The used ion energies in this thesis are marked by vertical lines. In this energy regions, the energy loss is mainly induced by electronic interactions.

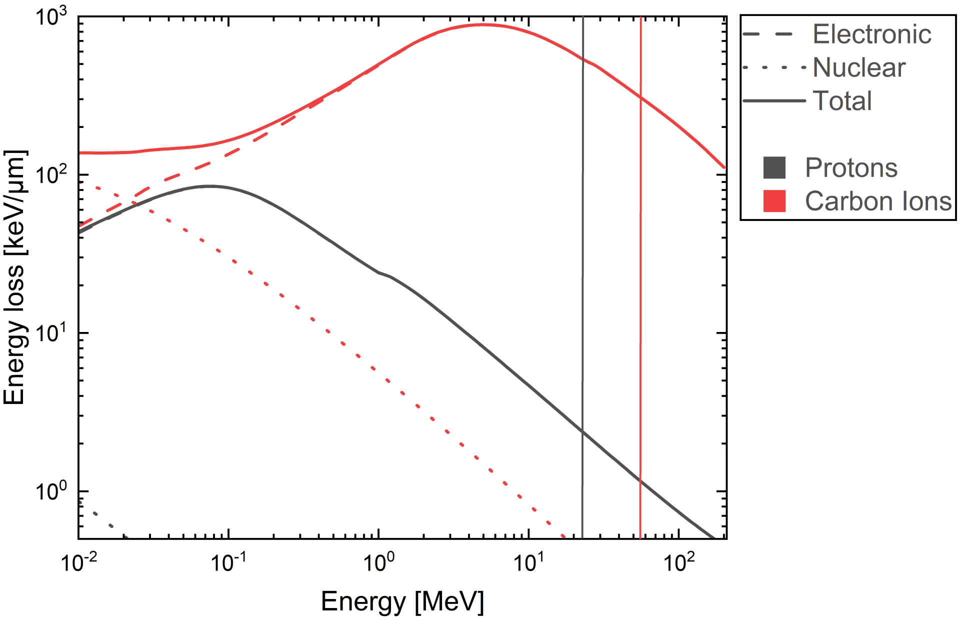

Figure 1.5: Energy loss induced by electronic (dashed line) or nuclear interactions (dotted) of protons (black) and carbon ions (red) with kinetic energies between 10 keV to 200 MeV simulated by SRIM [29]. The total energy loss is indicated by a solid line and is the sum of energy losses induced by nuclear and electronic interactions. The vertical lines indicate the ion energies used in this thesis (protons: 20.5 MeV, carbon ions: 55 MeV).

The nuclear interactions can be neglected [24]. The energy loss for this case can be described in good approximation with the Bethe-Equation [30]:

$$-\frac{dE}{dx} = \left(\frac{e^2}{4\pi\epsilon_0}\right)\frac{4\pi n}{m_e}\frac{Z^2}{v^2}\ln\left(\frac{2m_e}{I}v^2\right) + \text{relativistic terms} \tag{1.7}$$

where e is the electron charge, Z the atomic number of the particle, v its velocity, n the electron density of the target material, m_e the electron mass, ϵ_0 the electric field constant and I is the mean excitation potential of the target material. This equation also describes the typical course of energy loss, which is shown in Figure 1.6 for a 20.5 MeV proton and a 55 MeV carbon ion in water. Characteristic is here, that at the beginning of a particle track in the traversed matter, the energy loss is very small and becomes higher the deeper the particle penetrates the matter. The particle track ends in a high and narrow peak of energy loss. As carbon ions interact more often and more intense with matter along their particle tracks than protons, the energy loss per depth is higher and the penetration depth smaller than for protons.

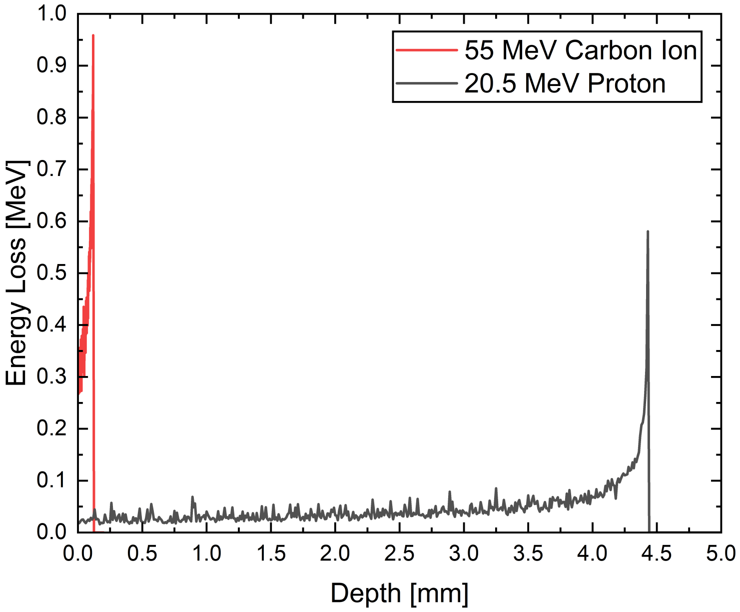

Figure 1.6: Energy loss of a single 55 MeV carbon ion (red) and a single 20.5 MeV proton (black) in different depths of a water phantom. The underlying data of both curves are simulated by using Topas (Version 3.8) [28] and provided by Aikaterini Rousseti.

Another important characteristic of charged particles are the density of ionizations. The density of particle tracks can be described by the LET (Linear Energy Transfer) and is defined as the energy ΔE which is deposited in the matter along the covered ion track of the length Δl:

$$LET = \frac{\Delta E}{\Delta l} \tag{1.8}$$

Particles like electrons and high energy protons have a low LET (LET $<$ 10 keV/µm). These particles produce usually many sparse tracks with single ionizations and only occasionally a larger cluster of ionizations [31]. High LET particles are low energy protons, alpha particles, carbon ions and other heavy ions. These particles produce usually much larger clusters along their tracks [31]. Due to stochastic characteristic of the interaction processes and the energy deposition along tracks, the dose is not homogeneously distributed. Therefore, the energy deposition can vary locally a lot, depending on, among others, the matter, the particle type, the location of the interaction and the type of interaction. The following applies here: The higher the LET the higher are spatial variations in dose deposition [32]. This variation of dose is part of the field of microdosimetry (cf. [33]). However, in most biological application a mean dose, which is deposited in a volume, is considered. This dose can be described by the fluence F, the LET and the density ρ of the target matter:

$$D = \frac{F \cdot LET}{\rho} \tag{1.9}$$

The fluence F is the number of particles that traverse a given area. In Figure 1.7, the dose deposition of a proton beam in different depths of a water phantom is shown. Similar to energy loss, less dose is deposited at the entrance of the water phantom. With increasing depth, the deposited dose increases and the maximum of dose is deposited in a peak, called the Bragg-peak. Behind the Bragg-peak no dose (protons) or small amounts of dose (heavy ions)[1] is deposited. This peak is broader than the peaks for single particles shown in Figure 1.6. This difference is due to stochastic variations in dose deposition at depth, as the interactions of the charged particles can vary between particle tracks due to material inhomogeneities and the stochastic nature of the interactions. The Bragg-peak is the main reason for the beneficial effects of using charged particles in radiotherapy. The Bragg-peak enables the possibility to deposit dose in a certain depth, where a tumor is located, while sparing the healthy tissue in front of and behind the tumor.

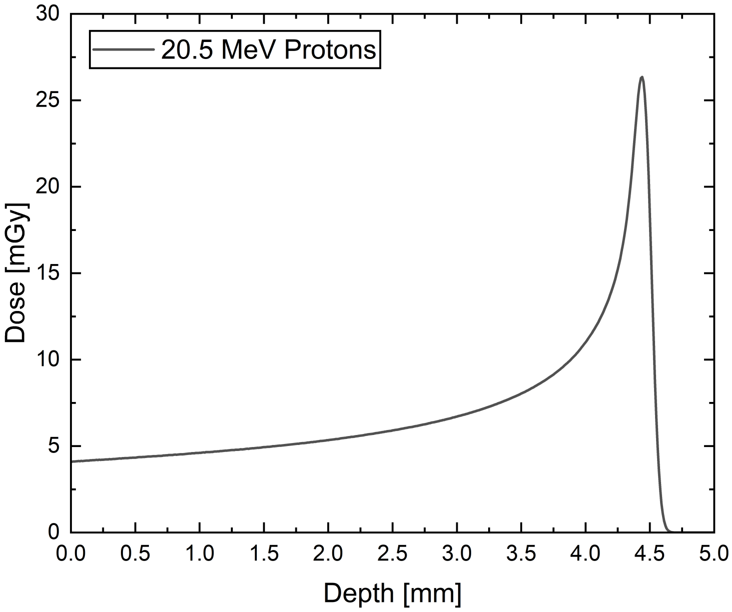

Figure 1.7: The Bragg-peak of a proton beam. The dose deposition of a 20.5 MeV proton beam of $1 \cdot 10^6$ particles is plotted against the depth in a water phantom. The underlying data are simulated by Topas (Version 3.8) [28] and provided by Aikaterini Rousseti.

1.2 Chemical interactions in biological matter after irradiation

After energy depositions in matter, the energy is distributed in the nearby environment of the location of interaction, mainly via thermodynamic processes. This can either happen by intramolecular or intermolecular energy transfer. The intramolecular energy transfer can lead to changes in the molecule structure, to dissociations of functional groups or to breaks in molecule chains. This type of interaction is called direct interaction, as biomolecules like the

---

[1] Heavy ions deposit also small amounts of dose after the Bragg-peak known as fragmentation tail. The fragmentation tail occurs when heavy ions with energies in the MeV range traverse matter and are partially fragmented. As the fragments are smaller, interactions with matter are becoming less possible and are less effective than for the original heavy ion resulting in an increased penetration depth[34].

DNA are directly damaged.

At the intermolecular energy transfer, mainly interactions with the molecules of the cell water come into play. Water molecules absorb the majority of the deposited energy in a process called radiolysis. In the radiolysis, it comes to split-offs of electrons or even to full fractures of the water molecules. Here, for instance, the following reaction process occurs:

$$H_2O \longrightarrow H^\bullet + OH^\bullet \tag{1.10}$$

where a water molecule breaks into hydrogen ($H^\bullet$) and hydroxyl ($OH^\bullet$), which are both so called radicals [24]. Radicals are uncharged atoms or molecules with one or more unpaired electrons in the electron orbits [35]. Due to the unpaired electron, radicals are highly reactive. The broken molecules, ionized molecules, radicals and free electrons react with each other and their surroundings and build new highly reactive radicals. Among these radicals, reactive oxygen species (ROS) are formed. ROS are a group of oxygen containing radicals, which interact with biomolecules via oxidation [36]. One ROS is for example hydroperoxyl ($HO_2{}^\bullet$), which is a result of the reaction of hydrogen with oxygen [24]. ROS are more reactive than other radicals and induce more complex damages at biomolecules like the DNA. Their formation is more probable in the presence of free oxygen. Therefore, free oxygen plays an important role in the radiation response. In presence of oxygen, the damage formation is increased up to a factor of three and is called oxygen effect [24]. This effect is the highest for low-LET radiation. For high-LET irradiation it plays a minor role. The oxygen effect is illustrated in Figure 1.8. For simplicity, the cells in this Figure contain only water molecules and some oxygen molecules, as water is the main component of a cell. The two cells are irradiated by high-LET or low-LET radiation, represented by one large yellow arrow or many thin orange arrows, respectively. Ionizations induced by radiation lead among others to fraction of water molecules in hydrogen ($H^\bullet$) and hydroxyl ($OH^\bullet$). High-LET radiation induces many of these radicals along the ion track, while low-LET irradiation induces sparsely distributed ionizations. For high-LET radiation, the radicals are formed in such close vicinity to each other that they interact with each other to form, for example, the ROS hydrogen-peroxide (H_2O_2). For low-LET irradiation, the radicals are formed in larger distances to each other, therefore, an interaction between the radicals is less probable [24]. The radicals interact with their surroundings, for example with oxygen, to form the ROS hydroperoxyl ($HO_2{}^\bullet$). These processes show that with increasing LET the probability of radical interaction to form ROS increases while the dependency on ROS formation promoters, like oxygen, decreases, which explains the LET-dependency of the oxygen effect [24]. In addition to the chemical reactions shown in Figure 1.8, many other reactions are involved in the formation of ROS after the radiolysis of water, but could not be shown here for the sake of clarity.

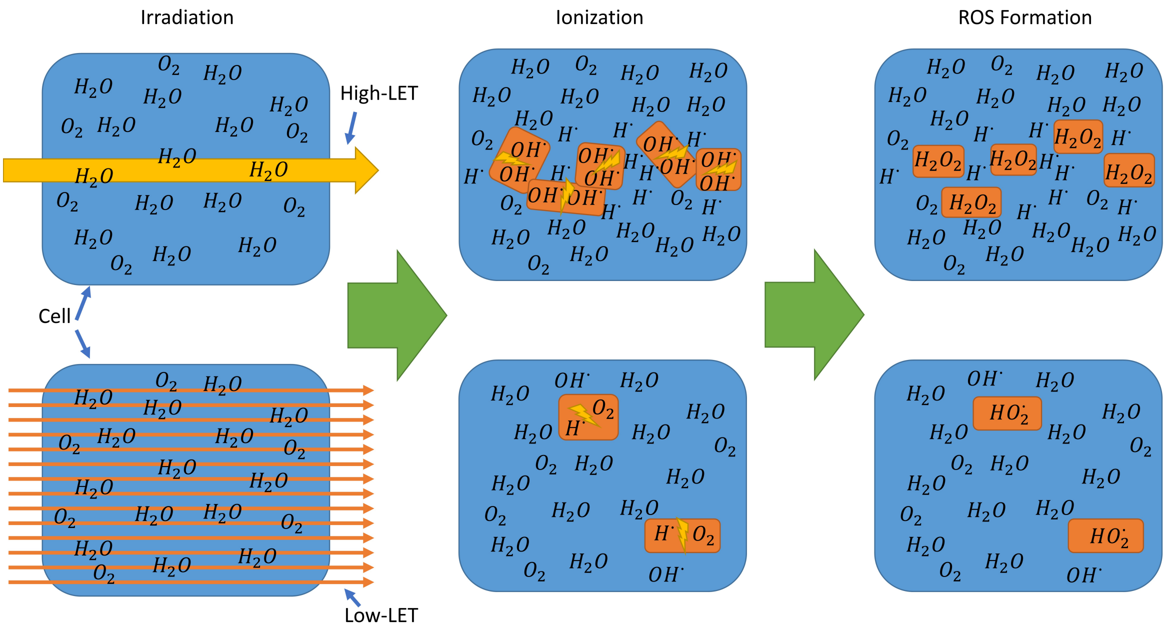

Figure 1.8: The role of oxygen in ROS formation after high- and low-LET irradiation. Cells, approximated by water and some oxygen molecules, were irradiated with high-LET (yellow arrow) or low-LET radiation (orange arrows). The irradiation leads to ionization of the water molecules, which can result in fracture of the molecules. For high-LET irradiation, the water molecules are ionized and fractured in close vicinity to each other along the ion track. Therefore, the formed radicals interact with each other, which is indicated here by the yellow lightning and thus form ROS, for instance H_2O_2. For low-LET irradiation, the ionizations producing radicals happen sparsely and ROS are formed by the interaction of the radicals with the molecules in their surrounding, for example oxygen. Oxygen is therefore an important promoter for the ROS formation after low-LET irradiation, but becomes less important with increasing LET. This is a simplified representation of the oxygen effect. There are a lot more possible ionizations and radical and ROS formations that could not be shown here for the sake of clarity.

As the damages to the biomolecules described here are formed via the radiolysis of water, these processes are summarized as indirect interaction of radiation with matter. Indirect interactions of radiation occur much more often than direct interactions, as the probability of hitting biomolecules like the DNA in a cell is much smaller than hitting water molecules due to the high water content in cells [24].

1.3 Biological response to irradiation damages

The radicals formed in the chemical interaction step react with the biomolecules in the cell, such as the DNA. These reactions lead to breaks in bondages and molecules and can result, for example, in damages of the DNA. These damages lead to structural and functional changes that determine the fate of the irradiated cell [24]. The lethality of the damages depends on the location, the amount, the density, and the complexity of the damages. Most crucial are the damages to the DNA. The DNA consists of two polynucleotide chains that form a double-helix structure. A nucleotide is one component of the polynucleotide chain and is composed of one out of four nucleobases (adenine, cytosine, guanine, or thymine), a sugar part deoxyribose and a phosphate group. Hydrogen bonds connect the two polynucleotide chains between the nucleobases. The DNA can be damaged either directly by an ion traversal or indirectly by radiation-induced radicals. These interactions with the DNA can then lead to damages on nucleobases, to single strand breaks (SSB) or double strand breaks (DSB). In SSBs, only one polynulceotide strand is harmed and can usually be repaired. Furthermore, interactions with DNA can result in breaks in both strands, either by direct particle interaction or by a clustering of nearby SSBs ($<$ 10 base pairs apart), which add up to a complete break in the DNA. There are a lot of repair strategies for these DNA damages. The success of the repair of these depends on the complexity, size and location of the damage. High LET irradiation induces more complex damages than low LET irradiation. Consequently, these damages are harder to repair[32]. Not or incorrectly repaired damages in the DNA lead to mutations or cell death. The cytoplasm, on the other hand, can bear a lot of irradiation damages. Nevertheless, damages which impair the functionality of organelles can also lead to tremendous dysfunctions of the whole cell [37].

A tissue consists of many cells. To understand how tissue reacts to radiation, the behavior of every single cell and the cells interplay with each other are most important in the radiobiologic research. Therefore, radiation effects on clonogenic cell survival, cell cycle and cell death are described in the following.

1.3.1 Clonogenic cell survival

Cells that have the ability to proliferate are called clonogenic cells. In the tissue, especially in tumors, these cells are responsible for the growth and the survival of the tissue. Therefore, it is the aim of radiotherapeutic treatment to remove these cells in order to hinder the tumour from survival. The clonogenic survival is usually measured by a colony forming assay (CFA). In the CFA, a defined, but low, number of cells is seeded after treatment in a cell culture container. Then, the cells are incubated for several days to form colonies. By default, a colony in this assay contains more than 50 cells [38]. Then the colonies are fixed, stained and counted. The clonogenic survival fraction (SF) is calculated as the percentage of seeded cells, which were able to form a colony. Performing the CFA for different doses results in a so-called cell survival curve. This curve is typically fitted by the linear-quadratic (LQ) model:

$$p(survival) = exp(-\alpha D - \beta D^2) \tag{1.11}$$

where $p(survival)$ is the probability of a cell to retain its ability to proliferate, D is the dose in [Gy], and α and β are fitting parameters with the units [Gy^{-1}] and [Gy^{-2}]. $p(survival)$ equals the $ln(SF)$. The cell survival curve has the shape of a shoulder on a semi-logarithmic scale with different bendings depending on the cell-model[2]. Exemplarily, cell survival curves are shown in Figure 1.9. The LQ-model is widely used in either clinical as also radiobiologic applications and is able to describe well the responses to radiation in-vitro and in-vivo [32].

---

[2] A cell-model includes cells of a cell line that are used for testing specific endpoints. A cell-model is used to study a specific scenario like the treatment of an illness there the tissue is modeled by cultured cells.

Another advantage of this model is its simplicity and intuitiveness. The mechanistic interpretation of this model is still under ongoing discussion. A general interpretation is that the linear component $exp(-\alpha D)$ serves as a description of directly induced DSBs, which increase linearly with dose. The quadratic component $exp(-\beta D^2)$ can be seen as the increase of DSBs based on accumulated SSBs (on a region $<$ 10 base pairs) [39]. Therefore, the ratio α/β can be seen as a measure for the directness of damage or the radiosensitivity. For high LET irradiation or at cell-models with a high radiosensitivity, the α/β-ratio is high, which results in a less bent curve on a semi-logarithmic scale, as shown by the red curve in Figure 1.9. Whereas, the α/β-ratio is low for low LET irradiation or for a low radiosensitivity of the cell-model [32, 40–42]. Here, the survival curve has a shoulder-like shape, as shown by the black curve in Figure 1.9. As discussed from S.J. McMahon [42] in 2018, the LQ-model fits well for most purposes in radiobiology for doses up to 5 Gy till tens of Gys depending on the cell model. Above these doses, a more linear shape of the survival curve would be more appropriate [43]. Also complex biological behaviors like the cell cycle dependence of radiosensitivity in cell populations with asynchronous cell cycles cannot be fully described requiring a more complex model [42].

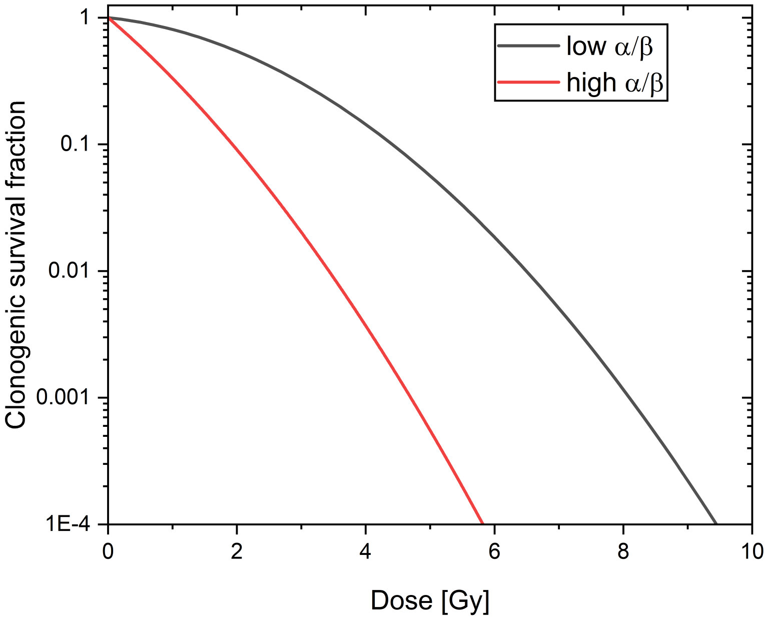

Figure 1.9: Two examples of cell surviving curves. In black, the cell survival curve for a cell-model with a low α/β-ratio is shown and in red for a cell-model with a high α/β-ratio. Different treatment sensitivities of different cell-models or different treatments with different efficiencies tested on the same cell model can lead to different α/β-ratios. For example, the irradiation with high-LET particles lead to a higher α/β-ratio than the irradiation with low-LET particles on the same cell-model.

1.3.2 The cell cycle and its role in radiosensitivity

Every cell undergoes several cell cycles during its whole lifetime. In each cell cycle, the cell divides into two daughter cells. The number of these cycles is limited in healthy cells, which also limits their lifespan. Tumor cells overcome this restriction and can be considered to have an endless lifetime.

The cell cycle is shown in Figure 1.10 and consists of four stages: The G_1 phase, S phase, G_2 phase and the M phase. In the G_1 phase, also called growth phase, the cell resumes biosynthetic activities on a high rate, which had been slowed down during the preceding M phase. The cell increases its supply of proteins and the number of organelles, such as mitochondria and ribosomes, and grows in size. Furthermore, the cell prepares for the DNA synthesis, which takes place in the S phase. The cell spends approx. 40 % of its cell cycle in the G_1 phase [44, 45]. In the S phase, the DNA is synthesized. This process implies the reading and duplication of the DNA via protein complexes and takes place at various locations of the DNA at the same time [46]. Upon its completion all chromosomes have been replicated. Protein synthesis is slowed down. This phase occupies about 30 % of the cell cycle [44, 45]. In the G_2 phase, the protein synthesis and cell growth is increased. The cell prepares for the M phase, where the cell division takes place. These preparations also include the reorganization of the microtubules to form a spindle apparatus, which is needed in M phase. The cell spends about 25 % of the cell cycle in the G_2 phase and only 5 % in the M phase [44, 45]. In the M phase, also called mitosis, the replicated chromosomes are separated into two cell nuclei. In this process, the DNA is condensed into densely packed chromosomes. These chromosomes have an X-like shape. The two strands of a chromosome are separated and dragged towards both sides of the cell nuclei by the spindle apparatus. First, the cell nucleus is separated into two nuclei and then the actual division of the whole cell takes place. Hereby, cytoplasm plus membrane containing cell nuclei and organelles are equally distributed and separated, which is called cytokinesis, resulting into two identical daughter cells. With the end of mitosis, the entire cell cycle is completed and starts all over again for both daughter cells.

Cells can also stop dividing and enter the G_0 phase from the G_1 phase. In the G_0 phase, the cells rest. Cells can remain for different amounts of time in this phase of quiescence. Cells, which remain permanently in G_0 phase are called senescent cells [47, 48]. Reasons for entering this phase can be stress and damages, especially to the DNA, e.g. induced by irradiation. Additionally, cells enter this phase for differentiation [49]. Cells can also arrest in the other phases of the cell cycle. The decision if a cell arrests or goes on in the cell cycle is mediated via checkpoints at different time points within the cell cycle. The checkpoints are shown in Figure 1.10 as red arrows. At these checkpoints it is checked whether DNA damages have occurred. Cells with DNA damages then go into arrest. The arrest allows the cell more time to repair its damages and prevents the conversion of lesions into more deleterious lesions through replication or mitotic processes [32].

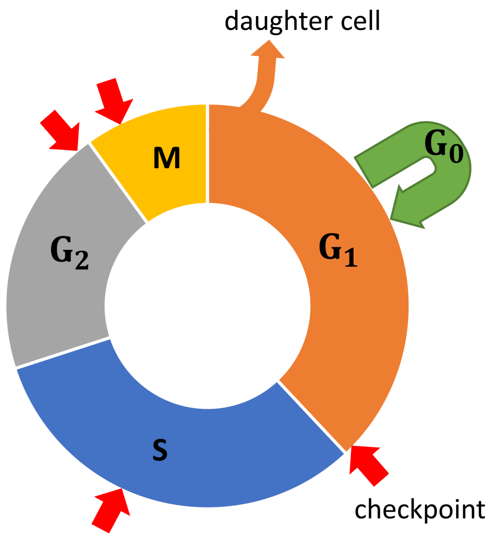

Figure 1.10: A schematic image of the cell cycle. The checkpoints are indicated by red arrows.

The radiosensitivity of cells varies considerably during the cell cycle. Studies have shown that cells are most resistant to irradiation in the late S phase while they are most sensitive in the very late G_2 phase and the M phase [32, 50]. It could be shown on synchronized Chinese hamster cells (CHO) that the difference in radiosensitivity of cells in different cell cycle stages creates a degree of synchrony in the cells which survive the irradiation [50]. Some of the cells lost their reproductive integrity due to irradiation. How fast and if the cells retain their reproductive integrity depends on the cell cycle phase they are in during irradiation. Cells irradiated in S phase are able to retain faster and therefore reach the next M phase faster than cells irradiated in M phase. Some time after irradiation, the surviving clonogenic cells will show the same distribution over the cell cycle as before the irradiation. This process is called redistribution [32, 51].

Usually, cells divide every cell cycle into two identical daughter cells. Occasionally, it can come to abnormalities in the cell cycle caused, for example, by external stressors like radiation. The cell division can result into multi-daughter mitosis, where cells divide into more than two cells [52]. On the other hand, a cell can fail to separate its membrane and cytoplasm during mitosis resulting in a binucleated cell with two cell nuclei [52]. The control checkpoints of the cell cycle are responsible for detecting abnormalities and damages in the cell and for inducing repair or in the lethal case apoptosis of the cell. Therefore, these checkpoints prevent the cell from continuing through the cell cycle with deleterious lesions. These checkpoint mechanisms may become non-functional due to radiation damage, mutations, or stress. These lost cell cycle regulations can then lead to these abnormalities in cell division [53, 54]. Furthermore, they are characteristic for precursors of tumors [54].

1.3.3 Cell death

There are many different mechanisms by which cells can die. The most prominent one is apoptosis. This form of cell death is also referred to as programmed cell death. Apoptosis is highly regulated and can be initiated either as a result of conditions occurring within the cell itself (such as DNA damages) or from signals generated externally such as those from surrounding tissue or immune cells [55]. It can be seen as ‘choice’ the cell made as a consequence of damage, stress or as a barrier against tumourigenesis. It is an important process for growth regulation in tissues. As a result, several human diseases, including cancer, are associated with alterations in apoptosis. Morphologically, apoptosis can be recognized by membrane blebbing, condensation and digestion of the DNA into small fragments. In apoptosis, the cellular contents are fragmented and enclosed in membrane, which form the characteristic bubbles. Therefore, this enclosed digestion of the cell spares the surrounding cells in tissue from potentially damaging cellular proteins. In tissue, the membrane enclosed apoptotic bodies are removed by phagocytes, which are cells that ingest harmful substances like bacteria to protect the body [32].

Another form of cell death is autophagy. This term means ‘self-eating’ and describes a process in which cells digest parts of their own cytoplasm in order to generate small macromolecules and energy. Autophagy is induced, for example, as a response to growth factor or nutrient removal (starvation). After its activation, the double membrane structure is formed, that engulfs cytoplasmic components forming cytoplasmic filled vacuoles called autophagosomes [56]. These are degraded by lysosomes, small organelles containing enzymes for digesting different substances, into primary components and energy that can be used to fuel the metabolism. The aim of autophagy is to sustain the overall cell survival during times of low nutrient environment. Although autophagy has a pro-survival role, the deregulated activation can lead to a distinct form of cell death. Morphologically, it is very similar to apoptosis, but without caspase activation or DNA cleavage [32].

Cell death by necrosis is considered to be an inappropriate or accidental death. It occurs under conditions that are extremely unfavorable, for example, extreme pH changes, energy loss or ion imbalances. Subsequently, necrosis can be seen as an uncontrollable, chaotic and irreversible form of cell death. It is characterized by swelling of the whole cell, membrane deformation, organelle breakdown and the release of different enzymes that attack the cell. These processes can induce infection and inflammation in tissue. Necrosis can be frequently observed in tissue after treatment with DNA damaging agents including irradiation [32].

The mitotic catastrophe can also be seen as a form of cell death. The mitotic catastrophe is a result of aberrant mitosis. This type of cell death occurs when cells proceed through mitosis in an inappropriate manner, i.e. cells enter mitosis with unrepaired or mis-repaired DNA damages. The reason for this are failures at the cell cyle checkpoints. Such checkpoint failures frequently happen after irradiation due to induced DNA-damages. The mitotic catastrophe can also serve as a trigger for other cell death pathways. As it can result in cell fusion, polyploidy and failure of cytokinesis, these processes lead, subsequently, to cell death by apoptosis, senescence, autophagy or necrosis. Morphologically, it is associated with the formation of multinucleated, giant cells and with the presence of chromosome aberrations and micronuclei [32].

The importance of different types of cell death after irradiation is a subject of frequent debates in radiobiology to predict radiation response in tissue. However, different cell death pathways can be induced in a cell simultaneously, but the cell dies preferably by the most rapid pathway, as it can die only once. Therefore, the investigation of cell death types gives only limited information about the reason for the cell death. M. C. Joiner and A. J. van der Kogel [32] suggest that it is less important to consider how cells die after irradiation, but rather why cells die. They further conclude, that the cell deaths should be classified into cell deaths that occurred relatively soon after irradiation and before cell division and cell deaths that occurred comparatively late or after cell division. The early, also called pre-mitotic, cell death class, can be observed in rapidly proliferating cell lines [32]. A pre-mitotic cell death occurs due to activation of cell death pathways in response to the initial cellular damage, for example through cell cycle checkpoints or when the cellular structure, e.g. the membrane, is damaged [32]. The vast majority of cells die after attempting one or more mitoses and belong so to the late cell death group, also called post-mitotic [32]. Here, a cell activates both cell cycle checkpoints and DNA repair. However, the cell is unable to induce apoptosis due to failures in this pathway [32]. Instead the cell tries to repair the DNA damages. The repair of complex lesions like DSBs in the DNA can lead to incorrect connections of two fragmented DNA strand ends. Such events can result in the formation of dicentric or acentric chromosomes [32]. Usually, chromosomes in the condensed state during mitosis have one center where the two strands of a chromosome are separated during mitosis. When a chromosome has more than one center or no center, then the cell struggles to undergo mitosis and might end up in mitotic catastrophe [32]. However, the cell might be able to proceed few cell cycles despite its deleterious lesions, but only with a loss of genetic material present as an acentric fragment of a chromosome. These acentric fragments are enclosed by the cell in small additional nuclei called micronuclei that are removed from the cell. This loss of genetic material may subsequently result in cell death [32].

There is one cell death form left, which is also described as response to radiation: the bystander-induced cell death. It describes the death of a cell that has not been irradiated itself, but has contact to irradiated cells and shows a similar response as the irradiated cells. This phenomenon could be described in several experiments and is not limited to cell death but occurs also in other biological radiation responses including DNA-damage, chromosomal aberrations, mutation, transformation and gene expression [57–60]. It has been observed in cells that have direct contact to irradiated cells, but also in unirradiated cell populations, which received the culture medium[3] of irradiated cell populations [61]. This leads to the assumption that the cells secrete factors that can be damaging to non-irradiated cells [32]. Also

---

[3] The culture medium is a nutrient solution used for in-vitro cultivation of cells.

a communication through direct connections like tunneling nanotubes [62] and gap junctions [63] are conceivable. However, the underlying mechanisms of the bystander effect are poorly understood yet and are subject of current research.

1.4 Response of tissue to radiation

Tissues are complex, well organized structures of differentiated cells. Each tissue has its own specific purpose or function. The response of tissue to radiation depends on its organization, the applied dose and the targeted volume. Furthermore, these parameters can be combined within the concept of functional subunits (FSUs). A FSU is defined as the maximal tissue volume that is able to recover from one surviving clonogenic cell without the loss of functionality of the tissue [64]. Therefore, the FSU gives the density of clonogenic surviving cells that is necessary to fully regenerate the tissue. FSUs are organized either in parallel or in series. In parallel tissue, the FSUs are independent of each other and only a minimum amount of FSUs is necessary to keep the tissue intact. Contrarily in serial tissue, the malfunction of one FSU is critical for the functionality of the whole tissue. However, no organ or tissue can be purely categorized as serial or parallel. Most of the tissues have properties of both groups with a tendency towards one of them [32]. This description of tissue organization can only be applied in healthy tissue, as tumour tissue has no vital function or structural benefit.

The tissue-response to radiation can be subdivided into early tissue reactions and chronic late reactions. The radiation-induced damages in the cells lead to necrosis and malfunction of the damaged cells, which also impairs the functionality of the entire tissue. This induces the humoral immune response, the part of the immune system, which is based on the fluids in the body, e.g. blood and lymph. As part of this response, macrophages are activated, which can remove, for instance, lethally damaged, mutated and necrotic cells in a process called phagocytosis. Furthermore, macrophages can activate T-lymphocytes. T-lymphocytes trigger inflammation reactions. They are, for example, responsible for increasing the blood flow by dilatation of the local blood vessels. Both, macrophages and T-cells communicate with and stimulate each other and their surroundings via cytokines. Cytokines are signal proteins of the cells that regulate different cell responses, the growth, and differentiation of cells [32].

The cytokine tumor necrosis factor α (TNF-α) is, for instance, released by macrophages to alert other immune cells in case of a damage event [65]. An increased local concentration of this cytokine leads to inflammation reactions in the surrounding tissue like swelling, reddening and hypothermia [66]. TNF-α also stimulates the phagocytosis in macrophages [67], inhibits the tumor formation [68] and viral replication [69]. After irradiation, TNF-α protein levels are elevated during the inflammation reaction [70].

Other important cytokines in the immune reaction are the interleukin 1α (IL-1α) and interleukin 1β (IL-1β). IL-1α is part of the activation pathway of TNF-α and is mainly produced by macrophages [71]. Due to its synergism with TNF-α, it also promotes inflammation reactions

[72]. IL-1β induces an increase of neutrophil granulocytes [73], which can also perform phagocytosis, and thrombocytes [74], which play a major role in hemostasis, and other cytokines like interleukin-6 [75]. Both IL-1 cytokines are directly upregulated by ionizing radiation [76]. IL-1β protein levels are increased immediately after irradiation and remained chronically elevated, while IL-1α increases slowly with time after irradiation [76]. Furthermore, these cytokines promote early dermatitis and fibrosis in skin after irradiation [76]. Dermatitis describes the inflammation of the upper part of the skin known as dermis. It is often accompanied by symptoms like itching, reddening, swelling and purulent discharge that lead to crust formation. Fibrosis is defined as irreversible damage to the structure of the skin. Fibrosis manifests in permanent loss of skin flexibility, stiffness and scarring of the tissue and leads locally to a loss of function of the affected skin tissue [32]. In patients, the fibrotic skin tissue can generate discomfort, pain and restrictions on movements [77, 78].

In the inflammation reaction, also the tumor growth factor β (TGF-β) plays an important role. TGF-β is produced mainly by platelets, but also by macrophages and T-lymphocytes [79] and has three distinct isoforms (TGF-β1, TGF-β2, and TGF-β3) [79]. While TNF-α, Il-1α and IL-1β trigger and support inflammation reactions, TGF-β has an anti-inflammatory effect on macrophages and thus regulates the immune response [80]. It promotes the healing process by inducing fibrosis [80]. Furthermore it hinders the proliferation of mutated cells by inducing apoptosis [73]. After irradiation, TGF-β, especially TGF-β1, is involved in the acute inflammatory phase, during tissue repair and in late and chronic responses [79]. Since the here described cytokines are strongly involved in the radiation response, they are important marker proteins to investigate inflammation reactions after irradiation. These cytokines can, for example, be measured in blood, but also directly in the tissue. As these cytokines react on different time scales after irradiation, especially monitoring over larger time scales is of great interest for understanding the inflammation processes over time.

The inflammation reactions together with cell death and malfunction of cells in the irradiated tissue can lead to a breakdown of the tissue structure and the loss of functionality of the tissue. Due to the breakdown of the tissue structure, secondary infections can be developed as protective tissue barriers are damaged. These processes are accompanied by healing. The healing process can either be performed by surviving stem cells within the irradiated volume or by stem cells of unirradiated sites migrating into the irradiated volume. Depending on the irradiated dose, an imbalance between cell production and cell death can occur, with more functional cells being lost than can be recruited and produced. Subsequently, this imbalance results in a progressive underdevelopment of the tissue accompanied by a loss of functionality. In skin, for example, this imbalance is responsible for the formation of dry and moist desquamation [32]. The dry desquamation is the shedding of the outer skin layers [81]. The moist desquamation is characterized by the release of wound fluid [82]. When blood and other exudates dry, a protective crust is formed [82].

In the late tissue response, the organization of the tissue comes into play. While skin acts mostly as a parallel organ [83], small blood vessels are serially organized [32]. In blood vessels, the irradiation leads to changes of the vessel walls, formation of blood clots, and occlusion of capillaries. Tissue damages in the surrounding of blood vessels result in loss of smooth muscle cells. Subsequently, enlarged blood vessels develop, which also contribute to the reddening of the tissue, what can be observed for example in skin tissue. Next to reddening, also dry and moist desquamation occur in irradiated skin tissue. Furthermore, hair follicles can be transiently or permanently destroyed. Ir-repairable damages result also in chronic fibrosis.

Chapter 2

Proton-FLASH irradiation

2.1 Dose rate dependence of radiation effects

The dose rate is along with the applied dose, the radiation type, the LET and the target type one of the key factors that influence the outcome of a radiation treatment in biological matter. It is defined as:

$$DR = \frac{D}{t} \tag{2.1}$$

where DR is the dose rate, D the applied dose and t is the duration of the exposure. The dose rate describes, therefore, the amount of radiation energy, which is deposited in a certain time in the target matter. As time is a component of the dose rate, the time structure of the different processes caused by irradiation of biological matter is responsible for the outcome of the radiation effects. These processes were discussed in Chapter 1 in detail.
The exact sequence of these processes can be divided into several temporal steps, which are illustrated in Figure 2.1.

The first step is the physical step. This step covers a time span of up to 10^{-15} s [84, 85]. Within this period, the interactions occur on an atomic level. The irradiation induces ionizations in the shells of atoms and molecules or lead to excitations of the electron states within the shells. In the physico-chemical step between 10^{-15} s and 10^{-12} s, these processes lead to molecular dissociations like separation of electrons, bondage breaks in molecules and formation of ionized molecules. These fractured molecule components can then interact with each other and their surroundings and form radicals. These radicals interact in the late chemical step with biomolecules like the DNA and damage them. The chemical step takes place in a time range from 10^{-12} s to 1 s [84, 85]. In the biochemical step, the cell reacts to the occurred damages by locating them. Also the repair of damages is initialized in this step. After an hour, cellular responses can be observed, like cell signaling, redistribution of the cell cycle and cell death. These responses influence the tissue. For example, the tissue reacts with repopulation by recruiting healthy unirradiated cells to replace lethally damaged cells in the irradiated tissue [84, 85].

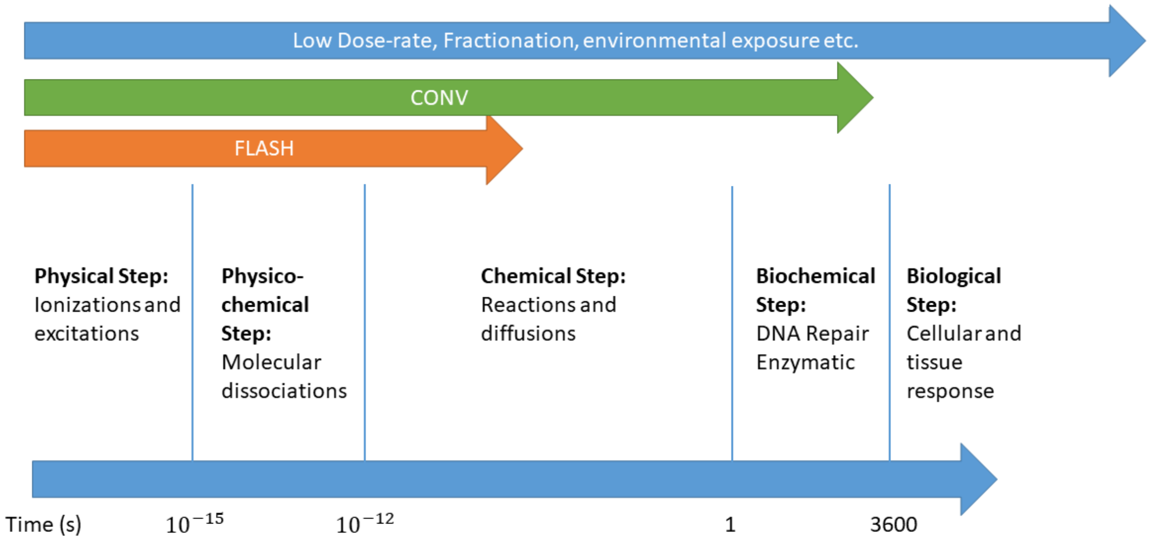

Figure 2.1: The temporal steps of the radiation response in biological matter. The exposure durations of the different irradiation methods are indicated by arrows at the top of the figure. CONV stands for irradiation with dose rates conventionally used in radiotherapeutic treatments (0.01 - 1 Gy/s). FLASH means irradiation with ultrahigh dose rates (> 30 Gy/s). Adapted from [10] with permission.

Conventionally, irradiation durations range from several minutes to one hour, as indicated by CONV in Figure 2.1. Here, the biochemical step is reached, where the cell responds to irradiation. If the exposure duration approaches one hour, considerable repair takes place, which can be influenced by the ongoing irradiation. In irradiation schedules much longer than one hour, for example, low dose rate brachytherapy, fractionation or environmental exposure, cells are able to repair themselves completely during the exposure. Due to the small dose rates, the doses applied in a certain time interval are smaller, therefore the repair of the cells is less complex and cells are able to recover fully during the irradiation. Therefore, the tissue is less damaged and the radiation side-effects are decreased compared to conventional dose rates. On the other side, FLASH irradiation is performed with dose rates > 30 Gy/s. Therefore, such irradiations are in the range of several milliseconds to 1 second. In this range, the chemical step takes place, while the biochemical step can not be reached during irradiation [84, 85]. FLASH dose rates are considered to spare tissue compared to conventional dose rates. The underlying mechanisms for the FLASH effect are still unclear and are intensively investigated.

2.2 The FLASH effect

In 2014, Fauvadon et al. coined the term FLASH irradiation to describe irradiation treatment with ultra-high dose rates (> 40 Gy/s) in their publication [6]. As presented in there, they irradiated C57BL/6J mice through bilateral thorax irradiation with a single dose of 15 Gy or 17 Gy of ^{137}Cs γ-rays at a conventional dose rate of 0.03 Gy/s (CONV) or with 17 Gy of 4.5 MeV electrons at a FLASH dose rate of 60 Gy/s. They tested the radiation-induced damages to the lung 8, 16, 24, and 36 weeks post-irradiation. Their results demonstrate a complete lack of acute pneumonitis and late lung fibrosis in the FLASH treated mice while 100 % of CONV treated animals developed pulmonary fibrosis. Moreover, they tested the effect of

FLASH versus CONV irradiation in two xenografted tumor models in mice. In a xenografted tumor model, tumor cells are implanted in immunodeficient mice, where they form a tumor. In this case, human breast cancer cells and human head and neck cancer cells were implanted. The irradiation with either FLASH or CONV dose rate at doses of 17 Gy and 25 Gy yielded an equivalent tumor control in both treatments. These results show, that FLASH is a tissue sparing effect in healthy tissue and is as effective in tumor control as conventional treatments.

Therefore, FLASH has the potential to widen the therapeutic window of radiotherapy, as due to the sparing effect of the healthy tissue higher doses could be administered to the patient to achieve a better tumor control. On the other hand, side effects in healthy tissue could be reduced, which would improve the life quality of cancer survivors. Because of these findings and the great potential FLASH offers, this dose rate effect has been highly investigated. It could be confirmed in several in-vivo studies on various animal models using different treatment methods.

For instance, the FLASH effect is observable in different organs. D. A. Simmons et al. [86] investigated the FLASH effect on the response to 30 Gy whole brain irradiation with 16 or 20 MeV electrons with dose rates of 200 or 300 Gy/s for FLASH and 0.13 Gy/s for a conventional dose rate to C57BL6/J mice. Novel object detection and object recognition were tested and it was found that FLASH reduces the cognitive impairment and associated neurodegeneration compared to the conventional dose rate. Levy et al. [9] found that abdominal FLASH irradiation reduces the radiation-induced gastrointestinal toxicity compared to a conventional irradiation. Here, the abdomen was irradiated with a 16 MeV electron beam with a FLASH dose rate of 216 Gy/s and a conventional dose rate of 0.079 Gy/s.

Also in higher mammals, a FLASH-effect could be found. Vozenin et al. [10] irradiated the skin of a mini-pig on different sites with doses ranging from 22 to 34 Gy with a conventional dose rate of 0.08 Gy/s or a FLASH dose rate of 300 Gy/s. At the skin sites irradiated with a conventional dose rate, the hair follicles were permanently destroyed and the skin showed a severe late skin fibronecrosis, which results in skin contraction. In the FLASH treated skin, the hair follicles remained intact and no skin alterations could be observed.

A tissue sparing effect can also be induced by applying FLASH dose rates with x-rays, protons and carbon ions. Montay-Gruel et al. [15] performed 10 Gy whole brain irradiations with synchrotron generated x-rays. Mice irradiated with FLASH dose rate (mean dose rate of 37 Gy/s and peak dose rates of up to 12,000 Gy/s) did not induce memory deficits. Furthermore, the hippocampal cell-division impairment was reduced and less reactive astrogliosis[1] occurred than in treatments with conventional dose rate (0.05 Gy/s). Cunningham et al. [16] irradiated the hind legs of mice with a 250 MeV proton beam with 35 Gy and dose rates of

---

[1] Reactive astrogliosis is an abnormal increase of astrocytes. Astrocytes are cells of the central nervous system that provide nutrients. The increase of these cells occurs as a reaction, for example, to the destruction of nearby neurons, trauma or infection [87].

1 Gy/s, 57 Gy/s and 115 Gy/s. The leg contracture and the skin toxicity were significantly reduced for the two FLASH dose rates compared to the conventional dose rate. Tinganelli et al. [19] injected osteosarcoma cells in the posterior limb of mice and allowed tumors to form for 7 days. Both hind limbs were irradiated with 240 MeV/n carbon ions with a dose rate of 120 Gy/s or a dose rate of 0.3 Gy/s. At both dose rates, the tumor control was successful. However for the FLASH dose rate, the structural changes in muscles were decreased and less lung metastases were formed.

As the FLASH effect is readily generalizable to different organs, species, and particle types, it has already made its way into the clinic. Konradsson et al. [88] treated 13 canine cancer patients and in 2019 the first human patient was treated by Bourhis et al. [89]. Theses studies were performed on electron beam lines. These linacs can be easily modified towards FLASH dose rates as for example presented in [90]. Due to the rather small penetration depth of electrons in tissue, this treatment method can only be applied for superficial tumors. To overcome this restriction, the use of very high energy electron (short: VHEE, with energy range of 100 to 250 MeV) beams is necessary and its modification towards FLASH dose rates is currently investigated [91, 92]. Deep seated tumors are typically treated with protons or x-rays. In coorperation with Varian, a Siemens Healthineers Company, two clinical trials FAST-01 [93] and FAST-02 [94] are performed at the moment. Here, the feasibility of the workflow and tissue side-effect reductions are tested by using proton-FLASH. The production of ultra-high dose rate x-ray beams is very challenging, as it is limited by the heat deposition of the electrons in the target of the x-ray tube. Therefore, FLASH x-ray beams have not been translated into clinics yet [95].

2.3 Requirements for inducing a FLASH effect

To be able to fully exploit the FLASH effect in clinical applications, the requirements for inducing such an effect must be investigated. The most important factor for inducing a FLASH effect is considered to be the dose rate. In literature, it is stated that a dose rate of > 40 Gy/s is necessary to induce a FLASH effect.

In Figure 2.2, the dose rates are listed at which a FLASH effect could be measured in-vivo in comparison to a conventional dose rate. The underlying data for this figure were collected via PubMed from in-vivo FLASH studies and are listed in the appendix Table A.1. Every star indicates a dose rate that induced a tissue sparing compared to a conventional dose rate (< 1 Gy/s). The coloring of the stars indicates the doses that were applied during irradiation. Clinical studies were not included here because of the lack of a direct comparison with a conventional dose rate administered in one fraction. In this figure, it can be seen that dose rates > 40 Gy/s induced a FLASH effect either for protons and for electrons. Furthermore, a FLASH effect was found in a high range of dose rates for electrons. Due to a better visualization, dose rates above 1100 Gy/s were not included. Dose rates in the range of several 10^5 Gy/s [96, 97] and several 10^6 Gy/s [7, 8, 98] were also shown to induce a FLASH effect. Yet no upper limit of dose rates could be found.

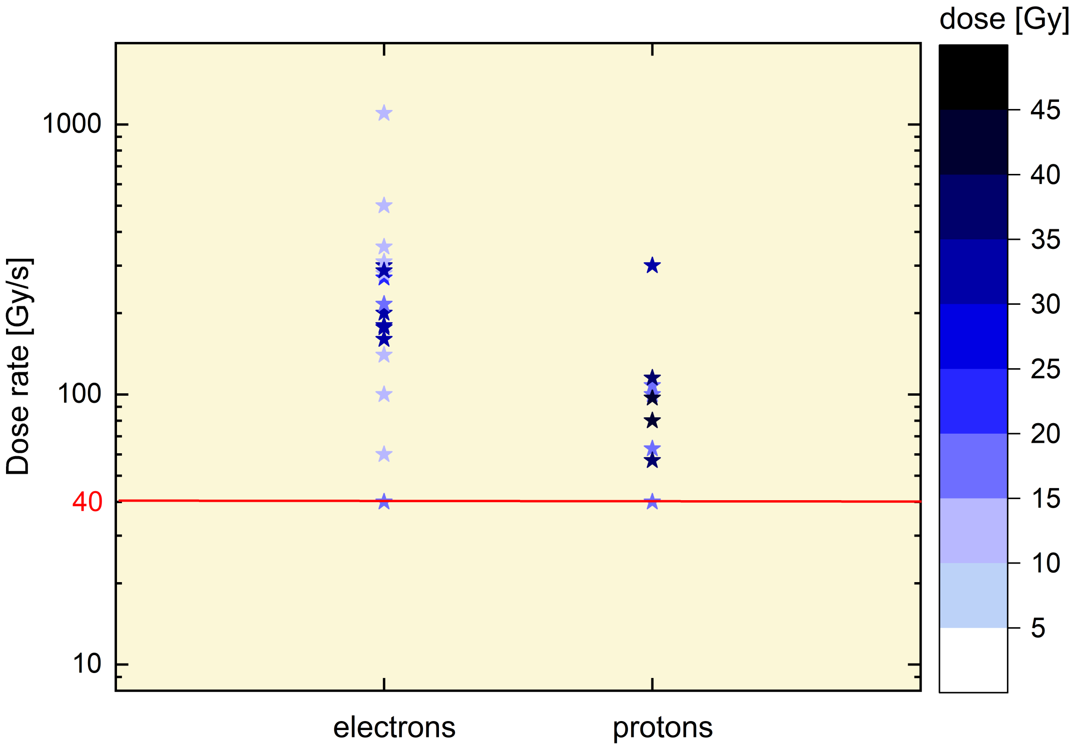

Figure 2.2: Dose rates at which a FLASH effect was observed in-vivo. All in-vivo FLASH studies according to PubMed were collected until February 2023. A list of these studies can be found in the appendix. Dose rates that induced a tissue sparing effect compared to a conventional dose rate were collected from these studies. In cases of pulsed dose rates, the mean dose rate was taken. Every dose rate is marked by a star. The color of the star indicates the dose, which was applied during irradiation. The underlying data to this figure are listed in Appendix Table A.1

Dose rates < 40 Gy/s were found to induce no FLASH-effect. For example, Montay-Gruel et al. [8] showed that the FLASH effect starts at a dose rate of 30 Gy/s with a small, not significant increase of tissue sparing, it increases with increasing dose rate until it plateaus at a maximum tissue sparing for dose rates > 100 Gy/s. Protons have been far less investigated than electrons. Here, only dose rates < 1 Gy/s and between 40 Gy/s and 300 Gy/s were investigated for inducing a FLASH effect. A dose rate higher than 300 Gy/s was solely investigated in Zlobinskaya et al. [99]. Here, a dose rate of $2 \cdot 10^{10}$ Gy/s was used for irradiation and equal tumor control was measured for the ultra-high dose rate and a conventional dose rate. In this study, solely the tumor growth was tested and no healthy tissue reactions. Therefore, no conclusions can be drawn here, whether there is an upper dose rate limit for inducing a FLASH effect or not. The FLASH effect induced by carbon ions or x-rays is hardly investigated and a successful induction can only be found in [19] and [15], where dose rates of 120 Gy/s and 37 Gy/s were applied, respectively.

The irradiated doses in the here discussed studies were applied in different time patterns, as the irradiation can be performed in a continuous beam mode or in a pulsed beam mode depending on the requirements of the used devices. Electron linacs, for example, can only irradiate in a pulsed beam mode, while for proton accelerators both modes are feasible depending on the adjustability of the beam currents. In a continuous beam mode, the dose rate is constant for the whole irradiation duration. Whereas in a pulsed beam mode, the dose is administered in pulses. Therefore, the intra-pulse dose rate is high and in between the pulses it equals zero. In Figure 2.2, the mean dose rate over the whole irradiation duration was taken when experiments were performed in a pulsed beam mode, instead of the peak dose rates in the pulses. Here, the question arises: Is there a difference between pulsed beam mode and continuous beam mode? Vozenin et al. [85] addressed this question in more detail in their review. They showed with data taken from [100] that the crucial factor for inducing a FLASH effect is the duration of the irradiation and not the pulsing of the beam. In this study, the tails of mice were irradiated and the dose that was necessary to induce 50 % necrosis in the tail was determined. Dose was administered in 1, 5, 10 and 50 pulses per second with a pulse length of 1 µs and a dose rate of $0.4 \cdot 10^6$ Gy/s in the pulses. Therefore, all mice were irradiated with the same peak dose rates, but the total dose was administered in different irradiation durations. For 50 pulses per second, the irradiation duration was the smallest with 3 s for 60 Gy and the irradiated tails developed significantly fewer necrosis than this was the case for the other pulse modes. The amount of necrosis was increased with increasing irradiation times (and less pulses per second). Therefore, it can be concluded that an irradiation duration of < 5 s led to a FLASH effect. In Montay-Gruel et al. [8], the time structure of the pulses was the same for all tested irradiation modes, but the intra-pulse dose rate was different resulting in different mean dose rates and different irradiation durations. Here, dose rates > 60 Gy/s and an irradiation duration < 200 ms were necessary to preserve memory after 10 Gy whole body irradiation of mice.

Another factor for the induction of a FLASH effect is the dose. As shown in Figure 2.2, a FLASH effect can be induced with doses > 10 Gy. However, this dose limit cannot be applied for all applications. For whole brain irradiation, this dose is sufficient to induce detrimental damages in the brain like memory loss [8, 15, 101]. If a small part of the body is irradiated, for example a field of 530 mm^2 on the skin of a mini-pig [10], doses of > 30 Gy are required to induce macroscopic damages (like depilation, erythema and desquamation) to the tissue. Beyreuther et al. [11] tested the dose dependence of the FLASH effect on zebrafish embryos. The zebrafish embryos recieved a total body irradiation with doses ranging from 10 to 42 Gy. A significant FLASH effect could only be found for 23 Gy. For doses smaller or bigger, no differences could be found. It seems that a tissue sparing effect can only be achieved, if the dose is high enough to induce damages to allow improvement by FLASH. On the other side, if the doses are too high, the damages are so lethal that they are also induced by a FLASH dose rate.

In conclusion, the FLASH effect can be induced in a certain dose range and with irradiation durations smaller than a certain threshold value. The dose range and the irradiation durations depend on the tissue and the irradiated volume. To use and predict the FLASH effect, these dependencies must be taken into account and have to be further investigated to understand under which circumstances a FLASH effect can be expected. The most important aspect here is to understand the underlying mechanisms for this useful effect, as suitable models for this effect are urgently needed to fully exploit the FLASH effect in clinical applications.

2.4 Underlying mechanisms of the FLASH effect

Understanding the underlying mechanisms of the FLASH-effect is the key factor for its application to patient treatments. 2014 the potential of the FLASH-effect was first shown in [6]. Since then, this effect has been intensively investigated to find the underlying mechanisms. In this process, various hypotheses were proposed, but none has been fully confirmed yet. The different proposed models can be roughly divided into three groups [102]: the oxygen depletion hypothesis, the DNA damage hypothesis and the immune hypothesis and they are presented and discussed in the following:

2.4.1 Oxygen depletion effect

The oxygen depletion effect is the most prominent hypothesis for the FLASH effect. As discussed in Section 1.2, irradiation can interact either directly or indirectly, as shown in Figure 2.3(a). In the case of indirect interactions, the water molecules are ionized. These ionizations lead to the formation of radicals. These radicals then interact with the biomolecules in their surroundings and can damage them. If oxygen is present, the radicals interact with oxygen to form the more reactive radicals perhydroxyl (H-O-O·) and peroxid (R-O-O-R·), which produce more complex DNA damages [24] and are the reason for the oxygen effect. The oxygen depletion hypothesis states that in FLASH irradiations the radical formation happens so rapid that all oxygen is depleted during the irradiation and no more oxygen-related radicals can be formed, causing a transient hypoxia in the well oxygenated normal tissue. Tumor tissue is already hypoxic, therefore no differential effect occurs [103–105]. In Figure 2.3(b), the oxygen depletion effect on tumor and normal tissue is shown. In detail, the FLASH irradiation happens on time scales of up to several hundred milliseconds or even 1 s. Therefore, the irradiation duration is so short that the chemical step is reached, but not the biochemical step [84, 85], as shown in Figure 2.1. Subsequently, the formation of radicals happens during irradiation, but neither the invasion of free oxygen from the surroundings nor the recovery of the molecules that formed the radicals after interaction with the bio-molecules. Due to the recovery of the radicalized molecules, free oxygen molecules are formed. If all oxygen is depleted and no free oxygen could be formed or invade during irradiation because of the shortage in time, the tissue reacts like a hypoxic tissue and is less radiosensitive. In contrast, in conventional treatments, the irradiation takes long enough for the molecules being radicalized and recovered several times and additional free oxygen can invade from the surroundings during irradiation. On the other hand, tumors contain typically less oxygen with a decreased oxygen concentration towards the center of the tumor, as in tumors the oxygen supply is decreased due to a lack of functional blood vessels or abnormalities in the blood vessels [32]. Therefore, the tumor is already a hypoxic tissue and experiences less oxygen-induced radical damage. Subsequently, an oxygen depletion effect plays a minor role here. Therefore, it can be concluded that the larger the difference in oxygen levels between healthy and tumor tissue, the better the differential response to FLASH [106].

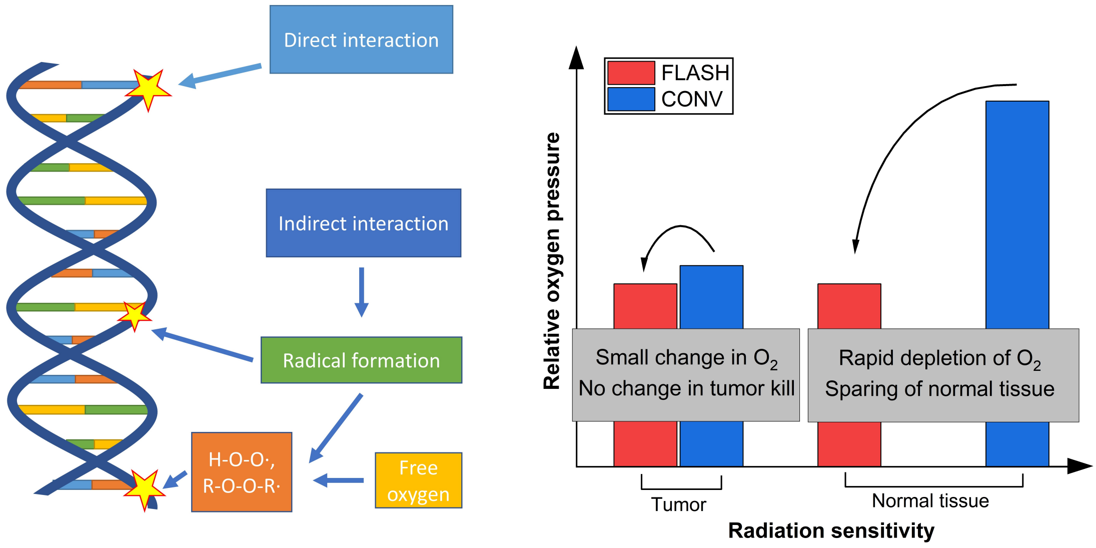

(a) Direct versus indirect interactions

(b) Oxygen depletion

Figure 2.3: The oxygen depletion hypothesis. In (a), a schematics of the direct and indirect interactions of irradiation with molecules in the tissue like the DNA are shown. (b) presents the idea of the oxygen depletion effect. Normal tissues contain typically higher concentrations of free oxygen compared to tumors. In a FLASH treatment, a rapid depletion of oxygen happens, which decreases the amount of available oxygen for the formation of radicals in normal tissues, while with a conventional treatment no oxygen is depleted and the amount of available free oxygen during irradiation is very high. Therefore, a transient hypoxia is induced by the FLASH treatment, which leads to sparing effects. In tumors, oxygen plays a minor role in the indirect interaction of irradiation. Hence, the oxygen supply stays constant for both treatment types and the tumor control remains the same. Adapted from [102, 107] with permission due to CC BY 4.0.

To test this hypothesis, several experiments were performed on different models in-vitro and by simulation. In Figure 2.4, the dose modifying factor (DMF) between FLASH and conventional irradiation is depicted for different oxygen concentrations. The DMF equals here the ratio of FLASH dose to the conventional dose rate dose both resulting in the same endpoint, where for both doses the same effects were induced. In-vitro cells and bacteria were kept under different oxygen levels before and during irradiation. The oxygen levels ranged from 0.36 % to 21 %. Irradiation was either performed with a FLASH dose rate or a conventional dose rate. As radiosensitivity end point, the survival of cells and bacteria were measured by colony forming assays and for P388 by a lethal tumor formation assay in mice [2] and the DMF was calculated

---

[2] For the lethal tumor formation assay, P388 murine leukaemia cells were taken from a tumor bearing

accordingly. The data were taken from [108–112] and summarized according to Vozenin et al. [85].

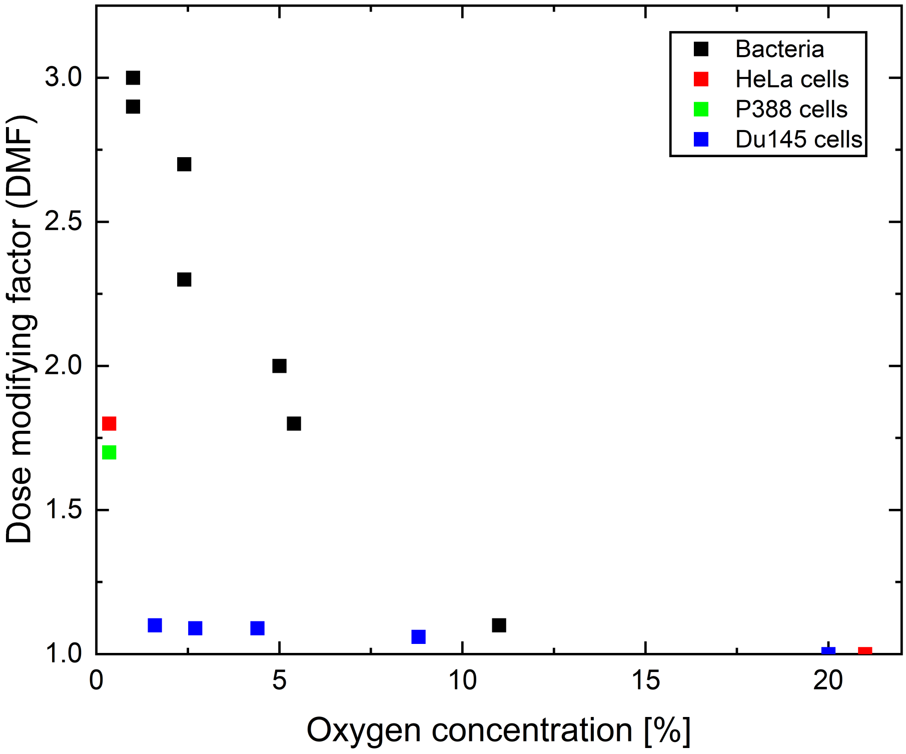

Figure 2.4: The dose modifying factor (DMF) for different oxygen concentrations. Bacteria and mammalian cells were irradiated with either conventional or FLASH dose rates while being kept under different oxygen concentrations. The survival of cells and bacteria was tested by colony forming assays and for P388 by lethal tumour formation assay in mice. The DMF is, hereby, the ratio of FLASH dose to the conventional dose rate dose both resulting in the same assay end point (isoeffective dose). Data are taken from [108–112] and summarized according to Vozenin et al. [85].

As shown in Figure 2.4, the DMF equals 1 for cells kept at oxygen concentrations of 20-21 %. Therefore, no difference between FLASH and conventional irradiation was visible. By contrast, the reduction of the oxygen concentration results in an increase of DMF. For bacteria, the DMF increased up to 3 for an oxygen concentration of 1 % and for HeLa and P388 cells, the DMF was increased to 1.7 and 1.8 for an oxygen concentration of 0.35 %. For the Du145 cells, the increase in the DMF was not as pronounced as for the other in-vitro models, but also here a slight increase in DMF when applying lower oxygen concentrations was visible. Here, the highest DMF of 1.1 was achieved with the lowest oxygen concentration of 1.6 %. Furthermore, it was tested whether such an oxygen dependency could also be found when

---

mouse. Cells were kept under hypoxic conditions and were irradiated. Then, cells were counted, diluted and injected into mice. The clonogenic survival of the tumor cells was measured by their ability to cause death of the mice within 100 days [108].

irradiating with high-LET particles. Tinganelli et al. [19] irradiated CHO cells kept under different oxygen levels ranging from 0 % to 21 % with 280 MeV/u carbon ions and measured the cell survival by a colony forming assay. They also found that the sparing due to FLASH irradiation was mostly pronounced for 0.5 % oxygen concentration and was absent for 0 % and 21 % oxygen. This shows that the FLASH effect is oxygen dependent, but independent from the LET. In cell culture, cells are well oxygenated with typical oxygen concentrations of 20 % to 21 % [113]. However, such a high oxygen supply is too much to be depleted during a FLASH irradiation. Here, lower oxygen concentrations are necessary to achieve depletion. Normal tissues typically have oxygen concentrations ranging from 4 % to 7.5 % depending on the tissue [113]. In tumor tissue, oxygen levels ranging from 0.3 % to 4.2 % can be found [113]. As the highest sparing effect was seen for the lowest oxygen concentrations of below 5 %, which is the typical regime of hypoxic tumors, the oxygen depletion effect as underlying mechanism for the FLASH effect observed in-vivo has to be questioned. The here presented in-vitro data suggest a higher differential effect with decreasing oxygen concentration until 0.35 %. On the other hand, in in-vivo data, a tissue sparing effect was observed for normal tissues but not for tumor tissues. However, no difference was seen in the complete absence of oxygen in-vitro [19]. Therefore, there seems to be a shift in the oxygen concentration required to trigger a FLASH effect from in-vitro models to in-vivo models to a higher oxygen content. To test this, further investigations are necessary which involve the measurement of oxygen concentrations in in-vivo models before, during, and after the irradiation.

Jansen et al. [114] proposed air tight water phantoms equipped with an optical sensor for measuring the oxygen dissolved in water. They irradiated the water phantoms with photons, protons and carbon ions with different dose rates[3] until the oxygen inside was completely consumed. For all particle types, it was measured that the higher the dose rate was the more dose was necessary to achieve a complete depletion. Here, for instance, doses up to 230 Gy were necessary to deplete 2.5 % oxygen with protons of a dose rate of 20 Gy/s. This shows that oxygen is rather depleted slower using higher dose rates and that oxygen depletion cannot be induced by clinical relevant doses. Therefore, the authors of this study conclude that oxygen depletion might not be a suitable mechanism explaining the FLASH effect. On the other hand, as in this study only the radiolysis of water and no interaction with biomolecules was investigated, the suitability of this model remains questionable. This shows once again the urgent need for direct oxygen measurements in in-vitro and in-vivo models.

2.4.2 DNA damage hypothesis

In the central dogma of radiobiology, the DNA is considered to be the major target of irradiation. Targeted irradiation in the cytoplasm and the cell nucleus showed that the cytoplasm is radioresistant to doses up to hundreds of Gy's [115], while the cell nucleus containing the DNA is the most radiosensitive region in the cell [116]. The damages to the DNA can end lethally for the cell, if they cannot be repaired or if they are repaired in the wrong way. Therefore, the damages to the DNA are considered to mainly determine the cells' fate after irradiation

---

[3] Photons: 1.0 Gy/s to 52 Gy/s, protons: 2 Gy/s to 20 Gy/s and carbon ions: 1.19 Gy/s and 2.43 Gy/s

[32]. Therefore, a closer look to DNA damages might provide more information about the differential effects observed after irradiation with different dose rates. Buonanno et al. [117] and Fouillade et al. [12] tested the effects of different dose rates on DNA damages with protons and electrons. In [117], normal human lung fibroblasts were irradiated with 0.05 Gy/s, 100 Gy/s and 1000 Gy/s and γH2AX[4], which marks DSBs by so called foci, was fluorescently stained in the cells 30 min after irradiation. Significantly less DSBs were measured for 1000 Gy/s at a dose of 20 Gy than for 0.05 Gy/s or 100 Gy/s. No significant differences were seen for smaller doses. In [12], DNA damages were measured in human lung fibroblasts (MRC5, IMR-90) and tumor cells (A-549) by staining of γH2AX and 53BP1 [5], which also marks DSBs, 30 min after an irradiation with 5.2 Gy. The cells irradiated in FLASH mode produced significantly less 53BP1 foci than irradiated in a conventional mode. Zlobinskaya et al. [120] showed also less γH2AX foci induced by ultra-high dose rates using protons. Here, it was observed that these foci tended to be bigger and more aggregated. Schmid et al. [121] measured less micronuclei when using a ultra-high dose rate for proton irradiation. However, the difference in these both studies were not significant. A significant difference was found in chromosome aberrations in human hamster hybrid cells [122]. Both micronuclei and chromosome aberrations are direct consequences of DNA damages which can not be repaired and therefore they are good endpoints to investigate complex, unrepairable and misrepaired DNA damages [123, 124]. Therefore, it can be concluded that differences in clustering, complexity and amount of DNA damages is observable for different dose rates. These differences seem to be more pronounced the higher the dose and the dose rate [117].

However, it is not understood yet, how the differences in DNA damages are related to the FLASH effect. It is thinkable that the FLASH effect can be induced by activation of different factors involved in DNA repair pathways or the immune system [102, 125]. For example, it has been found that FLASH induces less senescent cells than a conventional irradiation [12, 117]. The underlying reason might be the cGAS-STING pathway [102, 125]. This pathway is induced by cytosolic DNA, which originates from radiation-induced DNA-fragments. The cGAS-STING pathway promotes senescence, cell death and tissue injury [126]. Many cancer cells are already repleted with aberrant DNA fragments [126], which is not the case for normal cells [127]. Therefore, small differences in the amounts of cytosolic DNA due to differences in DNA damage caused by different dose rates might matter less than in healthy cells. By contrast, in healthy cells the increased amount of DSBs after conventional irradiation might have led to more cytosolic DNA, which results in more senescent cells. The higher amount of senescent cells can trigger more inflammation reactions [128] as this would be the case after FLASH irradiation. Therefore, this pathway might be a good explanation for both parts of the FLASH effect, the tissue sparing in healthy cells and the equal tumor control.

---

[4] γH2AX is the phosphorylated form of the histone H2AX, which is an essential part of the chromatin. yH2AX is developed in close vicinity to DSBs and accumulates there. Therefore, it was etablished in radiobiology as a very sensitive detection method for DSBs and is now commonly used to mark DSBs fluorescently [118].

[5] 53BP1 is a protein and one of the key mediators of DNA damage response. It also accumulates at DSBs and can be used to visualize them [119].

However, a direct relation between cytosolic DNA content and the differential response to FLASH irradiation has not been confirmed yet. Further investigations are necessary here.

2.4.3 Immune hypothesis

The immune system plays a critical role in the response to irradiation. It promotes and mediates, for example, inflammation reactions and is responsible for the cure of damaged tissues [32]. Small differences in irradiation effects due to different dose rates might change the expression and activation of immune factors and immune cells [125]. Moreover, tumor tissue and normal tissue differ in their immunological responses [125]. Therefore, differential behavior due to the immune system to FLASH or conventional irradiation in normal tissue and in tumor tissue is thinkable and might be responsible for the FLASH effect [102, 107, 125].

The cytokine TGF-β, as a master regulator of radiation-induced anti-tumor immune response [129], seems to play an important role here. Buonanno et al. [117] measured in normal human lung fibroblasts significantly less TGF-β after FLASH irradiation than after conventional irradiation. Also Cunningham et al. [16] found a decreased TGF-β production. They irradiated the hind legs of mice with protons of three dose rates (1 Gy/s, 57 Gy/s, and 115 Gy/s) and measured TGF-β in the blood plasma. Here, a not significant decrease of TGF-β was found 24 h after irradiation and a significant decrease 96 h after irradiation. At the latter time point, the two higher dose rates yielded similar results to the non-irradiated mice. TGF-β regulates the production of ROS and DNA repair [125, 130]. The different amounts of this cytokine induced by FLASH or conventional irradiation might explain the decrease in DNA damage observed for FLASH, as discussed in Section 2.4.2 [102]. However, this remains to be evaluated.

Another candidate for inducing the FLASH effect might be the irradiated blood volume [103]. As discussed in Section 2.3, the most important factor for inducing a FLASH effect seems to be the overall irradiation duration. The time an irradiation takes determines the volume of blood that is irradiated. Since the tissues are constantly supplied with blood and this blood is continuously exchanged, more blood flows through the irradiated area and is irradiated at high irradiation durations than in short irradiation times. In tumors, the vasculature is often malfunctional and purely formed. Therefore, the irradiated blood volume might play a minor role here. The different irradiated volumes might trigger different immune responses, which induce different amounts of cytokines, for example TGF-β. However, the exact correlations between the irradiated blood volume and inflammation reactions need to be examined more closely.

In conclusion, the hypotheses and studies presented here point to very different parts and levels of the irradiation response ranging from the physicochemical and chemical step, where the oxygen depletion takes place, to the biological step, where the immune reactions come into play. The mechanisms underlying the FLASH effect might most likely be an interplay of all the proposed factors and have to be investigated in future.

2.5 Proton-irradiation with different dose-rates at SNAKE

In this thesis, the proton-FLASH effect was investigated on different in-vitro models and an in-vivo mouse ear model. As shown in Figure 2.2, the FLASH effect has not been investigated yet for protons of dose rates higher than 300 Gy/s and between 1 Gy/s to 40 Gy/s. Therefore, I tested dose rate effects at dose rates of 930 Gy/s, 310 Gy/s and 9.3 Gy/s in comparison to a conventional dose rate to gain knowledge about the radiobiology in these dose rate ranges. Here, 930 Gy/s and 310 Gy/s were the maximum dose rates that could be achieved in-vivo and in-vitro experiments, respectively. For these experiments, the beam line had to be adapted to provide protons of such highly different dose rates and a new detection system was developed. A manuscript about the beam line set-up, the detection system and the in-vivo experiment is submitted for publication. Sections taken and adapted from this publication are marked by a star (*).

(*)
The proton-irradiations of this thesis were performed at the Maier-Leibnitz-Laboratorium in Garching near Munich. Here, the SNAKE beam line was adapted for irradiations with different dose rates. This beam line is equipped with an 90°-tilted microscope on a motorized stage. The whole microscope can be moved towards or away from the beam nozzle, where the beam exits the beam line [131]. Different containers for cells and artificial tissue, irradiation platforms for mice and adapters were designed for mounting at the microscope. Therefore, a large variety of biological experiments can be performed at SNAKE [131–136]. In this thesis, dose rates between 0.06 Gy/s to 930 Gy/s were used for irradiation in the experiments to test dose rate effects in different models. In the in-vitro experiments, the dose rates 0.06 Gy/s (Conv), 9.3 Gy/s (Flash9) and 310 Gy/s (Flash310) were applied. For the in-vivo experiment, the dose rates 0.06 Gy/s (Conv), 9.3 Gy/s (Flash9) and 930 Gy/s (Flash930) were used. A beam set-up was designed that enables a quick and easy switching between the different dose rates. This set-up was developed by Judith Reindl, Günther Dollinger, Andreas Bergmaier and me for proton irradiations with different dose rates and is presented in the following. A schematic image of the beam line is shown in Figure 2.5. As ion source, a multicusp ion source was used to yield the required maximum beam current of 15 nA at the sample. A 5 MHz chopper in front of the 14 MV tandem accelerator was used to adjust the dose rates by adjusting the ratio of beam-on and beam-off time. The terminal voltage of the tandem accelerator was set to 10 MV to obtain 20.5 MeV protons for irradiation. The beam was sorted by the 90° magnet to achieve a proton beam with a relative energy spread of smaller $2 \cdot 10^{-4}$. The beam was injected into the 0°-beam line of SNAKE. In the focus level of the 90° magnet, the beam was cut horizontally and vertically by object slits [137], which define the field size of the object. The next pairs of slits in the beamline are the divergence slits [137]. These restrict the divergence of the beam.

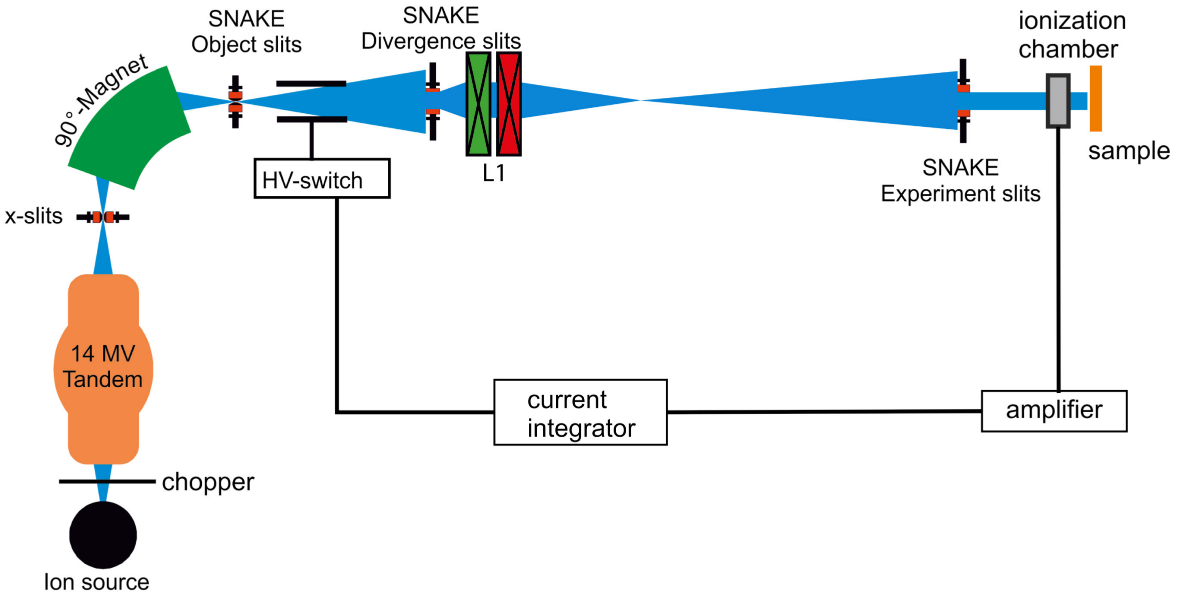

Figure 2.5: A schematic image of the beam line set-up designed for experiments with conventional to ultra-high dose rates. Adapted from [138] with permission.

For this application, they had an opening of 5 m in the horizontal direction and 8 mm in the vertical direction to enable a field size of several millimeters. A quadrupole-duplet lens (L1) downstream of the divergence slits focuses the beam to a certain spot in the beam line before the irradiation platform. At the irradiation platform, the beam is then defocused, which results in an irradiation field size of several centimeters. The experiment slits, which are located about 2 m before the irradiation platform, finally restrict the size of the irradiation field to the homogenous core of the beam. The homogeneity of the field with a size of 6.5 x 6.5 mm, prepared for this study, was measured with an EBT3 gafchromic film and had a standard deviation of 2 % which equals the uncertainty of this film type measured in previous studies [139, 140]. To adjust the beam currents and therefore the dose rates, the settings of the low-energy 5 MHz chopper and L1 were adjusted. For Flash930, the low-energy chopper was switched off and the focus of L1 was set to achieve a 15 nA beam current at the target. This beam current was the maximum beam current provided by the ion source that could be set up to a homogeneous irradiation field. For the in-vitro experiments, this highest does rate had to be lowered, as the detection system was not able to apply a low dose of 4 Gy accurately at such a high dose rate. Therefore, a dose rate of 310 Gy/s was chosen for the in-vitro experiments. To set the required beam current of 5 nA, the focus of L1 was changed and the 5 Mhz chopper was switched off. For Flash9, the 5 MHz chopper was set to pass a pulse width of 128 ns and a frequency partition of 26, resulting in a pulse to pulse distance of 12.8 µs. The focus of L1 was the same as for Flash930. For Conv, the pulse length and the delay of the chopper were the same as in Flash9, but the frequency partition was set to 28, resulting in a pulse to pulse distance of 15.2 µs. The magnetic field in L1 was increased to further decrease the beam current at the target to mean current of approx. 1 pA. The resulting beam-off and beam-on times for every dose rate are listed in Table 2.1. Configuring the dose rates via the 5 MHz chopper allows a quick change between the mean dose rates within seconds.

Dose rate	Beam-on time	Beam-off time	Exposure duration	Beam current	Abbreviation
0.06 Gy/s	0.128 µs	51.072 µs	9.17 min (33 Gy)	1 pA	Conv
9.3 Gy/s	0.128 µs	12.672 µs	3.55 s (33 Gy)	150 pA	Flash9
310 Gy/s	Whole irradiation	0 µs	12.9 ms (4 Gy)	5 nA	Flash310
930 Gy/s	Whole irradiation	0 µs	0.035 s (33 Gy)	15 nA	Flash930

Table 2.1: The four irradiation modes used in this thesis. 930 Gy/s was solely used for the in-vivo experiment. In in-vitro experiments 310 Gy/s were used as the highest dose rate due to detector restrictions.

2.6 Dosimetry of proton-FLASH irradiations

(*)

The dosimetry of large dose rate ranges, as typically used in FLASH experiments, is very challenging. The dose measurement needs to react very fast to accurately detect at beam currents as high as 15 nA. On the other hand, it needs to be sensitive enough for detecting also low dose rates. Conventionally at SNAKE, a photomultiplier is used. This photomultiplier was designed to detect and count single ions. However, it fails when it comes to beam currents larger than several picoampere, as used in this thesis. Therefore, a new detection system was designed by Andi Bergmaier, Günther Dollinger and Judith Reindl based on an ionization chamber. To detect different dose rates, the detector was built by adapting a detector as used for ERD[6] experiments at the Maier-Leibnitz-Laboratorium in Garching [141]. For its design, two requirements were aimed to achieve. First, the detector plus electronics need short reaction times. As the irradiations took at minimum several milliseconds, the reaction time should be much smaller than that. Second, the detector needs to measure accurately short events of very high beam currents and also periods of low beam currents. The ionization chamber was designed with a current measurement parallel to the beam. To ensure the ionization chamber can react fast enough, it was filled with CF_4 gas at room pressure. The gas circulated permanently at a constant gas flow of 10 mbar/min to avoid saturation due to damages to the detector gas. This gas flow rate was achieved by immersing the hose of the gas outlet 1 cm in water. The detector was 4 cm broad and had two windows made out of 7.5 µm thin Kapton foil, as shown in a schematic image of the detector in Figure 2.6(a). The Kapton foil held the gas inside the detector and was thin enough to keep the scattering of the proton beam at an acceptable level. Between the cathode and the anode, a voltage of -1300 V was applied. The cathode and anode were aligned parallel to the beam such that the electric field is perpendicular to the beam direction. The ionization chamber was integrated in the SNAKE beam line as follows: The proton beam induces ionizations inside the chamber. Free electrons and ions move toward the anode or cathode inducing a current. The current is amplified and integrated. If a certain dose level is reached, a high voltage switch (cf. HV-switch in Figure 2.5) upstream the beamline deflects the beam towards the wall and so the irradiation stops immediately. The detector was placed in front of the beam nozzle, as shown in Figure 2.6(b).

---

[6] Elastic Recoil Detection (ERD)

The samples, irradiated in the different experiments, were fixed behind the detector at the microscope.

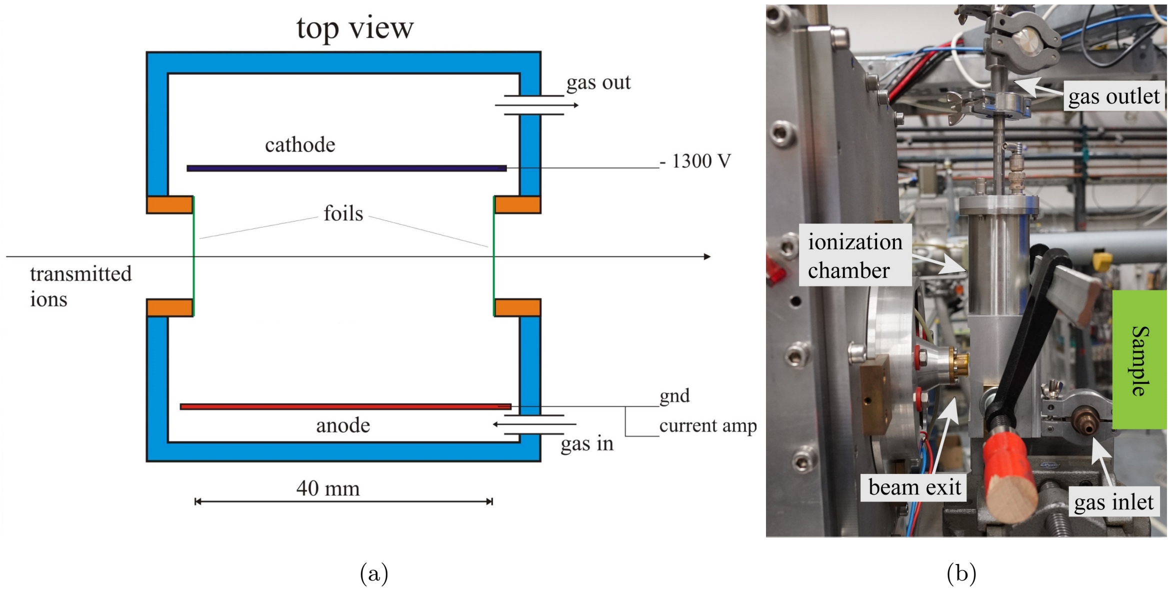

Figure 2.6: The ionization chamber designed and built for detecting high dose rate ranges. In (a), a schematic image of the detector is shown. The detector was placed in front of the beam nozzle, as presented in (b). The samples were irradiated behind the detector.

Figure 2.7: The EBT-3 gafchromic film irradiated for calibration by using the calibrated photomultiplier as detector. The doses 0.5 Gy, 1 Gy, 2 Gy, 3 Gy, 4 Gy, 5 Gy, and 7 Gy were irradiated in fields of 1.12 mm x 0.8 mm size.

Additionally, gafchromic films were used for calibration and dose verification. Gafchromic films are radiochromic photo-films that are functionalized in such a way that the darkening of the films can be accurately correlated to the applied dose [139]. In this thesis, two types of films were used, EBT3 and EBT-XD (Ashland Advanced Materials, USA). The EBT3 gafchromic films are sensitive between 0.1 cGy to 10 Gy and EBT-XD films are sensitive between 0.4 cGy and 40 Gy according to the producer and are insensitive to dose rate changes in a wide range of dose rates (from 0.25 Gy/s to 7500 Gy/s [142] and from 0.034 Gy/min to 3.4 Gy/min according to the producer) within these dose regions. The films were irradiated with doses covering the sensitive dose-region of the films to generate a calibration curve. The irradiated films are shown in Figures 2.7 and 2.8.

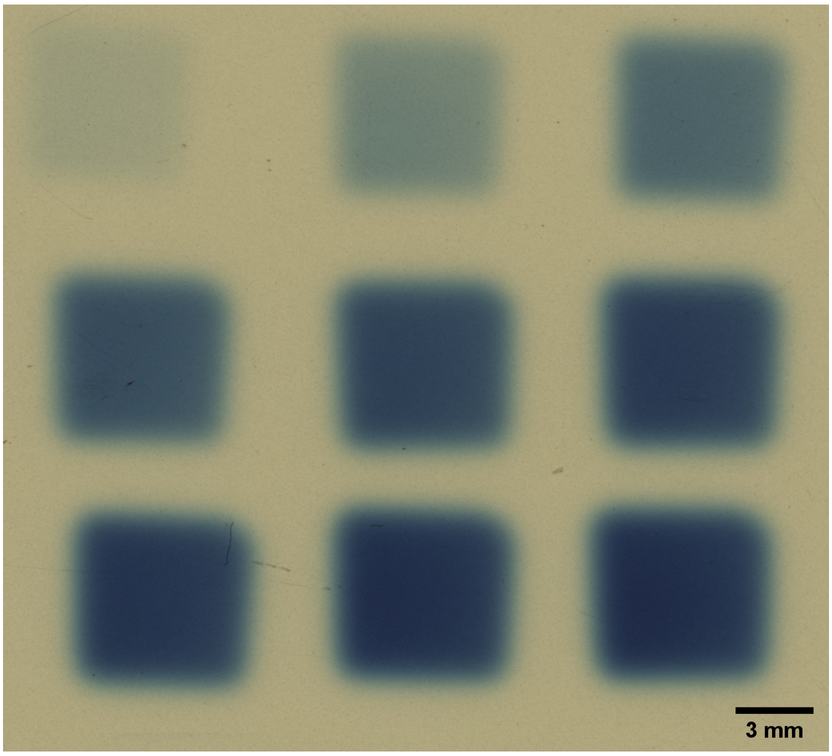

Figure 2.8: The EBT-XD gafchromic film irradiated for calibration by using the calibrated ionization chamber as detector. The doses 1 Gy, 5 Gy, 10 Gy, 15 Gy, 20 Gy, 25 Gy, 30 Gy, 35 Gy and 40 Gy were irradiated in fields of 6.5 mm x 6.5 mm size.

The irradiated films were scanned 48 h post-irradiation using Epson V700 photo scanner (EPSON Deutschland GmbH, Meerbusch, Germany). This time point was chosen to avoid post exposure effects, as it was found that at about 48 h the change in darkening over 3 h is < 0.3 % [139]. For scanning, the EpsonScan software was used in professional mode. Image correction methods were turned off and the transmission mode for positive films was chosen. The scans were digitized as 48-bit RGB image with a resolution of 1200 dpi and saved in tiff-format. For evaluation, the intensity of the irradiated fields were measured with Fiji ImageJ software in the red channel. Areas with scratches on the scans were avoided for measuring. The netto optical density (netOD) was calculated for every field by

$$\mathrm{netOD} = -\log \frac{R_{exp}}{R_0}, \tag{2.2}$$

where R_{exp} was the measured intensity of an exposed film and R_0 the measured intensity of an unexposed film. The obtained netODs were calibrated to the dose by

$$D = A \cdot \text{netOD} + B \cdot \text{netOD}^C, \tag{2.3}$$

where A, B and C are fitting parameters. The calibration curves for both films are shown in Figures 2.10 and 2.9. For both films, a netOD uncertainty of 1 % was assumed as given by the producer. The EBT3 film was calibrated by using the photomultiplier-detector, which is usually used for single ion counting at SNAKE. A dose error of 5 % was assumed, originating from the detector-beam control system of SNAKE as determined in [139]. EBT3 films were used for cross-calibrating the ionization chamber. The EBT-XD film was calibrated by using the calibrated ionization chamber. For irradiations with the ionization chamber as a detection system, a 9 % dose error was measured.

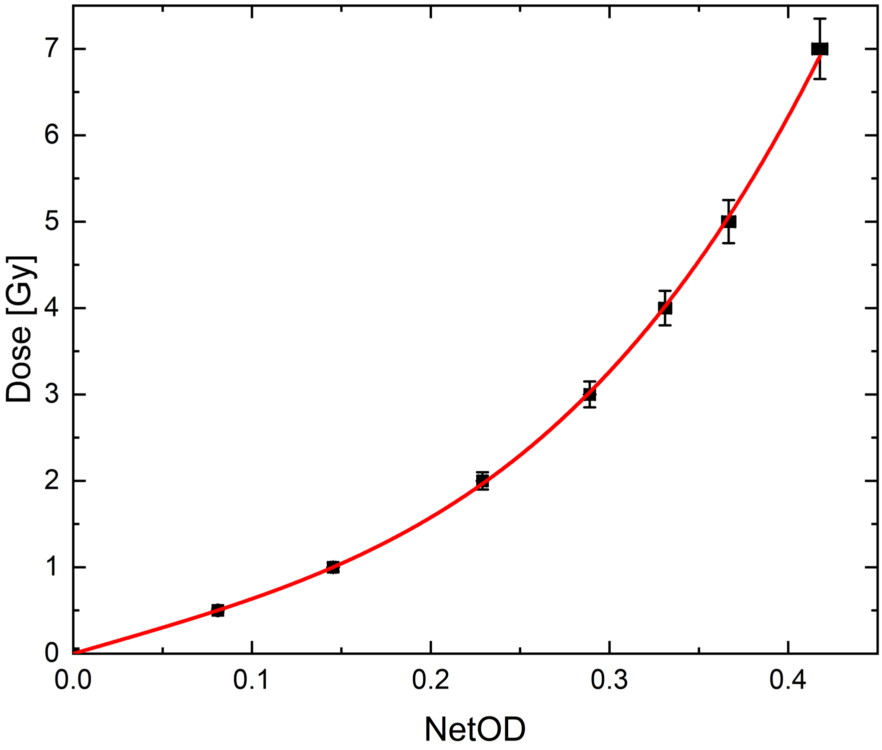

Figure 2.9: Calibration curve for the EBT3 film. The calibration curve was fitted with the following parameters: A = 5.96 ± 0.09, B = 80 ± 6, and C = 3.32 ± 0.08.

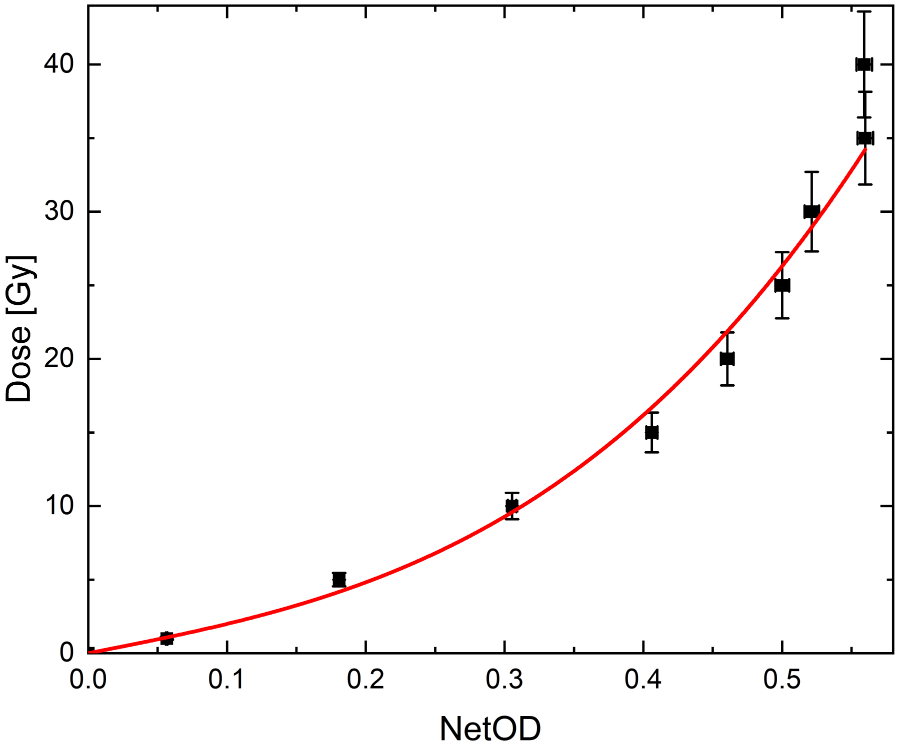

Figure 2.10: Calibration curve for the EBT-XD film. The calibration curve was fitted with the following parameters: A = 18.5 ± 2.1, B = 134 ± 41, and C = 3.0 ± 0.5.

The homogeneity of the irradiation field was measured with an EBT3 gafchromic film and had an acceptable standard deviation of the mean of 2 %, which is only slightly above the 1 % dose error given by the manufacturer.

The accelerator provided 21 MeV protons. These protons had to pass a 7.5 µm Kapton foil at the exit window, a 2 mm air gap between beam exit window and entry window of the ionization chamber, a 7.5 µm Kapton foil, 44 mm of CF_4-gas at room pressure, the exit window of the detector consisting of a 7.5 µm Kapton foil, and 30 mm of air before they reach the samples. The energy loss caused here was calculated with SRIM [29] to 0.5 MeV and results in an energy of 20.5 MeV at sample level which equals an LET of 2.6 keV/µm.

2.7 Effects of proton-FLASH irradiation in cell culture models

The FLASH effect was tested on three state of the art in-vitro models covering the most important radiobiologic endpoints. The cell survival was tested by a colony forming assay (CFA), the cell death by a Caspase3/7-Sytox assay and the DNA damage by a micronucleus test. These experiments are presented in the following. The methods and results of these experiments were partly published in my article [143]. The sections marked by two stars (**)

have been taken from this publication and have been adapted.

2.7.1 Cell culture

(**)

As the FLASH effect is an effect of the healthy tissue, the experiments were performed on CHO (Chinese hamster ovarian) cells. CHO is an epithelial cell line derived 1957 by Theodore T. Puck from a female Chinese hamster. The subtyp CHO-K1 is an ancestral subtyp and is often used in biological studies [144, 145] and for the production of therapeutics in industry due to its simple handling [146–148]. This subtyp is also well tested in radiobiology and a commonly used in-vitro model [136, 149, 150]. In the following, this subtyp will be referred to as CHO cells for a better readability.

CHO cells were cultivated in RPMI growth medium (R8758-500ML, Sigma Aldrich, USA), supplemented with 10 % FCS (F0804-500ML, Sigma Aldrich, USA), 1 % Penicillin-Streptomycin (P4333-100ML, Sigma Aldrich, USA) and 1 % Sodium Pyruvate (S8636-100ML, Sigma Aldrich, USA). The cells were grown at a temperature of 37 °C, 5 % CO_2 and 100 % humidity. These conditions were in the follwing denoted as cell culture conditions. Cells were passaged twice a week with a splitting ratio of 1/40 and were kept in T75 cell culture flasks (CELLSTAR, Greiner Bio-One, Germany).

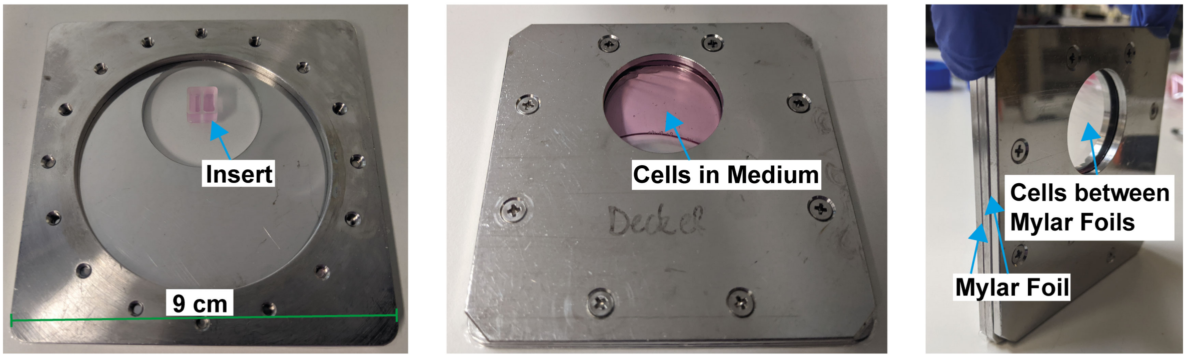

(a) (b) (c)

Figure 2.11: The cell container for irradiation at SNAKE. Cells were seeded on Mylar foil in the middle of the window in a restricted growth area by using a silicon insert, as shown in (a). For irradiation, the insert is removed, the container is filled with 6 ml medium and the container is closed with a lid, as shown in (b). (c) shows the container in side view. Two mylar foils are fixed between the three metal parts of the container. These Mylar foils cover the cells in the window and ensure there a saturated environment during irradiation while keeping the energy loss of the protons at an acceptable level.

For irradiation, special self-designed containers were used [151], as shown in Figure 2.11. These containers keep the cells under physiological conditions and saturated atmosphere, while the cells are not covered with medium during the irradiation. Furthermore, these containers are built for irradiating cells in an upright position, as the beam line SNAKE is a horizontal beam line. A detailed description of these containers can be found in [131, 151]. In these containers, the cells grow on a 6 µm Mylar foil coated with gelatin to encourage the growth on the foil. For coating, the gelatin was warmed up to 37°C and solved in distilled water to a 0.1 % (w/w) solution. Then, 1 ml of the solution was added on the Mylar foil in the area of the container, where the closed container has a window only covered by two Mylar foils, and incubated for 30 min at 37°C. Then the gelatin solution was removed and the sample holder was washed two times with PBS. Finally, the containers dried on air for a minimum of 2 h. For seeding the cells in a well-restricted area of approx. 6 mm x 6 mm, a silicon insert (Culture insert 2 well, Ibidi, Germany) was used. This insert restricts the growth area to two rectangular areas with a gap of 500 µm in between. The inserts stick themselves on the gelatin-coated stretched Mylar foil and every insert was put in the middle of the window area of the container at the same position by using a self-made template, as shown in Figure 2.11(a). In each well of the insert, 30.000 cells were added in 100 µl growth medium. CHO cells were incubated in the inserts for 24 h at cell culture conditions. Before irradiation, the insert was removed, 6 ml growth medium was added, and the container was closed (Figure 2.11(b)). This amount of medium ensures that the cells are covered with medium in horizontal position, but not in upright position during irradiation (Figure 2.11 (c)).

2.7.2 Proton-irradiation of cell culture models

For irradiation, the containers were mounted at the upright rotated microscope of the SNAKE beam line. With this microscope, the position of the cells could be visualized and the containers could be aligned to the beam. An EBT3 gafchrom film was attached on the side of the container window facing away from the beam for dose verification. The irradiation procedure in upright position lasted less than 10 min. Unirradiated sham samples were treated exactly the same as irradiated samples without switching on the beam.

Samples were irradiated with 4 Gy of 20.5 MeV protons at three different dose rates: 0.06 Gy/s (Conv), 9.3 Gy/s (Flash9), and 310 Gy/s (Flash310). The irradiation field had a size of 6.5 mm x 6.5 mm.

2.7.3 Equal cell survival after proton-FLASH irradiation

The colony forming assay is the gold standard for investigating cell survival [152]. It measures the reproductive ability based on the ability of single cells to grow into colonies after different treatments, for example irradiation [38], as discussed in Section 1.3.1. Hereby, the relationship between dose and the percentage of cells that were able to form a colony is usually described by parametric cell survival curves.

Colony forming assay

(**)

Immediately after irradiation, the cells were trypsinized to be removed from the mylar foil and counted two times in a Fuchs-Rosenthal chamber (C-Chip, NanoEntek, South Korea). A total number of 400 to 700 cells was counted for each sample. The cells of each sample were seeded in three 12-well-plates (Greiner, Germany). A seeding density of 100 cells/ml was chosen for unirradiated cells and 400 cells/ml for irradiated cells to ensure similar colony density on the 12-well-plates. In every well of the plates, 1 ml of the cell solution was added. The cells were incubated for 5 days at cell culture conditions in a water-jacketed incubator (Uniequip, Germany). After five days, the cells were rinsed with PBS (D8537-500ML, Sigma Aldrich, Germany) and fixed with Methanol (SupraSolv® Methanol, Merck, Germany) for 5 min. They were stained with a 0.1 % crystal violet (Kristallviolett, Merck, Germany) solution for 2 min and finally washed with water and dried at room temperature for one day according to [136, 153]. The plates were scanned with GelCount (Oxford Optronix Ltd., UK) and counted manually. For evaluation, only colonies were counted with a minimum of 50 cells. For the analysis, the plating efficiency (PE) is defined as the percentage of cells that have formed a colony of all seeded cells. To calculate the survival fraction (SF), the PE value for a sample was divided by the mean PE value of the unirradiated cells (PE_0)). The mean PE value for the unirradiated cells in this study was 0.53 ± 0.04, where the uncertainty (ΔPE) was the SEM (standard error of the mean) among 5 samples. This measured PE value correlates to the PE of previous experiments [136, 153], where a plating efficiency of 0.52 ± 0.08 was achieved. The SEM of SF (ΔSF) was calculated by using the Gaussian error propagation as

$$\Delta SF = SF \cdot \sqrt{\left(\frac{\Delta PE}{PE}\right)^2 + \left(\frac{\Delta PE_0}{PE_0}\right)^2}. \tag{2.4}$$

The results of the experiment were compared with a reference measurement with 200 kV x-rays [136, 153], where cells and treatment beside the irradiation were exactly the same.

Results

Possible differences in cell survival due to irradiation with different dose rates were tested with a CFA. This test was performed on 20 samples, 5 samples per dose rate plus 5 sham samples. In Figure 2.12, the results are shown in comparison to a survival curve derived from reference measurements on x-rays [136, 153]. The SFs of the samples irradiated at approx 3.6 Gy were the same for the three dose rates within the uncertainty levels (SEM). The Conv samples were irradiated with a mean dose of (3.7 ± 0.8) Gy (mean ± SEM) that resulted in a mean SF of 0.56 ± 0.05 (mean ± SEM). Flash9 samples were irradiated with a mean dose of (3.4 ± 1.0) Gy. The mean SF was here 0.55 ± 0.04. Flash310 samples were irradiated with a mean dose of (3.6 ± 1.5) that resulted in a mean SF of 0.52 ± 0.05. All measured SF values corresponded to the reference survival curve within their uncertainty levels. The results for all samples are listed in the appendix Table A.2.

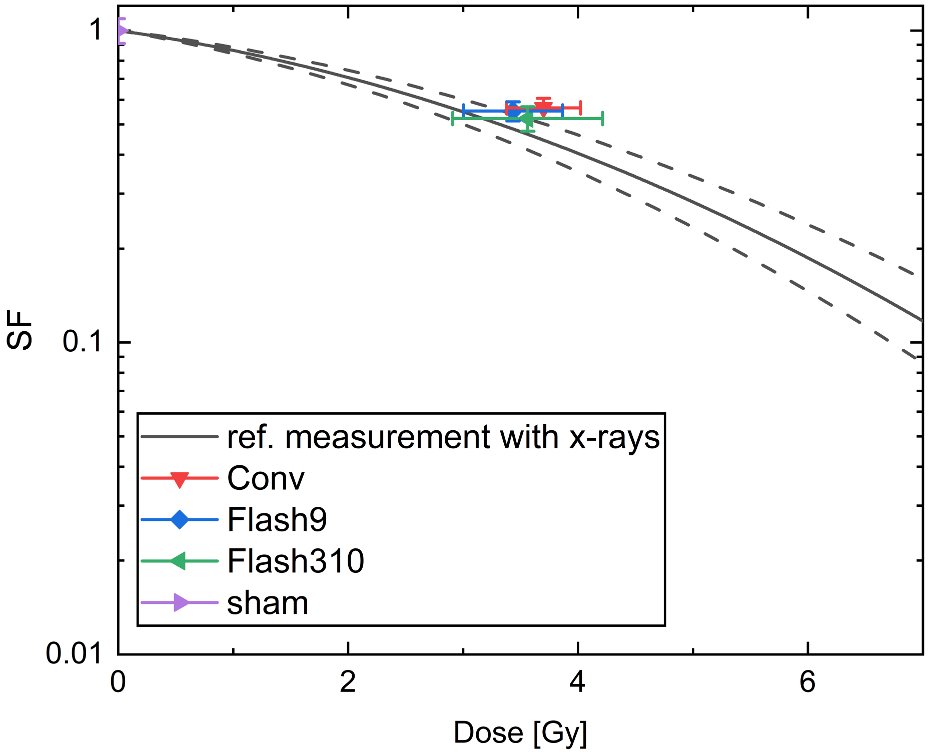

Figure 2.12: Results of the CFA for the three dose rates Conv, Flash9 and Flash310. The error bars denote the SEM. The black continuous line indicates the fitted survival curve derived from reference measurements with x-rays done by K. Ilicic [136, 153]. The dashed lines indicate the uncertainty range of the fit.

In Figure 2.13, the doses that were applied to each sample are depicted by rhombs, for every dose rate group in a different color. The mean doses of each group are indicated by horizontal lines and the whiskers show the SEMs. As can be seen there, the doses are distributed over a wide dose range, ranging in the Conv group from 2.3 Gy to 4.2 Gy, in the Flash9 group from 2.3 Gy to 4.8 Gy and in the Flash310 group from 2.1 Gy to 6.4 Gy.

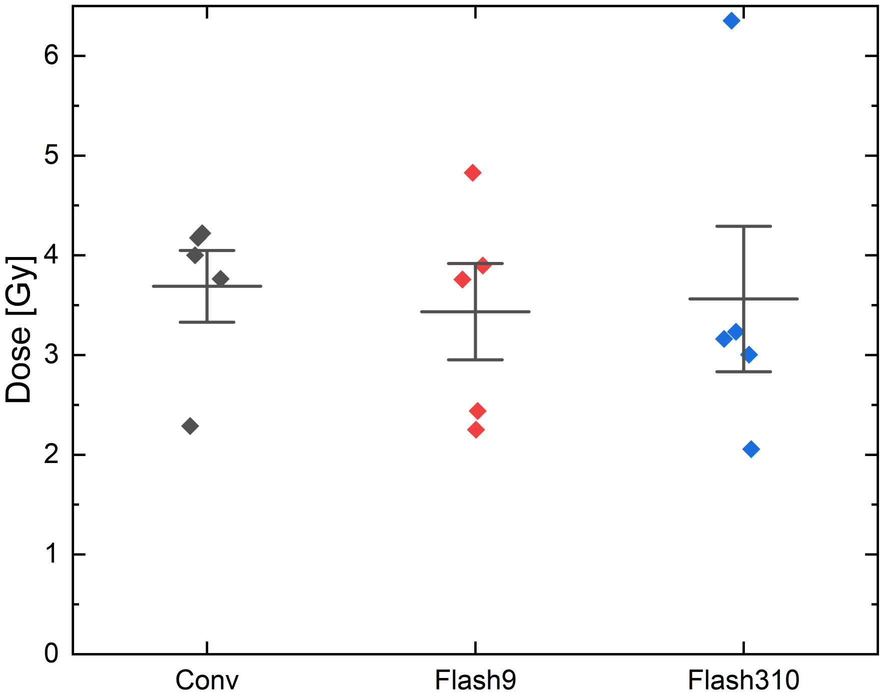

Figure 2.13: The applied doses in the CFA assay. The deposited doses to each sample are shown by rhombs. Black rhombs belong to the Conv dose rate group, red rhombs to the Flash9 dose rate group, and blue rhombs to the Flash310 dose rate group. The horizontal line indicate the mean of each group and the whiskers mark the SEM.

2.7.4 Decreased cell death of FLASH-irradiated cells

The cell death was investigated by a Caspase 3/7-Sytox assay performed on a flow cytometer (FACSCalibur flow cytometer, BD Biosciences, USA). With this assay, the percentage of apoptotic and necrotic cells can be measured in a sample. Apoptotic cells have a non-inflammatory effect on tissue due to the formation of apoptotic bodies, as discussed in Section 1.3.3. Apoptotic cells can be identified via detection of activated executioner caspases, such as caspase 3 and caspase 7 [154]. Caspases are a group of protease enzymes and are important enzymes for apoptosis. Caspase 3 and caspase 7 are activated during the apoptosis pathway to degrade cellular components [155]. The activated forms of these caspases can be fluorescently stained. Necrosis, on the other hand, is a cell death that always occurs in an unregulated fashion and is characterized by the loss of cell membrane integrity resulting in the release of intracellular components. Sytox is a fluorescent dye for nucleic acid that cannot enter healthy cells according to the producer [156]. Therefore, with this dye all cells can be detected that have a damaged cell membrane. This is the case for cells in late apoptosis or necrotic cells. With a flow cytometer, single cells can be checked whether they are stained with fluorescent dyes or not in a high throughput of 10.000 cells/ml. Therefore, several thousands of cells can be tested due to their staining in several minutes and the here described assay is well suited for investigating the forms and amounts of cell death.

FACS-fluorescent cell sorting

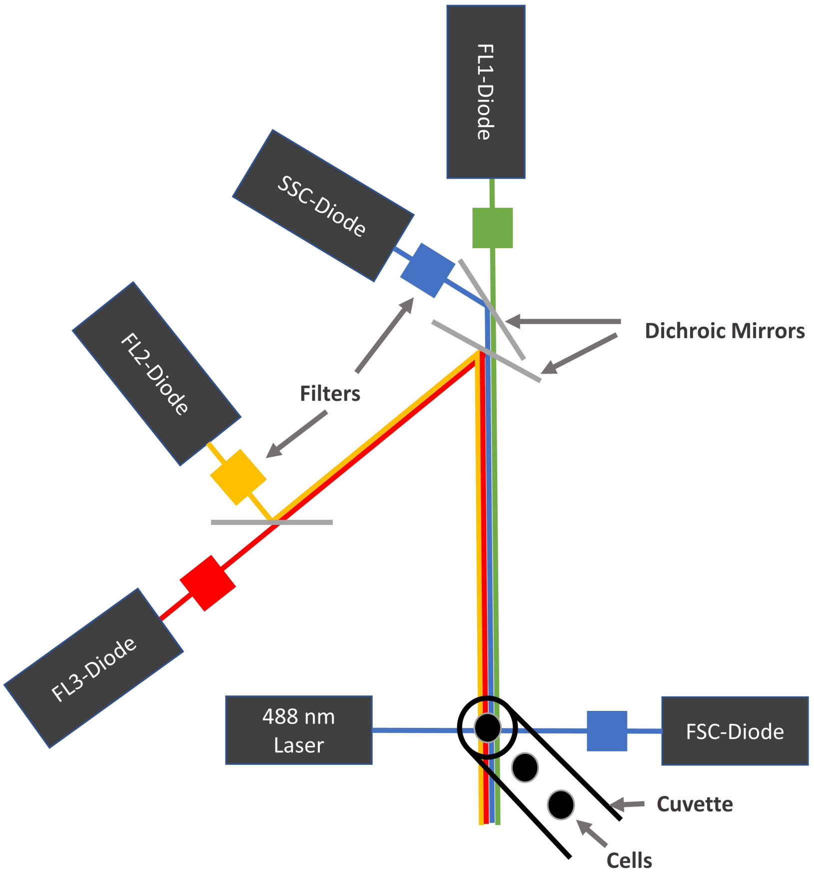

Figure 2.14: A schematic image of a flow cytometer. Cells pass the cuvette individually and are analyzed by a laser. The forward scattering light (FSC) and the side scattering light (SSC) were measured by diodes and provide information about volume and granularity. Fluorescent light coming from the cells is spectrally split by dichroic mirrors and filters and are measured by three fluorescent light (FL)-diodes.

A flow cytometer is a device for fluorescence activated cell scanning (FACS)[7] [157]. FACS enables the counting and analysis of physical and molecular properties of particles like mammalian cells in a liquid flow [157]. A schematic image of the FACS set-up is shown in Figure 2.14. For preparation of the cells for a FACS analysis, cells are trypsinized and suspended in a liquid, for example culture medium. Depending on the application, cells are fluorescently stained. The liquid containing the cells is sucked in a cuvette. This cuvette is so thin that only single cells can pass it one after another. The cells pass the laser beam and the light is scattered on the cells. The forward scattering (FSC) light is measured with a photodiode on the opposite side of the laser. The side scattering light (SSC) is collected and spectrally split

---

[7] FACS can also stand for fluorescent activated cell sorting. In this thesis, the sorting option of the flow cytometer was not used and is therefore not mentioned.

by a collection of dichroic mirrors and filters. By the spectral splitting of the light, the diodes analyze defined regions of wavelengths of the refracted light. The SSC-diode and the FSC-diode analyze light of the wavelength of the laser and the three fluorescent light (FL)-diodes measure the fluorescent light coming from the cells in different wavelength regions [158]. For the FSC measurement, the light diffracted in small angles from a cell provides a measure of the volume of the cell [157]. The SSC light measured by the SSC-diode provides information about the granularity of a cell [157]. The FL-diodes measure if a cell is fluorescent at different wavelengths. This analysis is done for every cell passing the cuvette seperately and can be performed in high throughput.

Caspase-3/7-Sytox assay

(**)

After irradiation of the cells, the medium was changed and the cells were incubated for 24 h at cell culture conditions. Then, the cells were trypsinized by keeping the supernatant of all steps. Afterwards, cells were stored at room temperature for 45 min while moving them to the analyzing laboratory. Finally, the solution of trypsinized cells and the supernatant were mixed and centrifuged at 500 g (gravitational acceleration) for 5 min at room temperature. After centrifugation, the supernatant was removed to the last 1 ml of the fluid, which also contained the cells. This solution was gently vortexed to distribute the cells equally in the fluid. The cells in the solution were stained with a Caspase 3/7 and a Sytox stain (CellEvent™ Caspase-3/7 Green Flow Cytometry Assay Kit, Invitrogen, USA) by following the instructions of the manufacturer. First, 1 µl of CellEvent™ Caspase-3/7 Green Detection Reagent was added to the solution to end up in a final concentration of 500 nM of the reagent and the samples were incubated at 37°C for 30 min. Finally, 1 µl of SYTOX™ AADvanced™ was added to the cell solution to obtain a concentration of 1 µM and the solution was incubated for another 5 min at 37 °C. The stained cells were analyzed using the FACSCalibur flow cytometer (BD Biosciences, USA). To detect Caspase 3/7, a 530/30 bandpass filter (FL1) was used to collect the fluorescence emission after a 488 nm excitation and for Sytox a 690/50 bandpass filter (FL3) was used. The data analysis was performed using CellQuest software (BD Biosciences, USA).

Results

The effect of irradiation with different dose rates on cell death was tested with a Caspase 3/7-Sytox assay. For each dose rate, 5 samples were irradiated with 20.5 MeV protons and 5 samples were sham irradiated. One sample of the sham group had to be excluded from evaluation as due to a leak in the sample the cells dried out during the 24 h incubation step. The irradiated doses for the three dose rate groups are depicted in Figure 2.15. The Conv group was irradiated with (3.3 ± 0.2) Gy (mean ± SEM), the Flash9 group with (3.5 ± 0.2) Gy and the Flash310 group with (3.1 ± 0.3) Gy. Therefore, the irradiated doses were the same within the given uncertainties. The Conv doses ranged from 2.7 Gy to 4.0 Gy, the Flash9 doses from 3.0 Gy to 3.8 Gy and the Flash310 doses from 2.5 Gy to 3.9 Gy and covered similar dose regions.

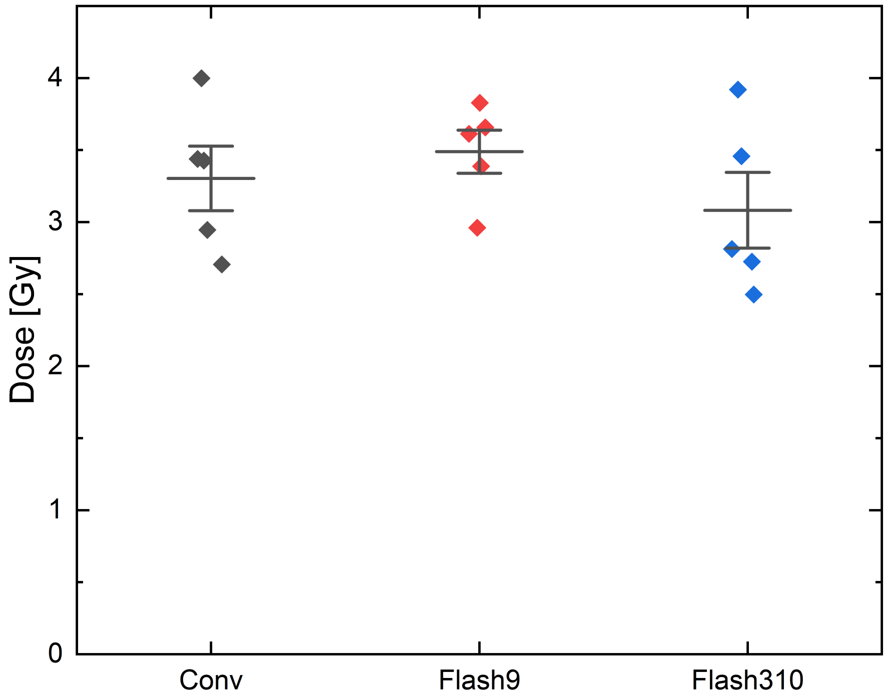

Figure 2.15: The applied doses in the Caspase 3/7-Sytox assay. The doses deposited to the individual samples are depicted by rhombs. The rhombs were black for Conv irradiated samples, red for Flash9 and blue for Flash310. The mean of each group is indicated by a horizontal black line and the whiskers mark the SEM.

In Figure 2.16, the results of the FACS analysis of the Caspase 3/7 and the Sytox staining of the cells are shown. Cells with a positive Caspase 3/7 and positive Sytox staining were classified as late apoptotic cells. Cells with a positive Caspase 3/7 and negative Sytox staining were classified as early apoptotic cells. Cells with a negative Caspase 3/7 and positive Sytox staining were denoted as necrotic cells and cells with no staining signal were classified as vital cells. Subsequently, the number of dead cells was determined by subtracting the number of vital cells from the number of all cells scanned by FACS. In this Figure, the fraction of cells with a certain staining of all evaluated cells are shown. The bars denote the mean values of the three dose rate groups and the Sham samples and the error bars the SEMs. The most common occurred cell death was apoptosis, necrosis was hardly found (< 0.08 %) and therefore not included in this Figure. In appendix Table A.3, the underlying data of all samples and the corresponding mean values are listed. The data for necrosis can be found there. In the Conv and Flash9 irradiated samples, the number of dead cells were approx. two times higher than in the Flash310 and the sham irradiated samples.

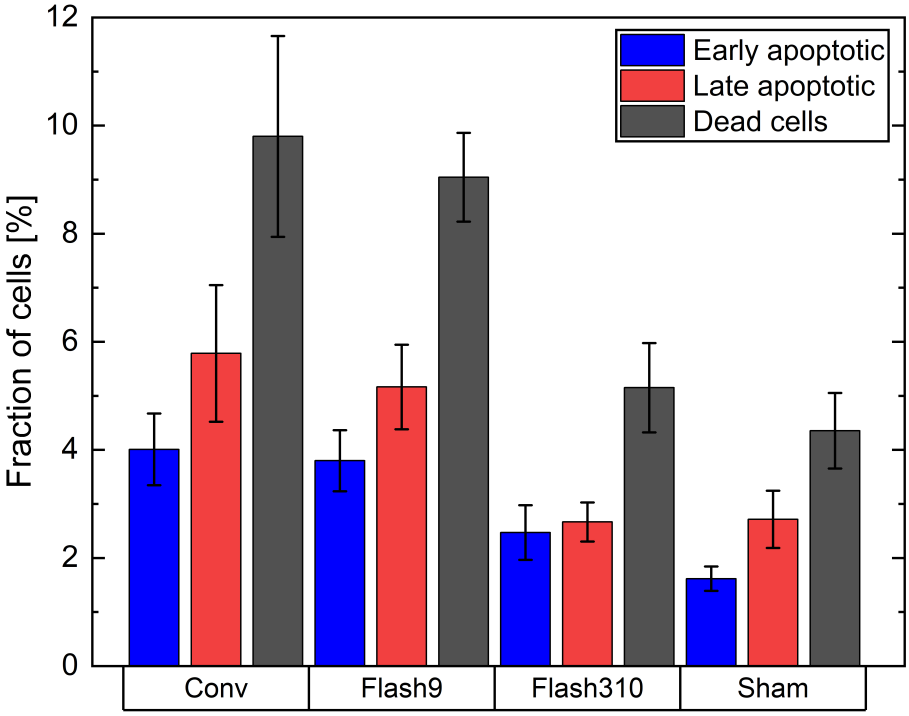

Figure 2.16: The results of the Caspase 3/7-Sytox assay. The fraction of cells with a certain staining from all evaluated cells are given in percent [%]. Early apoptotic cells were stained with Caspase 3/7 but not with Sytox and late apoptotic cells were stained with both Caspase 3/7 and Sytox. The fraction of dead cells was calculated by subtracting the fraction of all cells without staining from 100 %. As almost no necrotic cells occur, they were not included in this graph. The bars indicate the mean values of each dose rate group and the error bars the SEM.

More early and late apoptotic cells were found for Conv and Flash9 than for Flash310 and Sham. In the Conv, the Flash9 and the sham group, more late apoptotic cells occurred than early apoptotic cells, while for Flash310 similar amounts of early and late apoptotic cells were found. In Figure 2.17, the fraction of early apoptotic cells to late apoptotic cells are shown (early/late apoptotic cells: Conv: 0.69 ± 0.20, Flash9: 0.73 ± 0.16, sham: 0.60 ± 0.15 and Flash310: 0.9 ± 0.3). However, the fractions of early apoptotic cells to late apoptotic cells were the same for all dose rate groups and the sham group within the uncertainty range.

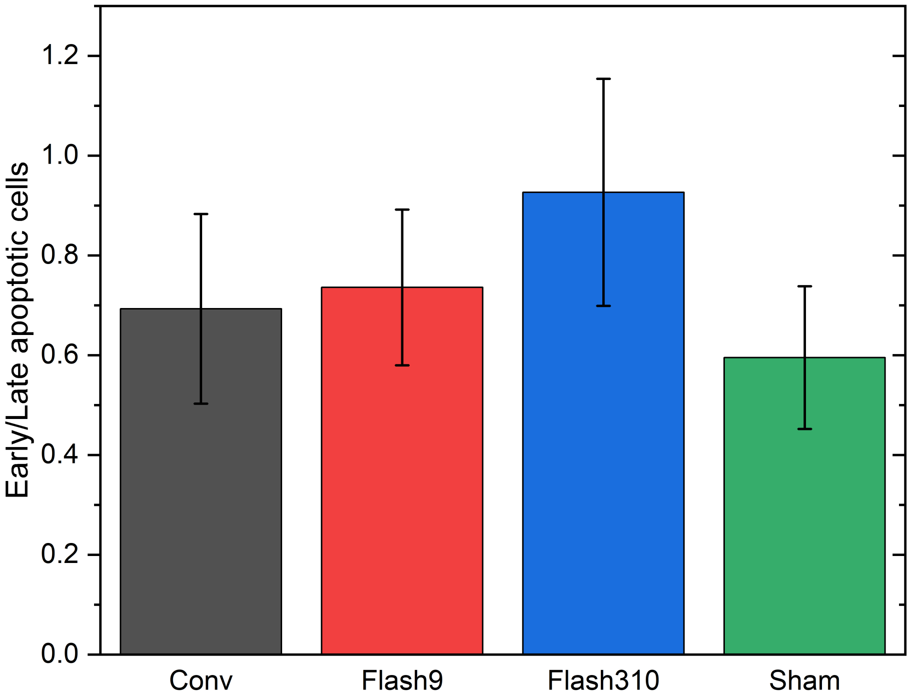

Figure 2.17: Here, the percentages of early apoptotic cells were divided by the percentages of late apoptotic cells for every dose rate group and the Sham group. The bars indicate the mean values and the error bars the SEMs.

In Table 2.2, 2.3 and 2.4, the significance levels of early apoptotic cells, late apoptotic cells and dead cells are shown, respectively. The significance levels were determined by comparing the results of two dose rate groups with a two-sample t-test. This was done for every combination of dose rate groups. If the p-value of a comparison was < 0.05, the table-entry was marked by a checkmark in a green box. For p-values between 0.05 and 0.075, the table entry was marked by a star in a yellow box and for p-values > 0.075, the table-entry was marked by a cross in a red box. For early apoptosis, a statistical difference was only found between Sham and Conv and between Sham and Flash9. For late apoptosis, the results of Flash9 and Flash310 were statistically significantly different, Flash310 and Conv and Flash9 and Sham were nearly significantly different. No difference was found between Conv and Flash9, Flash310 and Sham and between Sham and Conv. For the dead cells, a significant difference was found between Flash310 and Flash9 and between Sham and Flash9 and a nearly significant difference between Flash310 and Conv and between Sham and Conv. No differences were found here between Conv and Flash9 and between Flash310 and Sham.

	Conv	**Flash9**	**Flash310**	**Sham**
Conv	-	×	×	✓
Flash9	×	-	×	✓
Flash310	×	×	-	×
Sham	✓	✓	×	-

Table 2.2: Significance levels for early apoptosis. The results of all dose rate groups were compared with each other and the Sham group by a two-sample t-test. If the p-value of a comparison was < 0.05, the according table entry was marked with a checkmark in a green box. For p-values between 0.05 and 0.075, the table entry was marked with a star in a yellow box and for p-values > 0.075 the table entry was marked with a cross in a red box.

	Conv	**Flash9**	**Flash310**	**Sham**
Conv	-	×	∗	×
Flash9	×	-	✓	∗
Flash310	∗	✓	-	×
Sham	×	∗	×	-

Table 2.3: Significance levels for late apoptosis. Created like Table 2.2.

	Conv	**Flash9**	**Flash310**	**Sham**
Conv	-	×	∗	∗
Flash9	×	-	✓	✓
Flash310	∗	✓	-	×
Sham	∗	✓	×	-

Table 2.4: Significance levels for dead cells. Created like Table 2.2.

In total, this shows that Conv and Flash9 irradiation results in similar values as well as Sham and Flash310. Therefore, it can be concluded that with a dose rate of 310 Gy/s less cell death is induced than by a conventional irradiation or an irradiation with 9.3 Gy/s. Cell death was induced by Flash310 approximately as often as for Sham.

2.7.5 Decreased DNA damage in the micronucleus test

The micronucleus test is a state of the art assay to measure genotoxicity [159][160]. The key component of this assay is the formation of micronuclei. Micronuclei are formed by a cell in response to a genotoxic treatment like irradiation. Due to such a treatment, it can come to damages in the DNA. In case of DNA damage, a cell has different repair strategies. Nevertheless, it can come to an improper repair that might lead to cell death or formation of mutagenic lesions of different complexity. Such mutagenic lesions are dicentric chromosomes, translocations, acentric fragments, rings of chromosomes and chromatid type aberrations [123]. These lesions can be detected and removed from the cell by encapsulating these DNA fragments in a so-called micronucleus. The production of micronuclei is proportional to the irradiated dose [123]. Therefore, this assay can be used for biological dosimetry [161].

Micronuclei test

After irradiation, the medium was removed and 3.3 ml with 1 µl Cytochalasin B (3 µg/ml Cytochalasin B, Firma, Firmensitz) was added. Cytochalasin B is a cell-permeable mycotoxin[8] [162] and inhibits the cytokinesis in cells [163]. Therefore, the cells are unable to separate their membrane during mitosis that results in binucleated cells. To let the cells in this experiment become binucleated, cells were incubated for 27 h in the medium-Cytochalasin B solution at cell culture conditions. After 27 h, the solution was removed and cells were washed with PBS for 5 min. 1 ml of cold KCl solution was added drop by drop to avoid fracturing the cell membranes. Then, 1 ml of ice-cold methanol mixed with acetic acid (3:1 v/v) was added drop by drop and was removed. This step was repeated three times in total. The samples were stained with Hoechst, were washed with PBS, and were dried at air. One drop of prolong gold was placed on the cells and on a microscope slide. The microscope slide was placed below the cell container window, where the cells were grown on a mylar foil. A cover glass was put onto the cells and the foil was cut at the edges of the cover glass. Microscope slide, cells on the mylar foil and cover glass were softly pressed together, two sides were glued with nail polish and the resulting samples were dried on air over night. For evaluation, the whole cell area was imaged with a fluorescence microscope (Axio Observer Z1, Zeiss, Oberkochen) by using the MosaiX scan of AxioVision software (Zeiss, Oberkochen). The fluorescent Hoechst staining was imaged with the 405 nm LED (Colibri, Zeiss, Oberkochen), the Dapi filter and a 40 x objective. Binucleated cells (BN) were counted by applying the following criteria: A BN cell must contain two nuclei with approximately the same size, staining pattern and intensity. The two nuclei within a BN cell may be unconnected or may be attached by one or more fine nucleoplasmic bridges. They may touch each other but should not overlap. BN cells should not overlap each other. Micronuclei (MN) were scored in BN cells by applying the following criteria: The diameter of MN should be smaller than one third of the mean diameter of the main nuclei. The MN should not be connected to the main nuclei. The MN may touch but not overlap the main nuclei. Furthermore, the boundary of MN should be distinguishable from the boundary of the nuclei. In Figure 2.18, an example image of BN cells and a BN cell containing a MN is shown.

---

[8] A mycotoxin is a toxic substance produced by fungi.

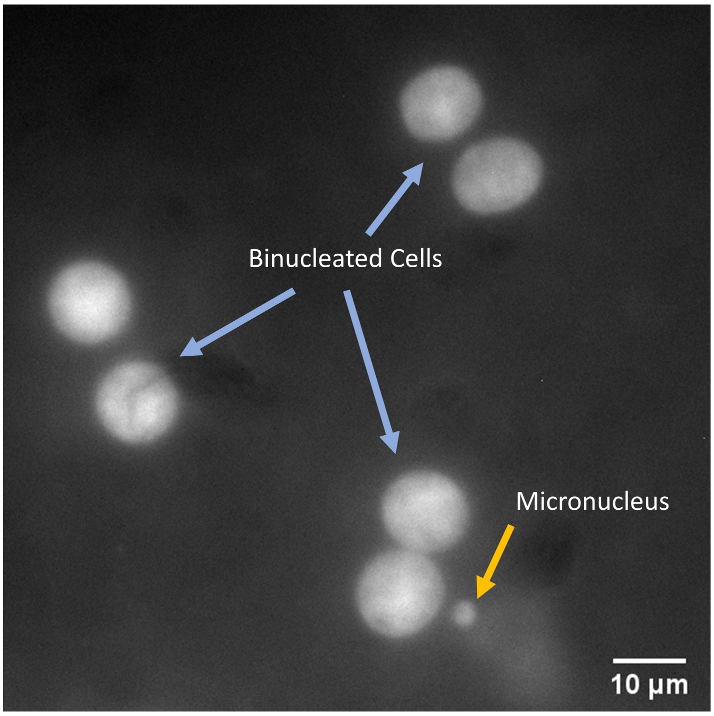

Figure 2.18: A fluorescence microscopy image of binucleated cells with and without micronuclei. The cells were stained with Hoechst to visualize the cell nuclei.

Results

A micronuclei test was performed to investigate the effect of different dose rates on the genetic damage. Five samples were irradiated for each tested dose rate Conv, Flash9, and Flash310 and five samples were sham irradiated. In the Flash310 group, one sample had to be excluded from evaluation as the fixation and staining process went wrong. The applied doses are shown in Figure 2.19. The Conv group recieved a mean ± SEM dose of (2.7 ± 0.2) Gy, the Flash9 group a dose of (3.64 ± 0.08) Gy and the Flash310 group a dose of (3.20 ± 0.12) Gy. The irradiated doses of each dose rate group are statistically significantly different from each other (two-sample t-test, $p\text{-value} < 0.05$, Origin 2021b). The doses irradiated at Conv dose rate were between 2.27 Gy and 3.28 Gy, at Flash9 between 3.32 Gy and 3.79 Gy, and at Flash310 between 2.90 Gy and 3.56 Gy. In Figure 2.20, the mean percentage of BN cells containing one or more MN is shown for every dose rate group and the Sham group. As shown there, the MN test results in the same percentage of cells containing MN within the standard error for the three different dose rates. In Conv irradiated cells, (29 ± 1) % of BN cells formed one or more MN, in the Flash9 group (32 ± 2) %, and in the Flash310 group (28 ± 4) %. The Sham irradiated cells produced significantly less MN ($p\text{-value} < 0.5 \cdot 10^{-6}$, one-way ANOVA, Origin 2021b). Only in (4.5 ± 0.6) % of the binucleated cells micronuclei were found.

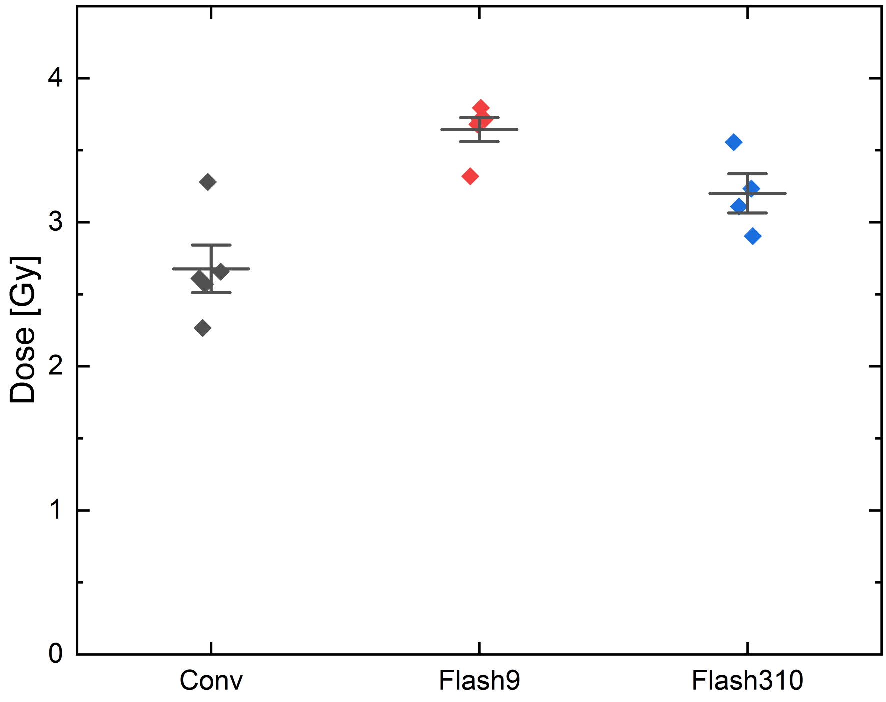

Figure 2.19: The doses applied to the samples of the microncleí test. These doses were irradiated using three different dose rates indicated by Conv, Flash9 and Flash310. The doses applied to each sample are depicted by rhombs. The mean values are shown by a horizontal black line and the whiskers indicate the SEMs.

A closer look to the found amounts of MN in MN containing BN cells provides Figure 2.21. Here, the mean percentage of BN cells containing 1, 2, or ≥ 3 MN are separately plotted for each dose rate group and the Sham samples, the error bars indicate the SEMs. In the MN categories 1 MN and 2 MN, the Sham samples had significantly fewer BN cells with MN (1 MN: p-value = $5.8{\cdot}10^{-8}$, 2 MN: p-value = 0.002, one-way ANOVA, Origin 2021b), which is indicated by three stars. No cell contained three or more MN in the Sham samples. The same percentage of BN cells with one MN was found in Conv and Flash9 with (24.1 ± 1.4) % and (25.3 ± 1.2) %, respectively. Flash310 irradiation produced almost significantly less cells with one MN than Flash9 (p-value = 0.06, two-sample t-test, Origin 2021b), indicated by two stars, resulting in (20 ± 2) %. This result was also smaller than that of Conv irradiation, but not significantly. For the category of two MN, Conv irradiation led to the smallest percentage of cells of this category with (3.5 ± 0.6) %, Flash9 produced more often two MN in BN cells with (5.4 ± 1.2) % and most often BN cells with two micronuclei were produced by Flash310 irradiation with (6.2 ± 1.1) %. The results of Flash310 and Conv were nearly significantly different with a p-value of 0.07 (two-sample t-test, Origin 2021b), indicated by one star. All dose rate groups induced the same percentage of BN cells with 3 or more MN within the determined uncertainties with (1.8 ± 0.4) % for Conv, (1.3 ± 0.5) % for Flash9, and (1.6 ± 0.6) % for Flash310. Conv samples were irradiated with the lowest doses of (2.7 ± 0.2) Gy, but more cells with 1 MN were found here than for Flash310 samples, which received a higher dose of (3.20 ± 0.12) Gy and a similar amount was found for the Flash9 group, which received (3.64 ± 0.08) Gy of dose. Therefore, it can be concluded that a lower dose applied in Conv mode induces similar amounts of cells with one MN than Flash9 and more cells with one MN than Flash310. Flash310 induces less cells with one MN but more cells with two MN than CONV and Flash9, although the dose was higher than for the Conv group and smaller than for the Flash9 group.

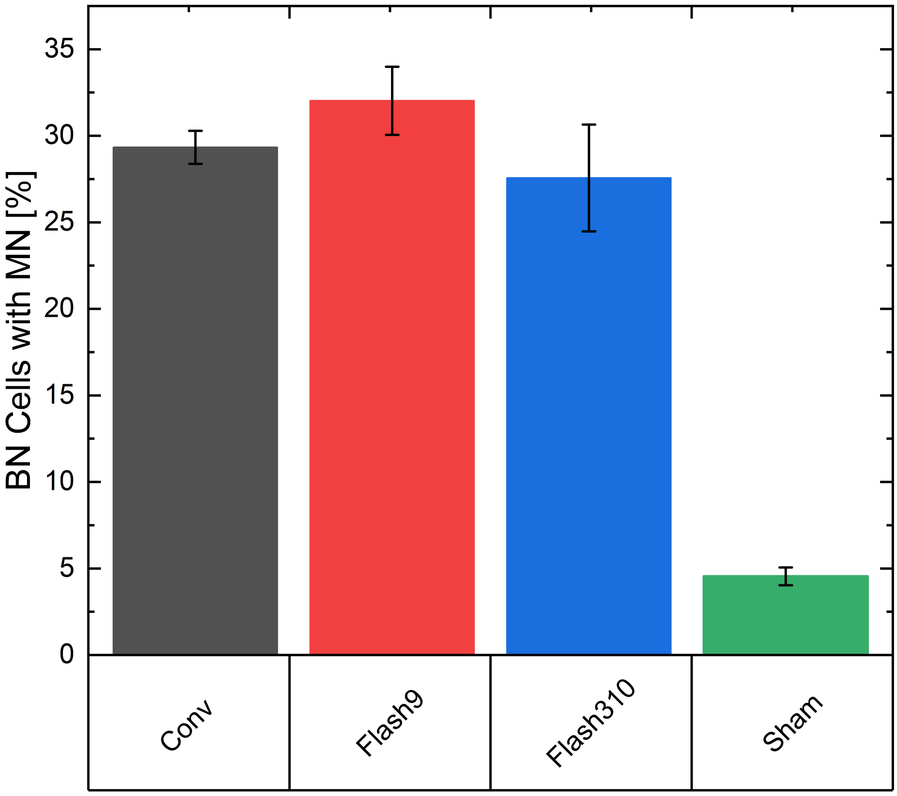

Figure 2.20: Mean percentage of binucleated cells containing one or more micronuclei for every dose rate group and the Sham group. The error bars denote the SEM.

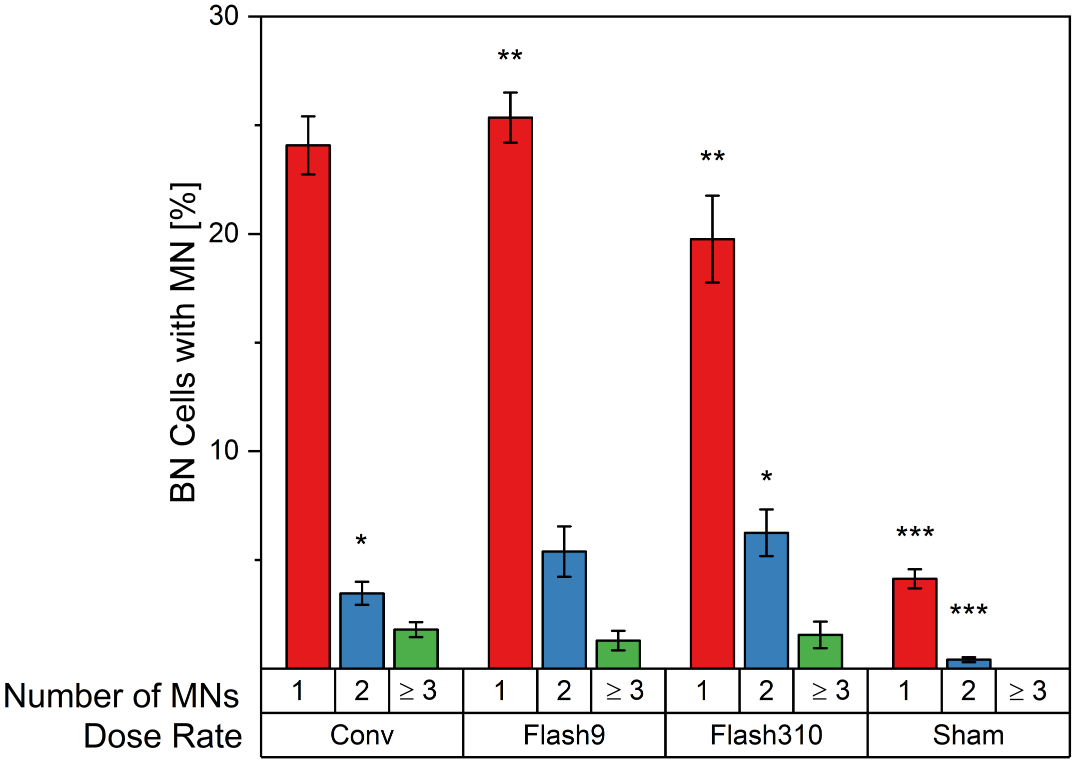

Figure 2.21: The percentage of BN cells with MN grouped according to the number of MN (1 MN, 2 MN, and ≥ MN) for three dose rates and the Sham group. The bars indicate the mean values and the error bars the SEMs. Bars marked with one star are almost significantly different to each other with a p-value of 0.07 (two-sample t-test, Origin 2021b), Bars marked with two stars are nearly significant to each other with a p-value of 0.06 (two-sample t-test, Origin 2021b), and bars of the Sham group marked with three stars are significantly different from the irradiated groups with p-values for 1 MN: $5.8 \cdot 10^{-8}$ and 2 MN: 0.002 (one-way ANOVA, Origin 2021b).

The dose dependence is shown in Figure 2.22. Here, the percentage of BN cells containing MN for every irradiated sample is plotted against the applied dose for every sample. The data of every group are fitted by a linear curve with a fixed intersection of the y-axis at 4.5 %, which equals the mean value of the Sham samples. As it can be seen there, the fitted curve for Conv is steeper with a slope of 9.1 ± 0.8 than the fitted curves of Flash9 (slope: 7.5 ± 0.6) and Flash310 (slope: 7.0 ± 1.3). The slopes for Flash9 and Flash310 were the same within the uncertainties of the fits. This representation supports the assumption that lower doses of Conv irradiation induces the same amount of cells with MN than higher doses of Flash9 or Flash310 irradiation. Similar to Section 2.4, the dose modifying factor (DMF) can be calculated here. To induce a percentage of BN cells with MN of (30.0 ± 1.3) %, which is the mean ± SEM percentage of BN cells with MN of all irradiated samples, a Conv dose of (2.8 ± 2.0) Gy is necessary, a Flash9 dose of (3.4 ± 2.4) Gy, and a Flash310 dose of (3.6 ± 2.6) Gy. This results in a DMF of 1.2 ± 1.2 for Flash9 and a DMF of 1.3 ± 1.2 for Flash310. The errors for dose and DMF are derived by using the Gaussian uncertainty propagation.

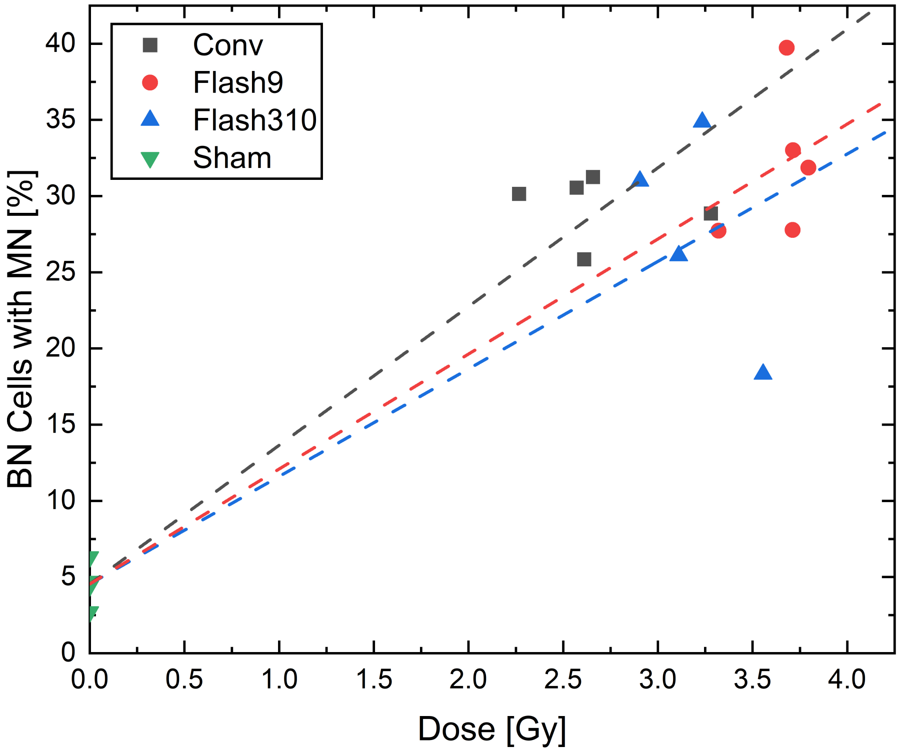

Figure 2.22: The percentage of BN cells with MN plotted against the dose for each sample. The results of the Conv irradiation are indicated by black squares, the results of Flash9 by red dots, the results of Flash310 by blue up-facing triangles, and the results of Sham are depicted by green down-facing triangles. The data of each group were linearly fitted with a fixed intersection of the y-axis at 4.5 %, which equals the mean of the Sham samples and the fits are shown by dashed lines. The fitted curves have the following slopes: Conv: 9.1 ± 0.8, Flash9: 7.5 ± 0.6, and Flash310: 7.0 ± 1.3

It can be concluded that Flash dose rates might lead to less genetic damage and, therefore, less micronuclei than Conv irradiation. The damages induced by a Flash dose rate seem to be more complex, as here more cells with more than one MN were found.

2.8 Proton-FLASH effect in a mouse ear animal model

As an in-vivo model, a mouse ear model was chosen. This model is well etablished and tested at my institute and showed its potential in several experiments investigating different radiation treatment modalities [132, 133, 164, 165]. The mouse ear model can be irradiated by 20.5 MeV proton beams, which have a maximum penetration depth of 4.5 mm, in shoot through mode, as a mouse ear has a thickness of approx. 240 µm. The mouse ear serves as a skin model and is used for investigating side effects in the skin. The skin is typically irradiated in a shoot through manner, as the Bragg-peak of the proton beam is located in the deeper seated tumor region. Furthermore, the mouse ear model provides various evaluations of skin radiation response. The swelling can be monitored by ear thickness measurements. Erythema, desquamation, depilation and morphology changes can be easily determined by inspection by eye. Also long time effects like scarring and permanent morphology changes of the ear can be evaluated, which are indicators of fibrosis. Due to the thin form of the ears, the blood vessels can be investigated. By transillumination of a mouse ear, the blood vessels can be visualized. With this technique, the irradiated blood volume can be determined. Additionally, photo acoustic microscopy enables non-destructive measurements of blood flow speed, hemoglobin concentration and oxygen saturation [166].

2.8.1 Proton-irradiation of a mouse ear animal model

(*)
The irradiation set-up described in Section 2.5 was used in this experiment and the dose verification was performed as described in Section 2.6. The right ears of 63 female Balb/c mice were irradiated with 0 Gy, 23 Gy, or 33 Gy at three different dose rates: 0.06 Gy/s, 9.3 Gy/s, and 930 Gy/s.

Balb/c mice were used due to their large ears and are an albino strain. Due to the white fur and their light skin, inflammation reactions of the irradiated skin can be easily detected. Furthermore, these mice have a calm character and are easy to handle, which was necessary for the daily handling in this experiment.

At the time of irradiation, the mice were 12 weeks old. The mice were held in a temperature-regulated animal facility with a 12-hour light/dark cycle and had ad libitum access to food and water at the animal facility of the Helmholtz Zentrum München. The cages were enriched with wooden sticks for gnawing, paper homes for retreat and paper strands, which serve as hay-substitute for building nests. The cages were exchanged once a week. The experiment was approved by the District Government of Upper Bavaria (Az. 55.2.1.54-2532-9-2017) and followed the animal welfare and ethical guidelines of our institutions. The animals arrived ten days before the experiment to acclimatize.

For irradiation, the mice were placed in a specially designed holder that kept the right ear of each mouse in the right position as described in Girst et al. [132] and as shown in Figure 2.23. The mouse was placed in a jig. The right ear is fixed with strips on a metal plate with a window, as shown in Figure 2.23(a). Thereby, the central part of the ear covers the window, through which the mouse is irradiated. The jig with the metal plate and the mouse was slid into a holder in front of the beam, as shown in Figure 2.23(b). With this setup, the central part of the ear was irradiated with the rear of the ear facing the beam. An EBT-XD film was placed onto the front side of the right ear covering the whole irradiation field for dose verification.

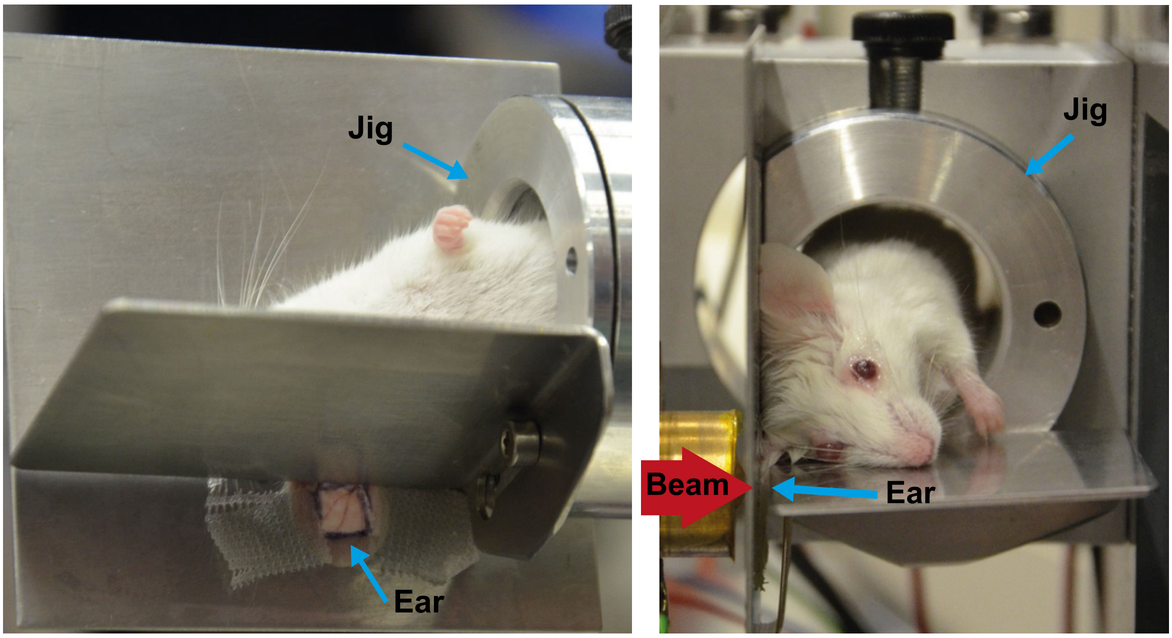

(a) (b)

Figure 2.23: Mouse holder for proton irradiation at SNAKE. (a) shows the holder from side view. The mouse is placed in a jig, and the right ear is attached to a metal plate using strips so that the center of the ear covers a window in the metal plate. Through this window the ear is irradiated as shown in (b) in front view.

During irradiation, the mice were kept under general anesthesia, which was induced by intraperitoneal injection of medetomidine (0.5 mg/kg), midazolam (0.5 mg/kg), and fentanyl (0.05 mg/kg). The antagonist atipamezole (2.5 mg/kg), flumazenil (0.5 mg/kg), and naloxone (1.2 mg/kg) were administered subcutaneously after irradiation.

2.8.2 Dose delivery and re-grouping

In this experiment, 63 mice were irradiated with three different dose rates (Conv, Flash9, Flash930) and two doses (25 Gy and 35 Gy) or were Sham irradiated. Sham irradiated mice were treated exactly the same as the other mice including anesthesia and fixation of the ear on the holder, but the beam was not switched on. The mice were distributed in 7 groups as shown in Table 2.5 such that each group contains 8 mice with one spare and the mice were irradiated accordingly.

For irradiation, the detector system was used as described in Section 2.6. An ionization chamber was placed between beam exit and mouse-holder that measured the dose. When the desired dose was reached, a chopper upstream in the beam line received a signal and switched off the beam. As extra dose verification, gafchromic EBT-XD films were placed behind the ears during irradiation. The dose measurements of the gafchromic films and therefore the actual irradiated doses for every mouse are shown group-wise in Figure 2.24.

Dose [Gy]	Dose rate [Gy/s]	Mice
25	0.06	8+1
35	0.06	8+1
25	9.3	8+1
35	9.3	8+1
25	930	8+1
35	930	8+1
0	Sham	8+1

Table 2.5: The original grouping of mice in the in-vivo proton-FLASH experiment.

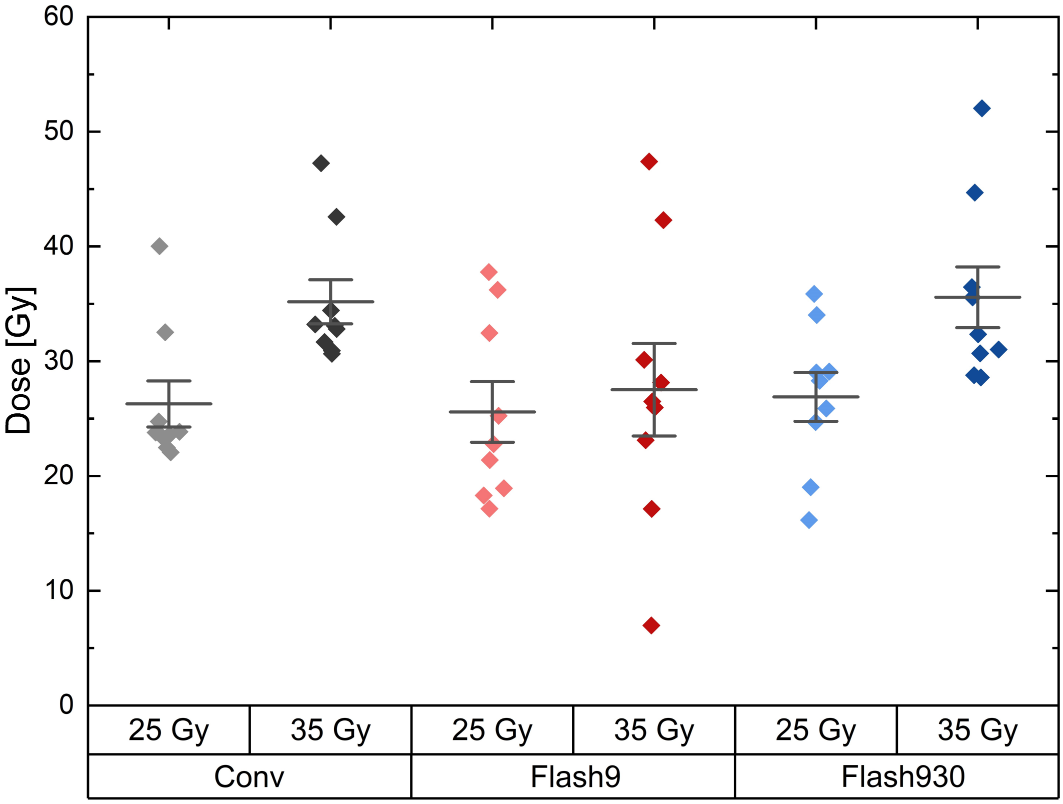

Figure 2.24: The gafchromic dose measurements of the irradiated doses in the mouse ear experiment in the original groups. The mice were distributed in 6 irradiation groups and a sham group and were irradiated with either 25 Gy or 35 Gy applied at one of three dose rates (Conv, Flash9, and Flash930). The dose measurements of Conv irradiation are indicated by gray or black rhombs, for Flash9 irradiation by red rhombs and by Flash930 irradiation by blue rhombs. A light coloring denotes a dose application that aimed for 25 Gy and a dark coloring marks a dose application that aimed for 35 Gy. The horizontal lines denote the mean values and the whiskers the corresponding SEMs.

The three dose rates are indicated by three colors: Conv is shown in gray to black, Flash9 in red, and Flash930 in blue. Light colors indicate a targeted dose of 25 Gy and dark colors a targeted dose of 35 Gy. It can be seen that the doses of the two Conv groups are tightly distributed around 23 Gy and 33 Gy in a range of ± 2 Gy with two outliers in each group. In the Conv 25 Gy group, the outliers were at 40.0 Gy and 32.5 Gy and in Conv 35 Gy group, the ouliers were at 42.6 Gy and 47.2 Gy. For the two Flash dose rates, the actual irradiated doses differ more. In the Flash9 25 Gy group, doses between 17.1 Gy and 37.8 Gy were irradiated resulting in a mean dose ± SEM of (25.6 ± 2.7) Gy. In the Flash9 35 Gy group, the dose range was the highest. Here, the doses ranged from 7.0 Gy to 47.4 Gy that results in a mean dose of (28 ± 5) Gy. The measurements of the Flash930 25 Gy group were distributed over a similar range as for the Flash9 25 Gy group. It ranges from 16.2 Gy to 35.9 Gy with a mean dose of (27 ± 3) Gy. The measurements of the Flash930 35 Gy group ranged from 28.6 Gy to 52.0 Gy with a mean dose of (36 ± 3) Gy. The performance of the ionization chamber in this experiment can be determined by calculating the deviation between the set dose and the actual irradiated dose. The standard deviation ΔD from the set dose is determined for every dose rate by:

$$\Delta D = \sqrt{\frac{\sum^{n}(D_{set} - D_{irr})^2}{n}} \tag{2.5}$$

where n is the number of mice irradiated with the same dose rate, D_{set} was the set dose and D_{irr} the actual irradiated dose. The percentage of the standard deviation ΔD% (the relative standard deviation) on the actual irradiated dose was calculated for every group. ΔD% was the highest for Flash9 dose rate for 25 Gy and 35 Gy with 30 % and 40 % and the lowest for Conv dose rate for 25 Gy and 35 Gy with 24 % and 16 %, respectively. For Flash930, it was 26 % for 25 Gy and 22 % for 35 Gy. This shows that the performance of the detector was dose rate depended. It was the best for Conv irradiation, but had troubles in detecting doses and switch off the beam in time for the two Flash dose rates. For the evaluation of biological effects, these dose variances were too high. Therefore, the mice were re-grouped according to the actual irradiated dose and the applied dose rate. Before re-grouping, data of mice that died or had to be euthanized during the experiment were excluded from evaluation. Mouse 12 and 14 were found dead in their cages two days after irradiation. Mouse 20 was found dead at the morning after new year's eve 20 days after irradiation. Mouse 27 had to be euthanized. This mouse received to much dose (> 50 Gy) due to a system failure during irradiation. Mouse 30 was euthanized two days after aneasthesia, as this mouse was persistently apathetic. Mouse 42 was euthanized 68 days after irradiation due to extended and persistent weight loss, which was a termination criterion according to animal welfare guidelines of the District Government of Upper Bavaria. Furthermore, mice were excluded that received too much (> 37 Gy) or too little dose (< 15 Gy).

The other 49 mice were distributed to new groups as listed in Table 2.6. The groups were arranged by taking into account the applied dose rates and it was aimed for similar mean doses. Here, it was found that in the Conv group the doses were closely distributed around 23 Gy and 33 Gy. Therefore, these new doses were chosen for grouping. As also listed in this Table, the number of mice in these groups vary. The Flash9 33 Gy group includes only 3 mice, while the groups Flash9 23 Gy and Flash930 33 Gy had 9 members, respectively. The other groups had 7 members. As this grouping aimed to ensure that the mean dose application was uniform between groups, this imbalance in group sizes could not be altered.

Dose [Gy]	**Dose rate [Gy/s]**	**Mice**
23	0.06	7
33	0.06	7
23	9.3	9
33	9.3	3
23	930	7
33	930	9
0	Sham	7

Table 2.6: The regrouping of mice to minimize dose variances.

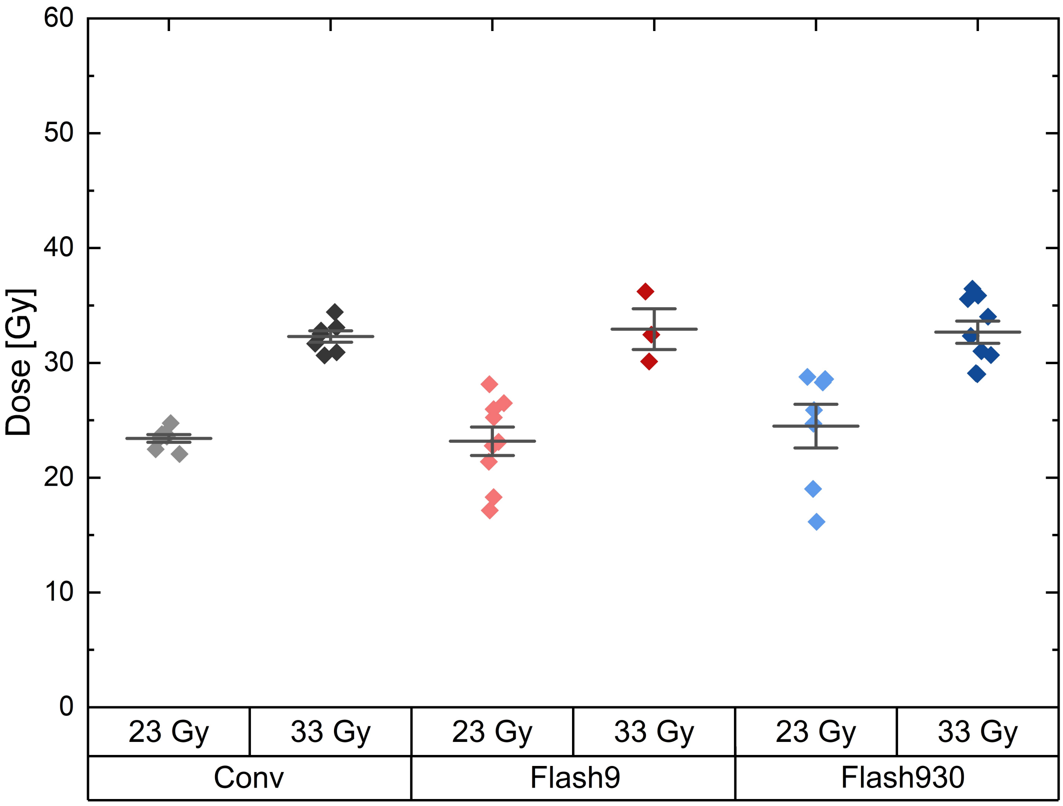

Figure 2.25: The gafchromic dose measurements of the irradiated doses in the mouse ear experiment in the new groups. This Figure was arranged in the same way as Figure 2.24.

In Figure 2.25, the actual irradiated doses are shown after regrouping. As can be seen there, the variances in each group are now decreased especially in the two Conv groups. In these groups, the dose varied < 2.4 Gy from 23 Gy and 33 Gy. In the Flash9 33 Gy group and Flash930 33 Gy group, the doses varied < 4.0 Gy from 33 Gy. For the two groups Flash9

23 Gy and Flash930 23 Gy, the dose variation was higher with maximal variances of 5.9 Gy and 6.9 Gy, respectively. The relative standard deviation ΔD% reduces at Conv dose rate for 23 Gy and for 33 Gy to 4 %, at Flash9 for 23 Gy to 15 % and for 33 Gy to 8 %, and at Flash930 for 23 Gy to 21 % and for 33 Gy to 9 %. Therefore, ΔD% was now for all groups below 15 % except for the Flash930 23 Gy group. The mean doses ± SEMs for the 33 Gy groups were (32.3 ± 0.5) Gy for Conv, (32.9 ± 1.8) Gy for Flash9, and (32.7 ± 1.0) Gy for Flash930. For the 23 Gy groups, the mean doses were (23.4 ± 0.4) Gy for Conv, (23.2 ± 1.3) Gy for Flash9, and (24.5 ± 1.9) Gy for Flash930. The biological endpoints were evaluated based on this grouping.

2.8.3 Mouse ear measurements

(*)

The measurements on the mouse ears were performed once before irradiation and after every second to seventh day for 180 days after irradiation depending on the inflammation reaction. Acute inflammation reactions were observed until the 38^{th} day and the monitoring was performed every second day in this period. After 38 days, the monitoring interval was increased to 4 days and after 61 days it was increased to 7 days.

Figure 2.26: The measuring gauge used for the ear thickness measurements.

Ear thickness measurement

The ear thicknesses of both ears of each mouse were measured using a specially adapted electronic external measuring gauge (C1X079, Kröplin GmbH, Schlüchtern, Germany), with measuring contacts of 6 mm diameter, as shown in Figure 2.26. Thereby, the mouse ear was put between the measuring contacts and the contacts were gently closed for measuring on three different spots within the central part of the ear, where the mice were irradiated. The mean value of the three measurements was calculated.

Skin reaction scoring

The inflammation reactions of the skin were measured by eye inspection using a scoring system following previous studies [132, 133, 164, 165]. The mouse ears were examined with regard to erythema, desquamation, hair loss, morphology changes and injuries of the ear. In this experiment, no hair loss and morphology changes were observed. Minor injuries of the ears were found in 9 mice 2-4 days after irradiation, which came from the fixation of the ear during irradiation and where located at the edges of the ears. All injuries, in the form of scratches found later came from extensive body care. For the scoring of the inflammation reaction, only desquamation and erythema were taken into account. Erythema is a consequence of dilated or congested superficial capillaries that increase the blood flow [167]. It was assessed with the following options: no, mild, definite and severe. Example images for each score are shown in Figure 2.27. A mild erythema is characterized by a slight reddening. In contrast, the definite erythema is more pronounced and more extended. The severe erythema is characterized by a dark red coloring and covers at least the whole irradiation region, but can also be more extended.

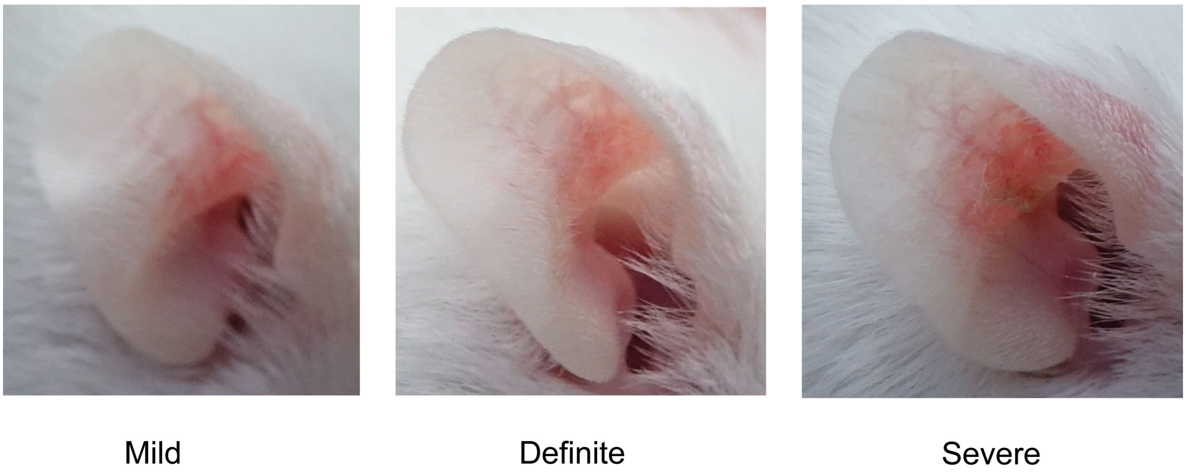

Figure 2.27: Examples for the three scores of erythema.

Desquamation is the rejection of the uppermost keratinized skin layer. It can be subdivided into dry and moist desquamation and crust formation. The dry desquamation is the shedding of the outer skin layers [81]. The moist desquamation is characterized by the release of wound fluid [82]. When blood and other exudates dry, a protective crust is formed [82]. This state is scored as crust formation. The crust formation results as a healing process of moist desquamation [82, 167].

Erythema	**Score**	**Desquamation**	**Score**
no	0	No	0
mild	0.5	Dry	1
definite	1.5	crust formation	2
severe	3	Moist	3

Table 2.7: The inflammation score. As inflammation reactions, erythema and desquamation were scored according to this table. The sum of both scores forms the inflammation score.

The corresponding scores to each erythema and desquamation category is shown in Table 2.7. The sum of both scores formed the inflammation score.

2.8.4 Decreased ear swelling due to proton-FLASH irradiation

The right ears of Balb/c mice were irradiated with three different dose rates while aiming to irradiate 25 Gy or 35 Gy. As discussed in Section 2.8.2, the doses varied especially when a Flash dose rate was applied. The ear thicknesses were measured for 180 days and the maximum ear thickness for every mouse was derived, which is shown in Figure 2.28 plotted against the irradiated dose. The maximum ear thicknesses were found for irradiated mice between 22 and 28 days after irradiation. In this Figure, the measurements of Conv irradiated mice are presented by black dots, for Flash9 irradiated mice by red up-facing triangles, for Flash930 by blue down-facing triangles and for Sham by green squares. It can be seen there, that mice irradiated with doses up to 22 Gy showed similar max. ear thicknesses than the Sham irradiated mice with max. ear thicknesses between 258 µm and 300 µm. At doses between 22 Gy and 32 Gy, some mice had increased max. ear thicknesses up to 390 µm and some mice had max. ear thicknesses similar to the Sham mice. At 31 Gy, the first mouse developed a max. ear thickness of above 400 µm. This mouse was from the Conv group. Four other mice of the Conv group that were irradiated with doses between 31 Gy and 34 Gy also developed max. ear thicknesses of above 400 µm. By contrast in the Flash9 and Flash930 groups only three mice had max. ear thicknesses of above 400 µm and these mice were irradiated with much higher doses of 35 Gy to 52 Gy. In general, it can be seen that with increasing doses the mice had increased max. ear thicknesses. However, Conv irradiated mice were more prone to develop higher max. ear thicknesses than mice irradiated with one of the two Flash dose rates. In the Conv group, there is one outlier. One mouse received a dose of 47 Gy but developed no ear swelling. The reason for that outlier could not be elucidated.

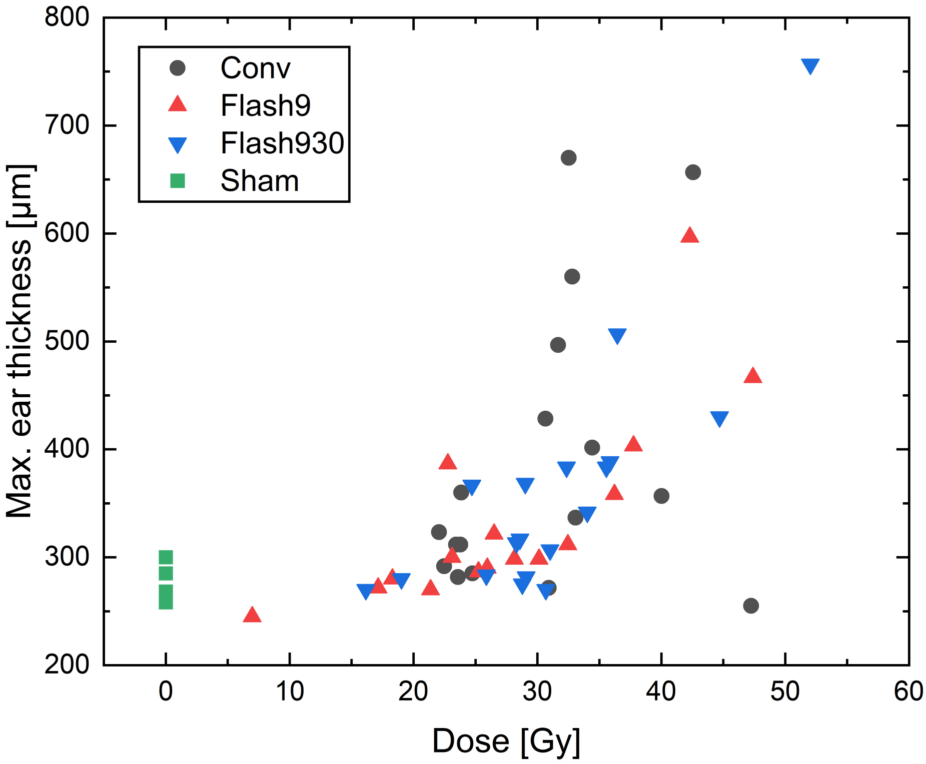

Figure 2.28: The maximum ear thickness measured for every mouse in the experiment plotted against the irradiated doses. The values of the Conv group were plotted with black dots, the Flash9 group with red up-facing triangles, the Flash930 group with blue down-facing triangles and the Sham group with green squares.

In Figure 2.29 and 2.30, the mean ear swelling of every irradiation group is shown over 180 days. The ear swelling $ES_i(t)$ of mouse i at each time point was determined by the following equation:

$$ES_i(t) = ET_i(t) - \overline{ET}_{Sham}(t) \tag{2.6}$$

where $ET_i(t)$ is the ear thickness of mouse i at time t and $\overline{ET}_{Sham}(t)$ the mean ear thickness of all Sham mice at this time point. In Figure 2.29, the ear swelling for 23 Gy irradiated mice is shown and in Figure 2.30 for 33 Gy irradiated mice. The error bars in both figures indicate the SEMs. For 23 Gy irradiated mice, no difference could be seen between the three dose rate groups. Conv, Flash9 and Flash930 irradiated mice developed an ear swelling starting at 14 days after irradiation. The maximum swelling was reached between 22 and 24 days. After 35 days, no ear swelling was detected. The maximum swelling of the Conv group was (49 ± 11) µm, for Flash9 (40 ± 14) µm, and for Flash930 (30 ± 17) µm. Therefore, the swelling of all dose rate groups was the same within the uncertainty (SEM) for 23 Gy irradiated mice.

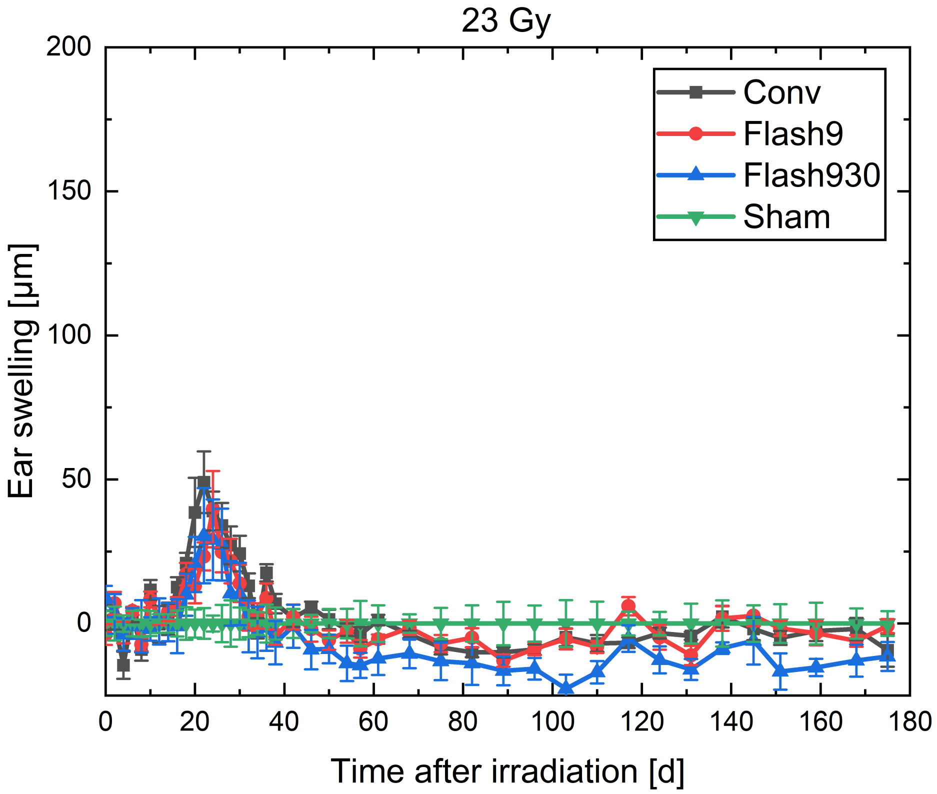

Figure 2.29: The ear swelling of mice irradiated with a mean dose of 23 Gy. The results for the three dose rate groups and the sham group are shown. The data points are the mean values of the groups and the error bars indicate the corresponding SEMs.

For 33 Gy, a dose rate effect was found. The ear swelling started 14 days after irradiation, reached the maximum between 22 and 24 days after irradiation and ended 46 days after irradiation. The mice of the Conv group had a mean maximum ear swelling of (155 ± 38) µm, the Flash9 group of (66 ± 18) µm, and the Flash930 group of (93 ± 19) µm. Therefore, the ear swelling of Flash930 was (40 ± 13) % reduced compared to Conv and in the Flash9 group it was reduced by (57 ± 12) % compared to Conv. The results of Flash9 and Flash930 were different to Conv with respect to the uncertainty ranges but not statistically significantly different with p-values of 0.21 (Flash9 compared to Conv, two-sample t-test, Origin 2021b) and 0.16 (Flash930 compared to Conv, two-sample t-test, Origin 2021b). The results of Flash930 and Flash9 were not different with respect to the uncertainty. However, Flash9 mice developed less ear swelling on average than Flash930 mice.

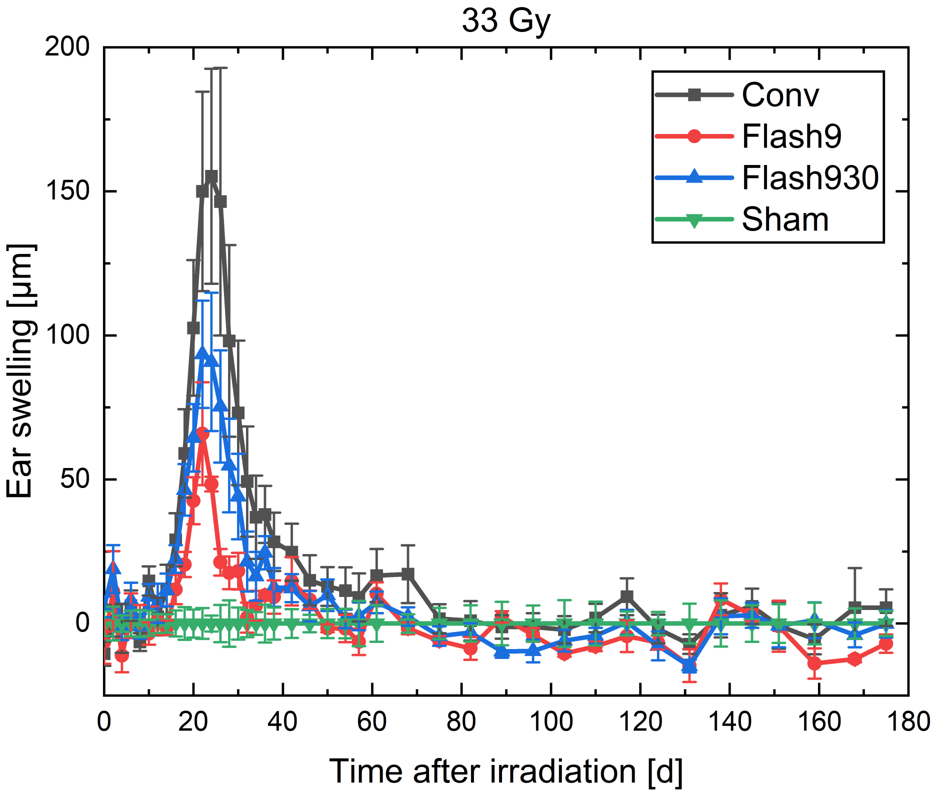

Figure 2.30: The ear swelling of mice irradiated with a mean dose of 33 Gy. The results are plotted according to Figure 2.29.

2.8.5 Decreased inflammation reactions due to proton-FLASH irradiation

The inflammation reaction was scored by the inflammation score that was composed of a scoring of erythema and desquamation. In Figure 2.31 and 2.32, the results of this scoring are shown. The results of the 23 Gy irradiated mice are shown in Figure 2.31 and of the 33 Gy irradiated mice in Figure 2.32. In both figures, the mean values of each group are plotted against time after irradiation. The error bars indicate the corresponding SEMs. The curves in both figures show very similar structures to the ear swelling. The inflammation score was 0.0 ± 0.2 at the beginning of monitoring (day 0). For 23 Gy irradiated mice, the inflammation reaction started at 16 days after irradiation in all dose rate groups, was the highest between 24 days and 26 days and returned to baseline at 42 days after irradiation. Conv mice had a mean maximum inflammation score of (0.57 ± 0.19), Flash9 mice of (0.57 ± 0.19), and Flash930 mice of (0.43 ± 0.19). These results were similar between all dose rate groups within the uncertainty (SEM) as this was the case for ear swelling.

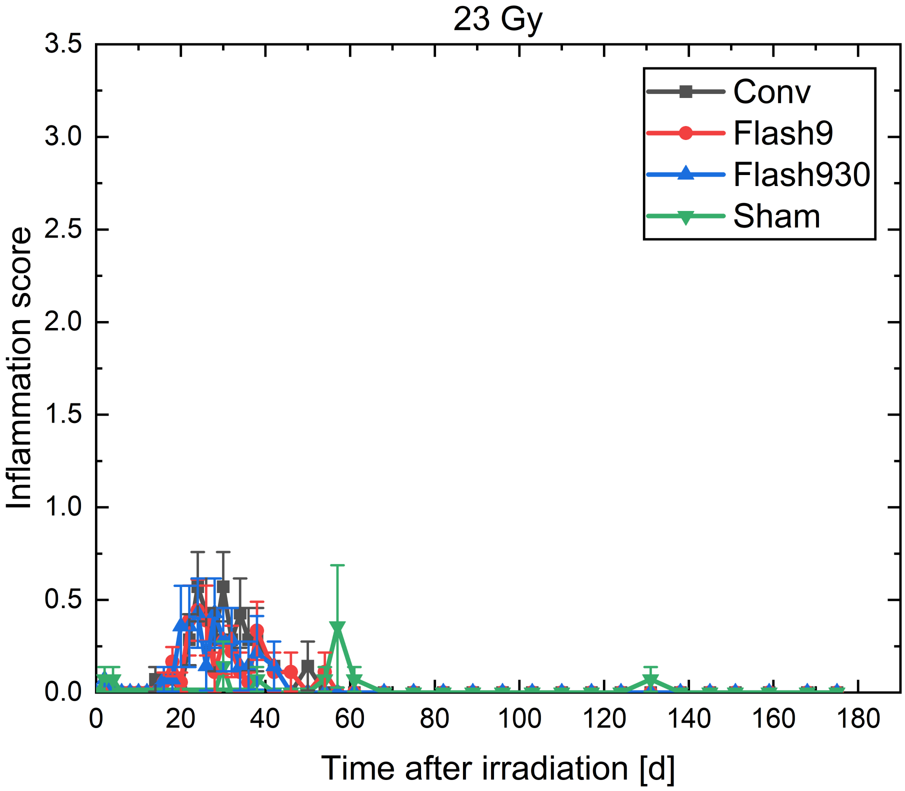

Figure 2.31: The inflammation score of mice irradiated with a mean dose of 23 Gy. Desquamation score and erythema score were summed up to form the inflammation score shown here for the three dose rate groups and the sham group plotted against time after irradiation. The data points are the mean values of the groups and the error bars indicate the according SEMs.

For 33 Gy irradiated mice, the inflammation reactions started 14 days after irradiation, were the highest 22 to 24 days after irradiation and ended for Flash930 after 42 days, for Flash9 after 57 days and for Conv after 50 days. The maximum inflammation score was in the Conv group 2.6 ± 0.6, in the Flash9 group 0.8 ± 0.4 and in the Flash930 group 1.2 ± 0.4. Therefore, the inflammation score was decreased by (50 ± 17) % in the Flash930 group and by (67 ± 17) % in the Flash9 group compared to the Conv group. The results of Flash9 and Flash930 were different from Conv with respect to the uncertainty ranges but not statistically significantly different with p-values of 0.16 (Flash9 compared to Conv, two-sample t-test, Origin 2021b) and 0.13 (Flash930 compared to Conv, two-sample t-test, Origin 2021b). The results of Flash930 and Flash9 were not different with respect to the uncertainty. However, Flash9 mice developed less inflammation on average than Flash930 mice. It has to be mentioned here that the Flash9 group consists only of three mice. Therefore, statements about results of the Flash9 33 Gy group are less meaningful than about the other groups and must be weighed carefully. In conclusion, the results of the inflammation score are in good agreement with the results of ear swelling.

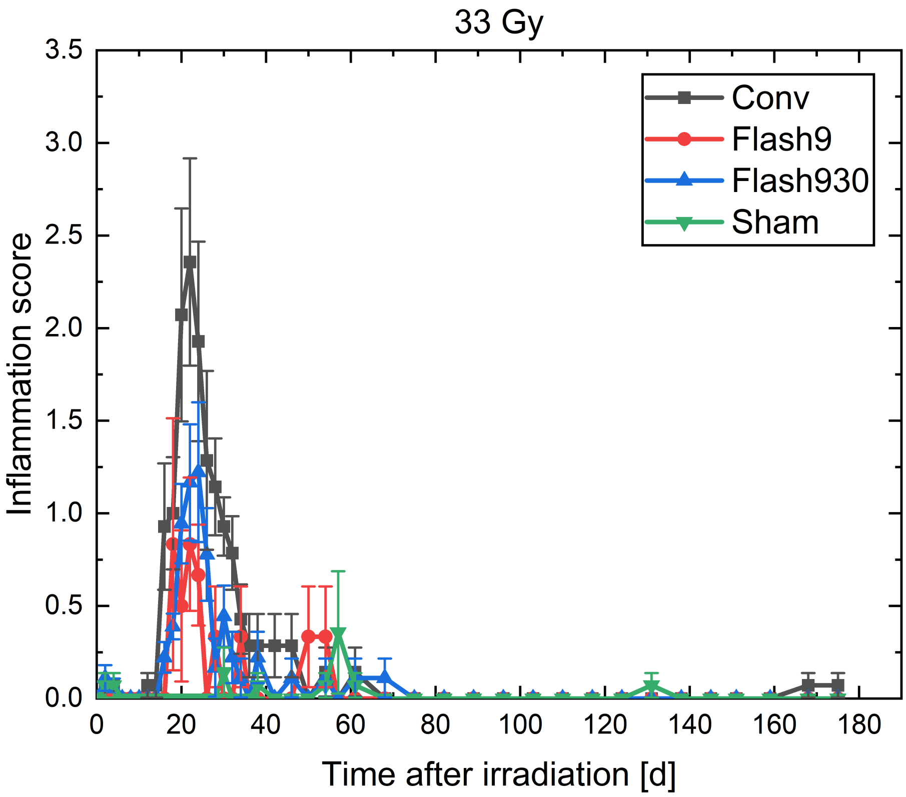

Figure 2.32: The inflammation score of mice irradiated with a mean dose of 33 Gy. The results are plotted according to Figure 2.31

2.8.6 Blood sampling

(*)
The effect of different dose rates on the inflammation reaction was additionally measured by cytokines in the blood. The blood was taken once a week for the first four weeks after irradiation from the tail vein. On termination day (180 days after irradiation), the blood was taken from the heart. The inflammation markers TGF-β1, TNF-α, IL1α and IL1β were analyzed via qPCR.

Before the sampling from the tail vein, the mouse was immobilized in a rack and warmed for 10 – 15 min with an infrared lamp. The blood was taken from the tail vein with a 25 G needle (BD MicroplaneTM 3, Nr. 18). On termination day 180 days after irradiation, blood was collected via cardiac puncture while the mice were under deep terminal anesthesia. Afterwards, mice were euthanized by cervical dislocation. From every blood sampling, between 5 to 6 drops of blood were collected into a tube filled with 3.8 ml Heparin. Prior to collection the Heparin (Heparin-Natrium-25000-ratiopharm 5000 IE/ml, ratiopharm GmbH) was diluted to 1000 IE/ml with PBS without Ca^{2+}/ Mg^{2+} in sterile conditions. The tube with heparin and blood was put on ice until it was centrifuged for 10 min at 2000 rcf at 4 °C. The supernatant was transferred to an 1.5 ml Eppendorf tube. The cell pellet was resolved in 100 µl NaCl and transferred to an RNAprotect Animal Blood Tube (Qiagen, Germany). The supernatant and the resolved cell pellet were then stored at -80 °C. RNA was extracted from the mouse blood samples using RNeasy Protect Animal Blood Kit (Qiagen, Germany). The concentration of RNA was measured by a Nanodrop™ spectrophotometer at 260 nm. RNA was reversely transcribed into cDNA using High Capacity cDNA Reverse Transcription Kits (Invitrogen, Darmstadt, Germany). The resulting cDNA was subjected to quantitative RT-PCR using primers directed towards the following genes TGF-β1, TNF-α, IL1α and IL1β. The genes B2M and GAPDH were used as a house keeping gene. The reaction mix was prepared according to the standard protocol of the kit. RT-PCR was carried out with a StepOnePlus (Applied Biosystems, San Francisco, USA) with a standard thermal profile.

qPCR

The PCR (polymerase chain reaction) is an in-vitro method to amplify DNA sequences of interest. The quantitative PCR (qPCR) uses the PCR to detect a specific gene and to quantify the amount of its expression. The qPCR is the most sensitive and accurate method for the analysis of the expression of a certain gene [168, 169]. It allows the quantification even of rare transcripts and small changes in gene expression [168].

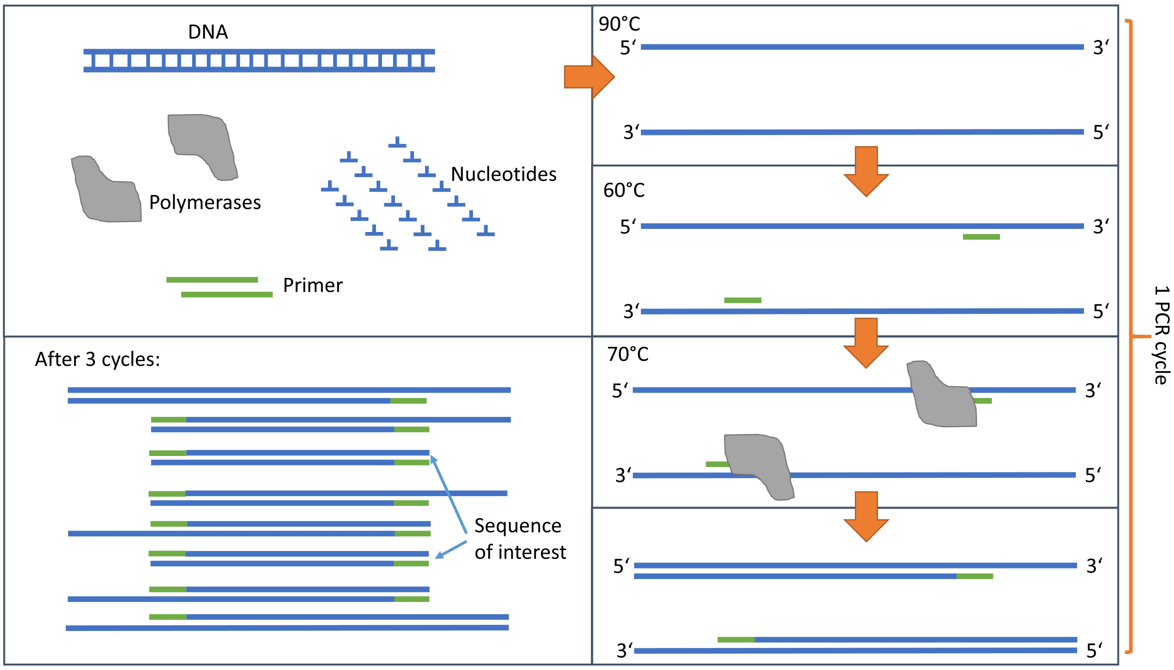

Figure 2.33: The principle of PCR.

In PCR, the ability of polymerases to synthesize a new DNA strand complementary to an offered DNA strand is used. Polymerases are enzymes that combine nucleotides to a chain of nucleotides. In this way, polymerases form a polymer like the DNA dependend on the type of polymerases. DNA-polymerases use thereby one DNA strand as template and bind the complementary nucleotides to the nucleotides of the template strand. Thus, a complementary strand is formed. In the replication process, the DNA is splitted into two strands and the

DNA-polymerases create the complementary strands resulting in two identical double stranded DNAs. The DNA-polymerase needs an initial starting point to start replicating, which is encoded in the DNA and called primer. Polymerases can only operate in one direction of the DNA strands from the 5' end to the 3' end. In PCR, short DNA sequences of interest are amplified. The principle of PCR is shown in Figure 2.33. The amplification is done by using double stranded DNA, polymerases, nucleotides and specifically designed primers. The primers are designed so that one primer binds with its 5' end to one strand of the DNA at the 3' end of the sequence of interest and the other primer binds with its 5' end to the complementary strand of the DNA at the 3' end, which corresponds to the other end of the sequence of interest. The sequence of interest is located between the two primers. The PCR consists of several heating cycles. In one cycle, all components of the PCR are heated to > 90 °C, where the DNA denatures into two DNA strands. Then, the temperature is reduced to about 60 °C that allows the binding of the primers to the DNA-strands. The temperature is increased again to about 70 °C to the ideal working temperature of the polymerases and the polymerases bind at the primer on both strands and create complementary strands. The polymerases thus form two double stranded DNAs starting from the primer to the end of the whole strand. This whole heating cycle is then repeated several times. In the repetitions, also double stranded DNA of the desired length are created due to the restriction of the two primers. In every cycle, where n is the number of cycles, $2^n - 2n$ DNA fragments of the desired length are created and $2n$ DNA fragments that are too long. The more cycles are performed the more DNA of the desired length is created and quickly prevails DNA of the false length due to exponential amplification in every cycle. After 8 cycles, the $2n$-term accounts for less than 1 % and can be neglected. In qPCR, fluorescent proteins are added that bind to the short DNA sequences of interest created during the PCR. These proteins produce a fluorescent signal when they detected a DNA sequence of interest and this signal is detected and analyzed every cycle resulting in a typical qPCR curve, as shown in Figure 2.34. Based on such curves a threshold is determined where the fluorescent signal is clearly distinguishable from the background signals. For every gene, the ct (threshold cycle) value is evaluated. The ct value equals to the number of PCR cycles necessary to reach the threshold of the fluorescent signal. A low ct value corresponds to a high DNA concentration and a high ct value to a low DNA concentration.

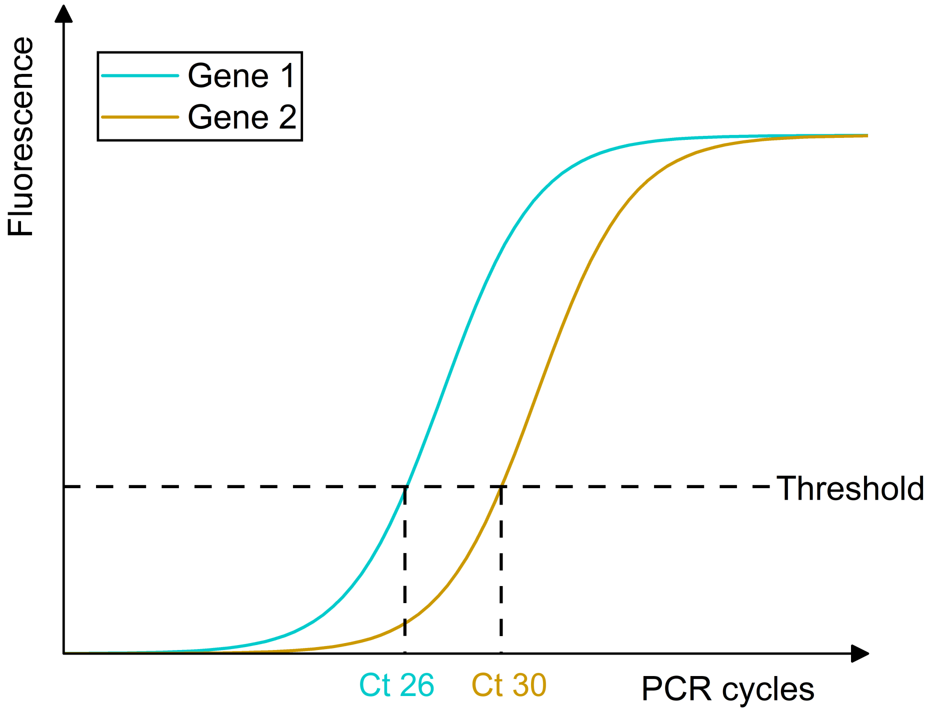

Figure 2.34: A typical qPCR curve. The detected fluorescence signal in every qPCR cycle is detected and plotted against the cycle number. The curves typically have a sigmoidal shape. A threshold is determined where the fluorescent signal is clearly distinguishable from background signals. The ct value, the number of cycles necessary to reach the threshold, of every gene is evaluated. A low ct value corresponds to a high DNA concentration and a high ct value to a low DNA concentration.

qPCR of inflammation markers in the blood

To detect cytokines in the blood, the mRNA (messenger ribonuleic acid) is derived from the blood. mRNA is a single stranded polymere that has a similar form as the DNA and consists of bases connected to a ribose backbone. In protein synthesis, the gene that describes the desired protein is transcribed into mRNA. The mRNA serves as a message that can now be sent from the cell nucleus to other parts of the cell, where the protein is synthesized based on the mRNA. Therefore, the amount of a specific mRNA correlates to the amount of the corresponding proteins. Cytokines are such proteins. Instead of detecting the proteins in the blood, the corresponding mRNA can be detected via qPCR that is a more sensitive method [168, 169]. For this method, the mRNA is synthesized into cDNA that is the complementary DNA. Based on the cDNA, the qPCR is performed and the ct value for every cytokine is evaluated. Next to the cytokines, the qPCR is also performed on so-called house keeping genes. These are genes that have a similar detection efficiency than the cytokines of interest but are not influenced by the investigated treatment. In this thesis, the house keeping genes B2M and GAPDH were used. For every mouse, the ct values of the four cytokines TGF-β, TNF-α, IL1α, and IL1β and the two house keeping genes were determined in three replicates. The mean value of the three replicates is calculated for every cytokine and house keeping gene in the blood of each mouse and is denoted as ct_{tech}. The mean ct_{tech} of every cytokine is calculated for each group (Sham, Conv, Flash9, and Flash930) and denoted as ct_{bio}. The mean ct_{tech} of the two house keeping genes is calculated (ct_{HK}) for every group and the ct_{bio} is normalized by ct_{HK} for each cytokine in each group

$$\Delta ct(\mathrm{group}, \mathrm{cytokine}) = ct_{\mathrm{bio}}(\mathrm{group}, \mathrm{cytokine}) - ct_{\mathrm{HK}}(\mathrm{group}). \tag{2.7}$$

This procedure ensures the comparability of the cytokine expression. According to [168], the fold change log2 is calculated for every group. First, the fold change is calculated by subtracting the $\Delta ct(\mathrm{group}, \mathrm{cytokine})$ of the Sham group from an irradiated group resulting in $\Delta\Delta ct(\mathrm{group}_{\mathrm{irr}}, \mathrm{cytokine})$

$$\Delta\Delta ct(\mathrm{group}_{\mathrm{irr}}, \mathrm{cytokine}) = \Delta ct(\mathrm{group}_{\mathrm{irr}}, \mathrm{cytokine}) - \Delta ct(\mathrm{Sham}, \mathrm{cytokine}). \tag{2.8}$$

The fold change (FC) is than calculated by

$$\mathrm{FC}(\mathrm{group}_{\mathrm{irr}}, \mathrm{cytokine}) = 2^{-\Delta\Delta ct(\mathrm{group}_{\mathrm{irr}}, \mathrm{cytokine})} \tag{2.9}$$

and equals to the normed difference in number of DNA fragments of the desired length produced between an irradiated group and the Sham group. For comparison of gene expression, usually the log2 of the fold change is given, as this value is less prone to outliers.

$$\mathrm{FClog2}(\mathrm{group}_{\mathrm{irr}}, \mathrm{cytokine}) = \log_2\left(\mathrm{FC}(\mathrm{group}_{\mathrm{irr}}, \mathrm{cytokine})\right) \tag{2.10}$$

2.8.7 Irradiation effects not measurable via blood sampling

In Figure 2.35 to 2.38, the results of the cytokine analysis of the cytokines TGF-β, TNF-α, IL1α, and IL1β for 33 Gy irradiated mice are shown. In these graphs, the fold change log2 in comparison to sham samples is presented. A fold change log2 of zero means an equal expression of a cytokine than the Sham samples. Negative values can be seen as a downregulation of the cytokine expression and positive values as an upregulation compared to Sham. The results of Conv irradiated mice are indicated by black bars, of Flash9 irradiated mice by red bars, and of Flash930 irradiated mice by blue bars. The error bars indicate the corresponding SEMs.

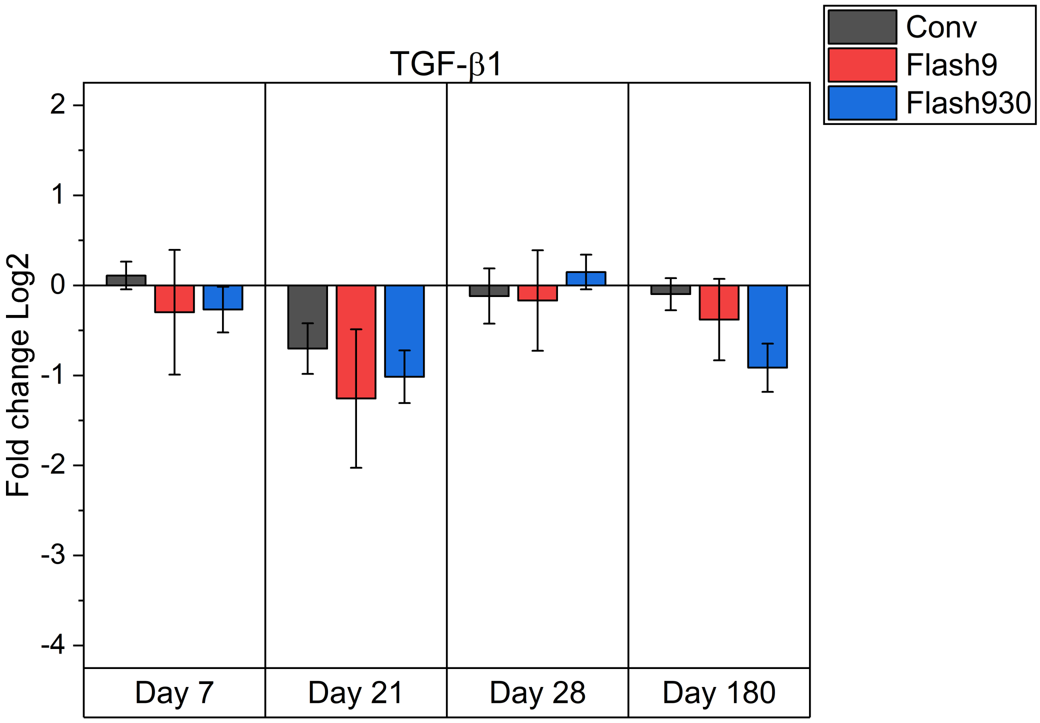

Figure 2.35: The analysis of the inflammation marker TGF-β1 after 33 Gy irradiation with three different dose rates. The fold change log2 is shown for day 7, day 21, day 28 and day 180. The results of Conv irradiated mice are shown by black bars, of Flash9 irradiated mice by red bars and of Flash930 irradiated mice by blue bars. The error bars denote the SEMs.

In Figure 2.35, it can be seen, that CONV, Flash9, and Flash930 had no changed TGF-β expression compared to sham at day 7 and day 28 after irradiation. Additionally, the results of the three dose rate groups are equal to each other within the uncertainty. Equal expression of TGF-β between the three dose rate groups was also found at 21 days after irradiation but here TGF-β was downregulated compared to sham. This downregulation was merely significant with a p-value of 0.067 (ANOVA one-way, Origin 2021b). At termination day, Conv and Flash9 showed a similar expression than Sham, while Flash930 was almost significantly downregulated compared to Sham (p-value = 0.052, two-sample t-test, Origin 2021b). However, it was not different within the uncertainty from Flash9.

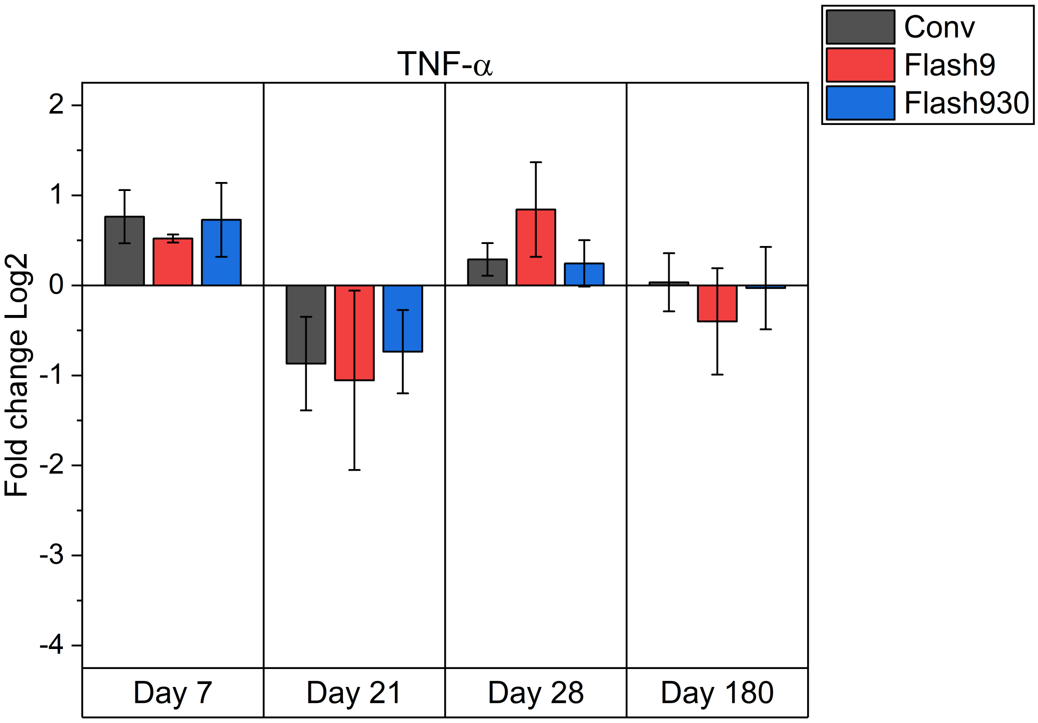

Figure 2.36: The analysis of the inflammation marker TNF-α after 33 Gy irradiation with three different dose rates. Figure is drawn according to Figure 2.35.

In Figure 2.36, the results of TNF-α are shown. Seven days after irradiation, TNF-α was slightly upregulated in all dose rate groups, but not significant compared to Sham (p-value = 0.57, ANOVA one-way, Origin 2021b). 21 days after irradiation, TNF-α was slightly downregulated in all dose rate groups, but also not significant (p-value = 0.41, ANOVA one-way, Oigin 2021b). 28 days after irradiation, Conv and Flash930 showed similar results than sham within the uncertainty, Flash9 was slightly upregulated compared to Sham but not significant (p-value = 0.55, two-sample t-test, Origin 2021b). No differences were found at termination day. Here, similar TNF-α expressions were found in all groups (Sham, Conv, Flash9, and Flash930). At all time points, no differences were found between the three dose rate groups.

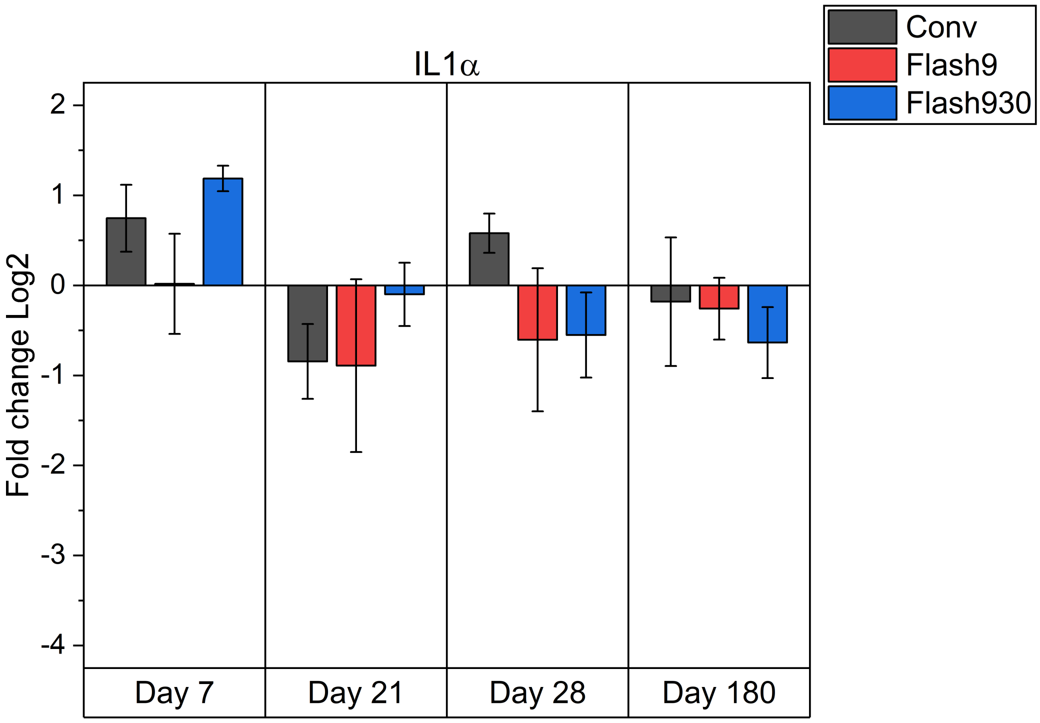

Figure 2.37: The analysis of the inflammation marker IL1α after 33 Gy irradiation with three different dose rates. Figure is drawn according to Figure 2.35.

Figure 2.37 presents the results of IL1α. Conv and Flash930 induced a slight upregulation of IL1α seven days after irradiation, while Flash9 was equal to Sham. This upregulation was not significant with a p-value of 0.35 comparing Conv to Sham and almost significant comparing Sham to Flash930 with a p-value of 0.056 (two-sample t-test, Origin 2021b). The uncertainties of Conv overlapped with Flash9 and Flash930. 21 days after irradiation, a slight down regulation is found in Conv that was not significant compared to Sham (p-value = 0.15, two-sample t-test, Origin 2021b). The two Flash dose rates showed no fold changes. The error bars of all irradiated groups overlap. 28 days after irradiation, a slight but not significant upregulation was found for Conv (p-value = 0.32, two-sample t-test, Origin 2021b) and a slight but not significant downregulation for Flash930 (p-value = 0.42, two-sample, t-test, Origin 2021b), both compared to Sham. Flash9 and Flash930 had similar results within the uncertainty. No fold changes were found for Conv and Flash9 180 days after irradiation. Flash930 showed a slight but not significant downregulation (p-value = 0.36, two-sample t-test, Origin 2021b). The results of the three dose rate groups highly overlap with each other.

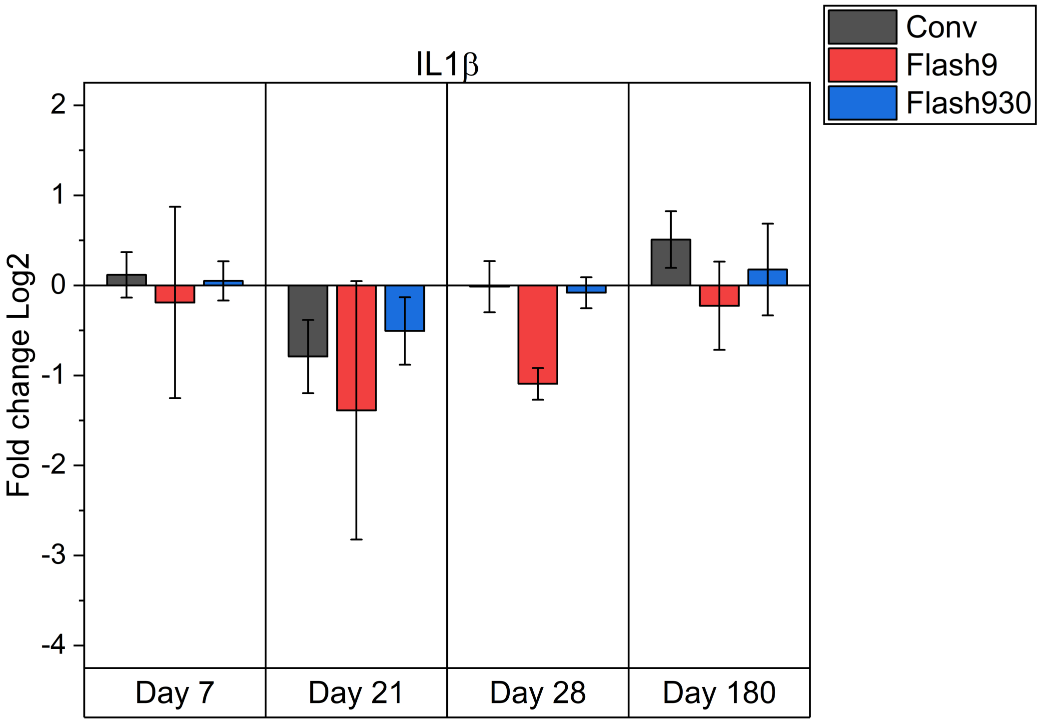

Figure 2.38: The analysis of the inflammation marker IL1β after 33 Gy irradiation with three different dose rates. Figure is drawn according to Figure 2.35.

In Figure 2.38, the results for IL1β are shown. No fold changes were found in all dose rate groups 7 days after irradiation. A slight but not significantly downregulation was induced in all dose rate groups 21 days after irradiation (p-value = 0.35, ANOVA one-way, Origin 2021b). 28 days after irradiation, no fold change was induced in Conv and Flash930 group, while Flash9 group was almost significantly downregulated compared to Sham, Conv, and Flash930 (p-value = 0.067, ANOVA one-way, Origin 2021b). No fold change was found in the two Flash groups 180 days after irradiation. Conv was slightly but not significant upregulated compared to Sham (p-value = 0.46, two-sample t-test, Origin 2021b). However, the results of all dose rate groups overlapped.

The p-values found in most of the comparisons between the dose rate groups and between the dose rate groups and the Sham group presented here were really high (> 0.2), therefore no clear differences could be detected. Exceptions were found for TGF-β1 at day 21 and day 180, for IL1α at day 7 and day 21, and for IL1β at day 28. TGF-β1 was downregulated 21 days after irradiation in all dose rate groups. At day 180, only the Flash930 group was downregulated compared to Sham and Conv but not compared to Flash9. The uncertainty of Flash9 overlapped with the results of all other groups. IL1α was upregulated in the Flash930 group. However, Conv showed similar results but with a high variation and the uncertainty of Conv overlapped with Flash930, Flash9 and Sham. At day 21, IL1α was downregulated compared to sham but not compared to Flash9 or Flash930. IL1β was downregulated at day 28 in the Flash9 group. Non of the found differences were statistically significant. The exceptions found here followed no rule and were not consistent. Therefore, they might be outliers. It can be concluded, that no irradiation effect in the expression of cytokines were visible and no differential effects in the different dose rates were observed.

2.8.8 Estimation of the irradiated blood volume

(*)

Due to their 2D-like shape, mouse ears are the perfect candidate to estimate the volume of irradiated blood by using trans-illuminated photographs of the ear. The irradiated blood volume can be divided into a static blood volume and a blood flow volume. The static blood volume is defined as the volume of blood that the irradiated area of the ear contains. This volume was estimated by photos of three mouse ears made directly after irradiation. To make the blood vessels visible, the ears were illuminated from the other side while the photo was taken. The mice that were used to do blood flow estimation are from a previous study [132] performed and provided by Stefanie Girst, where the mouse strain, the setup, and the handling were exactly the same besides the irradiation. For the approximation on each photo, a 6.5 mm x 6.5 mm field in the middle of the mouse holder window was marked. This is the area which was irradiated in this study. Inside this area, segmented lines along all visible blood vessels were drawn via ImageJ and are depicted in Figure 2.40(a).

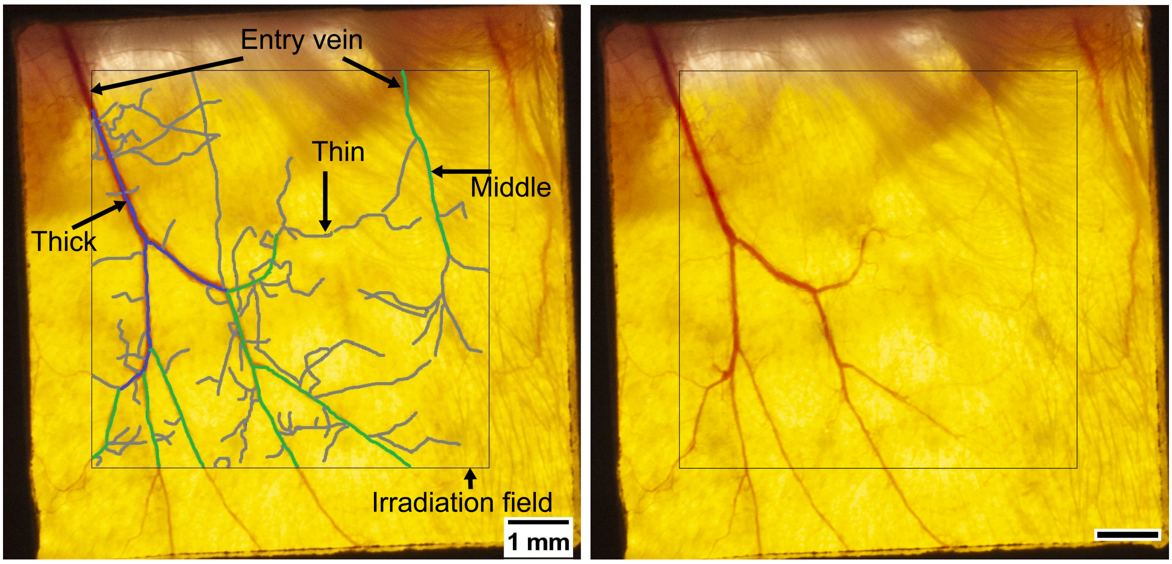

(a)

(b)

Figure 2.39: Blood volume estimation on mouse ear photos. In (a), the blood vessels are categorized and marked by lines in purple for thick vessels, in green for medium thick vessels, and in blue for thin vessels. The irradiation field is shown by a black outline and the entry veins are indicated. In (b), the original image is presented.

In Figure 2.39(b) the original image is shown. The segments of the lines marking the blood vessels were categorized by eye into three groups according to their thickness and on each photo, the diameters of three or more representative blood vessels for each group were measured at different locations. Thick blood vessels had a diameter of approx. 0.09 mm and are indicated by purple lines, middle thick blood vessels had a diameter of approx. 0.05 mm and are shown by green lines, and thin blood vessels had diameters of approx. 0.04 mm and are drawn with blue lines. The length of each segment marking a blood vessel was measured and the static volume V_{static} for all n blood vessels ($n = n_{\text{thick}} + n_{\text{middle}} + n_{\text{thin}}$) was calculated by

$$V_{\text{static}} = \sum_{i=1}^{n_{\text{thick}}} \pi \cdot \frac{d_{\text{thick}}^2}{4} \cdot l_i + \sum_{j=1}^{n_{\text{middle}}} \pi \cdot \frac{d_{\text{middle}}^2}{4} \cdot l_j + \sum_{k=1}^{n_{\text{thin}}} \pi \cdot \frac{d_{\text{thin}}^2}{4} \cdot l_k \tag{2.11}$$

assuming a cylindrical form of the blood vessels, where d_{thick}, d_{middle}, and d_{thin} are the mean diameters for the three categories and $l_{i,k,j}$ is the length of each vessel.

The blood flow volume describes the volume of blood which is exchanged during the time of irradiation. This exchange happens only at blood vessels entering the irradiation field from outside. To estimate the amount of blood volume, which is exchanged in a certain time, we calculated how much blood is pumped inside/outside the irradiation field. This was done by estimating the cross-sectional area of the entry blood vessels. These are the blood vessels which deliver the blood from the inner ear towards the irradiation field (see Figure 2.39(a)) or vice versa. For this estimation, only thick and middle-thick blood vessels were taken into account. We assumed that the entry blood vessels are mainly veins as these are bigger than arteries. The diameters of these veins were measured trice at the entry to the irradiation field. Veins in Balb/c mice have a blood flow speed of v ≈ 2 mm/s [166]. So the blood flow volume V_{flow} can be calculated by

$$V_{\text{flow}} = \sum_{i=1}^{m} \pi \cdot \frac{d_i^2}{4} \cdot v \cdot t, \tag{2.12}$$

where m is the number of entry veins, d their diameter, v the blood flow speed, and t the time required by an irradiation mode for a dose 33 Gy. The irradiation with Flash930 took $t_{\text{Flash930}} = 0.035$ s, with Flash9 $t_{\text{Flash9}} = 3.55$ s and with Conv $t_{\text{Conv}} = 9.17$ min.

The complete amount of irradiated blood V_{irr} was then calculated by

$$V_{\text{irr}} = V_{\text{static}} + V_{\text{flow}} \tag{2.13}$$

The irradiated volume is (0.20 ± 0.07) µl in case of Flash930, (0.37 ± 0.11) µl in case of Flash9 and (27 ± 7) µl in case of Conv. This means a fraction of (0.010 ± 0.004) % (Flash930), (0.019 ± 0.006) % (Flash9) and (1.4 ± 0.4) % (Conv) of the total blood volume of about 2 ml. Balb/c mice have 10.35 ml blood per 100 g of body weight [170]. The mice in this study had a mean body weight of (19.2 ± 1.1) g.

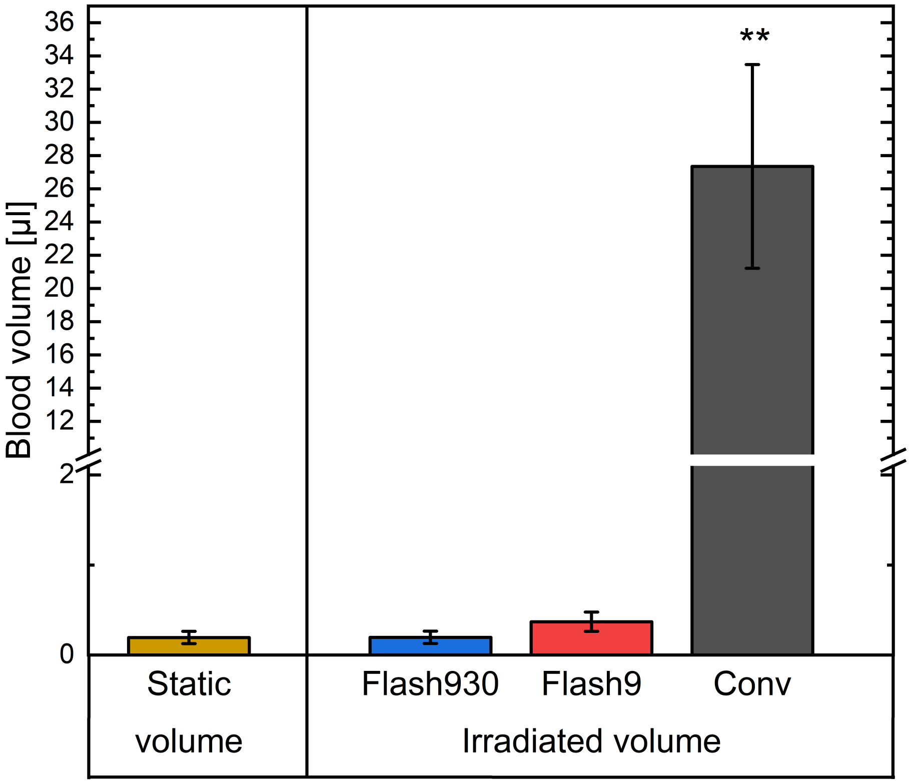

Figure 2.40: The results of the estimated irradiated volumes and of the static volume. The irradiated volume was estimated for a dose of 33 Gy for the three irradiation modes (Flash930, Flash9 and Conv) used in this experiment. The error bars show the standard deviation of the mean and two stars indicate p-values < 0.0004 (ANOVA, one-way, Origin 2021b). For a better visualization, the y-axes was interrupted between 2.1 µl and 10 µl with larger spaces between 0 µl and 2.1 µl.

In Figure 2.40 the static volume and the three irradiated volumes for a 33 Gy irradiation for the different dose rates are shown. As the static volume is independent of time, it is the same for all irradiation modes. In contrast, the blood flow volume and thus the irradiated volumes are time-dependent and were therefore estimated for each mode individually. It can be seen that the static volume and the Flash930 irradiated volume result in the same amount of irradiated blood. The Flash9 irradiated volume was about 1.9 times higher than for Flash930 and the static blood volume. However, this difference was not significant (p-value = 0.13, Anova, one-way, Origin 2021b). By contrast, the Conv irradiated volume is significantly different (approx. 100 times higher, p-value = 0.0004, Anova, one-way, Origin 2021b). This shows, that for Flash9 and Flash930 the irradiated volume consists mainly of the static volume, while for Conv the blood flow volume mainly determines the amount of the irradiated volume. Therefore, it can be concluded that with Flash930 the irradiated blood volume received the full dose of 33 Gy, with Flash9 17 Gy and with Conv the much larger irradiated blood volume received a dose of only 0.24 Gy.

2.9 Discussion on proton-FLASH

In this thesis, I investigated the effects of proton-FLASH in-vivo and in-vitro. In 2014, Favaudon et al. [6] showed in their studies the great potential of the FLASH effect. Since then, the FLASH effect has been intensively investigated. However, the results of these investigations showed how little is known about this dose rate effect and that further investigations are urgently needed as discussed in detail in Section 2.1 ,2.2, 2.3, and 2.4. The FLASH effect was observed in all typical radiation types used in radiotherapy: x-rays, electrons, protons, and carbon ions. However, due to technical limitations for producing x-rays of high dose rates [95] and the limited access to carbons ions and protons [19, 171], the FLASH effect is mainly investigated for electrons. Protons are easier accessible than carbon ions [19]. Therefore, protons are the second best investigated particles in case of FLASH [172]. In contrast to electrons, protons can also be used in radiotherapy for irradiating deep seated tumors [173]. Hence, protons are promising candidates for the clinical application of FLASH and it is especially important for this particle sort to find the requirements of inducing proton-FLASH and understanding the proton-FLASH effect. As the access to facilities that are able to perform proton irradiations at high dose rate ranges to cover conventional and FLASH dose rates is limited, new facilities with access for researchers are urgently needed [171]. Therefore, I presented in this thesis such a setup that is installed at a 14 MV tandem accelerator.

The setup was installed in the Maier-Leibnitz-Laboratorium in Garching near Munich at the beam line SNAKE and was presented in Section 2.5. For dosimetry, a new detector, an ionization chamber, was designed and built for dealing with a broad range of dose rates, as presented in Section 2.6. On this new set-up, a broad range of experiments were performed that address various important radiobiological endpoints and provide a good overview of effects and underlying mechanisms of proton-FLASH. In-vitro, the cell survival, the cell death and the genetic damage was investigated. In-vivo, the skin response, the inflammation reaction and the immune reaction via cytokines were tested. CHO-K1 cells served as an in-vitro model and the right ears of Balb/c mice were irradiated as in-vivo model. Both models were irradiated with 20.5 MeV protons homogeneously distributed in a field of 6.5 mm x 6.5 mm. In in-vitro experiments, the dose rates 0.06 Gy/s (Conv), 9.3 Gy/s (Flash9), and 310 Gy/s (Flash310) were tested and a dose of 4 Gy was targeted for irradiation. In in-vivo experiments, the effects of the dose rates 0.06 Gy/s (Conv), 9.3 Gy/s (Flash9), and 930 Gy/s (Flash930) were studied and a dose of 25 Gy or 35 Gy was targeted. 310 Gy/s was the highest dose rate that could be irradiated with a dose of 4 Gy with the here presented set-up and 930 Gy/s the highest dose rate for irradiations with a dose of 25 Gy or 35 Gy. For irradiating smaller doses like 4 Gy, faster reaction times of the detector and the electronics connecting the detector to a high-voltage switch are necessary, as the overall duration of irradiation is smaller than for irradiating higher doses at the same dose rate. Therefore, the highest dose rate for in-vitro experiments had to be reduced to 310 Gy/s. As direct controls, cells and mice were sham irradiated. Here, the cells or mice were treated exactly the same as the irradiated ones but without switching on the beam.

The new set-up was tested for the accuracy of dose application. Therefore, gafchromic films were placed behind the cell samples or mouse ears. The gafchromic films enabled a retrospective measurement of the actual irradiated doses by the detector-beam-switch system. In in-vitro experiments, it was targeted for 4 Gy irradiation. However, the actual irradiated doses ranged from 2.1 Gy to 6.4 Gy. Most often, doses between 3 Gy and 4 Gy were applied. The mean ± SD of all irradiated doses in all in-vitro experiments was (3.3 ± 0.8) Gy. Therefore, 0.7 Gy less dose was applied as originally targeted for. In all dose rate groups, high relative standard deviations from the targeted dose were found with $\Delta D\%_{\mathrm{Conv}} = 26\ \%$, $\Delta D\%_{\mathrm{Flash9}} = 20\ \%$, and $\Delta D\%_{\mathrm{Flash310}} = 30\ \%$. In the colony forming assay and the Caspase 3/7-Sytox assay, the mean doses of all dose rate groups were the same and therefore, the results of the dose rate groups could be directly compared despite these high deviations. In the micronuclei assay, the mean applied doses of the dose rate groups differed with 0.5 Gy. Here, a indirect comparison via a linear fit was done that might have influenced the outcome. In-vivo, the relative standard deviations of targeted dose to irradiated dose were similarly high as in-vitro between 16 % (Conv 35 Gy) and 40 % (Flash9 35 Gy). As the irradiated doses in each dose rate group differed in an unacceptable amount, mice were regrouped within the dose rate groups aiming for mean doses of 23 Gy and 33 Gy. With this procedure, the relative standard deviations could be dramatically reduced to $< 15\ \%$ except for Flash930 23 Gy group where $\Delta D\%$ was reduced to 22 %. The reason for the high relative standard deviations in-vitro and in-vivo is originated in the calibration of the detector. The experiments described in this chapter were all performed in the last beamtime at the Maier-Leibnitz-Laboratorium that was closed in the beginning of 2020. The detector was calibrated in this beamtime for the first time as problems in the construction of this detector delayed its completion and the detector could not be tested and calibrated in a previous beamtime as originally planned. Therefore, time was short for calibration and thus led to a lack of accuracy in the performance of the detector. In future experiments, a lot more time is necessary to understand how the detector reacts in detail to different dose rates and doses. This knowledge is necessary to perform a proper calibration of such a detector.

Nevertheless, the proton-FLASH effect could be investigated successfully in-vivo and in-vitro with the presented set-up. In-vitro, the cell survival was investigated with a colony forming assay, the cell death with a Caspase 3/7-Sytox assay and the genetic damage with the micronucleus test. No dose rate effect was found in the cell survival that was evaluated 5 days after irradiation. The results of all dose rate groups were equal to each other and to a reference measurement within the uncertainty. The Caspase 3/7-Sytox assay that was evaluated 24 h after irradiation resulted into less cell death in the Flash310 group than in the Conv group or Flash9 group. The same amount of cell death was induced by Flash310 as found in the Sham group. The by far predominant cell death type was apoptosis. Necrosis hardly occurred (in $< 0.08\ \%$ of all evaluated cells). In the micronucleus test, Flash9 and Flash310 seem to induce less micronuclei and, therefore, less genetic damage than Conv. Thereby, the genetic damage seems to be more complex the higher the dose rate, as more cells with two micronuclei were found the higher the dose rate was. These results are in good agreement to the literature. As discussed in Section 2.4.1, the FLASH effect on cell survival in-vitro depends on the oxygen supply. Cells in cell culture are well oxygenated (aerobic) with an oxygen concentration of 21 %. However in tissue, cells are less oxygenated with 4 % to 7.5 % [113]. In at least 13 publications of studies, no FLASH effect was found on cell survival of aerobic cells, as summarized in [85]. However, the more the oxygen concentration was reduced the more the cell survival was reduced after FLASH irradiation compared to conventional irradiation [108–112]. The underlying mechanism is supposed to be the oxygen depletion effect [103–105]. The data in this thesis therefore support this underlying effect. However, more measurements on oxygen deprived cells would be necessary to confirm it. On the other hand, the results of the micronucleus test are in good agreement to experiments supporting the DNA damage hypothesis, presented in Section 2.4.2. In several experiments, it has been shown that FLASH dose rates induce less DNA damage than conventional dose rates. This was mostly shown by fluorescent staining of DSBs [12, 117, 120], but also via micronucleus test [121] and in the evaluation of chromosome aberrations [122]. In this thesis, the differences found between the tested dose rates were more pronounced the higher the applied dose was [12, 117]. Buonanno et al. [117] found that the DNA damages were not reduced for a dose rate of 100 Gy/s, but for a dose rate of 1000 Gy/s. In my study, also a dose rate of 9.3 Gy/s induced less micronuclei. To find here the requirements for inducing less DNA damage more experiments are necessary. A dependency on the cell model is also thinkable. Furthermore, my results support the outcome of a previous study of my institute, where it was found that the DNA damages induced by a FLASH dose rate were more complex [120]. Reduced cell death via apoptosis after FLASH irradiation was found by Han et al. [174], similar to my study. They irradiated normal fibroblast cells with FLASH dose rates ($\approx 10^9$ Gy/s) at normoxic and hypoxic conditions. At both conditions, a reduction of apoptosis was found, but this reduction was more pronounced at normoxic conditions. The reason for the reduction in cell death might originate from the reduced DNA damage found after FLASH irradiation. The cGAS-STING pathway is induced by cytosolic DNA [125] and promotes senescence and cell death [126]. Less DNA damage produces less cytosolic DNA and therefore a reduced induction of this pathway that leads to less cell death. In the micronucleus test reduced genetic damage was also found after 9.3 Gy/s irradiation, but in the Caspase 3/7-Sytox assay no reduction of cell death was observed at this dose rate. To clarify this discrepancy, further investigations are necessary. Especially, the micronucleus test should be repeated in the future as the different doses applied only allow estimates to be made via fitting data by linear curves.

(*)
In-vivo, the right ears of Balb/c mice were irradiated. After irradiation, the mice were monitored for 180 days. The monitoring includes ear thickness measurement and scoring of inflammation reactions on the irradiated skin. Additionally for the first four weeks, blood was taken weekly from the tail veins and after 180 days from the heart and inflammation markers TGF-β1, TNF-α, IL1α, and IL1β were analyzed via qPCR.

The mouse ear model is a well-tested model and previous experiments showed its potential as a model for investigating side-effects of radiotherapy treatment in skin tissue [132, 133, 164, 165, 175]. The advantages of this model are that mouse ears are thin enough to shoot through with lower energy protons (here 20.5 MeV) and that the blood vessels can be visualized on a trans-illuminated photograph and, consequently, the irradiated blood volume can be easily estimated. The skin is irradiated in almost every treatment scenario. Irradiation damages on the skin lead to stiffness, discomfort, and pain [77, 78]. Therefore, it is an important target tissue to test the healthy-tissue-sparing effect of FLASH. The monitoring in this study lasted for 180 days so that long-term reactions could be tested.

The results of ear thickness and inflammation showed a sparing effect for Flash930 and Flash9. This sparing effect occurs only for a dose of 33 Gy and not for a dose of 23 Gy. For 23 Gy, the ear swelling and the inflammation score yield the same results for all dose rate groups, with a slightly increased ear swelling and inflammation score compared to the Sham group. This dose induced in the performed assay a very low inflammation reaction and is therefore not sensitive enough for testing dose rate effects. For 33 Gy, the ear swelling was reduced by (40 ± 13) % for Flash930 and by (57 ± 12) % for Flash9 compared to Conv at the maximum reaction. The inflammation score, consisting of scoring erythema and desquamation, was reduced by (50 ± 17) % for Flash930 and by (68 ± 17) % for Flash9 compared to Conv at maximum reaction. After 46 days, both ear swelling and inflammation score decreased to starting level. The differences between Flash930 and Flash9 for ear swelling and inflammation were not significant. It must also be mentioned here that only three mice were irradiated with 33 Gy at the Flash9 dose rate. However, these results show a trend towards a FLASH effect for such a low dose rate as 9.3 Gy/s, which gives a sparing effect with greater or at least equal magnitude than the ultra-high dose rate of 930 Gy/s. A FLASH effect in the skin was also observed before [10, 16, 176] and is in good agreement with our results. Vozenin et al. [10] showed that Conv irradiation with 34 Gy led to permanent destruction of hair follicles and severe late skin fibronecrosis, while the FLASH irradiated skin revealed comparable results to the unirradiated skin. Soto et al. [176] found that FLASH irradiation results in both a lower incidence and a lower severity of skin ulceration after a single fraction of hemithoracic irradiation of mice at high doses (30 Gy and 40 Gy). Cunningham et al. [16] investigated the FLASH effect with proton pencil beam scanning on a mouse leg contracture assay with 35 Gy. They found that the leg contracture was diminished by approx. 50 % for FLASH irradiation with both 58 Gy/s and 115 Gy/s compared to conventional irradiation. These studies showed similar to our findings that the FLASH effect is dose-dependent and occurs at doses as high as 30 Gy [10, 16, 176]. Furthermore, the FLASH effect seems to plateau in skin tissue at dose rates between 9.3 Gy/s and 930 Gy/s, as in [16].

The inflammation markers TGF-β1, TNF-α, IL1α, and IL1β were analyzed for 33 Gy irradiated mice. No differences were seen between the Sham mice and the irradiated mice and also between the three dose rate groups. Cunningham et al. [16] measured 12 different cytokines 12 weeks post-irradiation, among them IL1β and TNF-α. In this study, no differences between irradiated and sham-irradiated animals and between the dose rate groups were observed for

IL1β and TNF-α, which matches our data. Here, other cytokines might be better choices for measuring inflammation reactions after irradiation in the blood like Cxcl-1, G-CSF, and GM-CSF [16]. In the same study, also TGF-β1 was measured by ELISA one and four days after irradiation. Here, the Conv irradiated mice had a significantly increased level of TGF-β1 compared to sham mice and FLASH irradiated mice. However in this study, a much larger proportion of the mouse body was irradiated than in the study presented here. Therefore, also a higher blood volume was irradiated which might lead to a measurable increase of TGF-β1. By contrast in our study, only a blood volume of 0.098 % to 1.4 % of the total blood volume of a mouse was irradiated. Thus, these results suggest that sufficient blood volume must be irradiated to measure TGF-β1.

Nevertheless, the mouse ear model enables the possibility to estimate the irradiated blood volume. The veins can be easily made visible by trans-illumination. The blood flow, along with oxygen saturation and hemoglobin concentration can be measured in the mice ears via single-shot photoacoustic microscopy and are well characterized [166]. In this thesis, the estimation yields a 100 times higher irradiated blood volume for Conv irradiated mice than for Flash9 or Flash930 irradiated mice. The irradiated blood volume of Flash9 and Flash930 mice was similar to the static blood volume, with Flash9 slightly but not significantly increased by a factor of 1.9. In contrast, the irradiated blood volume of Conv mice was mainly composed of the blood flow volume. Therefore, the irradiation times for Flash930 and Flash9 are in a range where not much more than the volume of blood present in the mouse ear is irradiated. The time is too short for several blood circulations. In contrast for Conv dose rates, the blood can circulate several times during the irradiation. The Flash930 and Flash9 irradiated blood was present in the irradiated field during the whole irradiation or at least half of the irradiation and received, therefore, lethal doses of 17 Gy to 33 Gy. At these high doses in a very limited volume of blood, especially lymphocytes are damaged lethally and are removed by apoptosis and necrosis [177]. For Conv, the blood is exchanged several times during the irradiation and, therefore, it receives an average dose of 0.24 Gy. This dose is sublethal and led to damages like an increased formation of micronuclei in lymphocytes [178] in previous studies. The many damaged blood cells in a 100 times higher blood volume are an extra stressor to the immune system. These factors contribute, therefore, in an extended amount to the inflammation reaction and can explain the difference to the Flash9 or Flash930 irradiated mice. This demonstrates that the irradiated blood volume possibly plays an important role in stimulating a FLASH effect in-vivo and should be taken into account in future studies. As the blood is also the key part in the oxygen supply in tissue, its role should be further investigated. Here, measurements of the oxygen saturation and the exact blood flow during and after irradiation in in-vivo models such as the mouse ear model can be a reasonable method for getting a better insight into the role of blood in the FLASH effect.

In conclusion, the results of the studies performed for this thesis stand all in good agreement to the literature and provide a good overview of the proton-FLASH effect. However, more questions arise from these results. Less genetic damage was found after FLASH irradiation that led to less cell death also in aerobic cells. Both endpoints were evaluated one day after irradiation. Therefore, it could be expected that the cell survival after 5 days is increased after FLASH irradiation compared to conventional irradiation. However, similar to other studies in literature the cell survival is only increased at low oxygen concentrations. Usually, cell survival assays are evaluated days later than assays adressing genetic damage or cell death. Thus the question is here: What happens between one day after irradiation and 5 days after irradiation? Looking at the dose rate necessary to induce a FLASH effect, both FLASH dose rates 9.3 Gy/s and 930 Gy/s induced a tissue sparing effect in-vivo. In-vitro, the genetic damage was also decreased for both FLASH dose rates, but not the cell death, where a dose of 930 Gy/s was necessary to induce a reduction. Hence the upcoming question is here: Why does 9.3 Gy/s induce a FLASH effect in-vivo but not in all endpoints in-vitro? To answer these questions, more investigations are necessary. The direct comparison of different in-vitro assays with each other and to in-vivo results is often difficult. Most in-vitro assays, such as those presented here, do not provide information on temporal evolution because they are evaluated only for a specific time point. Furthermore, these assays address only one specific endpoint, for example, CFA investigates the cell survival and the Caspase 3/7-Sytox assay the cell death. To overcome these limitations new strategies are necessary. One possible new method is presented in the next chapter of this thesis.

Chapter 3

CeCILE-An artificial intelligence based cell detection and tracking

In this chapter, a novel approach is presented that evaluates several important radiobiological endpoints in one assay. In this method, cells are moved after irradiation to an inverted microscope equipped with a live-cell imaging set-up. Cells were monitored every 5 min via phase-contrast microscopy for several days. The obtained videos were evaluated with a semi-automatic algorithm CeCILE. CeCILE is able to track and detect each single cell on the videos based on artificial intelligence. To increase the accuracy, the user is able to correct the predictions made by CeCILE in two correction steps. CeCILE creates for every cell in the video a lineage and the following endpoints are evaluated: Number of cells per frame in each of the four possible morphological cells states, the time point of the first cell division of each cell, the cell cycle durations, the cell cycle abnormalities and the proliferation. This chapter starts with a description of the theoretical background of the methods used in CeCILE. Afterwards, the whole development process is presented and CeCILEs performance is tested on a test dataset. In the end of this chapter, the potential of this novel method could be shown by performing the here described method on two samples, one irradiated with 3 Gy of x-rays and one sham irradiated.

3.1 Introduction to artificial intelligence, machine learning and deep learning

Artificial intelligence (AI) refers to the ability of machines to perform tasks that would normally require human intelligence, such as learning, recognizing speech, identifying objects, and making decisions [179]. One major ability of AI is that it can analyze vast amounts of data quickly and accurately [179]. With the explosion of big data in recent years, AI has become an increasingly important tool for extracting insights and knowledge from massive datasets. AI algorithms can process data from various sources, including structured data (such as databases and spreadsheets) and unstructured data (such as text, images, videos and audio), and identify patterns, trends, and anomalies that might be difficult or too time-consuming for a human to analyze [179].

Machine learning is a subset of AI. It focuses on building systems that can automatically learn from data and improve their performance over time without being explicitly programmed. Machine learning algorithms use statistical techniques to analyze data and learn patterns or models that can be used to make predictions or decisions [179]. Machine learning algorithms can be categorized into unsupervised and supervised learning. Both types of algorithms are trained on a dataset. In supervised learning, the dataset is labelled. The dataset consists of sets of inputs and corresponding outputs. Based on this dataset, the algorithm learns to create the right output when given a certain input [179]. For example, an algorithm is given images of cats and dogs and is asked to predict whether on the input image is a cat or a dog. The dataset for this task consists of images of cats and dogs and the corresponding labels that should be predicted by the model. In this thesis, supervised learning algorithms were used and therefore this chapter discusses these types of algorithms.

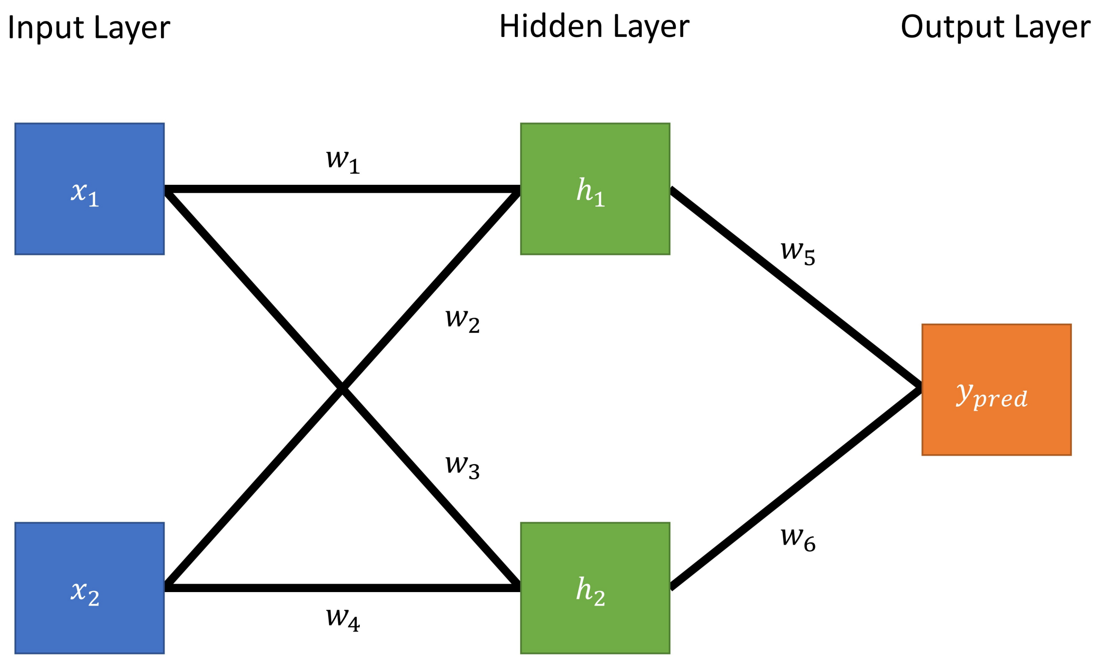

Figure 3.1: A simple example for an ANN.

An example for a machine learning algorithm is an artificial neural network (ANN) [179]. ANNs are designed to mimic the human brain and are trained on a dataset. A simple example of an ANN is shown in Figure 3.1. This small network consists of two inputs x_1 and x_2, which are indicated by blue boxes, a hidden layer with two neurons h_1 and h_2 shown as grenn boxes and an output layer with one neuron y_{pred} depicted as orange box. The weights connect all inputs with the neurons of the hidden layer and the neurons of the hidden layer with the neurons of the output layer and are shown by black lines. A neuron is the basic unit of an ANN [179]. In detail, in every neuron the following calculations are made. The neuron takes

m weighted inputs $w_i x_i$ forwards them with a bias b through an activation function f, and provides an output that is forwarded to the next neuron:

$$\text{output} = f(\sum_{i=1}^{m} w_i x_i + b) \tag{3.1}$$

The activation function is a non-linear function that adds a non-linearity to the neuron and enables the neuron to model non-linear relationships between input and output [179]. The choice of an activation function for a neuron depends strongly on the model and the application [179]. In hidden layers, often ReLUs (Rectified Linear Unit)[1] are used, while for output layers sigmoid functions are chosen [179].

The learning process can be divided into three parts, the feedforward, the calculation of the loss and the backpropagation. In the feedforward of the neural network shown in Figure 3.1, the inputs of the input layer are forwarded via weighted connections to the neurons of the hidden layer. Then, the outputs of the hidden layer are forwarded via weighted connections to the neuron of the output layer. In detail, the following calculations are done

$$h_1 = f_1(w_1 \cdot x_1 + w_2 \cdot x_2 + b_1) \tag{3.2}$$

$$h_2 = f_2(w_3 \cdot x_1 + w_4 \cdot x_2 + b_2) \tag{3.3}$$

$$y_{\text{pred}} = f_3(w_5 \cdot h_1 + w_6 \cdot h_2 + b_3) \tag{3.4}$$

The output of the feedforward is the prediction of the neural network based on the input [179]. The actual learning of an ANN model takes place using a training dataset. Usually, 70 % to 90 % of the whole dataset is used for training, whereas the rest of the dataset is used for validation and testing [179]. In the training, the feedforward is performed on a so-called batch of input training data, which is a subset of the training dataset.

The loss is calculated on the outputs of the batch by a loss function L that is chosen according to the model. In this simple neural network, the MSE (mean squared error) loss L_{MSE} can be used that is defined as

$$L_{\text{MSE}} = \frac{1}{n} \sum_{i=1}^{n} (y_{\text{i,true}} - y_{\text{i,pred}})^2 \tag{3.5}$$

where n is the batch size, $y_{\text{i,pred}}$ is the prediction of input i and $y_{\text{i,true}}$ is the true value for input i. A high loss corresponds to many false predictions, where the $y_{\text{i,pred}}$ does not match $y_{\text{i,true}}$ and a low loss corresponds to many correct predictions. Therefore, the training aims for minimizing the loss. To minimize the loss, the weights in the ANN model are adapted by backpropagation [179].

The backpropagation is done by an optimization algorithm such as the gradient decent (GD). In GD, the weights are updated using the partial derivative of the loss function L to the weight w_i:

---

[1] ReLU is a function that returns the input directly if it is positive and returns zero otherwise

$$w_{\mathrm{i,new}} = w_i - \alpha \frac{\partial L}{\partial w_i} \tag{3.6}$$

where α is the learning rate. The learning rate describes the stepsize of the optimization in every training step to minimize the loss [179]. The choice of the learning rate is crucial for the training of a neural network. If the learning rate is too high, the optimization steps will be too big to find the optimal weights. In contrast, if the learning rate is too small the training will take too long [179]. Next to GD, there are a lot of different optimization functions. The choice of the optimization function depends on the application [179]. One passage of these three learning steps is called epoch. In a training, several epochs are passed through. After a predefined number of epochs, the performance of the training is tested on the part of the dataset used for validation. Based on the performance of this validation dataset, the network is adjusted in a process called hyper-parameter tuning. Here, non-learnable parameters, e.g. the number of neurons in a hidden layer, the optimization, the loss function, the activation functions, the batchsize, the number of epochs, and the learning rate are adapted until an optimal configuration is found. Non-learnable parameters can not be optimized in the training process as these parameters are hard-coded in contrast to learnable parameters like weigths whose optimal configurations are learned in the training process. For more complex tasks, the performance of a neural network can be increased by increasing the number of hidden layers, thus making the network deeper. Therefore, the training process of a neural network containing more than one hidden layer is called deep learning [179].

3.2 Convolutional neural networks for image classification

In this thesis, image data from a microscope are evaluated. Such images contain 1388 x 1040 pixels (px). A standard ANN takes as input only vectors and so the image needs to be vectorized that would result in an input vector with 1,443,520 entries. The training of such a huge vector requires many trainable parameters. Furthermore, spatial information is lost via the process of vectorization. Therefore, another network architecture is needed that overcomes these issues. Such a network is the CNN (Convolutional Neural Network). The CNN is based on ANNs but designed to preserve spatial information by exploiting the local connectivity of adjacent pixels [180]. It can extract different features by learning patterns on images and requires fewer trainable parameters as weights are shared in a CNN across different parts of the image [180]. CNNs are typically used for image classification, but also serve as basis for various computer vision tasks on images like object detection [179].

3.2.1 Mathematical concept behind CNNs

CNNs take as input images of a certain size and depth. The images received from the microscope have only one channel therefore the input has the form 1388 x 1040 x 1. From a mathematical perspective, an image can be represented as a matrix where each entry corresponds to the intensity of a pixel. For a better visualization, images are in the following presented as matrices. CNNs are comprised of three types of layers: the convolutional layers, the pooling layers and the fully connected layers [180]. The convolutional layer uses learnable kernels that are convoluted with the input image. The convolution of an input matrix with a kernel matrix is shown in Figure 3.2.

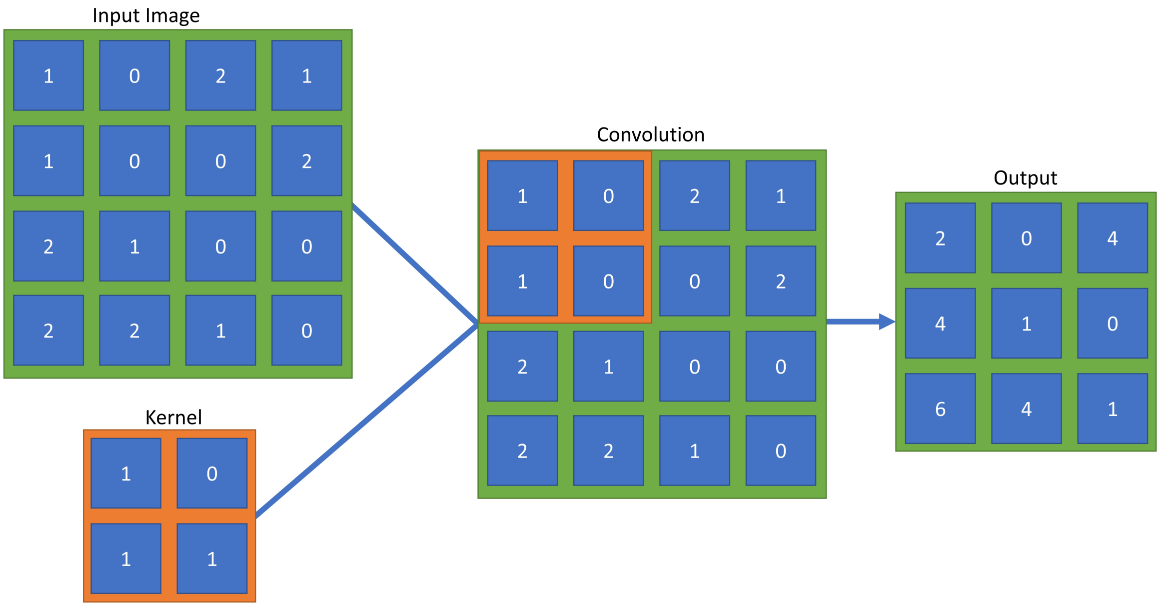

Figure 3.2: The convolution of an input matrix with a kernel matrix.

Here, an 4 x 4 input matrix is convoluted with a smaller 2 x 2 kernel matrix. The convolution is defined as

$$S(i,j) = \sum_m \sum_n I(i+m, j+n)K(m,n). \tag{3.7}$$

where $S(i,j)$ is an entry at the ij^{th} position of the output matrix, where i corresponds to the row-wise position and j to the column-wise position, K is the Kernel matrix and $K(m,n)$ being the mn^{th} position in the Kernel matrix and I is the input matrix[179]. Therefore, every convolution produces one entry of the output matrix and the next convolution is performed by sliding the kernel matrix to the next position of the input matrix until the whole image has been covered. The stepsize of the sliding is called stride. In the example, a stride of 1 was used resulting in a 3 x 3 matrix. A stride of 2 would result in 2 x 2 matrix. Therefore, the process of convolution can be seen as a downsampling of the input image while emphasizing a certain pattern in the image given by the kernel. In the input image of the example, the pattern of the kernel occurs in the lower left corner. Subsequently, the value of the output image is the highest in the lower left corner.

In the pooling layer, a predefined number of pixels is pooled by a certain rule. The most common types of pooling are the maximum-pooling and the average-pooling. At maximum-pooling, the highest value is forwarded and at average-pooling, the average of the pooled pixel values is calculated and forwarded. With this technique, the image is downsampled while preserving spatial information of the features [179].

The last type of layers are fully connected layers. They are implemented at the very end of the network. A fully connected layer consists of a predefined number of neurons like the ANN that are connected to all entries of the output of the previous layer. The fully connected layer outputs a vector. After every layer, an activation function is applied [179].

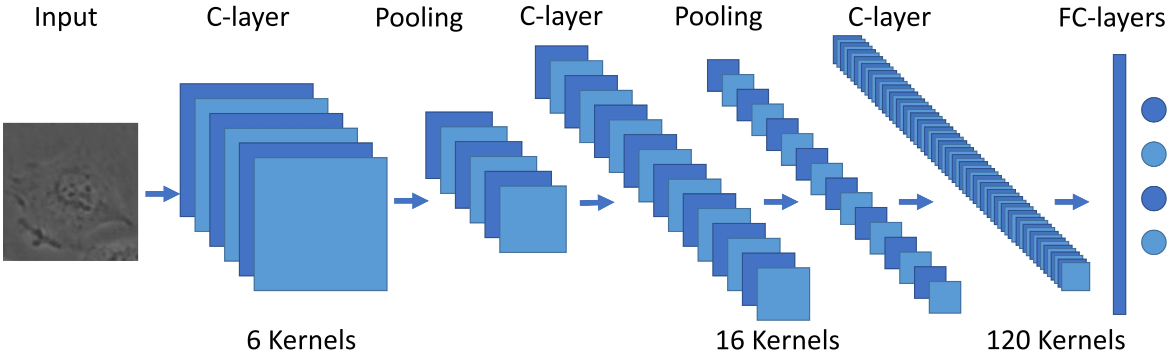

Figure 3.3: The CNN LeNet5, adapted from [181]. The CNN takes as input an image, in this case the image of a cell and predicts the according class. Convolutional layers are indicated as C-layers and fully connected layers as FC-layers. In the first C-layer, 6 kernels are applied on the input image resulting in 6 feature maps shown by blue squares. The second and third C-layers are presented accordingly with 16 feature maps and 120 feature maps. The first FC-layer is shown by a blue line and has 84 neurons. The output layer is an FC-layer with 4 neurons representing 4 classes that can be predicted by this network.

In Figure 3.3, the CNN LeNet5 [181] is shown as a simple example for a CNN. The presented network has three convolutional layers (C-layers), two pooling layers and two fully connected layers (FC-layers). In the convolutional layers, a set of kernels is applied on the image resulting in one feature map for every kernel. These feature maps are downsampled by a pooling layer. The fully connected layers convert the feature maps into an output vector of the desired length. In this case, the output vector has a length of four that correspond to four classes that can be predicted. After every convolutional layer and the first fully connected layer, a hyperbolic tangens is applied as activation function and after the pooling layer a sigmoid. The last fully connected layer is activated by a softmax

$$\sigma(\vec{z})_i = \frac{e^{z_i}}{\sum_{j=1}^{K} e^{z_j}} \tag{3.8}$$

where $\vec{z}$ is the input vector, z_i the elements of the input vector, e the exponential function, and K is the number of classes that are predicted by the CNN [179]. The softmax is commonly used for a classification task with multiple classes and outputs a probability that the input image shows an object of a certain class [179]. The probability is calculated for every class and the probabilities for all classes add up to 1. For such a classification task, a categorical cross-entropy loss can be applied that is defined as

$$\mathcal{L}_{\text{CE}} = -\frac{1}{N} \sum_{i=1}^{N} \sum_{j=1}^{C} y_{i,j} \log(p_{i,j}) \tag{3.9}$$

where N is the number of samples, C is the number of classes, $y_{i,j}$ is the true label for sample i and class j, and $p_{i,j}$ is the predicted probability for sample i and class j [182]. The categorical cross-entropy loss measures the difference between the true probability distribution and the predicted probability distribution. The true distribution is a one-hot vector with a 1 in the index corresponding to the true class and 0 elsewhere [182]. The cross-entropy loss encourages the predicted probability to be close to 1 for the true class and close to 0 for all other classes. The logarithmic term in the formula penalizes the model heavily for predicting a low probability for the true class and a high probability for any other class.

3.2.2 Metrics for classification

The performance of a CNN to classify images is usually scored by precision and recall. Both scores are based on the categorization of the predictions into true-positive, true-negative, false-positive and false-negative. In a classification task, this categorization is done for every class individually. True-positives (TP) of one class are predictions that match the groundtruth. False-negatives (FN) were categorized into another class although they should be in the observed class based on the groundtruth. False-positives (FP) are predictions that were assigned to the observed class but belong to other classes and true-negatives (TN) are predictions that are rightly assigned to other classes. The precision score is defined as

$$\text{Precision} = \frac{\text{TP}}{\text{TP} + \text{FP}}. \tag{3.10}$$

Therefore, precision is the fraction of right predictions of all predictions made for this class and provides information about how good are the predictions of the model. The recall is defined as

$$\text{Recall} = \frac{\text{TP}}{\text{TP} + \text{FN}}. \tag{3.11}$$

The recall can be seen as the fraction of right predictions of a class from all instances that belong to this class and provides the sensitivity of detecting the instances of a class. If both scores are relevant for scoring the performance of a model, a combined score can be applied. Such a score is the F1-score that is the harmonic mean of precision and recall and is defined as

$$\text{F}_1 = \frac{\text{Precision} \cdot \text{Recall}}{\text{Precision} + \text{Recall}} = \frac{2\text{TP}}{2\text{TP} + \text{FP} + \text{FN}}. \tag{3.12}$$

3.2.3 ResNet family

One approach to improve the performance of a CNN is to increase the depth of the network by adding more convolutional and pooling layers, which allows the CNN to learn more complex patterns. However, as the depth of the network increases, the backpropagation of gradients during training can become problematic. In backpropagation, the gradients are calculated and the weights are updated by going backwards through the network, as discussed in Section 3.1. In this process, the gradients of activation functions are calculated and multiplied due to the chain rule. Activation functions like the sigmoid and the hyperbolic tangens result in gradients in the range $(0,1]$ that result in "vanishing" gradients when going deeper into the network. The use of ReLU as an activation function can mitigate the problem. However, small initialized weights or negative weights lead also to a vanishing of the gradients. These vanishing gradients prevent that weights in the earlier layers of the network are updated and therefore hinder the network from learning. To mitigate the problem of vanishing gradients, new network architectures were designed. Such a network architecture is the ResNet (Residual Network) [183]. ResNet is a CNN that employs "skip connections" to enable the training of very deep networks.

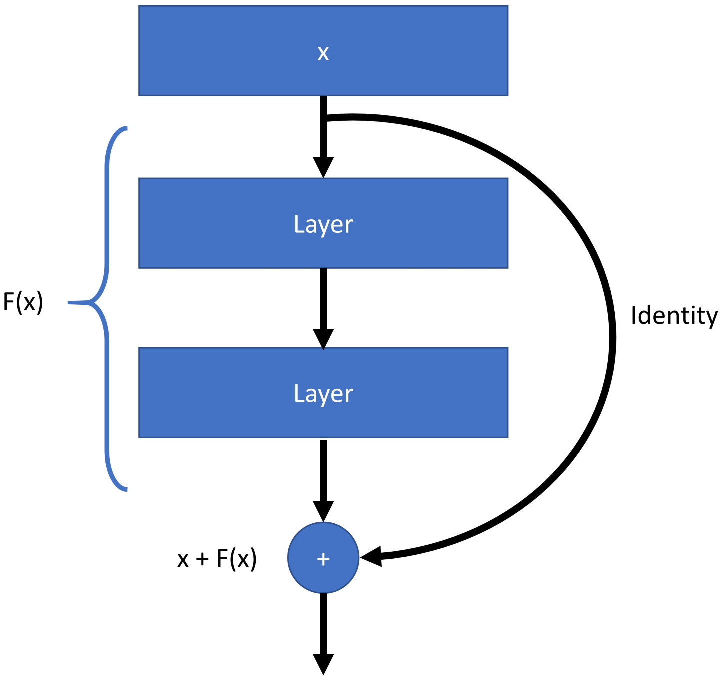

Figure 3.4: The residual block of a ResNet. The output x of a previous layer is either forwarded through some layer and its identity is forwarded via a skip connection. The outputs of both paths are added. Adapted from [183]

These skip connections allow the input to be passed through the network, bypassing certain layers and merging the input with the layer outputs by addition, as shown in Figure 3.4 [183]. These skip connections are also called residuals and the part of the network where such a residual occurs is called residual block. With this residual block, the vanishing of the gradients in the skipped layers does not affect the updating of weights in earlier layers, as the identity is forwarded by skipping these layers. In this thesis, the ResNet50 and the ResNet101 were used. The numbers in both names denote the number of layers. The architectures can be found in detail in He et al. [183].

3.3 Object detection

Unlike a classification task, where only the class is predicted, object detection algorithms predict the class label and the coordinates where an object is located in the image. Object detection algorithms can predict many objects of different classes in an image. There are many different approaches to detect objects in an image. They can be roughly divided into one-stage and two-stage detectors based on CNNs, and detectors based on new approaches like so-called transformer models [184]. In this thesis, the two-stage detector faster RCNN was used and is detailed described in Section 3.3.2. This detector is very accurate in detecting many small objects [184]. Since it is implemented in the TensorFlow object detection API (see Section 3.3.3), it can be easily applied to custom object detection projects. Before describing the architecture of the faster RCNN, some basic concepts of scoring predictions of an object detector are presented.

3.3.1 Object detection scores

To score the predictions of an object detection model, two parameters are relevant: the classification and the localization of an object. The performance of the localization is measured by the box-overlap of the predicted box with a groundtruth box by using the IoU (intersection over union) score. The IoU is defined as

$$\mathrm{IoU} = \frac{\mathrm{Intersection}(\mathrm{Box}_\mathrm{P}, \mathrm{Box}_\mathrm{GT})}{\mathrm{Union}(\mathrm{Box}_\mathrm{P}, \mathrm{Box}_\mathrm{GT})}, \tag{3.13}$$

where Box_P is the predicted box and Box_GT the groundtruth box. The intersection of two boxes is the area covered by both boxes and the union is the area covered by each box alone plus the area of the intersection, as shown in Figure 3.5.

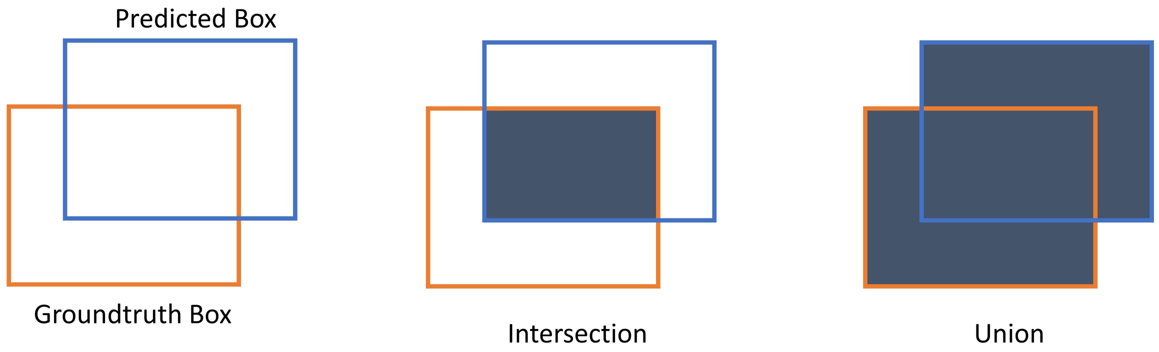

Figure 3.5: The intersection and the union of two boxes.

The performance of an object detector is measured by the mAP (mean average precision) score. To calculate the mAP score, the AP (average precision) score is calculated for each class individually, and the mAP score is the average AP score over all classes. For the AP score, the predicted bounding boxes are sorted by their confidence score and classified as either true-positive or false-positive. Object detectors return a confidence score in addition to the bounding box coordinates and class labels. The confidence score is the probability that a bounding box contains an object of a given class, and is the measure of how confident the detector is about the prediction. True positives are all bounding boxes that overlap a groundtruth box by more than the specified IoU threshold and whose class labels match the groundtruth labels. Consequently, a box that does not overlap sufficiently with a groundtruth box, or its class label does not match the groundtruth label, or both, is reported as a false positive. False negatives are all boxes that occur in the groundtruth but were not predicted. If multiple predictions match the same groundtruth box, the predicted box with the highest confidence score is marked as a true positive and the other bounding boxes are marked as false positives. Starting with the bounding box with the highest confidence score, precision and recall are calculated for each bounding box with respect to all boxes with a higher confidence score. For example, the first three bounding boxes are true positives, followed by one false positive box, and there are a total of 6 groundtruth boxes. The precision for the first three boxes is 1 and for the fourth box with respect to all previous boxes is 0.75. The recall for the first box is 0.17, for the second box is 0.33, and for the third and fourth boxes is 0.5, since only the previous boxes are considered and the missing boxes are counted as false negatives. Based on the calculated precisions and recalls, a precision-recall curve is drawn and shown as a red curve in Figure 3.6.

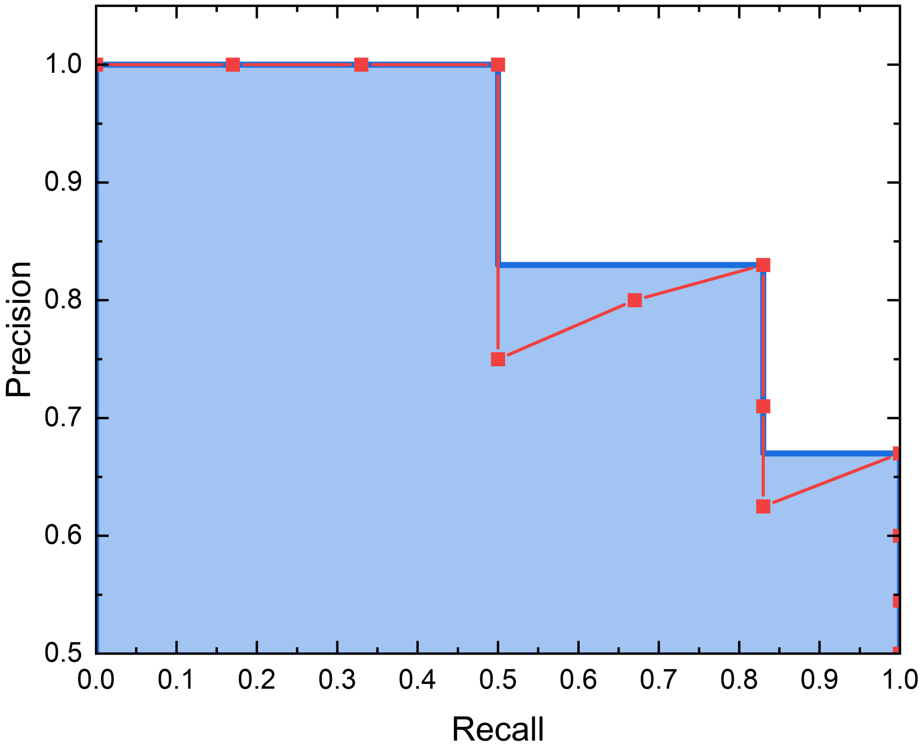

Figure 3.6: The precision-recall curve. In green, the original curve is shown and in blue the interpolated. To extract the AP score, the area under the curve is determined, indicated in light blue.

This curve is interpolated as follows:

$$p_{\mathrm{interpolated}}(r) = \max_{r' \geq r} p(r'), \tag{3.14}$$

where the precision value p of the recall r' is replaced with the maximum precision for any recall ≥ r' and the interpolated curve is shown in blue in Figure 3.6. Based on the resulting curve, the area under the curve is calculated and defines the AP score:

$$\text{AP} = \int_0^1 p_{\text{interpolated}}(r)dr \tag{3.15}$$

The mAP score can be calculated with different IoU scores. In computer vision, the COCO[2] mAP evaluator is the gold standard. Here, the mAP is calculated by averaging the mAPs with IoU-thresholds between 0.5 and 0.95 with a stepsize of 0.05 [185, 187]. Additionally, the mAP.50 (mAP with an IoU-threshold of 0.5) and the mAP.75 (mAP with an IoU-threshold of 0.75) are often provided.

3.3.2 Faster RCNN

The object detection algorithm faster RCNN (region-based convolutional network) was designed by Ren et al. [188] in 2015. This algorithm was the improvement of the former two-stage object detectors RCNN and fast RCNN and was the first end-to-end trainable two-stage object detector [188]. Object detection can be divided into three main steps: region proposal generation, feature extraction and classification. Region proposals are parts of the input image marked by bounding boxes that are possible candidates for containing an object. In Figure 3.7, the schematic architecture of the faster RCNN is shown.

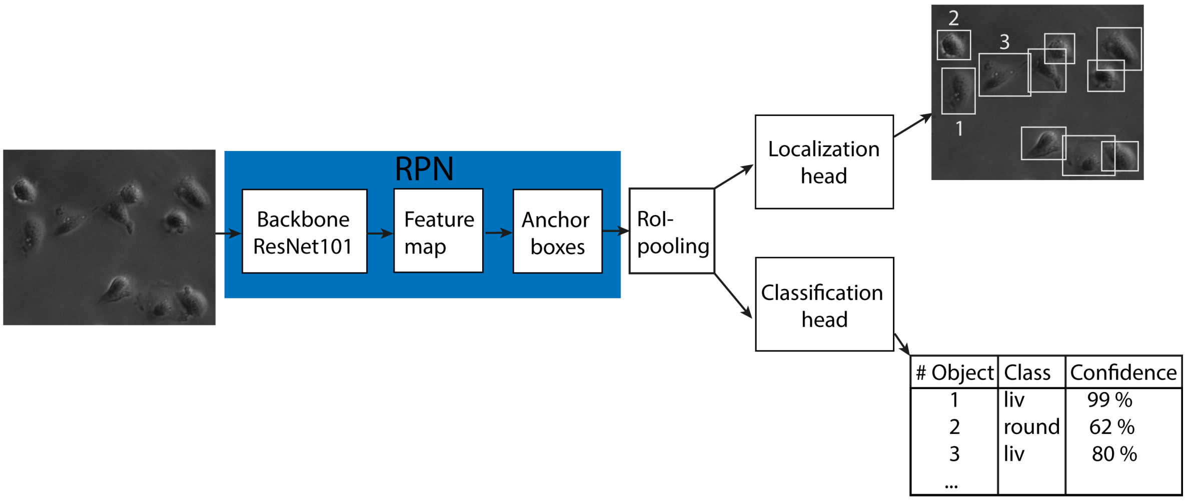

# Object	Class	Confidence
1	liv	99 %
2	round	62 %
3	liv	80 %
...		

Figure 3.7: The faster RCNN [188] with a ResNet101 as a backbone CNN. This network architecture is used to detect cells and their according classes on a microscope image by using a region proposal network (RPN) to generate region proposals.

Faster RCNN uses a region proposal network (RPN) to generate region proposals. In the RPN, the input image is fed into a backbone CNN. In this thesis, a ResNet101 was used as the backbone CNN. The CNN generates a feature map. Based on this feature map, anchor boxes are created. The number of anchor boxes is determined by the user.

---

[2] COCO or MS COCO stands for Microsoft common objects in context and is a dataset for object detection used as a standard dataset for comparing the performance of different object detectors [185, 186]. The performance of these detectors is typically measured by the COCO mAP evaluator.

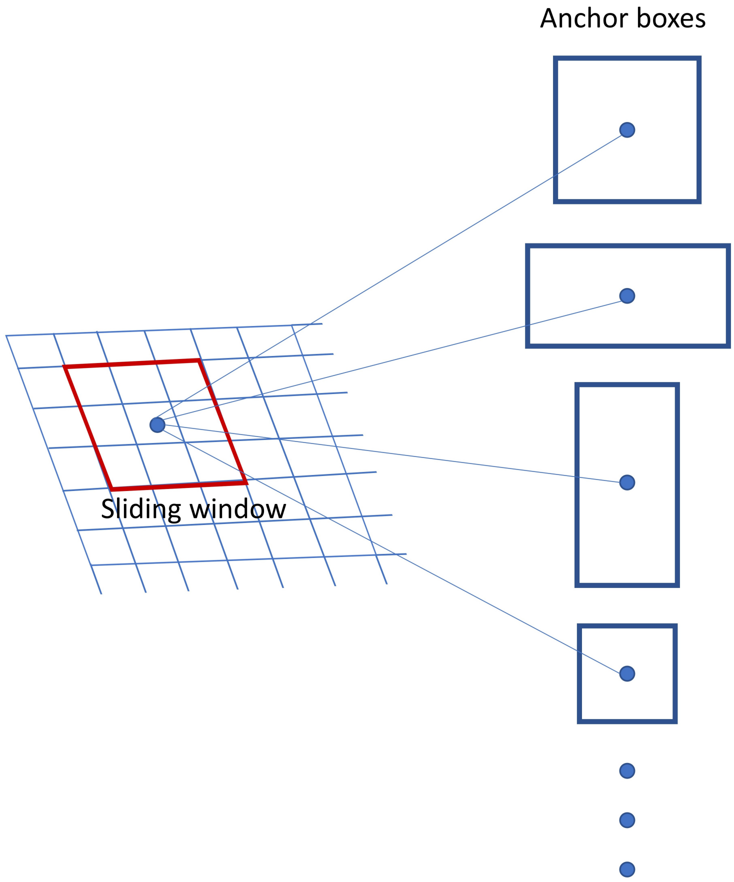

Figure 3.8: The generation of anchor boxes. For each entry of the feature map, a predefined number of anchor boxes is generated. Adapted from [188].

The anchor boxes are created in different scales and aspect ratios. By default, three scales with box sizes of 128^2 px, 256^2 px, and 512^2 px and three aspect ratios of 1:1, 1:2, and 2:1 are used, resulting in 9 anchor boxes. The aspect ratios 1:2 and 2:1 are created by redistributing the pixels according to these scales. Example anchor boxes are shown in Figure 3.8 on the right. To generate the anchor boxes, the algorithm glides over all pixel values of the feature map using a sliding window, as shown in Figure 3.8 on the left. At each pixel of the feature map, 9 anchor boxes are created with their center point located at the pixel of the feature map. In the RoI-pooling layer, equal-length feature vectors are extracted from the anchor boxes and these vectors are sent to the localization head and the classification head. In the localization head, the bounding boxes are refined to match the groundtruth boxes as closely as possible. This layer outputs the coordinates of the upper left corner of the bounding boxes and the width and height of the bounding boxes. The classification head determines the class of the objects in the anchor boxes. These classes are the predefined classes plus a class for the background in case an anchor box does not contain an object. In addition to the class, a confidence score is output that indicates how confident the detector is about the predicted class label. Only boxes with a confidence score $>$ 30 % will be output. To avoid outputting more than one bounding box for each object, a filtering method called non-maximum suppression (NMS) is used. In NMS, the box with the highest confidence score is selected and the overlap with all other boxes is calculated. The boxes that overlap more than the given IoU threshold are removed. This process is repeated for each box, going from high confidence scores to low confidence scores.

3.3.3 TensorFlow object detection API

In this thesis, the TensorFlow object detection API [189] is used for object detection. TensorFlow is an open source software library for artificial intelligence and was developed by Google. It is written in the programming languages Python and C++. API stands for application programming interface and is an interface that connects computers or pieces of software to each other. The TensorFlow object detection API provides a collection of pre-trained object detection models as well as tools to train custom models. Furthermore, it simplifies the process of training and deploying object detection models by providing high-level abstractions like model configuration, dataset handling and tools for training and evaluation.

3.4 A dataset for CeCILE

For the detection and tracking of cells in videos, a dataset was created during this thesis. To create such a dataset, several videos were taken under different conditions and from three cell types: HeLa, CHO-K1 and LN229 were included in the dataset to increase the ability of CeCILE to generalize. All videos were recorded with the inverted microscope Observer Z1 (Zeiss, Oberkochen, Germany). Inverted microscopes have the illumination and condenser above the stage where the specimens are placed. The objectives are placed below the stage. In biology, this type of microscope is typically used because cells and organisms are often kept in a nutrient solution in a container and are at the bottom of such a container due to gravity, making it easier to observe them from below. As a camera, the AxioCam mRM (Zeiss, Oberkochen, Germany) was used that provides images of the size of 1388 x 1040 pixels and a pixel size of 6.45 µm x 6.45 µm of the camera sensor.

3.4.1 Phase-contrast microscopy

The phase-contrast microscopy was invented in 1934 by Frits Zernike and is used for the visualization of unstained thin specimens like cells (5 µm to 10 µm thick) that are transparent and barely absorb light. The standard bright field microscopy of such objects results in images with poor contrast where the objects are barely distinguishable from the background due to low absorption. However, these objects have slightly different refractive indexes compared to the surrounding (cells: 1.35 to 1.40, culture medium: 1.33 [190]) that can be used for visualization in phase-contrast microscopy. The principle of this technique is shown in Figure 3.9. The light is provided by a halogen lamp that is part of the Köhler illumination, a technique for a homogeneous illumination of the whole field of view [191]. In phase-contrast microscopy, a phase stop is placed between the light source and the condensor lens. The phase stop is an aperture with a ring-shaped opening through which the light can pass. In the focus plane of the condensor, the objects are placed. The light is diffracted by the objects and brought into parallel by the objective lens. The light then passes through the phase plate. The ring-shaped phase plate partially absorbs the undiffracted light and shifts the phase of these light waves by λ/4 (λ is the wavelength), while allowing the diffracted light to pass unchanged. The partial absorption of the undiffracted light results in the suppression of background light, and the phase shift results in the enhancement of small refractive index changes in the image. This technique produces images with a dark background and bright object edges. The contrast in these images is higher the thicker the object and the greater the refractive index difference, since more light is diffracted in this case.

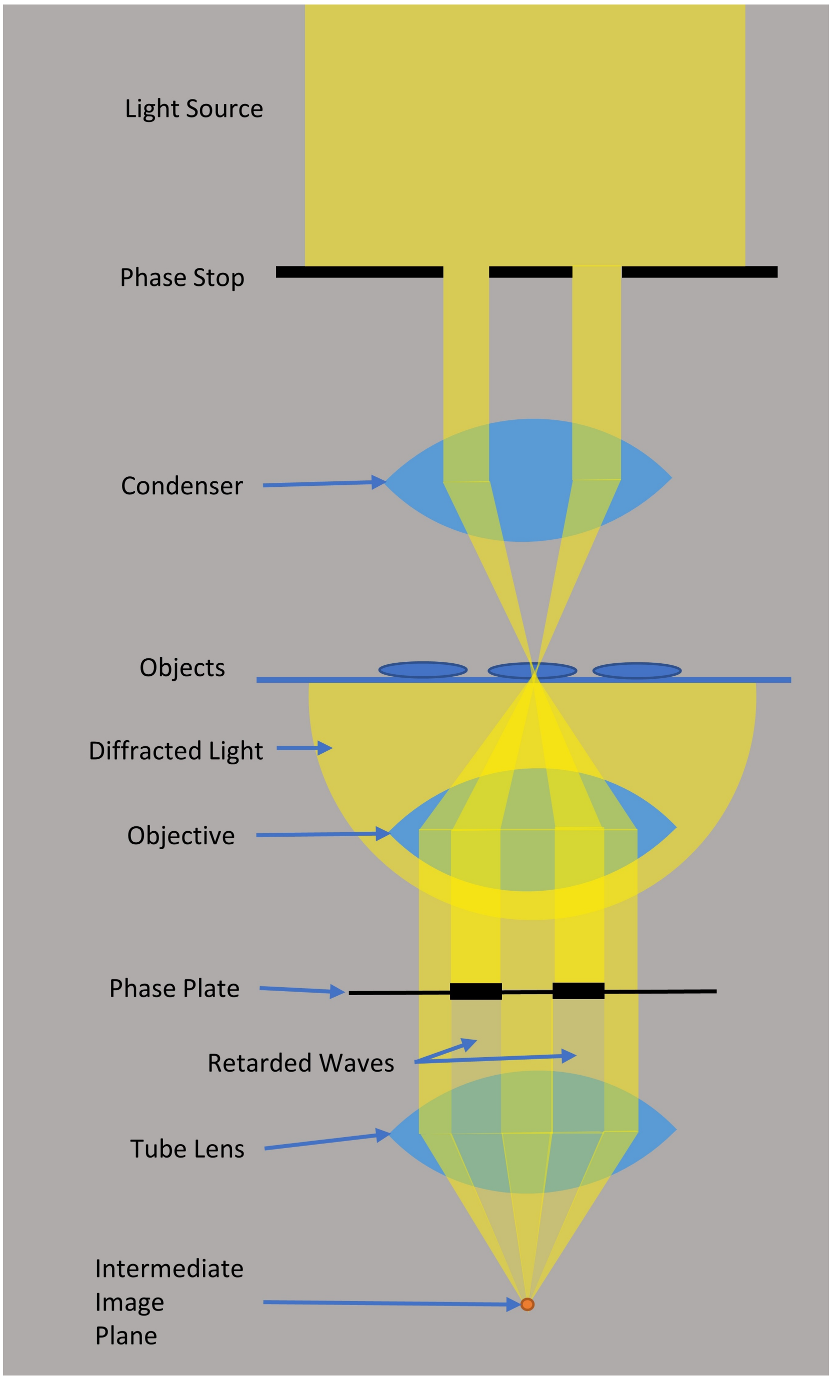

Figure 3.9: The principle of phase-contrast microscopy.

3.4.2 Live-cell microscopy

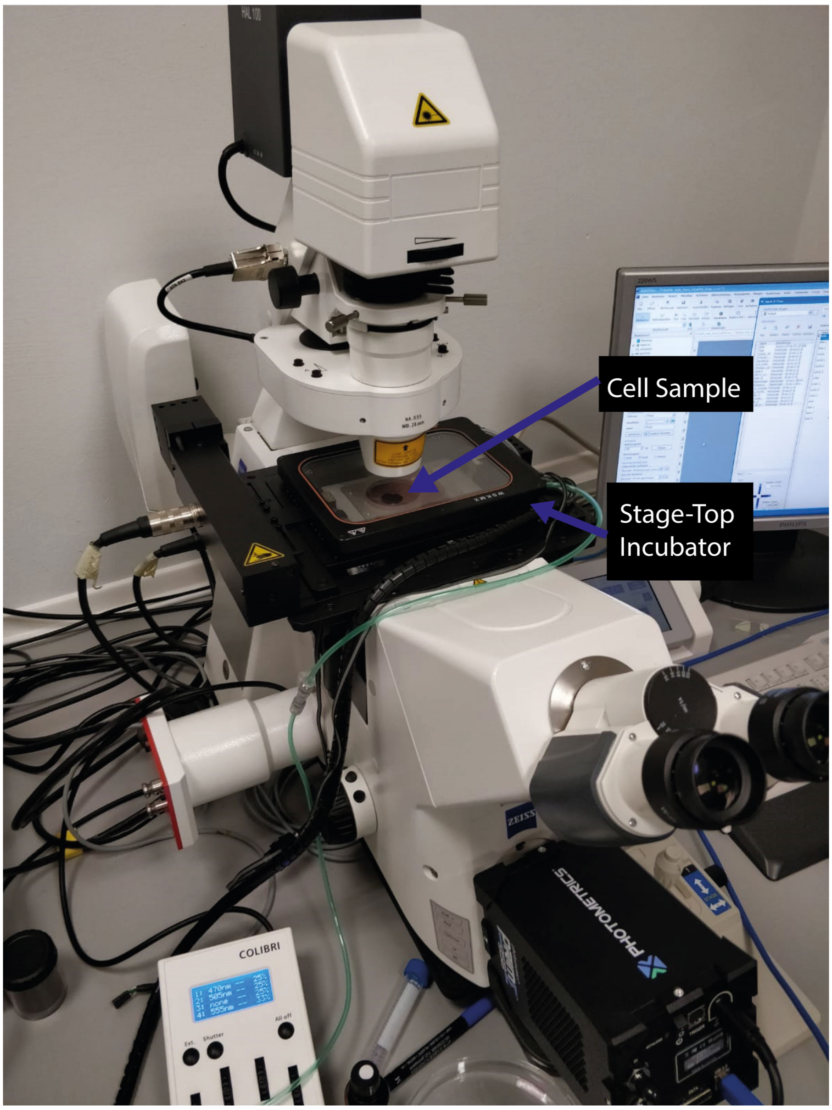

Figure 3.10: The microscope used for live-cell imaging equipped with a stage-top incubator.

Cells were imaged for up to 4 days via live-cell microscopy. Therefore, the microscope was equipped with a stage-top incubator (Tokai-hit STX, Tokai-hit, Japan), as shown in Figure 3.10. The incubator enables the cells to be kept under cell culture conditions (37°C of temperature, 5 % CO_2 concentration, and 100 % humidity). The water reservoir in the stage-top incubator was refilled every day during recording and the growth medium for the cells was refilled every second day. The water reservoir, the high humidity and the refill of the medium prevented the cell sample from drying and ensured optimal physical conditions and nutrient supply for the cells during observation. For imaging, a 10 x objective (Plan-Apochromat 10x/0.45 Ph1, Zeiss, Germany) was used. Cells were imaged in two modes: in standard phase-contrast by using the phase stop Ph 1 (Zeiss, Germany) as suggested from the manufacturer and is denoted in the following as mode 1. Furthermore, videos were recorded in a brightfield-phase-contrast mode by using phase stop Ph 2 (Zeiss, Germany), denoted in the following as mode 2. Both imaging methods were included into the dataset to increase the robustness of the detection algorithm and encourage the algorithm to learn rather the structure and pattern of the different morphologies of cells than intensity patterns.

Example images of HeLa cells recorded in both modes are shown in Figure 3.11. Images recorded by using mode 1 have a dark background with bright edges. Cells with a round morphology have a bright corona surrounding the object. This characteristic is typical of standard phase-contrast imaging because more light is diffracted on thick objects such as round cells and is enhanced by phase-contrast as described in Section 3.4.1. Images recorded by using mode 2 have a brighter background and a dark shadow where cells are thicker and the cells absorb more light. An example for that is the cell with the round morphology on right side in Figure 3.11a or on the left side in Figure 3.11b. Standard phase-contrast enhances the contrast of thin objects like cells and simplifies the detection of cells that have a flat and stretched out morphology. Due to the bright corona occurring at thicker objects, like the round cell, resolution of the structure within such an object is decreased compared to brightfield mode 2.

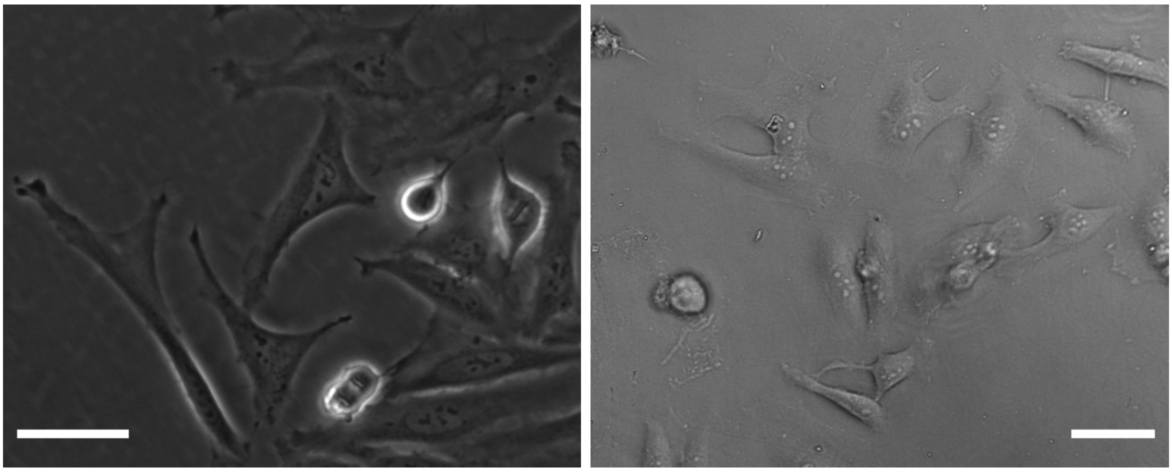

(a) Mode 1

(b) Mode 2

Figure 3.11: Images of HeLa cells in both imaging modes. In (a), an example image of imaging mode 1 is shown. This image was recorded with standard phase-contrast. In (b), an example image of mode 2 is shown. This image was recorded in brightfield-phase-contrast. The scale bars indicate a length of 50 µm.

3.4.3 Cell culture treatments

CeCILE is designed to analyze cell behavior on different live-cell videos for different applications and cell models. Three different cell lines - HeLa, CHO-K1 and LN229 - have been included in the dataset to ensure a high generalizability, also to new cell lines. Cells were treated with different methods to mimic different experimental scenarios for future applications. For example, some of the cells were irradiated with x-rays, protons and carbon ions. Such irradiations with different particles or x-rays requires different containers with different optical properties. Some applications require different seeding methods, such as seeding on restricted growth areas. Therefore, different cell culture treatments have been included in the dataset and are described below.

Cell cultivation

CHO cells and HeLa cells were cultivated in the growth medium RPMI 1640 (R8758-500ML, Sigma-Aldrich, USA) supplemented with 10 % FCS (Fetal calf serum, F0804-500ML, Sigma-Aldrich, USA) and 1 % Penicillin-Streptomycin (P4333-100ML, Sigma-Aldrich, USA). Additionally, 1 % Sodium Pyruvate (S8636-100ML, Sigma-Aldrich, USA) was added to the medium for CHO cells. LN 229 cells were cultivated in the growth medium DMEM high glucose (D6429-500ML, Sigma-Aldrich, USA) supplemented with 10 % FCS and 1 % Penicillin-Streptomycin. Cells were grown in an incubator at a temperature of 37 °C, 5 % CO_2 and 100 % humidity and were passaged twice a week.

Cell container

Cells were seeded 24 h before recording in one of three possible containers used for the generation of this dataset. The containers are 6-well plates (Cell culture multiwell plate 6-well, Greiner, Frickenhausen, Germany), round dishes with glass bottom (µ-Dish 35 mm, Ibidi, Martinsried, Germany) or live-cell imaging containers (short: LCIs). A 6-well plate and a µ-dish are shown in Figure 3.12. An LCI is shown in Figure 3.14.

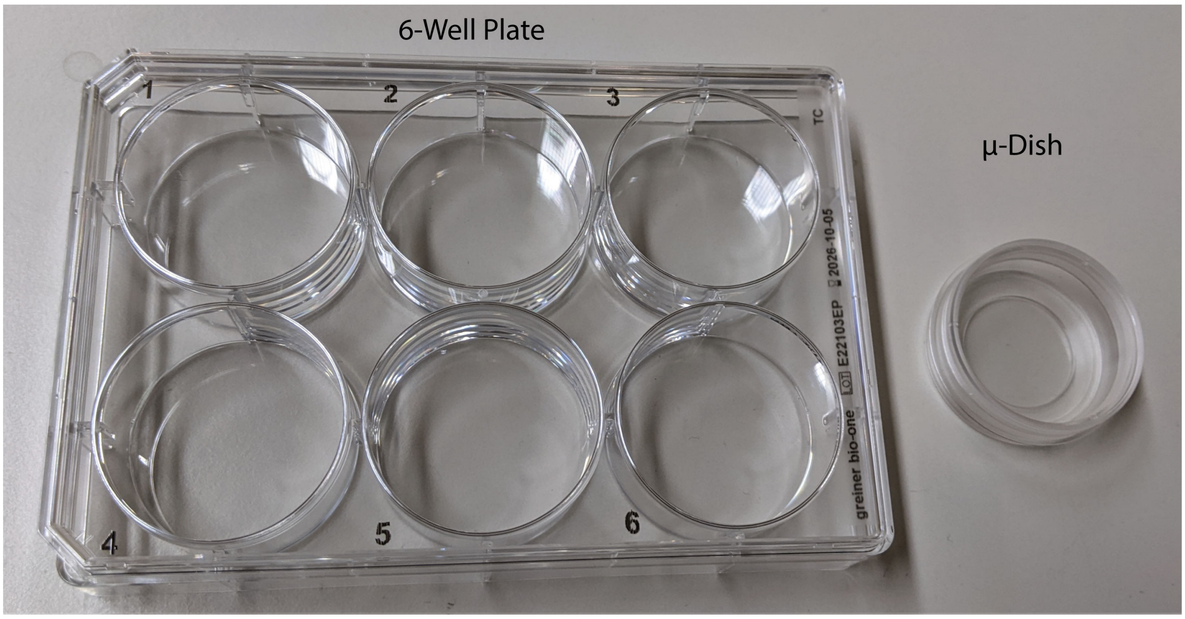

Figure 3.12: A 6-well plate and a µ-dish. Both container types were used for cultivating cells during microscopic observation.

The 6-well plates are made of the same material and have the same surface as the cell culture flasks used for cultivating the cells. This allows the cells to be observed in their familiar environment while minimizing external influences (such as a different growth surface). However, 6-well plates are not optimal for imaging, as they create a background pattern. This background pattern can be seen in Figure 3.13(a). The µ-dish, on the other hand, creates no background pattern and has ideal optical properties for imaging, as shown in Figure 3.13(b).

Inverted microscopes are designed for the use of a cover glass with a thickness of 170 µm between the objective lens and the specimen and provide the best resolution for such a set-up. The µ-dish has a 170 µm glass bottom and is therefore the optimal choice for live-cell imaging.

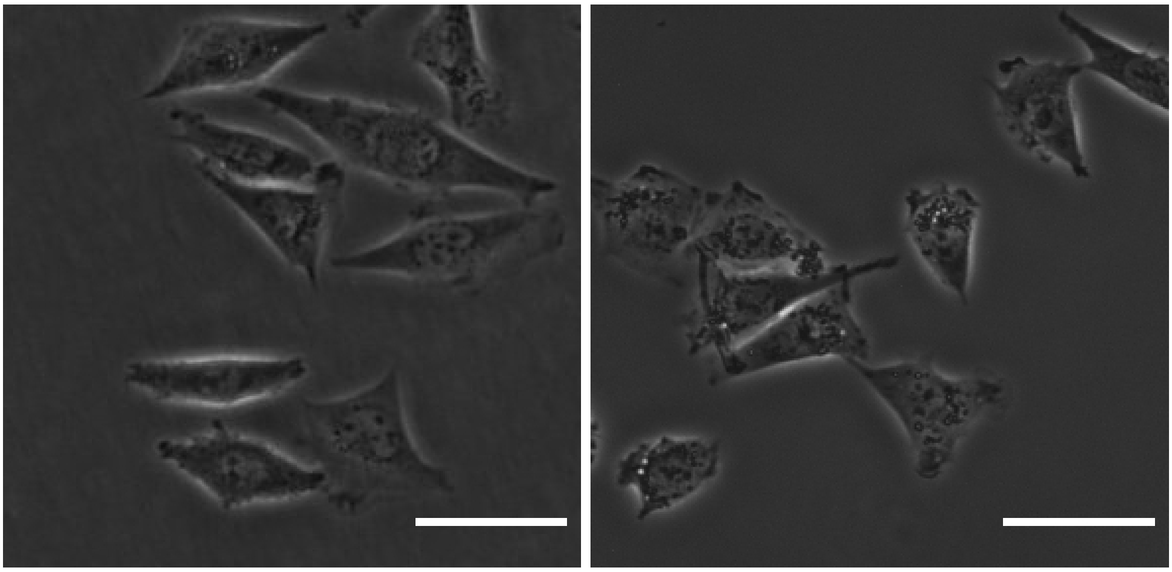

(a) 6-well plate

(b) µ-dish

Figure 3.13: Example images of cells growing in a 6 well plate (a) and of cells growing in a µ-dish (b). The scale bar indicates a length of 50 µm.

Cells that were irradiated with x-rays were kept in µ-dishes. In contrast, cells that were irradiated at SNAKE with either protons or carbon ions require special containers that are designed for irradiations at a horizontal beamline. Such containers are the LCI (live-cell imaging) containers designed by Volker Hable [138] and an example is shown in Figure 3.14. For protons, a glass window with a thickness of 170 µm was mounted with silicon to the bottom plate. When irradiating with carbon ions, a scintillator (EJ 228, Eljen Technology, Sweetwater, USA) window with a thickness of 170 µm was mounted. This type of scintillator is transparent and has a similar refractive index than glass (refractive index of the scintillator: 1.58 [193], glass: 1.51). Due to the smaller range of carbon ions (120 µm in water for 55 MeV carbon ions) in matter compared to protons, a scintillator close to the cells was needed for the detection system in SNAKE [138]. The cover plate of the LCI container was covered with a 4.7 µm thick polypropylene foil that is glued to the corners of the cover plate to keep the medium inside the container by using the Plastix superglue (Pattex, Henkel AG & Co.KGaA, Düsseldorf, Germany). For irradiation, the LCI container was placed in an upright position into the 90°-tilted microscope of the SNAKE beam line with the cover plate of the LCI container facing the beam. The LCI container was moved by the microscope so close to the nozzle of the beam exit that the polypropylene foil of the container was slightly pushed in. With this method, the distance between cells and beam nozzle was reduced to 32 µm and ions had to pass a 7 µm Kapton foil on the beam exit, the 4.7 µm polypropylene foil and approx. 20 µm of medium that covered the cells during irradiation. To ensure an optimal environment for the cells, the LCI container and the beam nozzle were heated to 37°C.

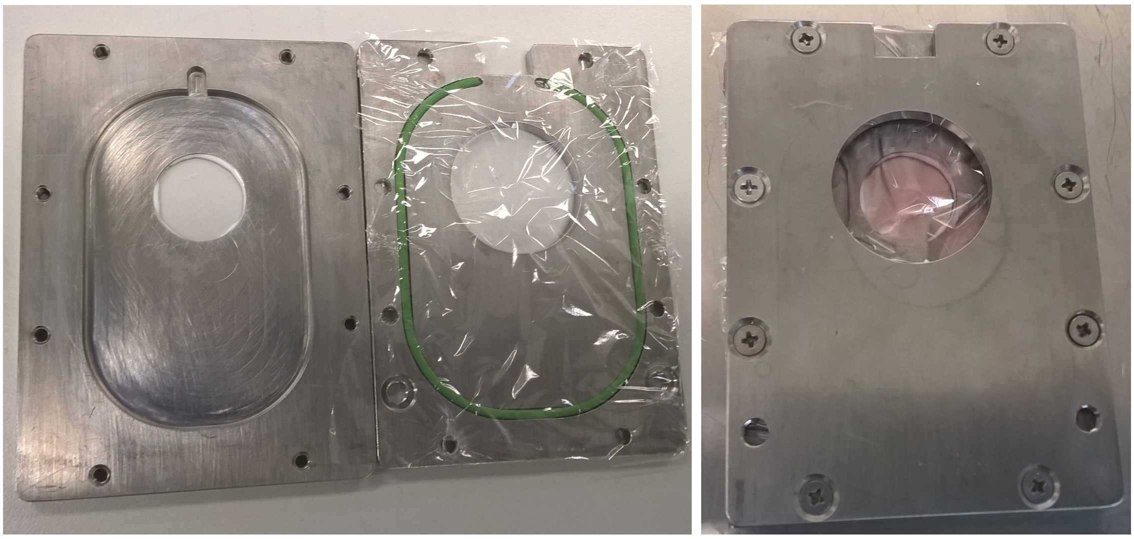

(a) (b)

Figure 3.14: The LCI (live-cell-imaging) container is designed for live-cell imaging during and after irradiation at the SNAKE beam line [138]. In (a), an open LCI container is shown. Either a scintillator or a cover glass is mounted with silicon into the window of the bottom part. The cover part of the container is glued with a polypropylene foil. In (b) the LCI container is filled with growth medium (the light pink liquid) and is closed with 8 screws. The images are taken from [194].

Coating

The container used in this study were either coated with CellTak (3.5 µg/cm^2, Corning), with gelatin, or were used uncoated. CellTak was dissolved in $NaHCO_3$ (30x buffer, 0.1 M, Sigma-Aldrich, USA). The LCI window was covered with 5 µg of the CellTak solution and the LCI container was incubated for 20 min at room temperature (20°C). Afterwards it was rinsed with water and dried on air. The gelatin coating was performed as described in Section 2.7.1. A coating stimulates the cells to grow also on glass and plastic scintillators that offer no ideal surface to adhere and prevents the cells from sliding downwards due to gravity when they are irradiated in an upright position.

Techniques for imaging different samples in parallel

In every irradiation experiment, an unirradiated control sample was prepared and imaged in parallel to the irradiated samples. This method ensures that environment and cell treatment are exactly the same and enables a direct comparison. For x-rays, this was accomplished by preparing another µ-dish additional to the µ-dishes that are prepared for irradiation. This extra dish was treated exactly the same as the irradiated dishes without switching on the beam. For live-cell imaging at the microscope, a holder was designed by me and built by Lukas Hackel and Ralf Schubert that can carry up to 6 dishes, as shown in Figure 3.15. This holder enables a parallel imaging of up to 6 dishes by using the motorized stage of the microscope. The different positions can be approached and recorded one after the other in less than 2 min. With this method, up to 5 different irradiation modes plus sham sample can be investigated in parallel and analyzed by CeCILE.

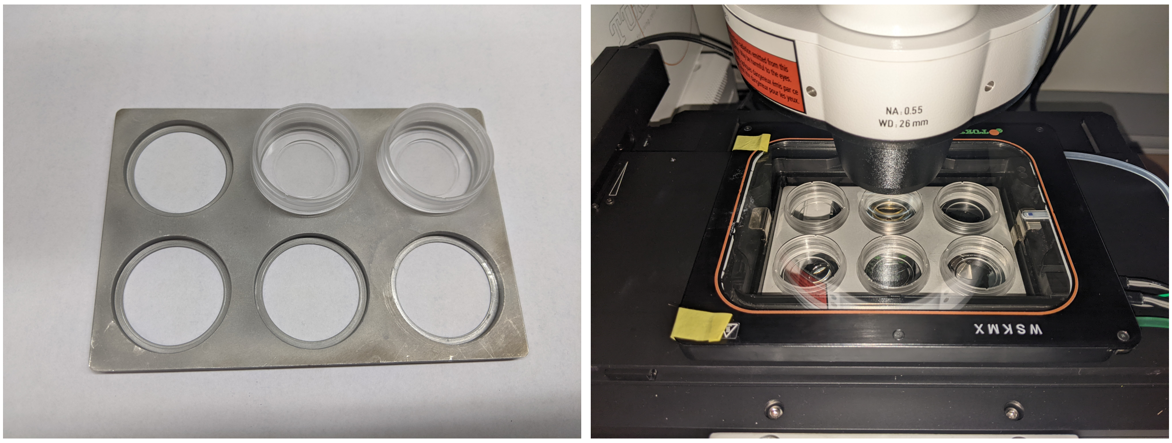

(a) (b)

Figure 3.15: A parallel imaging of up to 6 dishes was accomplished by a self-made holder, as shown in (a). In (b), the holder is mounted into the stage-top incubator of the microscope and all positions are filled with dishes that can be imaged in parallel by using the motorized stage of the microscope.

For LCI containers, a different method was established by me during my master thesis [194] that enables to investigate the effects of four different irradiation modes (including sham irradiation) on cells behavior on one sample. This was done by seeding the cells on restricted areas with the help of two types of inserts. Both insert types are made out of silicon, adhere to even surfaces like glass and are shown in Figure 3.16.

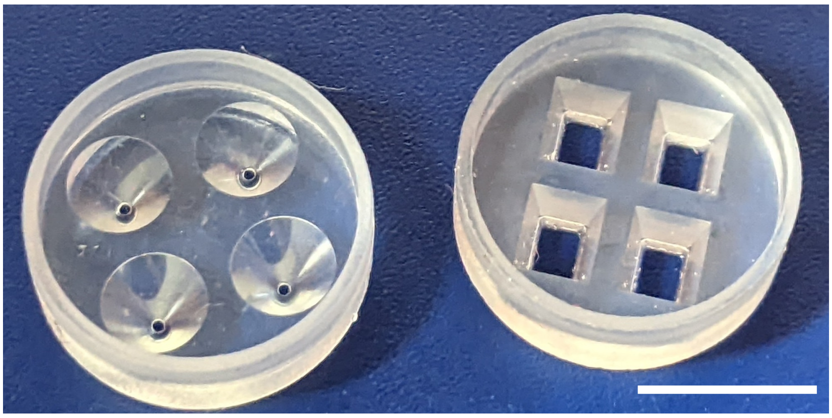

Figure 3.16: The micro-Insert 4 Well FulTrac (short: FulTrac) is shown on the left and the micro-Insert 4 Well (short: micro-Insert) is shown on the right. Both inserts are made of silicon and stick on plane surfaces. They are used for restricting the growth area of cells to four isles. By using these inserts for seeding, the four cell isles can be irradiated with different modes and irradiation responses of the four cell isles can be investigated and directly compared by parallel live-cell imaging. The scale bar indicates 1 cm.

A FulTrac (micro-Insert 4 Well FulTrac, Ibidi, Martinsried, Germany) was used for seeding cells in four small circular areas with a diameter of 0.4 mm that can be completely imaged with a 10x objective. The micro-Insert (micro-Insert 4 Well, Ibidi, Martinsried, Germany) was used for seeding cells in four rectangular areas with a size of 2.0 mm x 1.5 mm. An insert was placed in the middle of the LCI window, as shown in Figure 3.17 on the left.

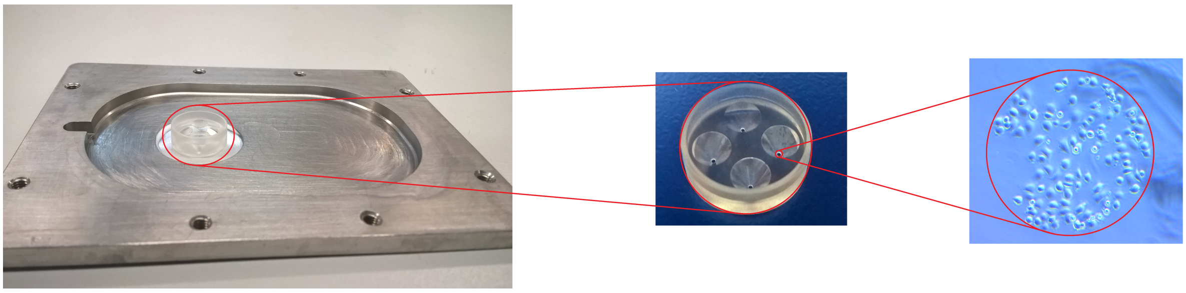

Figure 3.17: For seeding cells in four restricted areas, an insert was placed in the middle of the LCI window, as shown on the left. The insert is designed to adhere to even surfaces like glass. In the middle, the insert FulTrac is shown. This insert restricts the growth area for cells to four circular areas with a diameter of 4 mm each, as shown on the right. This image is taken from [194].

Each well of the insert was filled with 10 µl of a medium-cell-solution with a predefined concentration of cells. In the case of FulTrac, the insert was removed after one hour of incubation and the sample was incubated for another 23 h. In case of micro-Insert, 300 µl of medium was additionally added at the top of the insert and the sample was incubated 24 h before the insert was removed. With this method, the seeded cells grow in four restricted areas, as shown in Figure 3.17 on the right.

3.4.4 Irradiation

As CeCILE is meant to evaluate the response of cells to different treatments, especially irradiation treatments, data from different irradiation treatment scenarios were included into the dataset. Cells were irradiated with either protons, carbon ions, and x-rays directly before recording.

Proton irradiation at SNAKE

For proton irradiations, cells were irradiated with the setup described in Section 2.5. A 21 MeV proton beam was focused to a homogeneous field of 6.5 mm x 6.5 mm. Cells were seeded on an LCI container in four restricted areas by using a micro-Insert. Before irradiation, the micro-Insert was removed, the LCI-container was filled with 6 ml growth medium and the LCI container was closed. The LCI container was mounted to the 90°-tilted microscope at SNAKE that is equipped with a motorized stage. Each cell isle on the LCI sample was irradiated differently by aligning the sample via the motorized stage of the microscope that only one cell isle is irradiated at a time while the other cell isles received no dose until three of four cell isles are irradiated. The three cell isles were irradiated with 4 Gy each and dose rates of either 0.06 Gy/s, 9.3 Gy/s, and 310 Gy/s. One cell isle was left unirradiated as a sham control.

Carbon ion irradiation at SNAKE

For carbon ion irradiation of the cells, the carbon ions were focused to a microbeam with a diameter of $\sim$ 1 µm at the SNAKE beam line. For focusing the beam to a microbeam, a quadrupole triplett of supraconducting lenses was used instead of the quadrupole lens L1 (cf. Section 2.5). This triplett is located downstream of the experimental slits that the focus plane is at sample level. For irradiation, the microbeam was scanned over a 500 µm x 500 µm field that mimics a homogeneous irradiation. In this thesis, the beam preparation of a microbeam will not be further discussed as a homogeneous irradiation was performed and the resulting data were only used for the dataset and not for evaluations. However, a detailed description of the focusing procedure of the SNAKE microbeam, the beam preparation and the detailed setup can be found in my publication [195]. Cells were seeded in four restricted round cell isles with a diameter of 400 µm by using the insert FulTrac. Irradiation was performed similar as with protons (cf. Section 3.4.4). Each area was aligned one after another by the motorized stage of the microscope such one cell isle was fully covered and the others not before irradiation. The cell isles were irradiated with 2 Gy, 3 Gy and 4 Gy at a conventional dose rate (< 1 Gy/s) that was not determined. One cell isle was sham irradiated.

X-ray irradiation with CellRad

For irradiation with x-rays, a x-ray cabinet (CellRad, Precision, USA) was used. Cells were seeded into two µ-dishes 24 h before irradiation. One dish was irradiated with 3 Gy of x-rays (130 kV) and a dose rate of 0.067 Gy/s and the other dish was sham irradiated.

3.4.5 Manual labeling of the data

The dataset was created by a manual labeling of images and videos of cells. For labeling, the images or frames of a video were uploaded in the open-source browser-based software VGG image annotator (VIA) [196].

In each image of the dataset, all cells were manually labeled with bounding boxes. A bounding box contains an entire cell, and the edges of the cell should touch the edges of the bounding box, as shown in Figure 3.18 on the left. Here, the red arrows mark the points where the edges of the cell touch the edges of the bounding box. When two cells overlap, each bounding box is positioned so that all parts of the cell are included, even if this results in a large overlap with another bounding box, as shown in Figure 3.18 on the right by a blue arrow. Additionally, a class label was assigned to each bounding box.

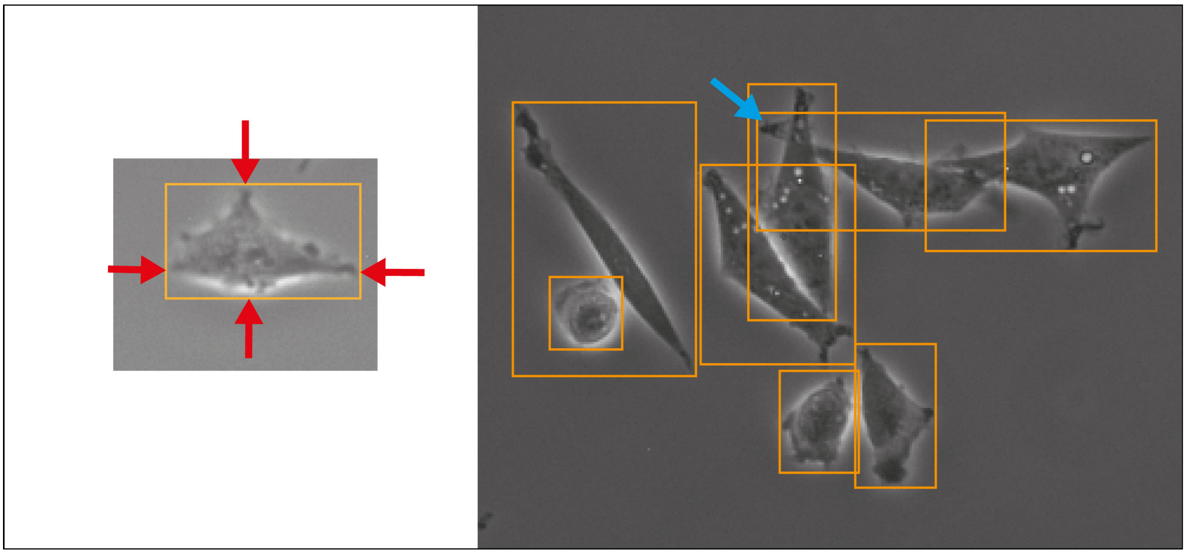

Figure 3.18: Manual annotation of cells with bounding boxes. A cell with its associated bounding box is shown on the left. The bounding box is positioned so that the cell touches the four edges of the bounding box marked by red arrows, while the entire cell is covered by the bounding box. On the right, an image with 8 cells is shown, and each cell is marked with a bounding box. When two cells overlap, as indicated by the blue arrow, the bounding box is drawn to include all parts of the cell.

3.4.6 Four classes for cell cycle evaluation

(**)

The aim for CeCILE was to follow the cells during the whole cell cycle and to be able to detect them in every state. Throughout the cell cycle, the morphology of a cell changes. This change can be assigned to three classes. The three classes show a transition circle, which is shown in Figure 3.19.

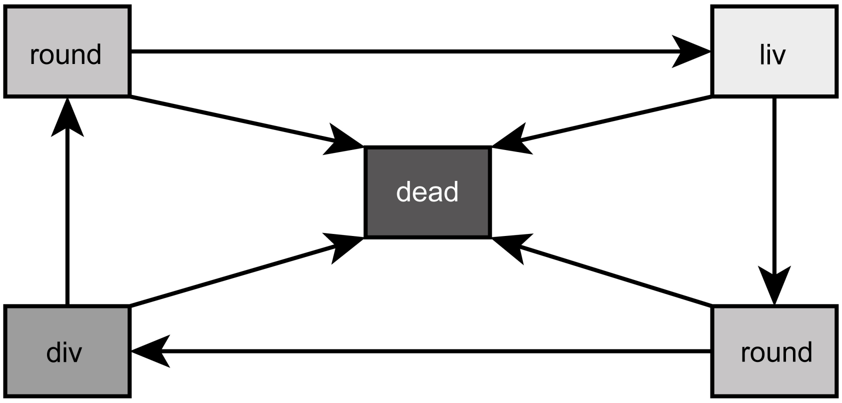

Figure 3.19: The morphological states in a cell cell cycle and all possible transitions. Adapted from [143] with permission.

(**) In the first state, the cell is attached to the surface of the container and shows a very flat “fried egg” like shape, where the cell nucleus looks like the yolk and the surrounding part of the cell containing the cell plasma and the organelles looks like the egg white, as shown in Figure 3.20(a). Cells of the same cell line can have very different outlines in this stage depending on the environment and mutations.

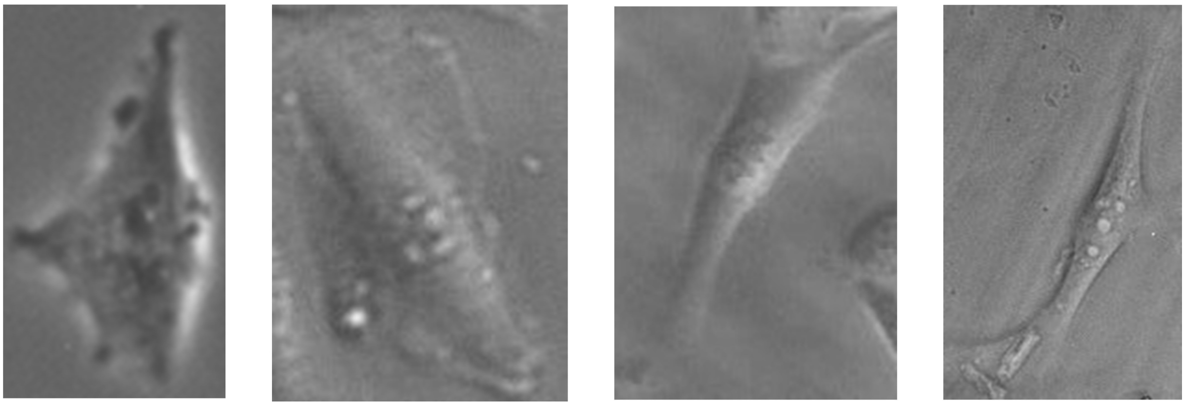

(a) liv

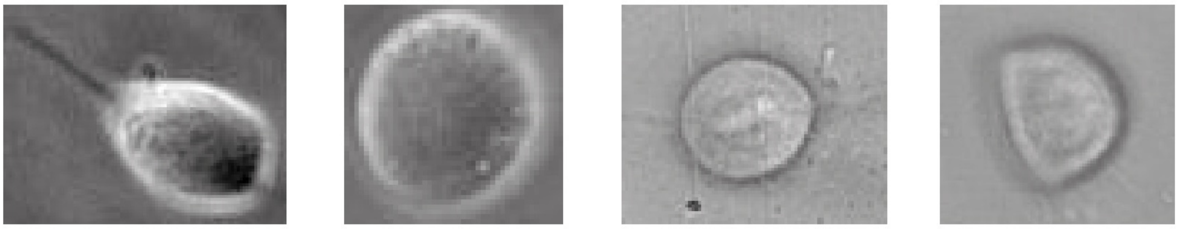

(b) round

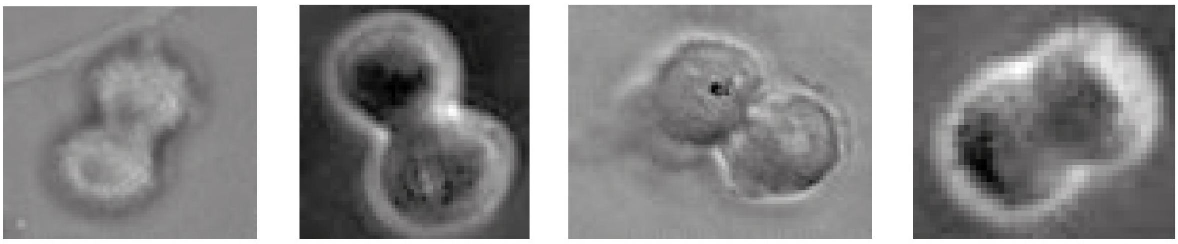

(c) div

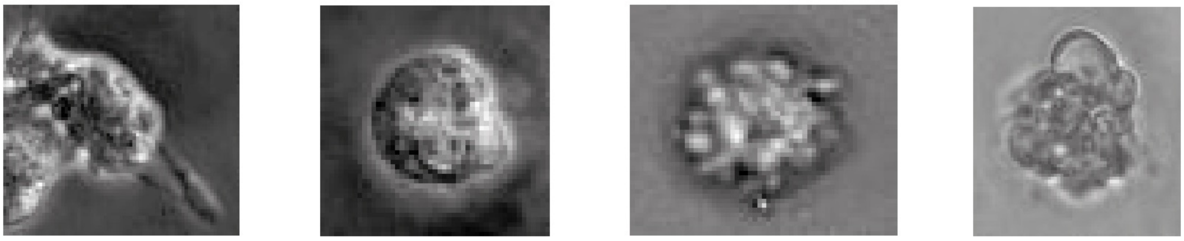

(d) dead

Figure 3.20: Example images of cells assigned to the four morphological classes liv (a), round (b), div (c), and dead (d). Adapted from [143] with permission.

All of them belong to the class living cell (liv). In the second class, the cells are no longer attached to the surface and show a round shape. Therefore, this class is called round cell (round). This state occurs during mitosis shortly before cell division or shortly after division. The round cell has, unlike the living cell, a high contrast at its edges, as shown in Figure 3.20(b). Since the transition between living cell and round cell state is smooth, a cell is labeled as round cell when more than half of the cell edges show this high contrast and therefore, most of the cell is no longer attached to the surface. The third class is named cell division (div) and contains cells that undergo cell division, as shown in Figure 3.20(c). A cell is counted as div if it is no longer round, the ongoing separation can be seen and as long as the two daughter cells are not completely separated from each other. These three classes describe vital cells. However, cells can die at any stage of the cell cycle (cf. Figure 3.19). Therefore, we included a fourth class (dead) in our algorithm, which contains all dead cells. Dead cells typically turn dark inside during the dying process and form bubbles, as shown in Figure 3.20(d).

3.4.7 Overview dataset

To train CeCILE, a dataset was created by Rika Ramson, students of the lab course radiation biology in 2022, and me and all labeled data were checked and corrected by me. For this dataset, 20 videos of cells of three different cell lines were recorded via live-cell imaging with a standard inverted microscope (cf. Section 3.4.2). During recording, cells were kept in a stage-top incubator that ensures a healthy environment for the cells and enables a continuous monitoring for up to 5 days. From the recorded videos, frames were chosen to be labeled and included into the dataset. In the first 13 videos, a distinct time intervall of 20 min or 100 min was chosen between the labeled frames and in videos 14 to 20 only frames were chosen to be included into the dataset where at least one cell was in the state cell division. Cells were imaged after different treatments, under different conditions and with different imaging modes resulting in heterogeneous videos that represent a wide range of experiments. Cells were seeded into three different containers that have different optical properties. The containers were coated with either gelantine or CellTak or left uncoated. The detailed description of the cell containers and the coating can be found in Section 3.4.3. Cell samples were irradiated either with protons (H^+) or carbon ions (C^{6+}) as described in Section 3.4.4 or left unirradiated. An overview of CeCILE's dataset is provided in Table 3.1. For testing CeCILE's performance in object detection and tracking on videos, two videos were labeled. To create the videos of the test dataset, CHO cells were seeded on two µ-dishes without coating. After 24 h of incubation, one µ-dish was irradiated with 3 Gy of x-rays (cf. Section 3.4.4) and the other one was sham irradiated. Both µ-dishes were placed in the live-cell-imaging setup of the microscope and recording of the videos with the microscope started immediately after irradiation. The recording was performed for 4 days. For the groundtruth, 457 frames of the irradiated sample were labeled, corresponding to a time range of 38 h, and 341 frames of the unirradiated sample were labeled, corresponding to a time range of 28.3 h. The different numbers of labeled frames were chosen, because the irradiated sample has a decreased growth rate compared to the sham sample. In the evaluated time ranges, the cells in both samples were able to divide three times and could be still tracked accurately as the cell densities were not too high. To create a groundtruth of these videos, the videos were labeled by CeCILE's object detector and tracker and the labels were manually corrected after object detection and after tracking using VIA image annotator software [196]. An overview of these videos is presented in Table 3.2.

CeCILE's Dataset														
	# Frames	Intervals	Cell line	# Liv	# Round	# Div	# Dead	Total	Container	Coating	Insert	Irr.	Dose	Im.
1	11	100 min	CHO-K1	1342	238	5	23	1608	LCI/glass	gelantine	micro-Insert	H^+	4 Gy	1
2	10	100 min	CHO-K1	2456	473	11	75	3015	LCI/glass	gelantine	micro-Insert	H^+	4 Gy	1
3	11	100 min	CHO-K1	208	167	1	40	416	LCI/glass	gelantine	micro-Insert	H^+	sham	1
4	11	100 min	CHO-K1	2526	346	9	33	2914	LCI/glass	gelantine	micro-Insert	H^+	4 Gy	1
5	10	100 min	CHO-K1	1608	373	8	122	2111	LCI/glass	gelantine	micro-Insert	H^+	4 Gy	1
6	10	100 min	CHO-K1	2209	352	9	44	2614	LCI/glass	gelantine	micro-Insert	H^+	4 Gy	1
7	11	100 min	CHO-K1	403	269	3	25	700	LCI/glass	gelantine	micro-Insert	H^+	sham	1
8	11	100 min	CHO-K1	365	167	2	18	552	LCI/glass	gelantine	micro-Insert	H^+	4 Gy	1
9	70	20 min	HeLa	1135	209	3	1515	2862	LCI/scinti	CellTak	FulTrac	C^{6+}	1 Gy	2
10	70	20 min	HeLa	2093	145	4	1669	3911	LCI/scinti	CellTak	FulTrac	C^{6+}	2 Gy	2
11	42	20 min	HeLa	2302	100	13	1573	3988	LCI/scinti	CellTak	FulTrac	C^{6+}	4 Gy	2
12	42	20 min	HeLa	1154	110	15	1331	2610	LCI/scinti	CellTak	FulTrac	C^{6+}	sham	2
13	7	100 min	CHO-K1	552	102	8	24	686	LCI/glass	gelantine	micro-Insert	H^+	4 Gy	1
14	12	random	CHO-K1	967	101	13	91	1172	dish/glass	no	no	no	no	1
15	21	random	LN229	2108	119	38	82	2347	6-well	gelantine	no	no	no	1
16	17	random	LN229	1412	93	41	147	1693	6-well	gelantine	no	no	no	1
17	13	random	LN229	738	65	17	44	864	6-well	gelantine	no	no	no	1
18	4	random	LN229	244	51	7	25	327	6-well	gelantine	no	no	no	1
19	20	random	HeLa	901	29	28	61	1019	6-well	no	no	no	no	1
20	20	random	HeLa	982	35	25	103	1145	6-well	no	no	no	no	1

Table 3.1: The dataset of CeCILE. This dataset was used for training and finetuning CeCILE. Frames of 20 different videos were labeled manually for the dataset. Different time intervals were chosen between the frames. If the time interval was random, only frames were taken where cell divisions took place to increase the occurrence of cells in the class div. As containers, either LCIs with glass bottom (glass) or scintillator bottom (scinti), dishes with glass bottom or 6-wells were used. The abbreviation Irr. stands for the type of irradiation and Im. stands for the imaging mode that was used.

Test and Tracking Video Dataset

	# Frames	Intervals	Cell line	# Liv	# Round	# Div	# Dead	Total	Container	Coating	Insert	Irr.	Dose	Im.
1	457	5 min	CHO-K1	24042	2447	106	5430	32025	dish/glass	no	no	X-rays	3 Gy	1
2	341	5 min	CHO-K1	23574	1159	117	2704	27554	dish/glass	no	no	X-rays	0 Gy	1

Table 3.2: Two test videos. The cells of the first videos were irradiated and in the second video they were sham irradiated. The groundtruth labeling of these two videos contains also the tracking IDs. The abbreviation Irr. in the first row stands for the type of irradiation and Im. stands for the imaging mode that was used.

3.5 Classification

(**)

In the first step of developing an algorithm for object detection, it was tested whether the classes could be well classified by a CNN. Therefore, a simple CNN based on LeNet-5 [181] was trained and tested on the dataset instead of a more advanced CNN like ResNet-101, because of the much shorter training time. In this CNN, each of the convolutional layers was followed by a max-pooling layer to minimize the number of learnable parameters. The first convolutional layer applied 32 filters to the images of the dataset, the second convolutional layer had 64 filters and the last two convolutional layers applied 96 filters each. Two fully connected layers with 512 and 4 connections followed the convolutional layers. As activation function ReLU (Rectified Linear Unit) was chosen, which is commonly used in CNNs. ReLU was applied in all convolutional layers and the first fully connected layer. In the second fully connected layer, a softmax function was implemented as activation. The network had a total number of 4,143,236 trainable parameters. This algorithm is python based and was implemented using the TensorFlow 1.12.0 backend. The CNN was trained on the classification dataset. For this dataset, the labeled boxes of a part of the dataset of CeCILE were cropped to obtain images containing only one object. The classification was tested at an early stage of this thesis and was only performed on the part of the dataset that was created at that time. The dataset has been extended since then. The classification dataset was created from the images of the videos 1-13 of the dataset of CeCILE, as listed in Table 3.1. To tackle class imbalances, the images of the classes div and round were upsampled via data augmentation methods. In the class round, every second image was vertically flipped and for the class div the augmentation methods enhance brightness, contrast, and sharpness, lower brightness and contrast were applied on the images and on vertically flipped images to increase the number of images in this class by a factor of 11. During training time, the augmentation methods random rotations, random zoom, random width shift, random horizontal shift and horizontal flip were used for all classes to make the training more robust and to improve the generalization. The augmentation only adds minor changes to the images, which do not affect the appearance of the cells themselves, but for the algorithm, it results in completely new images. A further advantage of augmentation is that these changes make the algorithm more robust and prevent overfitting. However, if too many augmentation methods are applied the algorithm tends to overfit and will then not be able to generalize well for analyzing completely new images. Hence, careful evaluation of the classification was performed at each step of the training. For training and testing the CNN, the classification dataset was randomly split into 75 % for training and 25 % for testing.

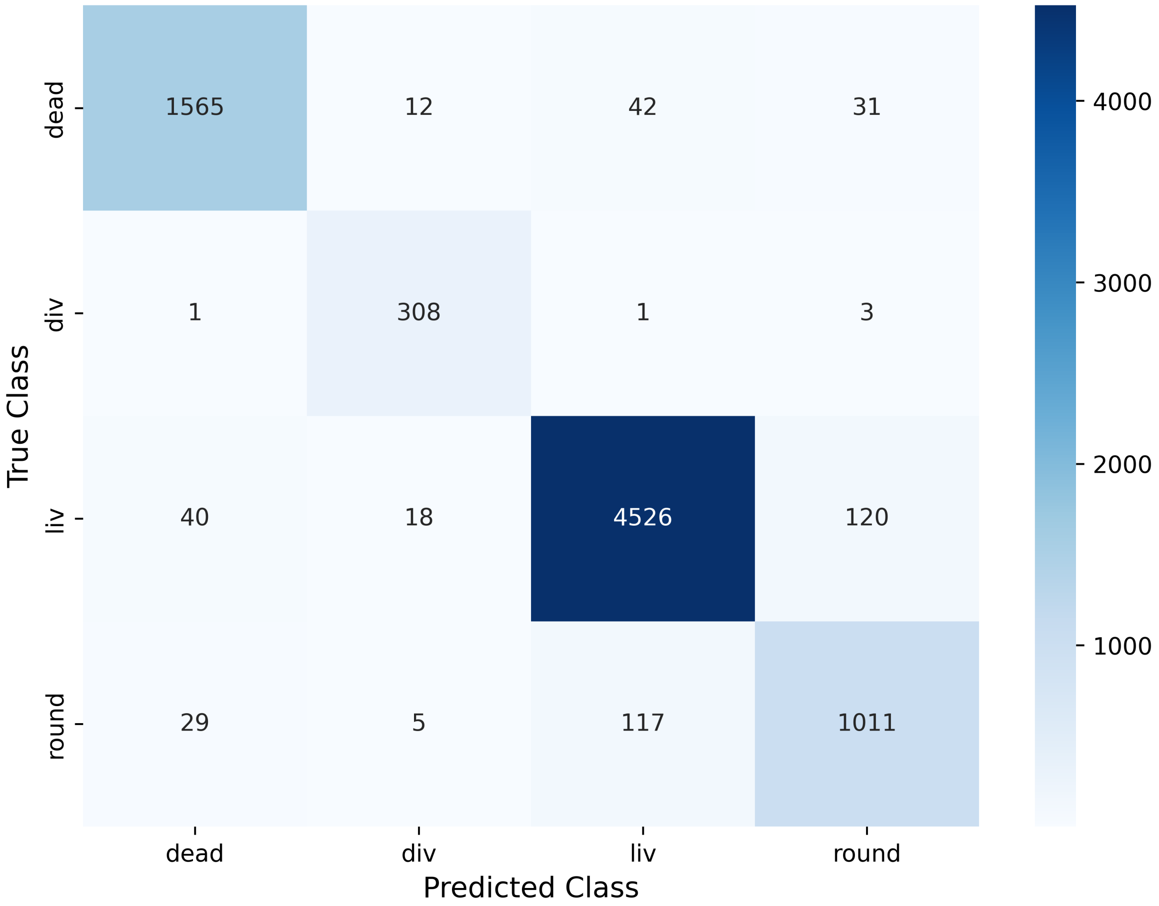

Figure 3.21: The confusion matrix of the classification. The true class corresponds to the groundtruth classes that were manually labeled and the predicted class corresponds to the predictions made by the CNN after training. The confusion matrix was created on the predictions on the test dataset. This figure was adapted with permission from [143].

One important evaluation step is to analyze the confusion matrix on the classification test dataset (containing 25 % of the classification dataset) depicted in Figure 3.21. The confusion matrix shows the correlation between the manually labeled classes (True Class) of the dataset and the prediction from the algorithm (Predicted Class) for all cells. The better the algorithm, the more entries are on the main diagonal. Figure 3.21 shows that in our case most of the entries are on the main diagonal and therefore most of the images of the test dataset were classified correctly. Overall, 5.5 % of the cells were classified in the wrong class. 5.1 % of the dead cells, 1.6 % of the dividing cells, 3.8 % of the living cells, and 13.0 % of the round cells were predicted wrong. The largest error of the algorithm is between the classes round and liv, where 237 cells were predicted wrong. This corresponds to 5.0 % for the class liv and 20.4 % for the class round.

Table 3.3 lists the precision, the recall, and the F1-score of all classes, as described in Section 3.2.2. The precision and recall scores for all classes lay between 0.87 and 0.98. The classes dead, liv and round have similar precision and recall scores, while the recall score of the class div (0.98) is higher than its precision score (0.90). The class liv shows the highest score with an F1-score of 0.96 followed by dead and div with F1-scores of 0.95 and 0.94, whereas the class round has the smallest F1-score of 0.87. The mean F1-score of all classes is 0.93, which is a very good value and proofs the successful classification using the four classes and acquired dataset.

	Precision	**Recall**	**F1-score**
dead	0.96	0.95	0.95
div	0.90	0.98	0.94
liv	0.97	0.96	0.96
round	0.87	0.87	0.87
mean	0.93	0.94	0.93

Table 3.3: The results of precision, recall and F1-score of the classification of the CNN into the four classes dead, div, liv, and round. This table was taken from [143] with permission.

3.6 Detection of cells in live-cell phase-contrast videos

As the cell classification was tested successfully, an object detection algorithm was set up. The faster RCNN was chosen as an object detection model, which is described in detail in Section 3.3.2. The faster RCNN is implemeted in the TensorFlow object detection API and therefore easy to use and to adapt to custom datasets. Furthermore, this model is very accurate in detecting many small objects on a crowded image [197] and therefore it is a good choice for detecting cells on videos. To save computational time, transfer learning with a pretrained ResNet-101 model trained on the COCO dataset [198] from the TensorFlow 2 Model Detection Zoo was used. Transfer learning provides the basic low level features. For identification of the cell specific appearance, classification, and location, CeCILE was trained and finetuned on CeCILE's dataset. Therefore, CeCILE's dataset was split randomly into a training datatset and a validation dataset with 75 % of images in the training dataset and 25 % in the validation dataset. Training was performed on the training dataset, and for fine-tuning, the object detector's predictions were evaluated during training on the validation dataset. This way, the training process could be inspected and the parameters finetuned accordingly. The data preparation and training pipeline for faster RCNN is implemented as described by Rosebrock [199] and on official website of the TensorFlow 2 object detection API [189] with modifications due to the input data. The training setup was configured by Julian Reindl and me. The training and fine-tuning was performed by Lucas Villaverde Zimmermann during his master thesis under my supervision and by me. I created the code for object detection predictions in videos and the evaluation.

3.6.1 Training and finetuning

In the training process, the following parameters were finetuned: number of epochs, learning rate, aspect ratios and scales of the anchor boxes, data augmentation, non-maximum suppression, localization loss weight, classification loss weight and objectness loss weight. The number of epochs describes how often a model is trained on a subset (a batch) of the dataset. In this thesis, a batch size of 1 was chosen, as this was the maximal batch size that was possible to train on a NVIDIA GeForce RTX 2080 super graphics card (NVIDIA, USA) with 8 GB VRAM (video random access memory). For training, a number of 100.000 epochs was chosen, as after 100.000 epochs no more success in training was achieved.

Learning rate

As a learning rate a cosine decay learning rate schedule was used. For large models, it is common to change the learning rate during training. For example, a higher learning rate is chosen in the beginning of the training process that decreases with the ongoing training. In the beginning, the model learns the coarse features and the accuracy improves fast. Therefore, the learning steps can be bigger. With ongoing training, the model learns more detailed and complexer features. As the learning progress is decreased here, a smaller learning rate helps the model not to miss any good training progresses. The cosine decay learning rate as described in Loshchilov and Hutter [200] provides a schedule of learning rate changes and was used for CeCILE. It starts with a warm-up phase. For this phase, the following parameters were adapted during fine-tuning: the warm-up steps, the warm-up learning rate, the learning rate base and the number of steps. The warm-up steps were set to 3000 that is 3 % of the total number of epochs. One step equals here to one epoch. The warm-up learning rate was set to 0.001. In this warm-up phase, the training starts at the warm-up learning rate and with each training step the learning rate is linearly increased so that after the warm-up steps the learning rate base is reached. If for warm-up learning rate and learning rate base the same value is chosen, the learning rate stays constant for the warm-up steps. This was the case here, as a learning rate base of 0.001 was chosen for CeCILE. After that, the cosine decay phase begins. It starts at the learning rate base and decreases in a cosine decay so that after 100.000 epochs a learning rate of zero is reached. A warm-up phase that starts with a small learning rate and increases during the warm-up steps can be useful for the beginning of a training. At the beginning of a training, the weights in the network need to be initialized. A warm-up phase can help here to prevent the training from going into the wrong direction by starting with small learning rates. As for CeCILE a pretrained network was used, the weights were already well trained for detecting different shapes. The network only needed to learn which of the four classes had which shapes. Therefore, to start here with a constant high learning rate for the first 3000 steps and continue then the training with cosine decayed learning rates turned out to be the best choice for CeCILE.

Aspect ratio

The aspect ratios of an object detector should describe well the shape of most of the bounding boxes in a dataset. The aspect ratios 0.5, 1.0 and 2.0 described the dataset used here very well. The scales 0.25, 0.5, 1.0 and 2.0 were chosen, where 1.0 equals an area of 256 x 256 pixel. For data-augmentation the best results were achieved by applying the following methods: random horizontal flip, random adjust brightness, random adjust contrast and random square crop by scale. The random horizontal flip flips images horizontally during training with a probability of 50 %. In random adjust brightness, the brightness of an image is changed by adding a random delta between 0 and 0.2 to the pixel values of the image. Random adjust contrast changes the pixel values by adding random values between 0 and 1.25 to the pixel values of the image or subtracting random values between 0 and 0.8 from the pixel values in the image. Random square crop by scale crops randomly a square out of the image with a scale between 0.6 and 1.3 with respect to the maximal spatial dimension of the image.

Non-maximum suppression

The non-maximum suppression sorts out all boxes that accidentally represent the same image. This sorting occurs two times in faster RCNN. In the first stage of the detector it is implemented after the region proposal generation and in the second stage during the post-processing of the bounding boxes. The first stage IoU-threshold was set to 0.3 and the second stage IoU-threshold was set to 0.35 that turned out to provide the best results. The localization loss weight can also be adjusted in the first and in the second stage.

Loss weights

The objectness loss weight is adjusted in the first stage, where the algorithm learns to differ between objects and background and the classification loss weight in the second stage, where the classification is learned. The loss weights determine the extent to which the algorithm should focus on that task during training. For CeCILE, the best choices were a localization loss weight of 3 and an objectness loss weight of 1.5 in the first stage, and a localization loss weight of 2 and a classification loss weight of 1 in the second stage. These parameters were manually finetuned by carefully observing the training progress on the validation dataset during training. The finetuning was done by Lucas Villaverde Zimmermann in his master thesis under my supervision. The detailed process of finetuning can be found in his thesis [201].

3.6.2 The performance of the object detection

The performance of the object detection was tested on the two videos of the testing and tracking video dataset. The videos were fed into CeCILE's object detection and the predictions were compared to a groundtruth. To create the groundtruth, I corrected the predicted videos manually by using the software VIA image annotator [196]. In the performance test, either the localization of the bounding boxes as also the classfication was tested. The localization was tested by determining the number of true positives, false negatives and false positives and calculating the precision, recall and the F1-score as described in Section 3.2.2. True positives are all boxes that overlap with a groundtruth box with an IoU > 0.5. False positives are all boxes that are falsely predicted by the object detector but have no match in the groundtruth. This occurs for example when two boxes are predicted for one object. The false negatives are objects that are not predicted by CeCILE's object detection. The accuracy of localizing objects in a video are shown for a video of irradiated cells in Figure 3.22 and for a video of unirradiated (sham) cells in Figure 3.23. In the irradiated cell video, the object detector achieved in almost all frames a higher recall than precision. The recall was between 0.82 and 1.0 and increased more often to 1.0 in the first 200 frames, while after 200 frames the recall was decreased to around 0.95. The precision was between 0.78 and 0.98 and followed the course of the recall. The object detector achieved a mean precision over all frames of 0.88, a mean recall of 0.93 and a mean F1-score of 0.90 in the video of irradiated cells.

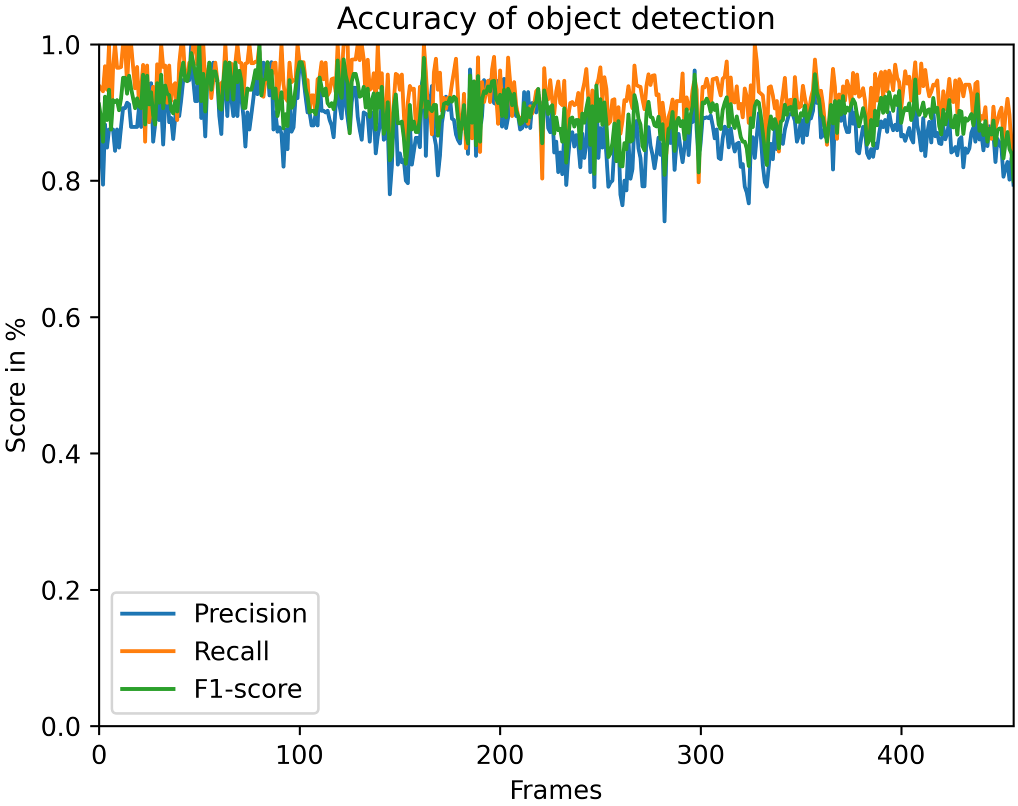

Figure 3.22: The accuracy of object detection of cells in a video of irradiated cells. The precision is shown in blue, the recall in orange and the F1-score in green. These scores were evaluated for 456 frames that correspond to a time range of 38 h.

A better localization performance was achieved by the object detector in the unirradiated video. Here, the recall was between 0.95 and 1.0 and the precision was between 0.80 and 0.92. While the recall stayed at a high level throughout the video, the precision was slightly decreased in the first frames, frame 0 to frame 20, between frame 140 and frame 160 and from frame 180 to frame 340. The mean recall over all frames was 0.96, the mean precision was 0.88 and the mean F1-score was 0.92. Therefore, the precision achieved was the same as in the video of irradiated cells, while a higher recall and F1-score was achieved for the video of unirradiated cells.

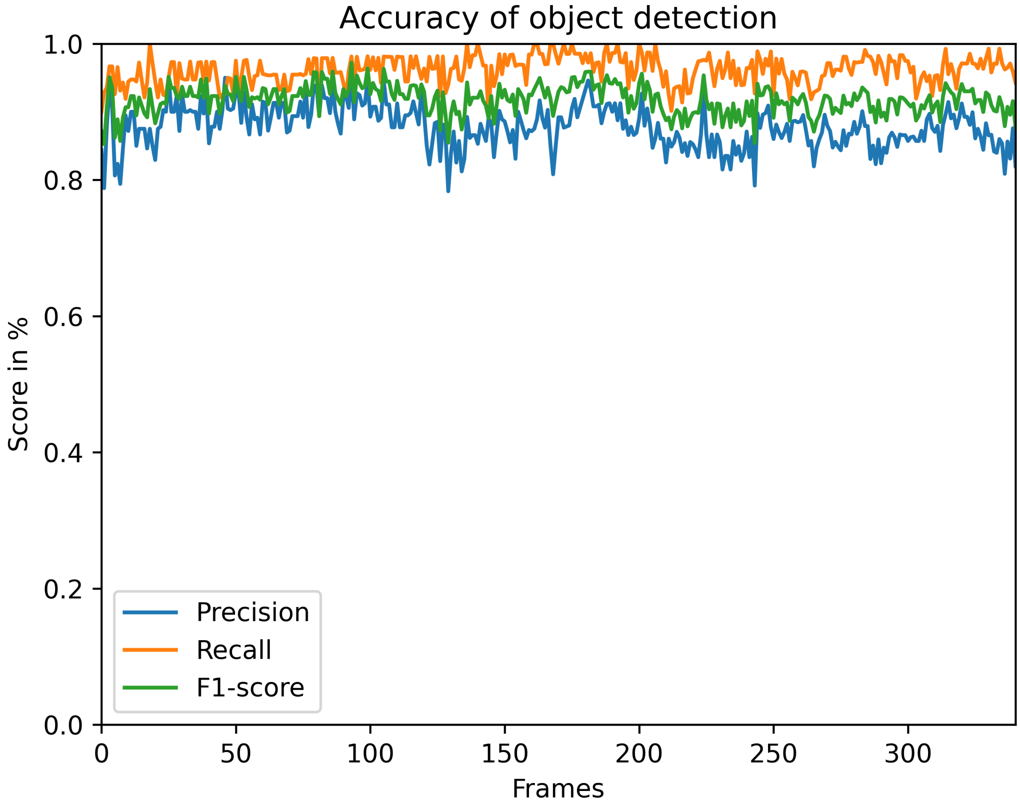

Figure 3.23: The accuracy of object detection of cells in a video of unirradiated (sham) cells. The precision is indicated by a blue line, the recall by a orange line and the F1-score by a green line. These scores were evaluated for 340 frames that correspond to a time range of 28.3 h.

For scoring the classification, the mAP score was used as described in Section 3.3.1. The mAP scores for each frame in the two videos are shown in Figure 3.24 for the video of irradiated cells and in Figure 3.25 for the video of unirradiated cells. The mAP score was calculated for each class individually with an IoU threshold of 0.5 (mAP liv, mAP round, mAP div and mAP dead). If a class did not appear in the predictions and the groundtruth, a mAP of 0 was assigned to this class. mAP was defined as the mean over all classes that were present on each frame. In both videos, the object detector achieved the highest mAP scores for the living cell class, the second highest for the dead cell class, followed by the round cell class and the lowest mAP scores were achieved for the cell division class. In the irradiated video, the mAP liv was at the beginning the lowest with approx. 0.90 and increased after 50 frames towards the end to approx. 0.95. The mean mAP liv was 0.95. The mAP dead was in the beginning of the video the highest with values around 0.85 and was slightly lower between frame 300 and frame 456. The mean mAP dead was 0.82. A mAP round of approx. 0.7 was achieved in most frames till frame 150. After that, several frames occurred with a mAP of 0 till frame 240. The mAP round was then increased again to starting level till the end except from four frames where the mAP was 0. The mean mAP round was 0.72. Cell divisions did not occur in most of the frames, therefore the detector found only few cell divisions. The mean mAP div was 0.5.

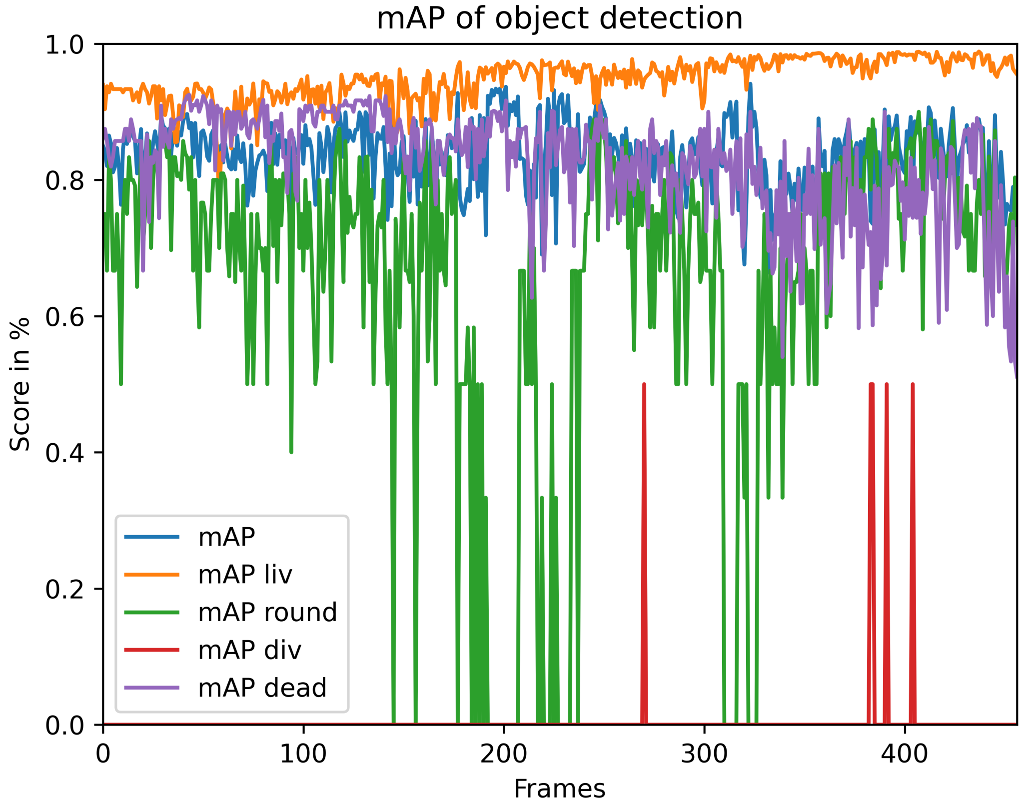

Figure 3.24: The mAP scores of the video of irradiated cells. The mAP score for living cells is shown in orange, for round cells in green, for dead cells in violet and for dividing cells in red. The mean over all classes is indicated in blue.

The object detector achieved better results for mAP liv in the video of unirradiated cells than in the video of irradiated cells. The mAP liv started at 0.94 and increased towards the end to a mAP of 0.99. Furthermore, the mAP liv had less fluctuations in the unirradiated video than in the irradiated video. The mean mAP liv was 0.97. The mAP dead and the mAP round were decreased in the video of unirradiated cells compared to the video of irradiated cells. The mAP dead remained at a constant level throughout the video of unirradiated cells, but with high fluctuations between 0.55 and 0.98, resulting in a mean of 0.69. The mAP round was often zero between frame 30 and frame 240 and had a high variability between 0 and 0.75 in this range. After 240 frames, the mAP round increased to values between 0.5 and 0.88. The mean mAP round was 0.60. The mAP div was also here rarely higher than 0. The mean mAP div was 0.5. The mean mAP over all classes was 0.78.

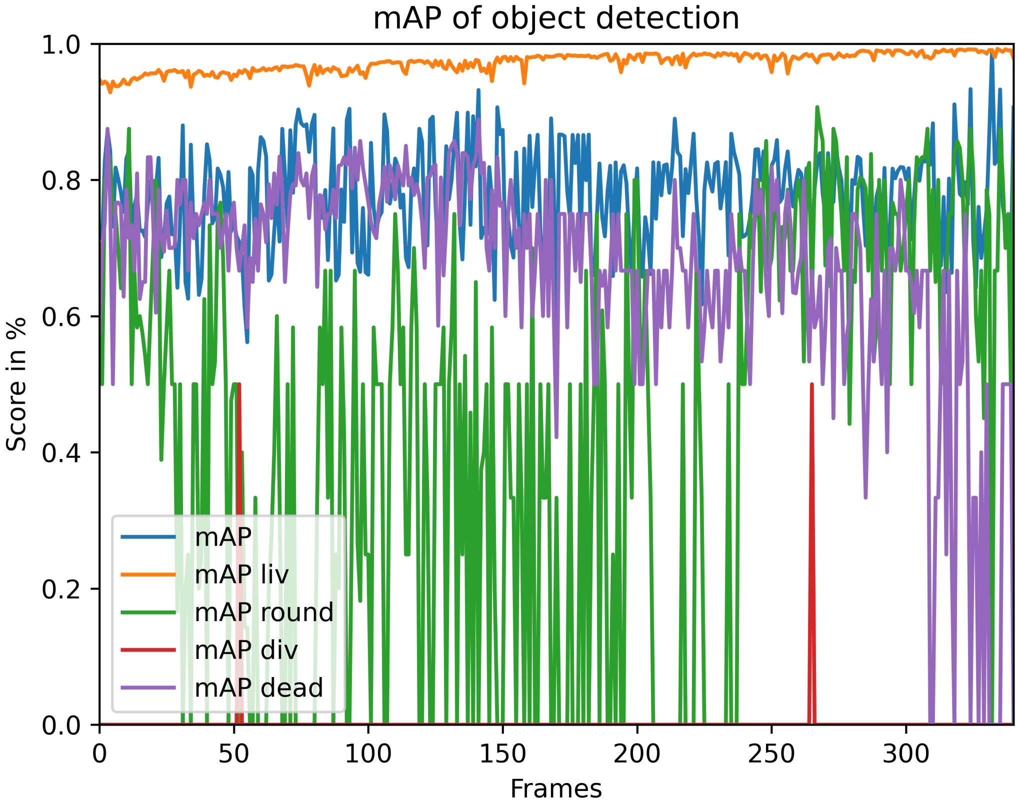

Figure 3.25: The mAP scores of the video of unirradiated (sham) cells. The mAP score for living cells is shown in orange, for round cells in green, for dead cells in violet and for dividing cells in red. The mean over all classes is indicated in blue.

3.7 Cell tracking

The obtained bounding boxes from the detection can now be forwarded to a tracking algorithm. By implementing a tracking algorithm that uses the bounding boxes received from the object detection, CeCILE will be able to follow each cell throughout the whole video. The tracking algorithm assigns to every bounding box in the first frame of a video an unique ID. In the next frame, the tracking algorithm matches the bounding boxes to the bounding boxes of the previous frame. If a matched bounding box is found it receives the same ID as its matching partner. If there is a bounding box in the current frame that has no matching partner in the previous frame, it receives its own unique ID. This matching process is repeated for all frames of the video.

To find matched bounding boxes, several criteria can be applied. One possible criterion is the location of the boxes. In this case, boxes are matched that have the shortest distance to each other. This can be used when objects do not move long distances between frames. In cell videos with a frame to frame time interval of 5 min, cells hardly move. Therefore, this criterion is well suited. Also the appearance of the objects can be taken into account for matching. Here, the morphology, shape, size and brightness can be used to find matching objects. This criterion can be applied when objects do not change their appearance in the video. However, for cells this is typically not the case. Cells change their appearance several times during a video. For instance, in order to find nutrients, they change their shape by reaching out in different directions. Furthermore, they strongly change their morphology during the cell cycle when they transit from the living state into the round state, into the cell division state, again into the round state and the living state (cf. Figure 3.19). Therefore, this criterion cannot be used as a major criterion for tracking. Another example for a tracking criterion is to assume that objects move towards a certain destination and move there on the shortest path. Therefore, matching bounding boxes are only expected along this path between previous location and destination. This criterion can be applied for all objects that show such directional movements. Cells can show such a directional movement in special experimental setups, for example like wound healing assays or chemotactic assays where the cells are encouraged to move into a certain direction. In cell culture applications as described in this chapter, where cells are sparsely seeded in a container surrounded by a nutrient solution, cells show random movements, therefore such a criterion that uses directional movements is not suitable.

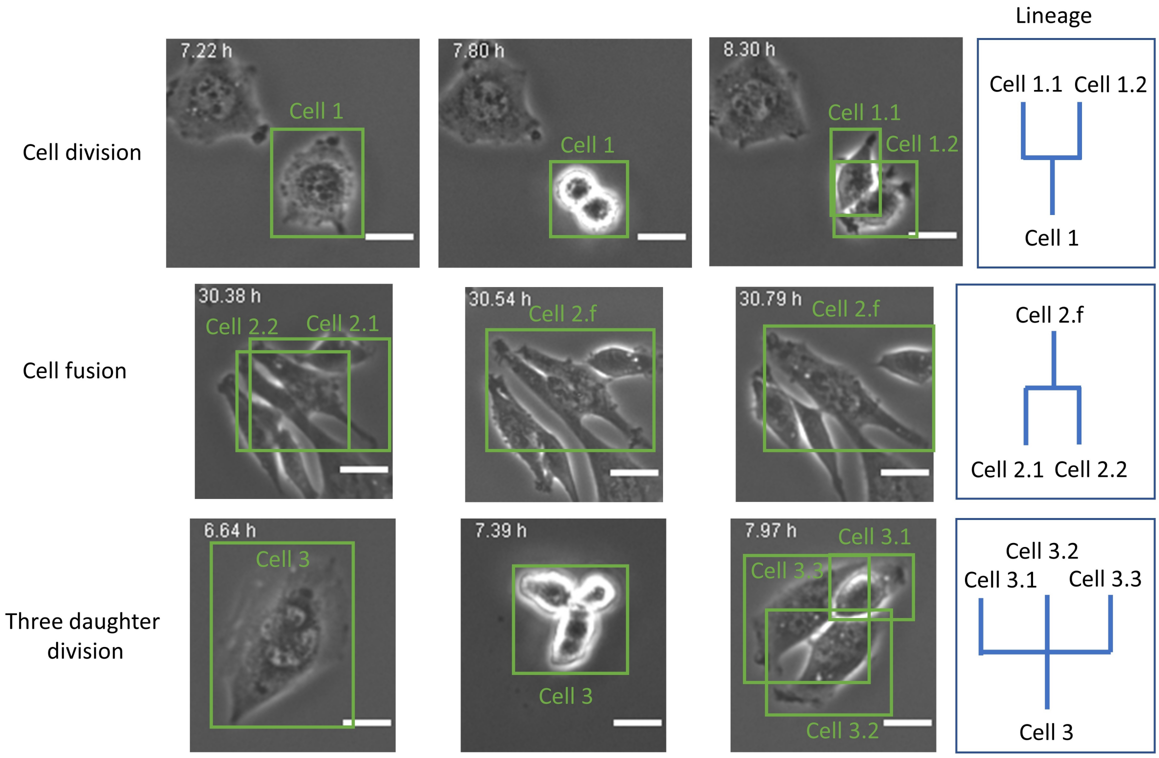

Figure 3.26: The tracking annotation for cell division, cell fusion and three daughter division. In the first four columns, the different scenes are presented on phase-contrast images along with the correct annotations. The scale bars indicate a distance of 20 µm. In the last column, the corresponding lineages are shown, which are read from bottom to top.

A special feature of the tracking of cells is the cell division. Here, a cell divides into two daughter cells which in terms of tracking means that one tracking path splits into two subsequent paths. In this thesis, I introduced a special notation to unambiguously assign daughter, mother cells and the respective generation. In Figure 3.26, the notation is shown. In the first three columns, the correct annotation of three different scenes are presented on phase-contrast images. In the last column, the corresponding lineages are shown. In a normal cell division (cf. Figure 3.26 in the upper row), the mother cell that was assigned to the unique ID 1, divides into two daughter cells that receive the IDs 1.1 and 1.2. Especially in irradiated cell populations it can come to either fusion or division into more than one daughter cell, as discussed in Section 1.3.2. In the case of fusion, two daughter cells fuse some time after cell division into one cell, this is notated as follows: the cells with the IDs 2.1 and 2.2 become one cell with ID 2.f (cf. Figure 3.26 in the middle row). In case of multi daughter division, just more daughter IDs are assigned. For example in a three daughter division, the daughter cells received the IDs 3.1, 3.2 and 3.3 (cf. Figure 3.26 in the lower row).

3.7.1 Centroid tracking

To track the cells based on their location and the bounding boxes received from the detection, I implemented the centroid tracker developed by Adrian Rosebrock [202] into CeCILE and adapted it to meet the specific needs of cell tracking. This object tracker uses the OpenCV library in Python. A detailed description and the original code of Rosebrocks centroid tracker can be found on his website: `https://pyimagesearch.com/2018/07/23/simple-object-tracking-with-opencv/`. In the first step of the centroid tracker, the centroids of each bounding box in a frame are computed by calculating the center of the bounding box based on the box coordinates

$$\text{centroidX} = \frac{\text{startX} + \text{endX}}{2} \tag{3.16}$$

$$\text{centroidY} = \frac{\text{startY} + \text{endY}}{2}, \tag{3.17}$$

where centroidX and centroidY are the coordinates of the center of a bounding box in x- and y-direction, startX and startY are the x- and y-coordinates of the upper left corner of a bounding box and endX and endY corresponds to the x- and y-coordinates of the lower right corner of a bounding box. In the first frame of the video, all bounding boxes are assigned to an unique ID by the function *register*. This function stores the IDs as keys and the bounding box coordinates as values in the dictionary *objects*. In the original version of the centroid tracker, the tracker stores here the centroid coordinates, but as I wanted to use the whole bounding box in the following part, I adapted the code. In every subsequent frame n, the bounding boxes are matched to the bounding boxes of the previous frame $n-1$ by using the Euclidean distance. Here, the Euclidean distances between the centroids of each pair of existing bounding boxes in frame n and frame $n-1$ are calculated and stored in a matrix, where the columns corresponds to the bounding boxes of frame $n-1$ and the rows to the bounding boxes of frame n. Now, the algorithm searches in every row of the matrix for the smallest value. These values are ordered in ascending order while storing also the position of each value in the matrix. Beginning with the first and smallest value, the corresponding bounding boxes in frame n and frame $n-1$ are derived based on the position in the matrix.

It can be assumed that these two bounding boxes contain the same object, as they have the closest distance to each other. Therefore, the ID of the bounding box in frame $n-1$ is assigned to the bounding box in frame n. This step is repeated for all smallest values of all rows. To prevent a double assignment of bounding boxes of both frames, the indexes of the used bounding boxes in frame n and frame $n-1$ are stored. Before every new assignment of an ID, it is checked whether the bounding box of frame $n-1$ was already matched to a bounding box of frame n or vice versa. For every matching of bounding boxes, the dictionary *objects* is updated assigning to the key ID, which was found to be the matching ID, the value tuple that contains the coordinates of the matched bounding box of frame n. Finally, it is checked if there are any bounding boxes in frame n or $n-1$ that were not matched to a box of another frame. If a bounding box of frame n has no matching partner, the function *register* is executed. In case of a missing matching partner for a bounding box of frame $n-1$, the function *deregister* is executed. This function deletes the ID and the coordinates of this bounding box from the dictionary *objects*. This procedure is repeated for every frame of the video.

The algorithm provides two extra features that can be chosen. First, when applying the tracker to a video the variable *maxDisappeared* can be assigned to an integer number ≥ 0. When assigning this variable with a value > 0, objects of frame $n-1$ are not deleted if no matching partner was found and are forwarded to the next frame. To keep track how often this object was missing in the consecutive frames, the dictionary *disappeared* is implemented that stores each ID as a key and as values the number 0. In the case of no matching partner for a bounding box in frame $n-1$, the value to the corresponding ID is increased by 1 in the dictionary *disappeared*. If this value is greater than the value of the variable *maxDisappeared*, the object is deleted from the dictionary *objects* and from the dictionary *disappeared*. If in the consecutive frames this bounding box finds a matching partner before it is deleted, the value of the ID is set to 0 in the dictionary *disappeared*. This allows the tracker to track objects even when a bounding box is missing in one frame of the video. In this thesis, a value of 1 was chosen for the variable *maxDisappeared*, as this was the best compromise of being able to recover from missing bounding boxes in a frame and prevent bounding boxes to interfere to much with each other in crowded areas. In crowded areas, the additionally forwarded bounding boxes for matching can lead to an incorrect matching with a nearby bounding box. Therefore, a higher value for the variable *maxDisappeared* would lead to more wrong ID assignments.

Second, I implemented the possibility to match not only the center of bounding boxes but also the box overlap. This option can be used by changing the variable *weight_iou* to any number > 0 and ≤ 1. If *weight_iou* equals 0, the box overlap is not taken into account during the matching. In addition to the distance matrix, also an IoU matrix is created that contains the IoU overlaps as defined in Section 3.3.1 of every combination of bounding boxes from frame n and frame $n-1$. Both matrices, the distance matrix and the IoU matrix, are combined by the following formula:

$$M_{\text{matching}} = M_{\text{dist}} + weight\_iou - weight\_iou \cdot M_{\text{IoU}}, \tag{3.18}$$

where M_{matching} is the matrix on which the matching is based, M_{dist} is the distance matrix and M_{IoU} is the IoU matrix. With this method, the entries in matrix M_{matching} are all uniformly increased by adding *weight_iou* to the distance matrix. This addition does not change the outcome of the matching process, as all entries have been incremented in the same way. If two bounding boxes overlap, the term $weight\_iou \cdot M_{\text{IoU,ij}} > 0$, where $M_{\text{IoU,ij}}$ is the corresponding entry of the IoU matrix, and the corresponding entry of M_{matching} is decreased by this term. This method favors the matching of bounding boxes with a high overlap and results in a robuster tracking. Especially, when two bounding boxes in a frame have a similar center, it often comes to an identity swap. Identity swap means thereby that two objects are incorrectly assigned with the ID of the other box. Using not only the center coordinates of the bounding boxes but the whole bounding box for tracking, improves the outcome of the tracking.

The centroid tracker is well suited to track the cells in between cell divisions, but it is not able to track cells across a cell division and split the tracking path into two paths. For this event, a more advanced tracking method is necessary and it is planned to implement such a method in future. However, the centroid tracker already shows what a tracking based on the location of the center of the bounding boxes and the box overlap is a well suited approach for cell tracking. In the next section, the performance of this tracking method is scored in all tracks in between cell divisions.

3.7.2 Tracking accuracy

To score the accuracy of the tracking, the centroid tracker was applied on the bounding boxes of the two test videos (cf. Table 3.2) that were derived from the object detection of CeCILE and were corrected manually by me. The IDs that were assigned to each bounding box by the tracker, were compared to the IDs of a groundtruth, which was created by be. The aim was to score the consistency of a track in between the cell divisions while ignoring the specific ID changes across cell divisions. Therefore, the IDs of each object of a frame $n > 0$ was compared to the ID of the very same object in the previous frame $n - 1$ in the tracks created by the centroid tracker (prediction) and the tracks created by me (groundtruth). If the ID of an object did not change in the groundtruth and the prediction between frame n and frame $n - 1$, the variable *right_ID*, which was initially 0, was increased by 1. If the ID of an object changes in the prediction, but not in the groundtruth, the variable *wrong_ID*, which was initially 0, was increased by 1. This was performed for all bounding boxes and frames in the video. Afterwards, the tracking accuracy t_{acc} was calculated by using the following formula

$$t_{\text{acc}} = \frac{right\_ID}{right\_ID + wrong\_ID}. \tag{3.19}$$

First, it was tested whether a better tracking accuracy can be achieved by using the implemented option of taken into account the box overlap in the matching process. The variable *weight_iou* was set to 0.1, 1 and 0 and with these settings the centroid tracker was applied to the first 100 frames of a test video (cf. Table 3.2 Video 2). With *weight_iou* = 0, a tracking accuracy of 99.25 % was achieved, with *weight_iou* = 0.1, a tracking accuracy of 99.32 % was achieved and with *weight_iou* = 1, the same tracking accuracy was achieved as for *weight_iou* = 0.1. Therefore, it can be concluded that the tracking accuracy could be improved by the implementation of the IoU into the matching process. It was also shown that every value > 0 and ≤ 1 for *weight_iou* gives the same tracking accuracy. In the distance matrix, all entries are given in the unit pixel (px). The bounding boxes were created based on the condition that pixels are discrete and therefore bounding boxes could not be created with a resolution < 1px. Therefore, the addition with a *weight_iou* between 0 and 1 does only interfere with the centroid based tracking, when the centroids of two neighboring bounding boxes are closer than one pixel. In this case, the box overlap is > 0, as the bounding boxes cover much more than one pixel (they cover typically around 8,000 px) and the matching is performed solely on the box overlap. Hence, the choice of *weight_iou* plays no role here as long as the value is > 0 and ≤ 1. In the following, *weight_iou* was set to 0.1.

Finally, the tracking accuracy was determined for both test videos (cf. Table 3.2), the irradiated one and the sham one for the first 456 frames and the first 340 frames, respectively. For the irradiated video, the centroid tracker achieved a tracking accuracy of 97.77 % and in the sham video 98.51 %. In total in the irradiated video, the tracking accuracy was determined from 31,120 ID assignments. 30,427 of the ID assignments were correct and 693 incorrect. In the sham video, there were in total 26,946 ID assignments scored. 26,544 ID assignments were correct and 402 incorrect. It can be concluded, that the centroid tracker was able to track almost all bounding boxes correctly. The tracking accuracy achieved in both videos was similar. Therefore, the centroid tracker is well suited for the tracking of irradiated and sham cells in phase-contrast videos.

3.7.3 Difficult scenes for CeCILE

As discussed in Section 3.6.2 and Section 3.7.2, CeCILE showed a good performance in object detection and tracking. However, there are some scenes in cell videos where CeCILE, but also the human annotator struggles when annotating and tracking the video frame by frame that lead to the decrease in performance in object detection and tracking. Object detectors like the faster RCNN, which was used in this thesis, detect the objects frame by frame without knowing what happens in the frames before and after. Therefore, the object detector can only use the information it receives from the frame it is currently working on. The centroid tracker uses only the information of the previous and the current frame to track the cells. Hence, also for tracking only a small part of all available information is used. In the following, there are typical scenes described, where CeCILE failed.

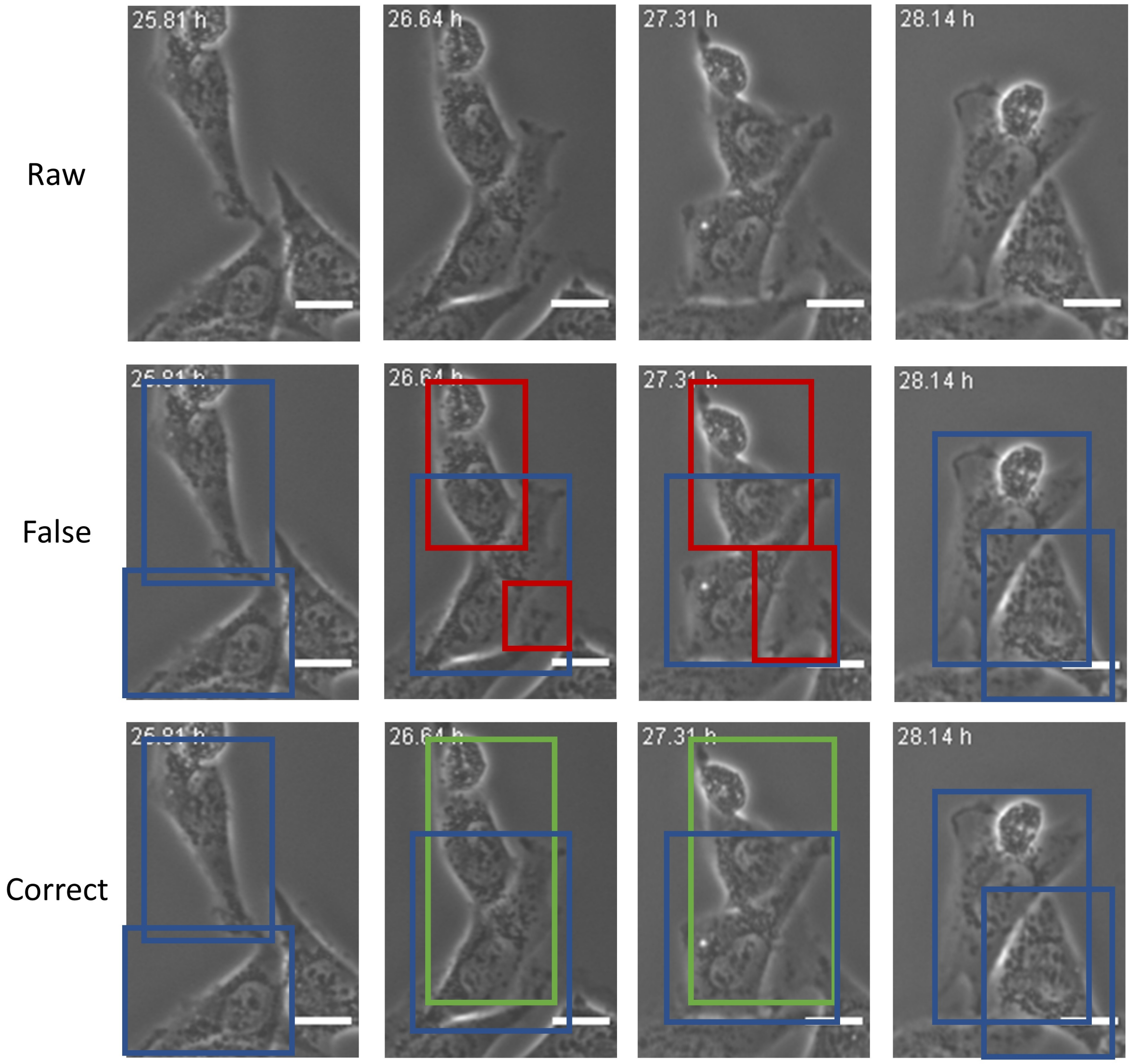

Figure 3.27: An example scene with two cells moving on top of each other. The first row shows the raw phase-contrast images of this scene. In the second and third rows, the two crossing cells are annotated with bounding boxes. In the second row, the scene is annotated as CeCILE would incorrectly predict this scene, and in the third row, the scene is presented as this scene would be correctly annotated. The red bounding boxes indicate incorrect annotations and the green bounding boxes indicate correct annotations. The scale bar indicates a distance of 20 µm.

The first scene is shown in Figure 3.27. This scene shows two cells moving on top of each other. For the object detector, this scene looks like there are three cells on the image, as the detector does not know that cells can move one over another and that the two parts of the lower cell that are visible on the image belong to the same cell. Therefore, it annotates the scene with three bounding boxes (cf. Figure 3.27 second row) instead of the correct two overlapping bounding boxes (cf. Figure 3.27 third row). In the dataset, such scenes are annotated as shown in Figure 3.27 in the third row. Nevertheless, CeCILEs object detector struggles here, as it has no 3D understanding of this scene that would be necessary to learn to deal with such a scene. This scene is also problematic for tracking, as the tracks of both cells cross each other and it can come easily to an identity swap.

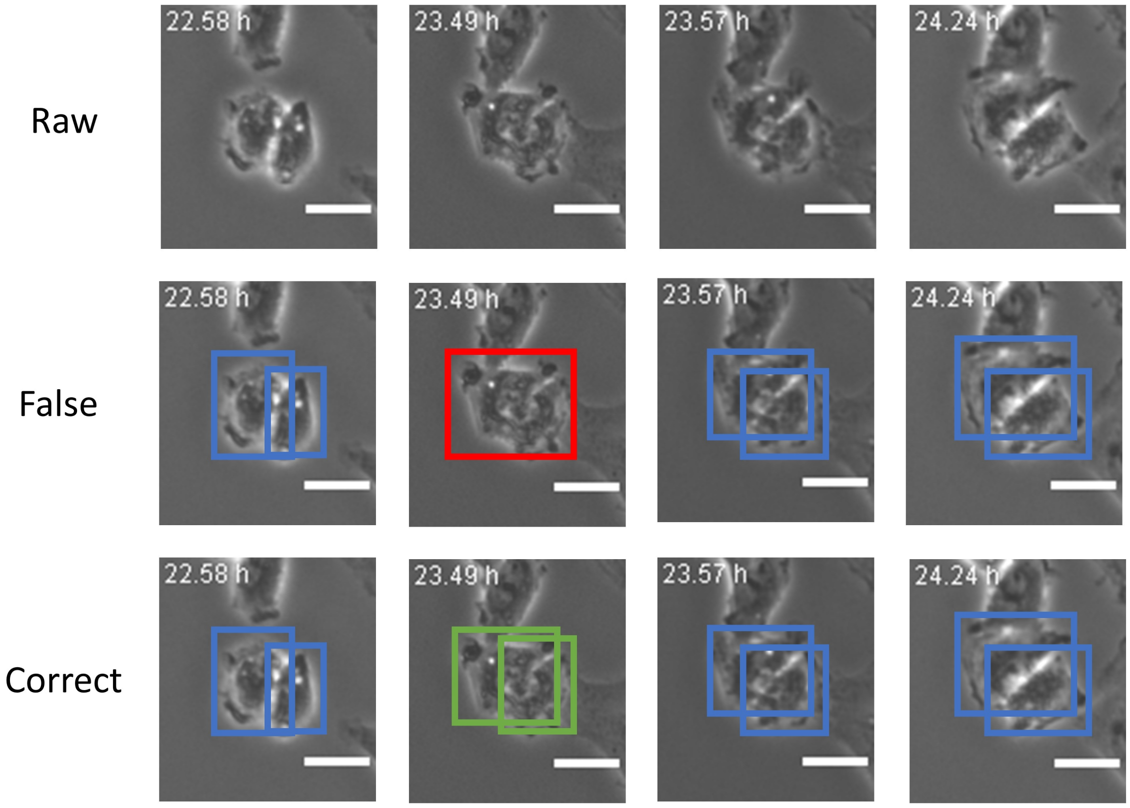

Figure 3.28: An example scene of two cells that are so close to each other that they appear as one cell. This Figure follows the same scheme as Figure 3.27. The scale bars indicate a distance of 20 µm.

Another difficult scene is shown in Figure 3.28. Here, two cells are so close to each other that they look like one cell. When looking at some previous and consecutive frames, one can easily see that here are two cells. The object detector predicts typically only one bounding box and misses the second cell, as shown in Figure 3.28 in the second row. This means for tracking that bounding boxes are missing and the track of the second cell ends too early. When after some time the cells can be well distinguished from each other, the second cell will be tracked with a new ID. As in the scene before, an identity swap can easily happen.

The last scene is only problematic for the classification. In Figure 3.29, a cell is shown that looks in the second image very similar to a dead cell and is therefore falsely classified as a dead cell. However, when checking the cell state on some previous and consecutive frames it becomes clear that this cell is not dead, but a vital cell and should be labeled in this scene as a living cell. There are also cells in the round cell state that look similar to dead cells or vice versa and cells in cell division state that look similar to round cells or dead cells or vice versa. The problem is that cells are not necessarily in one cell state, they can also be in between two states that makes them difficult to classify. In the dataset, the cell state of every cell was determined by also checking the cell states of this cell on the frames before and after. To enable CeCILE to deal with such scenes, it must be able to also use the information provided by previous and consecutive frames. This can be implemented for example as a preprocessing of the tracks to correct them for consistency in the future. For example, a cell cannot have a vital state after a dead state or a div state must be followed by the nearby occurrence of a new cell.

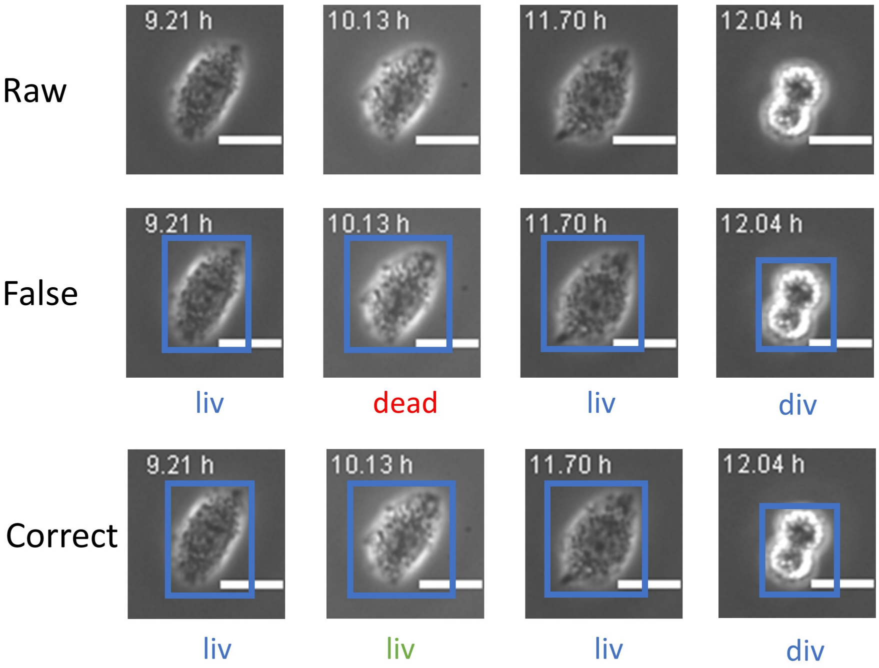

Figure 3.29: An example scene where a cell is misclassified. In the presented scene, a cell in cell state liv looks like a cell in cell state dead (second column). The corresponding annotated class labels of the cell in the bounding box are shown below each image in the second and third rows. In the second row, the cell is labeled as CeCILE would incorrectly annotate it, and in the third row, the correct classification is shown. The scale bars indicate a distance of 20 µm.

3.7.4 MCMC tracking

As the difficult scenes show, the tracking and detection of cells is a complex task. Hard coded approaches like the centroid tracker can achieve good results, but fail when it comes to such difficult scenes. Here, more complex algorithms are needed. One approach to improve the tracking and detection is a Markov Chain Monte Carlo (MCMC) algorithm. During this thesis, a cooperation was started with PD. Dr. Hai Huang of the Institute of Visual Computing at the Universität der Bundeswehr München to implement an MCMC algorithm in CeCILE. The Markov Chain is a mathematical model that represents a sequence of events where the outcome of each event depends on previous events. MCMC algorithms use such Markov Chains to perform probabilistic simulations. An object tracker based on an MCMC algorithm computes the probability that two bounding boxes represent the same object for any matching combination of bounding boxes of two consecutive frames. Here, the algorithm takes different features into account like the location of bounding boxes, the shape, the appearance, the box overlap etc. Also information of previous frames can be taken into account for matching the boxes. This can be especially used for tracking across cell divisions. In Figure 3.19, all possible transitions of the four cell states are shown. A cell that undergoes cell division transits from the state liv into the state round and then into the state div. When a cell leaves the state div, a new cell appears in close vicinity. The MCMC algorithm increases the probability for splitting one track into two tracks due to cell division, when a cell shows these transitions of cell states in a short period of time and expects the appearance of a new cell in close vicinity. MCMC algorithms can also correct missing bounding boxes in a track or misclassifications by checking the consistency of the tracks. Therefore, these class of algorithms are well suited to improve the performance of CeCILE and will be implemented in future.

3.8 Semi-automated workflow

As presented in the previous sections, CeCILE could show that the detection works very well on live-cell phase-contrast videos. The implemented tracking can accurately track the bounding boxes but is not able to track across cell divisions. For the evaluation of the cells' cell cycle, however, a 100 % accuracy is necessary, as missing bounding boxes or difficult scenes easily lead to an identity swap of the tracking labels or to a track ending too early. To reach a 100 % accuracy and to enable the tracking across cell divisions, manual correction steps were implemented in CeCILE's workflow. These manual correction steps allow the user to correct bounding boxes, box labels and box IDs after each step of the workflow. The workflow is presented in this section. The code for CeCILE is available on the online platform github a free platform for distributing and managing software projects and codes. CeCILE can be found on the following link: `https://github.com/jreindl/CeCILE`.

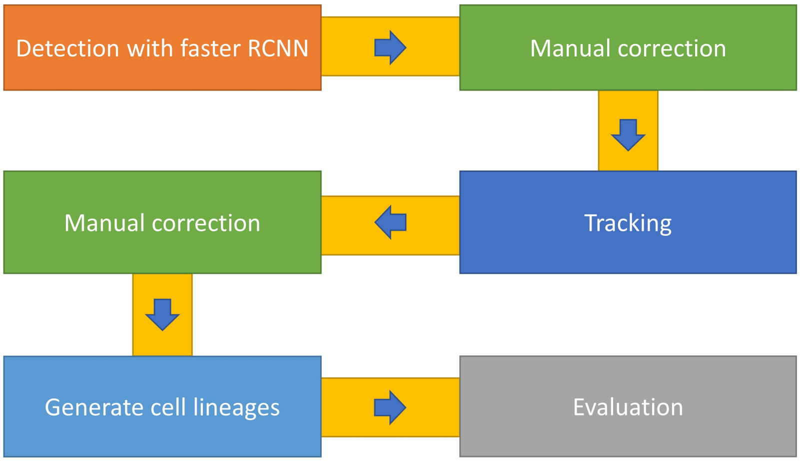

Figure 3.30: The semi-automated workflow of CeCILE.

The complete workflow of CeCILE is shown in Figure 3.30. First, the cells on a video are detected by using the faster RCNN object detection algorithm that can be executed with the python code predict_video_neuSR.py. This algorithm provides a json-file that stores the coordinates and labels of each bounding box of each frame of the video. The json-file is formatted so that it can be loaded and edited in the software VGG image annotator (VIA)

[196], which was also used for the creation of the dataset. Then the tracking is performed by center_track_from_json_final.py on the corrected json-file that assignes to each bounding box an ID. These IDs are also stored along with the bounding boxes in a json-file. Corrections of bounding boxes, labels and the ID can be performed using the software VIA. Wrong IDs can also be easily changed in CeCILE by executing the python-code Change_ID.py and following the instructions given by the code. This program takes as input the file path to the json-file, the ID, which should be changed, the new ID, and the start and end frames between which the ID should be changed. Then this program assigns a new ID in the desired frame range to each bounding box containing the wrong ID. After one ID is changed, the program will ask again for the next ID to change. This way several IDs can be changed easily. When the user does not want to change IDs anymore, a video and a json-file containing the correct IDs is outputted and the json-file can be forwarded to the cell lineage generation and evaluation by executing the code evaluation.py. Here, the minimum number of frames in which a cell should appear to be included into the cell lineage can be inputted. In this way, cells can be rejected that appear only for a short time in the video and then disappear again, for example, at the edges. Additionally, the number of frames for which the evaluation should be performed can be adjusted. The program outputs a cell lineage and three csv-files. The csv-file Number_of_cells_at_each_timepoint.csv contains a table with the number of cells per frame that are in the classes liv, round, div and dead. Furthermore, the number of vital cells, cells of the classes liv, round and div, per frame is given. The csv-file cell_cycle_duration.csv provides a table with all IDs that occurred and the duration between the first and the last occurrence of an ID. From these data, the duration of the cell cycles and the time points of the first cell division can be derived. The csv-file daughter_cells.csv gives to every mother cell ID the number of daughter cells and the csv-file max_cell_divisions.csv provides the maximum number of cell divisions for every mother cell ID.

3.9 Evaluation of an irradiation experiment with CeCILE

To test the semi-automatic workflow and to show the potential of CeCILE in a real application, an irradiation experiment was performed and evaluated. In this experiment, CHO cells (25,000 cells in 3 ml) were seeded into two µ-dishes and were incubated for 24 h. One µ-dish was irradiated with 3 Gy of x-rays (cf. 3.4.4) and the other one was sham irradiated. Both µ-dishes were placed in the live-cell-imaging setup of the microscope and recording of the videos with the microscope started immediately after irradiation. The recording was performed for 4 days. The obtained videos belong to the test and tracking video dataset of CeCILE (cf. Table 3.2 in Section 3.4), which were also used before to score the performance of CeCILE. As the cells are reproducing themselves, the recorded area is quickly completely filled with cells. For the sham cells, it took 67 h till full coverage of the growth area and for the irradiated cells, a full coverage was achieved 90 h after irradiation. In Figure 3.31, the frames at 0 h, 24 h, 48 h, 72 h and 96 h after irradiation of each video are shown. As can be seen, the cells in both videos started with the same number of 23 vital cells and show a reduced growth rate for the irradiated cells compared to the sham cells.

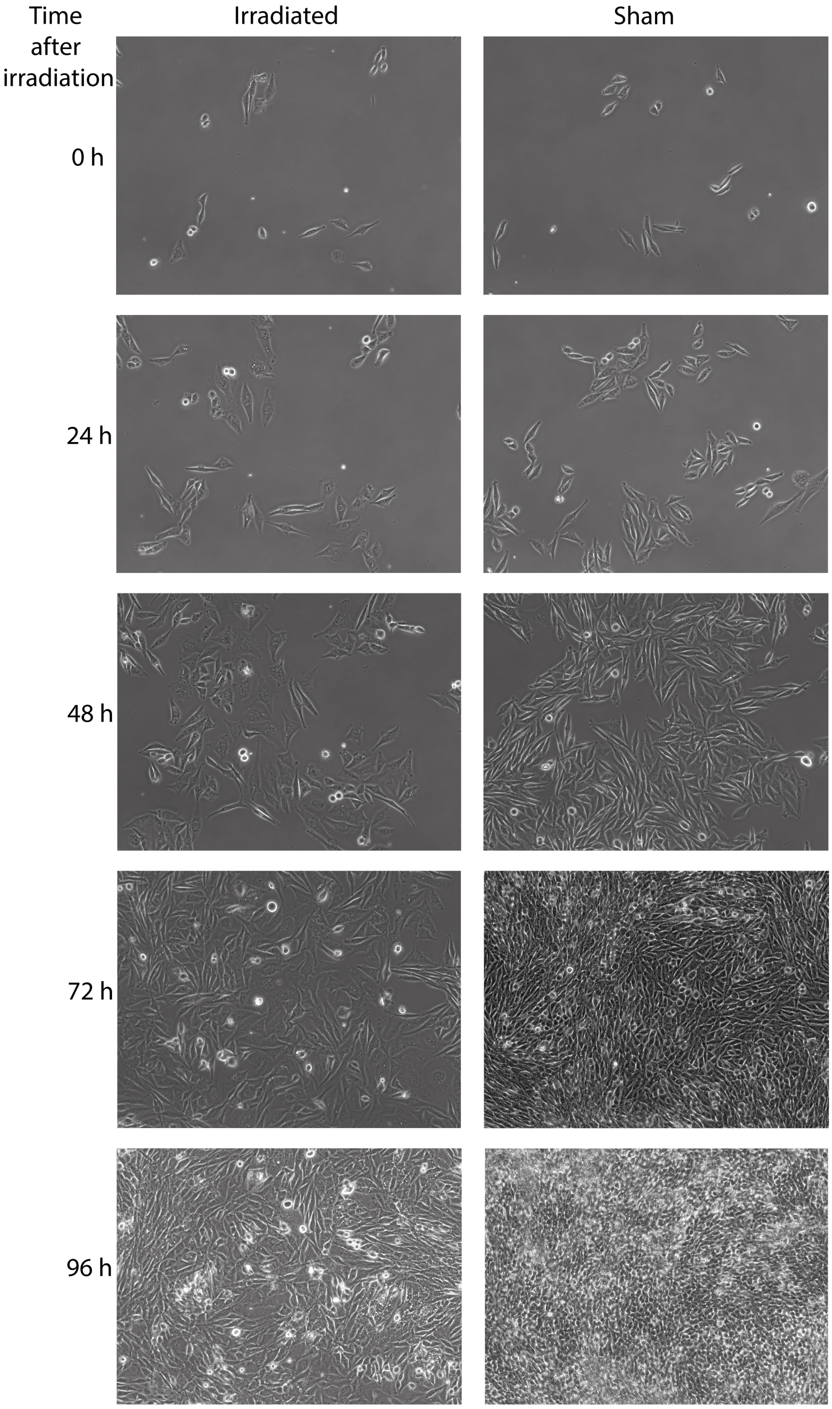

Figure 3.31: The live-cell phase-contrast videos of irradiated CHO cells and the sham CHO cells. The frames at 0 h, 24 h, 48 h, 72 h and 96 h are shown for the irradiated cells on the left and for sham cells on the right.

A detailed evaluation was performed with CeCILE for the first 28.3 h on the sham video and for the first 38 h on the irradiated video. These time ranges were chosen, as the cells in both videos were able to divide themselves 3 times in the chosen time ranges and are still well distinguishable from each other till the end of these time ranges that is necessary for a proper tracking of the cells.

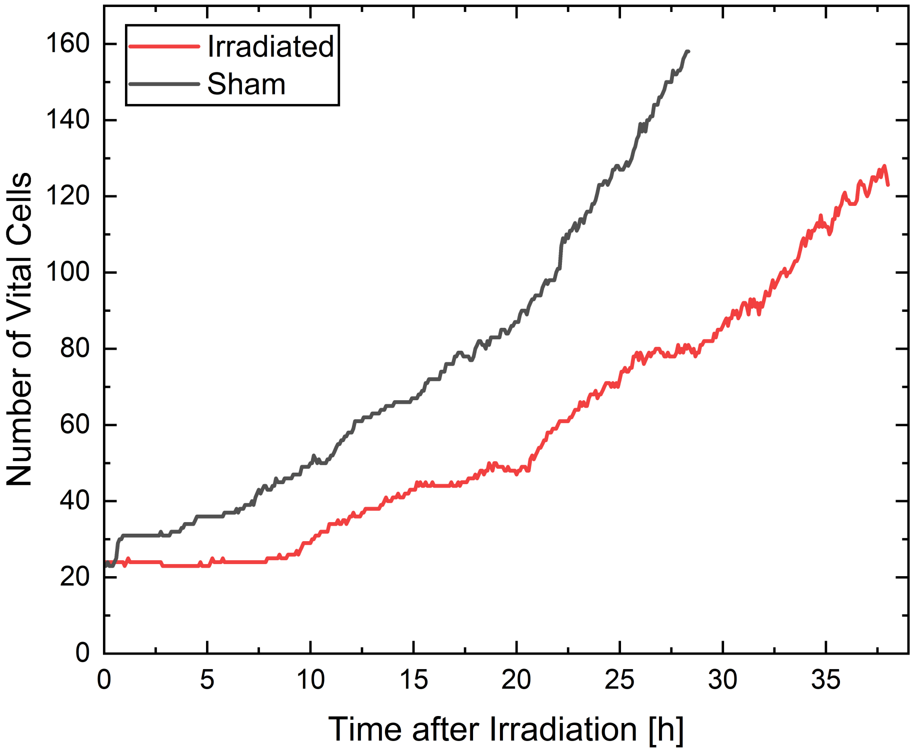

Figure 3.32: The number of vital cells in each frame, given in hours after irradiation, is shown in red for the video of the irradiated cells and in black for the video of the sham cells.

Based on the results of the object detection, the number of objects of each class can be evaluated for each frame. In Figure 3.32, the number of vital cells per frame, given in hours after irradiation, is shown. Vital cells are cells in the cell states liv, round and div. Both videos start with 23 vital cells. While the number of vital cells stays constant for the irradiated cells for 9 hours, the sham cells start immediately to reproduce. The cell growth of the vital cells in the sham sample increases exponentially and results at 28.3 h in 158 cells. In the irradiated sample, the cells also show exponential growth. However, the growth rate is reduced compared to the sham sample resulting in 81 cells at 28.3 h and 123 cells after 38 h. In Figures 3.33 and 3.34, the number of cells in each cell state were shown separately for the irradiated sample (Figure 3.33) and the unirradiated sample (Figure 3.34). The majority of cells in both videos are in the living cell state followed by the dead cell state, the round cell state and finally the cell division state. The living cells therefore show a similar course to the vital cells with an increased growth rate of the sham cells compared to the irradiated cells.

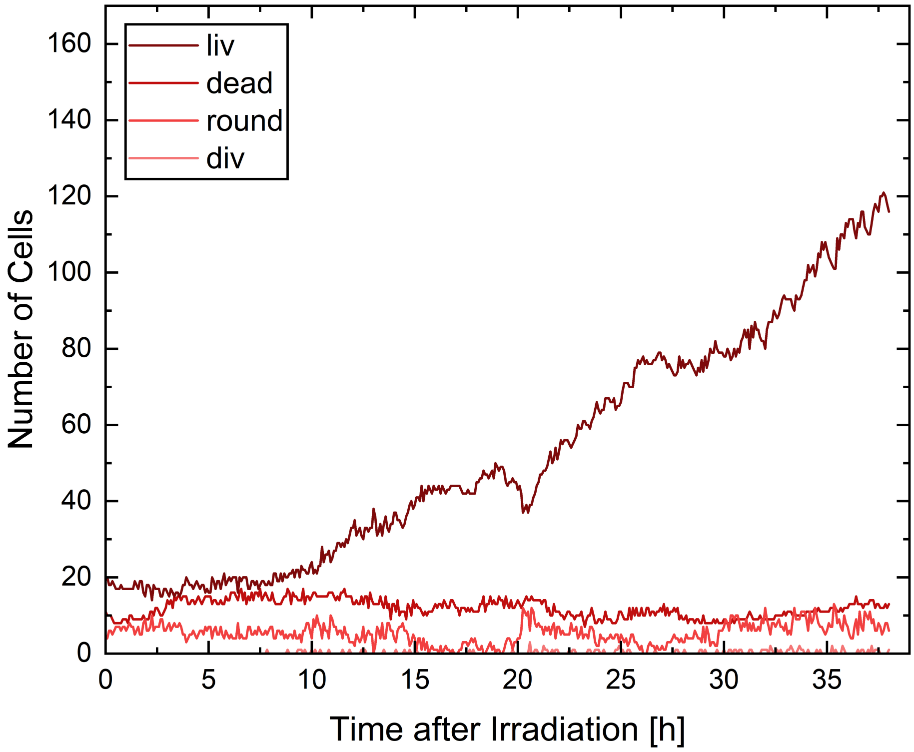

Figure 3.33: The number of cells in classes liv, round, div and dead per frame, given in hours after irradiation, is displayed for the video of irradiated cells.

In the irradiated video, there are more dead cells with 11.88 ± 0.11 (mean ± SEM) dead cells per frame than in the sham video with a mean of 7.93 ± 0.12 dead cells. This difference is also statistically significant with a p-value < 0.05 (two-sample t-test, Origin 2021b). In the first 2 h, both samples had similar amounts of round cells between 3 and 8 round cells. After two hours, the number of round cells stays almost constant in the irradiated video until 15 h after irradiation, while the sham sample had almost no round cells (mostly between 0 and 3 round cells per frame) in this time range. Between 15 and 20 h, also almost no round cells were observed in the irradiated sample similar to the sham sample. After 20 h, the number of round cells was increased in both samples except from a short decrease of the amount of round cells in the irradiated sample between 26 and 28 h. Cell divisions occur twice as often in the sham sample with 117 cell divisions in 28.3 h compared to the irradiated sample with 55 cell divisions in 28.3 h. These results show that also a simple evaluation of the data provided by object detection can reveal significant differences in treatment response of the samples. A closer look on how the single cells react to irradiation is provided by the tracking based evaluation.

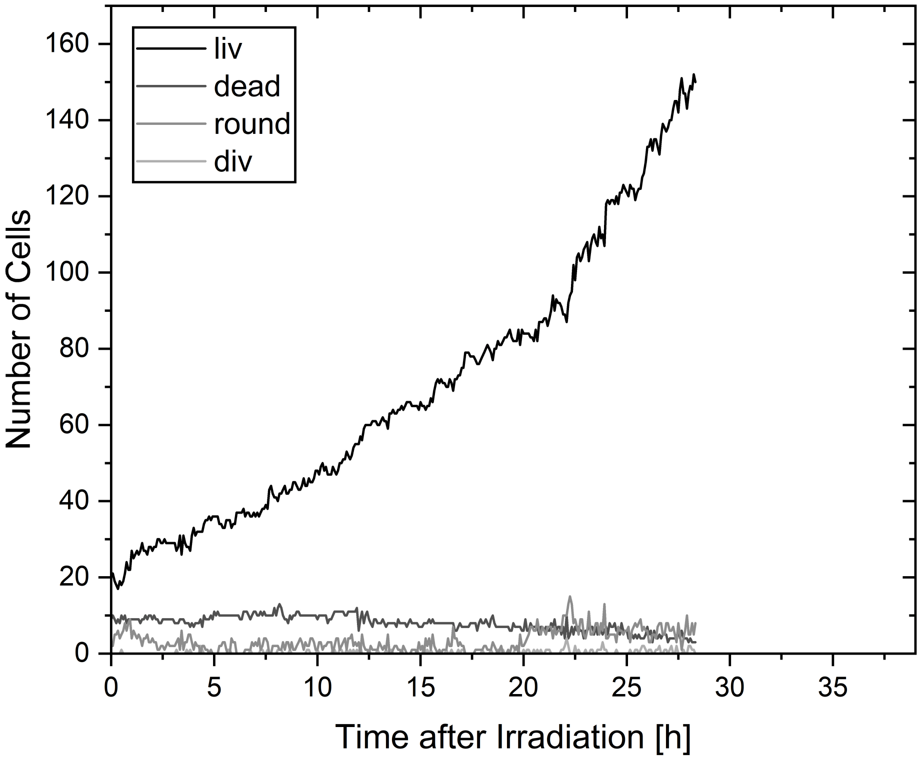

Figure 3.34: The number of cells in the classes liv, round, div and dead per frame, given in hours after irradiation, is shown for the video of sham cells.

Cell lineages for both videos were created for all cells that were more than 300 frames in the video based on the tracking data for the selected time ranges of 38 h (irradiated sample) and 28.3 h (sham sample). The lineages are shown in Figures 3.35-3.39 for the irradiated cells and in Figures 3.40-3.45 for the sham cells. Lines in the lineages appear dark blue for living cells, light blue for round cells, green for dividing cells, and red for dead cells. Black connections between two cells indicate a fusion of the membranes of two connected cells.

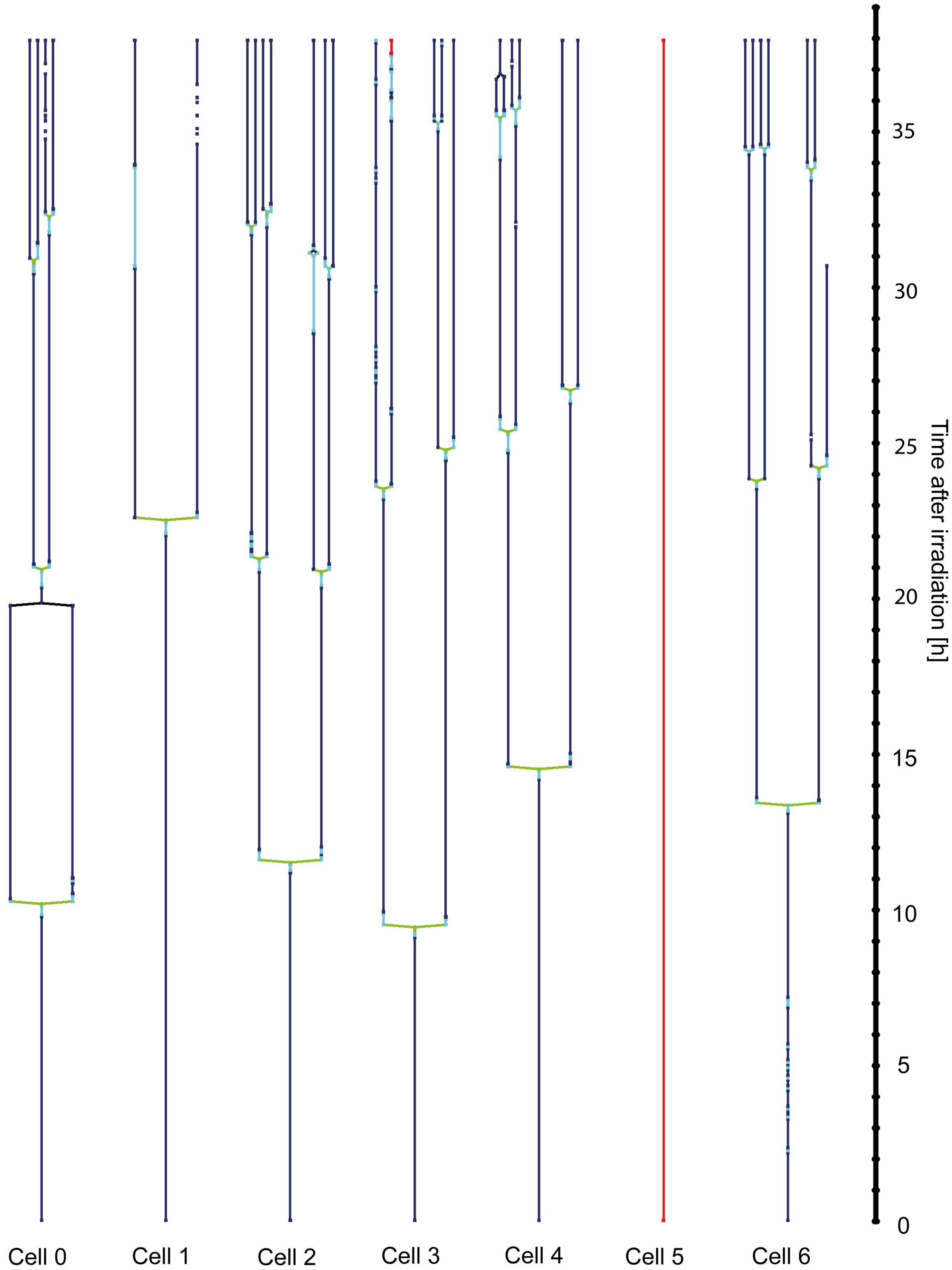

Figure 3.35: Lineages of irradiated cells part 1. The coloring of the lineages indicates the cells states. Dark blue stands for the living cell state, light blue for the round cell state, green for a cell division and red for dead cell state. Black connections between two cells denotes a fusion of the membranes of the two connected cells.

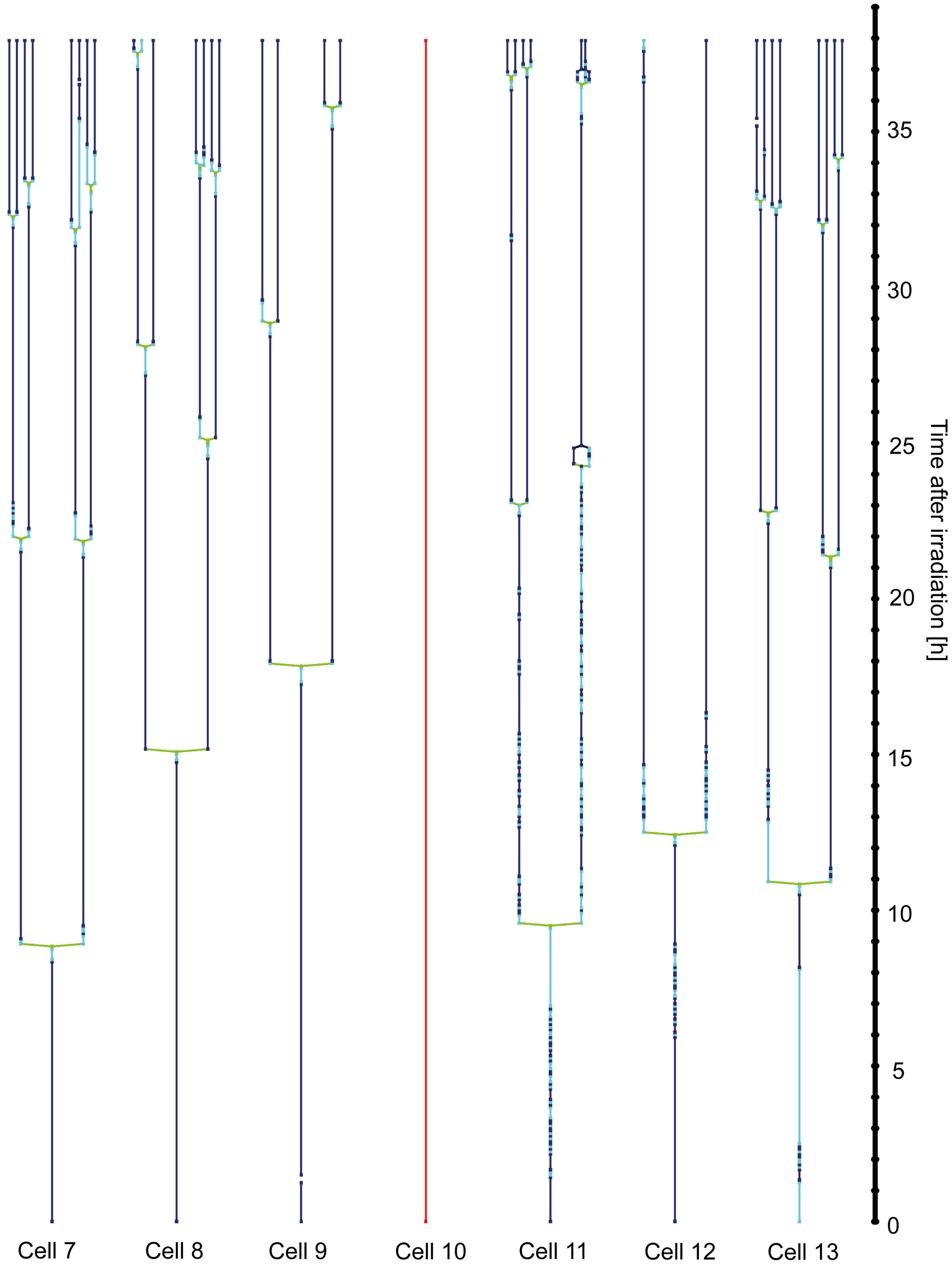

Figure 3.36: Lineages of irradiated cells part 2.

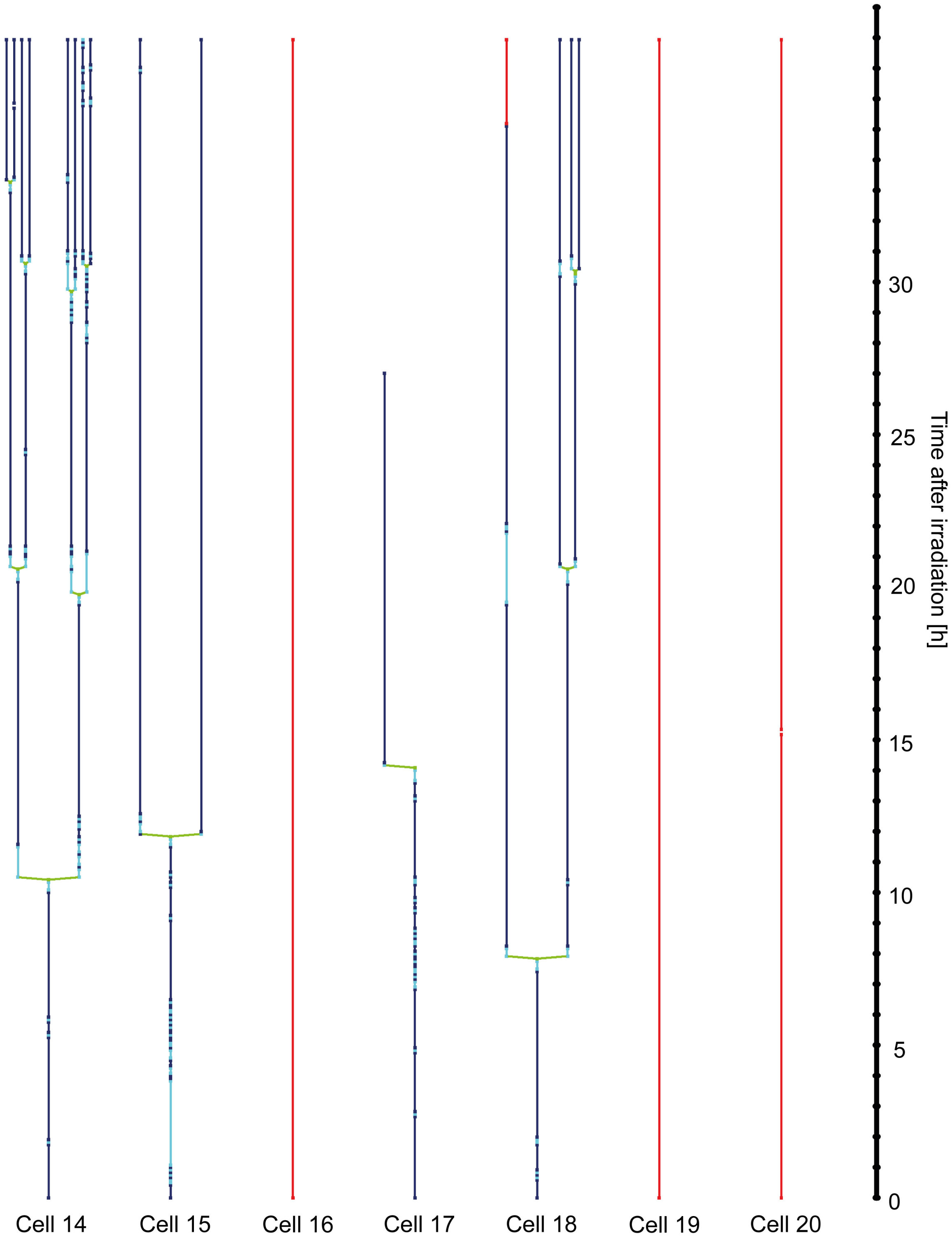

Figure 3.37: Lineages of irradiated cells part 3.

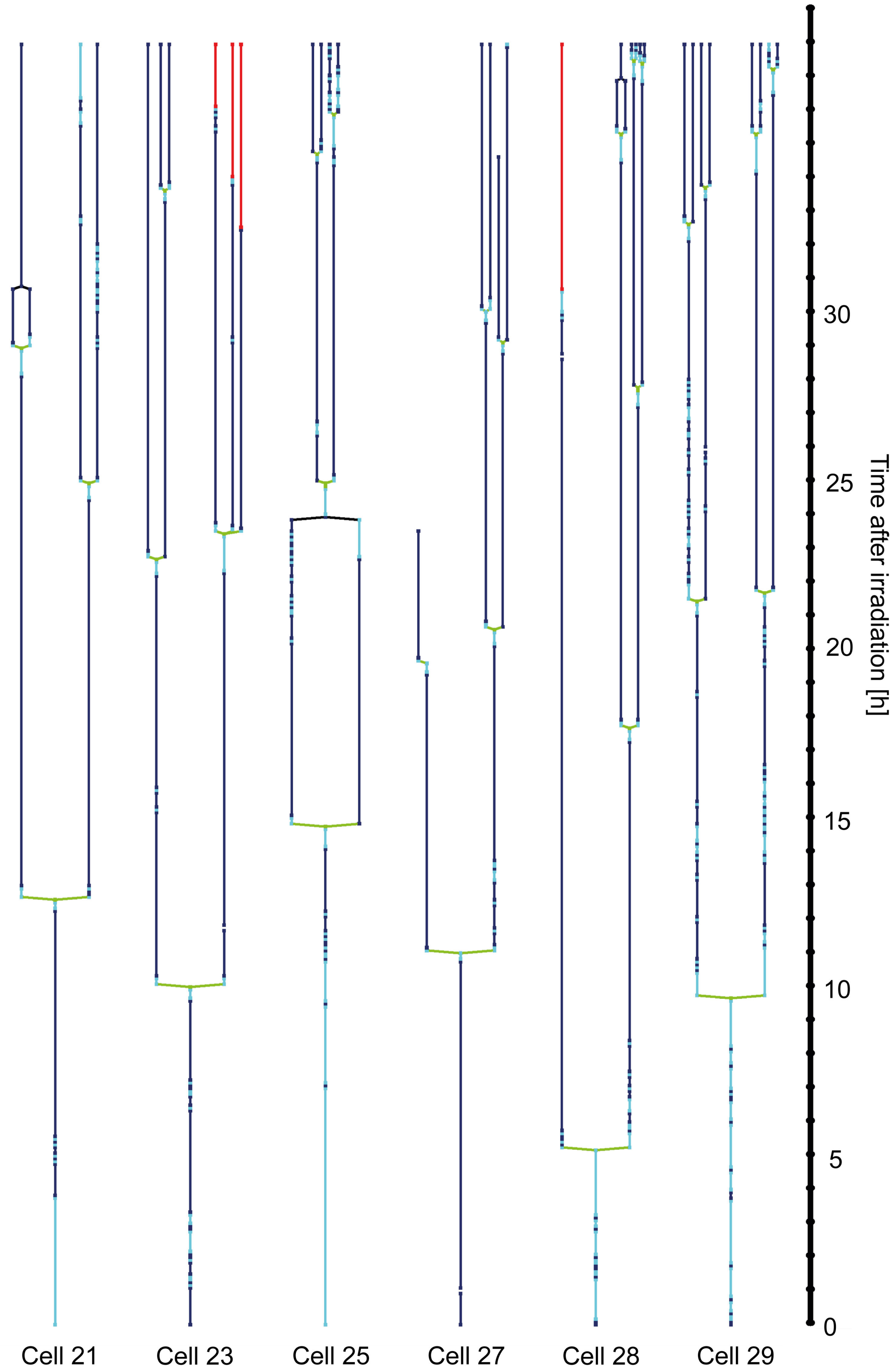

Figure 3.38: Lineages of irradiated cells part 4.

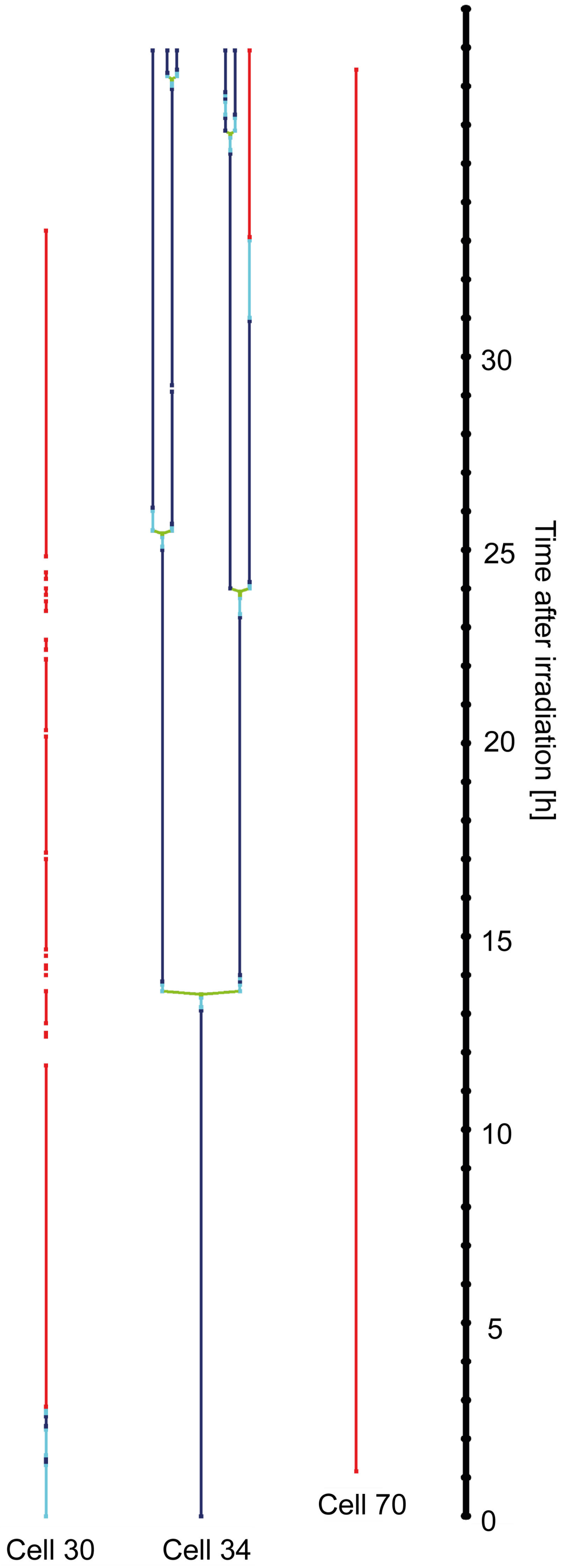

Figure 3.39: Lineages of irradiated cells part 5.

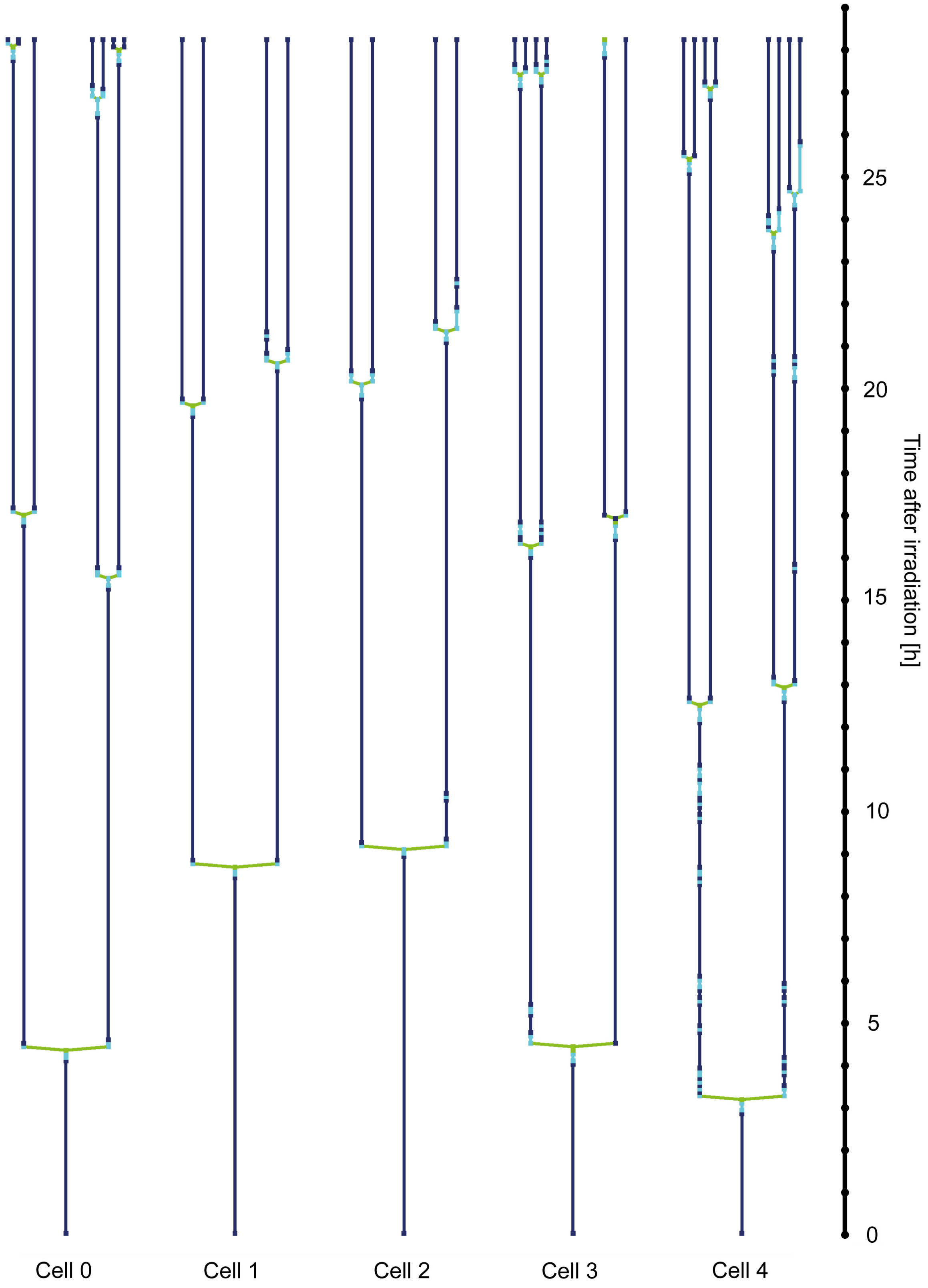

Figure 3.40: Lineages of sham cells part 1.

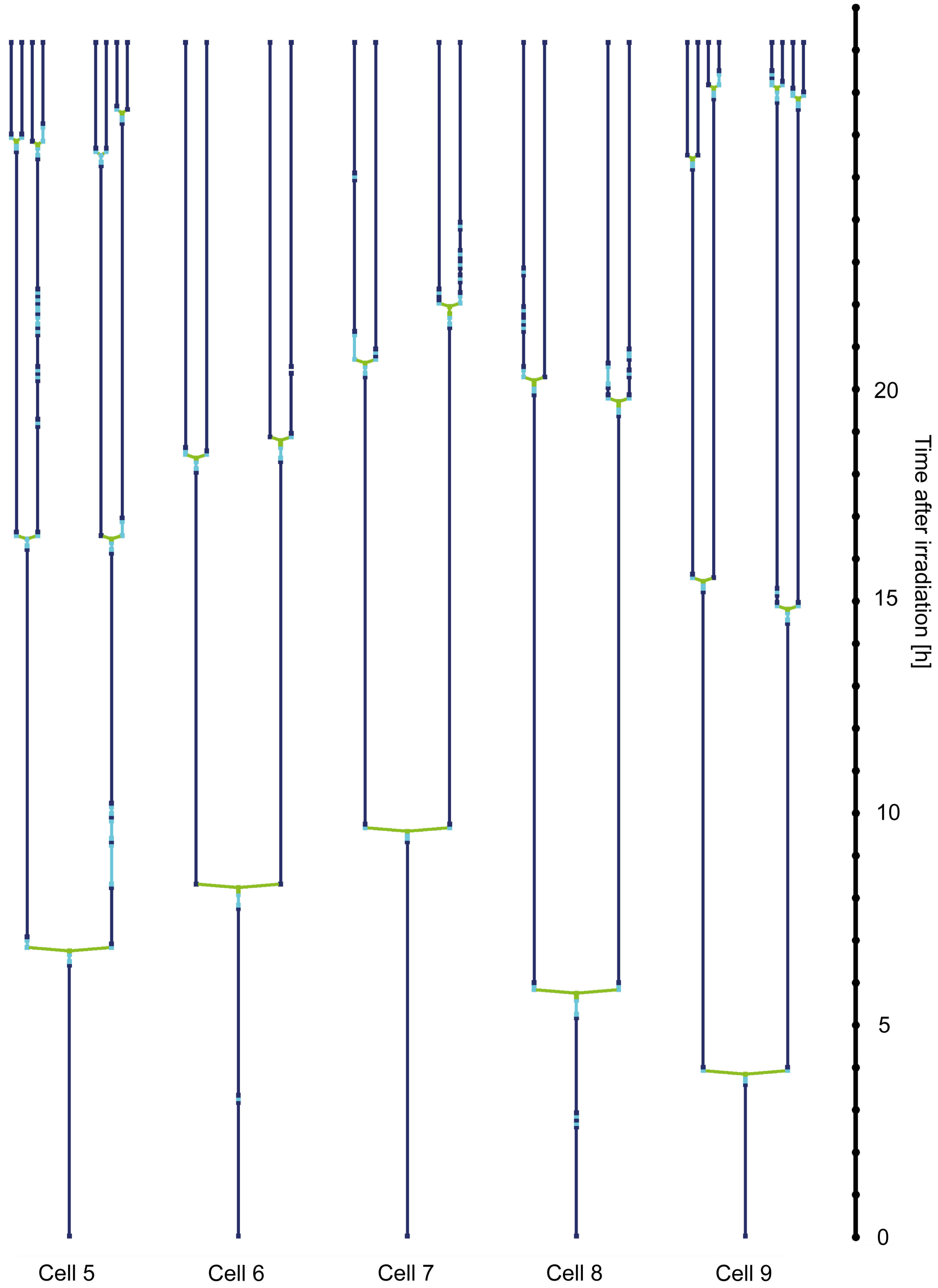

Figure 3.41: Lineages of sham cells part 2.

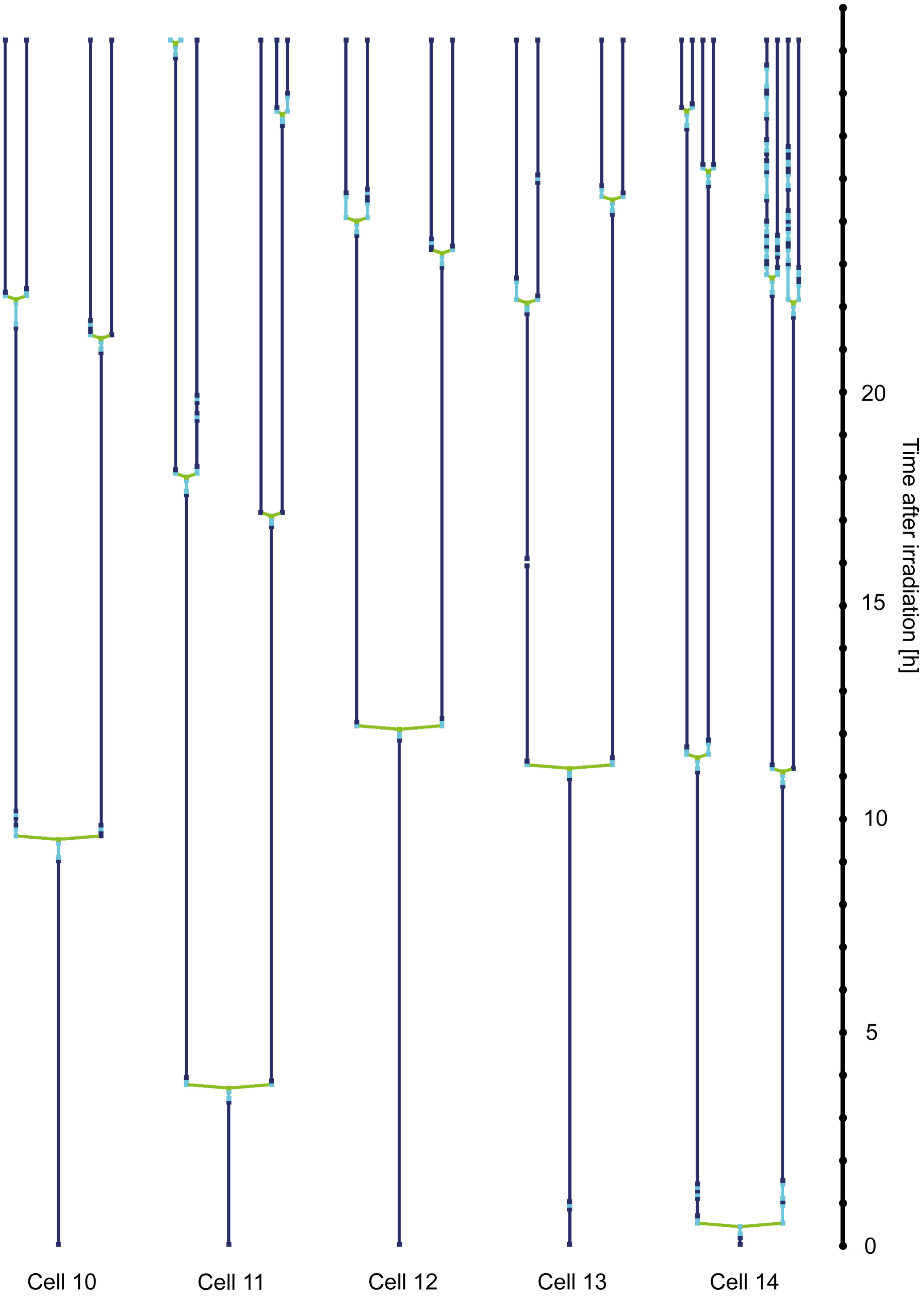

Figure 3.42: Lineages of sham cells part 3.

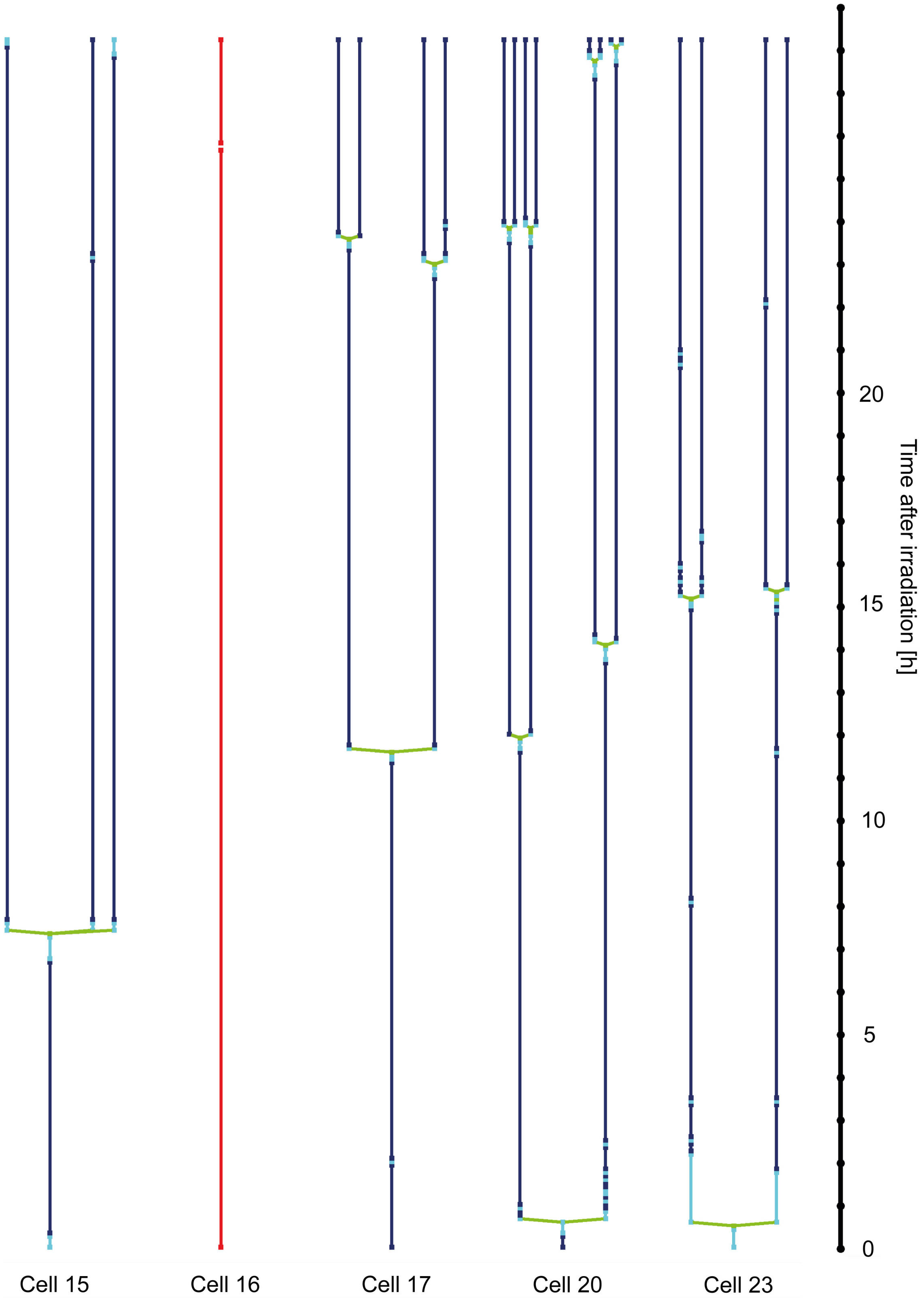

Figure 3.43: Lineages of sham cells part 4.

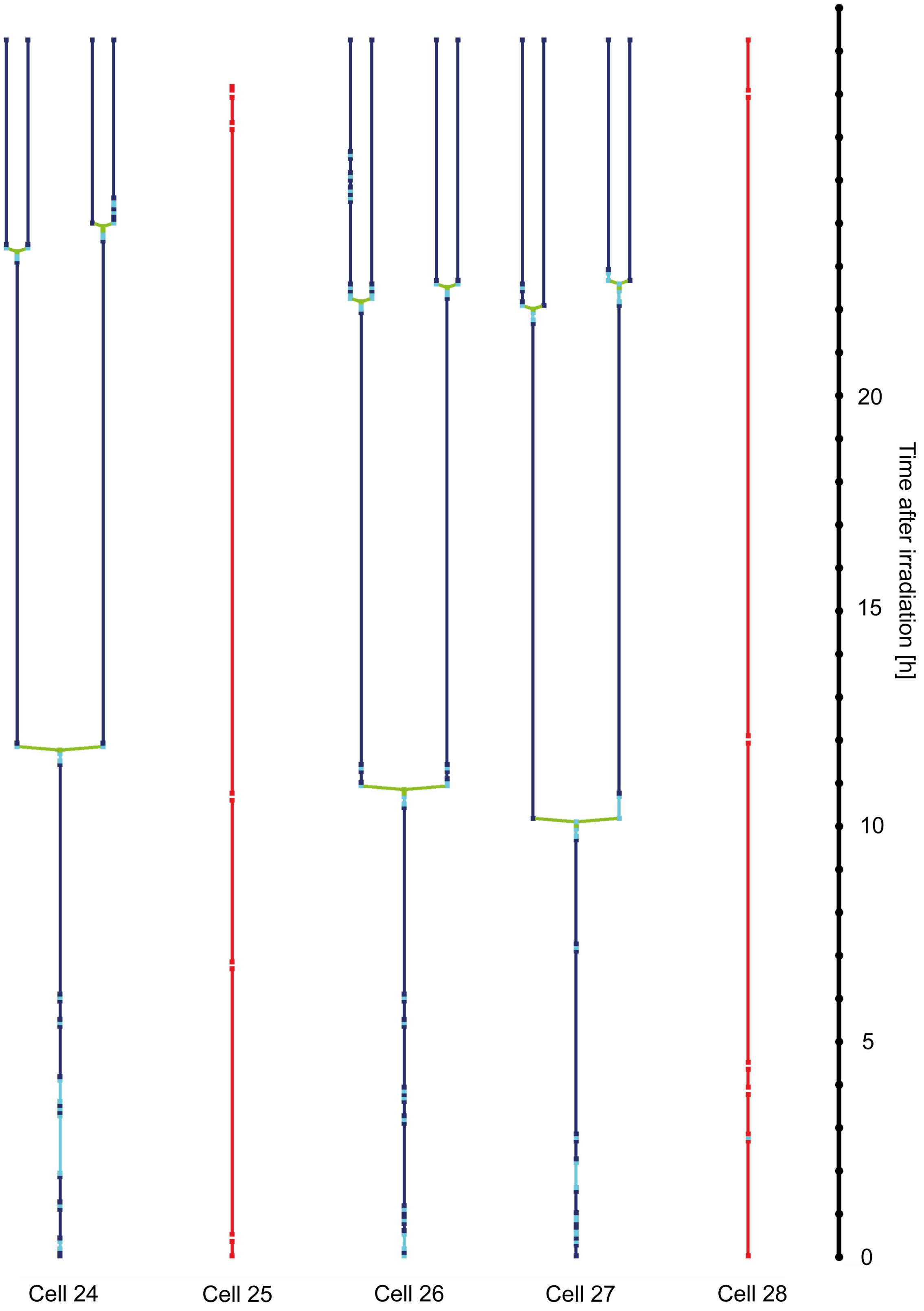

Figure 3.44: Lineages of sham cells part 5.

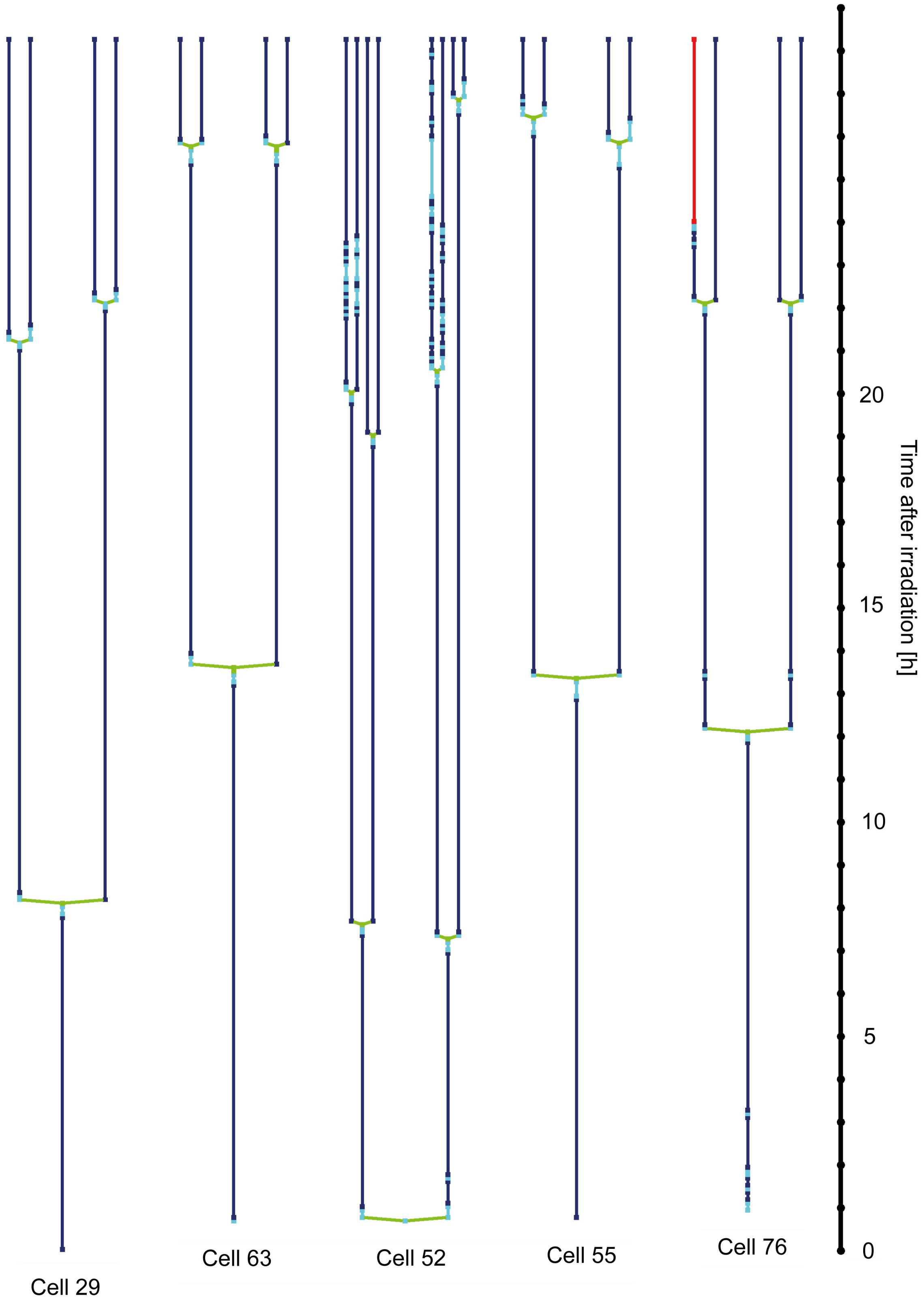

Figure 3.45: Lineages of sham cells part 6.

In the cell lineages, it can be seen that the cell divisions start later in the irradiated sample than in the sham sample. In Figure 3.46, the time cells needed until their first division is shown for the irradiated cells in red and the sham cells in black. Each rhomb stands for an individual cell. The black horizontal lines depict the mean and the whiskers the standard deviation. As shown there, the sham cells divided for the first time on average after (7.3 ± 0.8) h (mean ± SEM), while the mean first cell division in the irradiated sample was after (12.0 ± 0.8) h. This difference was statistically highly significant (p-value < 0.0001, two-sample t-test, Origin 2021b). In the sham sample, the first cell (cell 52, cf. Figure 3.45) underwent cell division 5 min after the start of the recording, and three more cells (cell 14, cell 20 and cell 23, cf. Figures 3.42 and 3.43) divided within the first hour. In the irradiated sample, the first cell division occurred 5.2 h after irradiation (cell 28, cf. Figure 3.38), other cells followed 7.8 h, 8.8 h and 9.4 h after irradiation (cell 3, cell 7 and cell 18, cf. Figures 3.35, 3.36 and 3.37). At 12.9 h, the last cell (cell 63, cf. Figure 3.45) of the sham sample underwent a cell division. In the irradiated sample, the latest first cell division was at 22.5 h of cell 1 (cf. Figure 3.35).

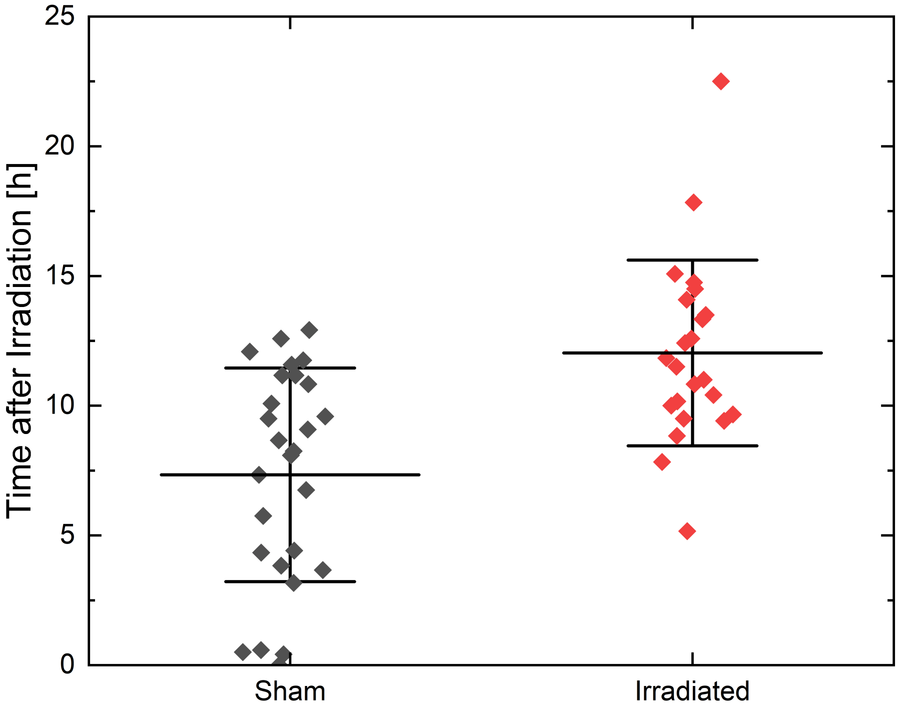

Figure 3.46: Time after irradiation for the first cell division. The results of the sham sample are shown with black rhombs and of the irradiated sample are depicted with red rhombs. Each rhomb represents the time it took a cell to divide after irradiation. The black horizontal lines indicate the mean and the whiskers the standard deviation.

The durations of the first and the second cell cycles for each cell were calculated by the mean of all first or second complete cell cycles that were performed by the daughter cells. A complete cell cycle starts and ends with a cell division. In Figure 3.47, the durations of the first and the second cell cycles are shown for the sham sample as black and gray rhombs and for the irradiated sample as red and light red rhombs. The first cell cycles of the sham sample took on average (11.6 ± 0.4) h and were as long as the second cell cycles, which took on average (11.7 ± 0.5) h. The shortest cell cycle lasted only 6.7 h of cell 52 (cf. Figure 3.45) and the longest 14.7 h of cell 23 (cf. Figure 3.43). In the irradiated sample, the first cell cycles took on average (12.0 ± 0.5) h and the second cell cycles took (10.6 ± 0.5) h. The longest cell cycle was 14.4 h of cell 9 and the shortest was 8.9 h of cell 8 (cf. Figure 3.36). Therefore, the cell cycle duration of the first and the second cell cycles were equally long and also equal for the irradiated and the sham cells.

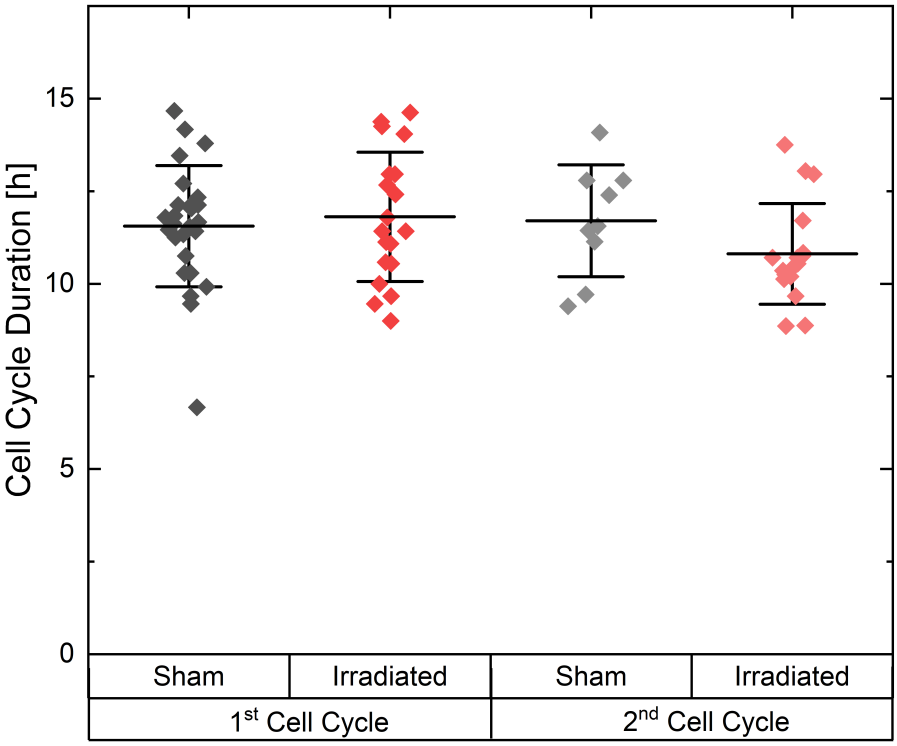

Figure 3.47: Cell cycle duration of the first and the second cell cycles of each cell in the irradiated and the sham sample. The rhombs indicate the cell cycle duration of one cell and are shown in red for the irradiated cells and in black for the sham cells. The horizontal line indicates the mean and the whiskers the standard deviation.

The mean cell cycle duration was calculated by calculating the mean of the first, the second and in case of cell 28 in the irradiated sample also of the third cell cycle duration for every cell separately. In Figure 3.48, the mean cell cycle durations for every cell in the sham and the irradiated sample are depicted by black and red rhombs. The mean of each group is shown by a horizontal line and the whiskers represent the standard deviation. The mean cell cycle of the sham sample results in (11.7 ± 0.3) h and of the irradiated sample in (11.4 ± 0.4) h. Therefore, the mean cell cycle duration were the same for the irradiated and the sham cells. The mean cell cycle duration of both samples was (11.6 ± 0.2) h.

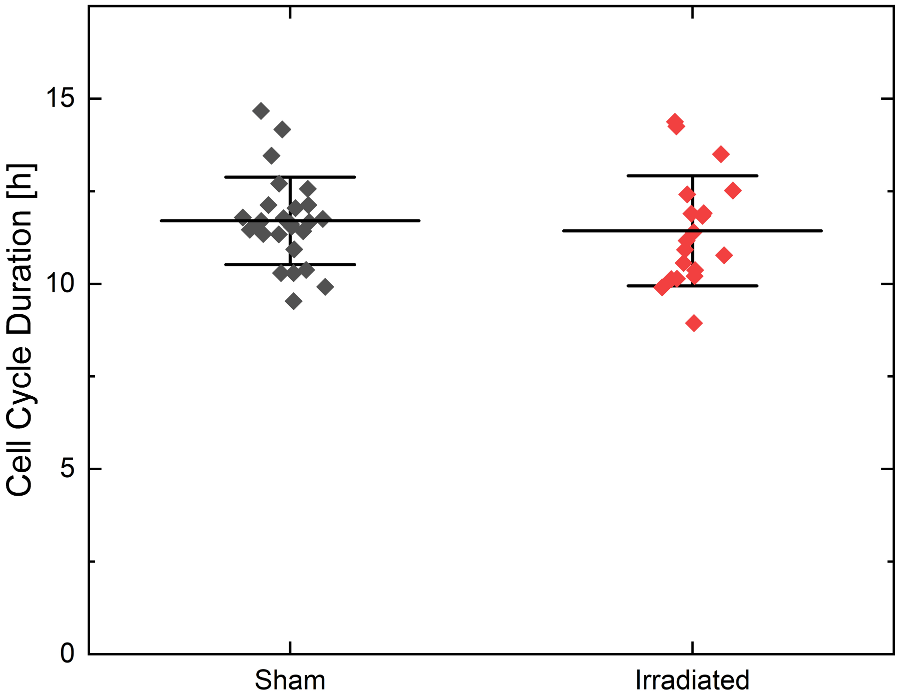

Figure 3.48: The mean cell cycle of each cell in the irradiated and the sham sample. Each rhomb indicates the mean cell cycle duration of one cell in red for irradiated cells and in black for unirradiated cells. The horizontal line depicts the mean and the whiskers the standard deviation.

In the cell lineages of the irradiated cells in Figures 3.35-3.39, some cells showed abnormalities in cell division. Thereby, two types of cell division abnormalities were detected. In the first type, the cell is not able to completely separate the cell membranes between the daughter cells during cytokinesis. The two daughter cells fuse after some time and form a binucleated cell. The second type is the cell division in more than two daughter cells. In this experiment, only cell divisions in two or three cells were observed. The fusion of two daughter cells was observed in cell 0, cell 2, cell 4, cell 11, cell 21, cell 25 and cell 28. The division in three daughter cells was observed in cell 11 and cell 23. In the sham sample, only one abnormality occurred. Cell 15 divided into three daughter cells (cf. Figure 3.43). In Figure 3.49, the percentage of cells that showed abnormalities during the observation time is depicted. The red bars depict the results for irradiated cells and the black bars for sham cells. In total, 35 % of the irradiated cells showed abnormalities during their cell cycles and only 4 % of sham cells. In the irradiated sample, the most often occurring abnormality was the fusion, which occurred in 30 % of the cells. No fusion was observed in the sham group. The division into three daughters occurred in 9 % of the irradiated cells and in 4 % of the sham cells.

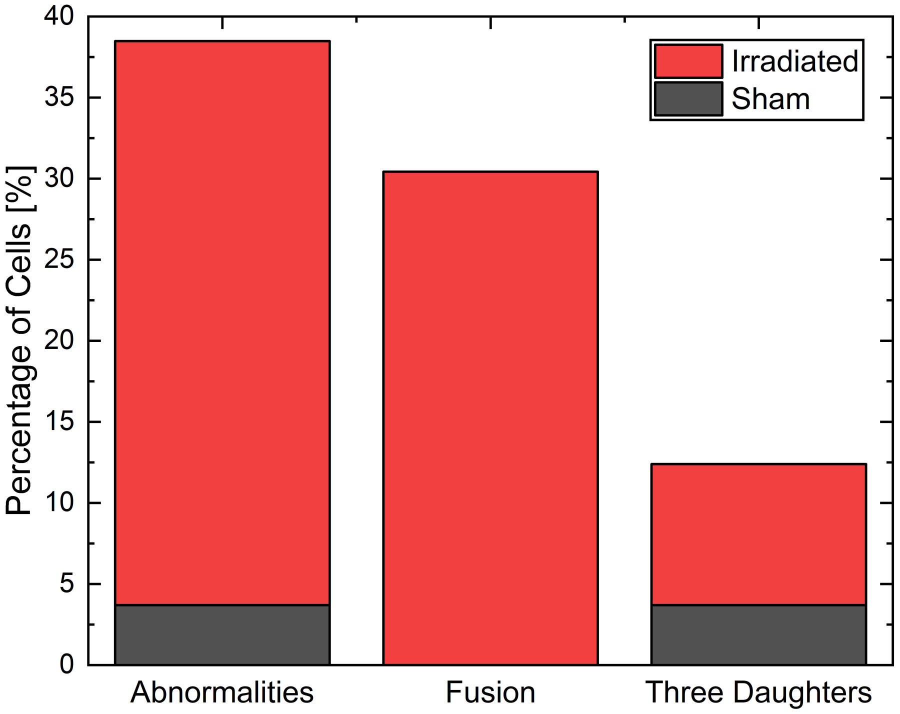

Figure 3.49: The cell cycle abnormalities in irradiated and sham cells. The percentage of cells that showed one or both of the abnormalities fusion and three daughter division (three daughter) are depicted by bars in red for the irradiated cells and in black for the sham cells. The abnormalities bars show the sum of the percentage of cells that underwent fusion and the percentage of cells that divided into three daughters.

Proliferation is the ability of a cell to reproduce progeny and therefore undergo cell divisions. It can be described by the maximum number of cell cycles a cell has undergone in a given period of time and the number of daughter cells produced by one cell. Like for the creation of the lineages, only cells were included into the evaluation that appeared on more than 300 frames in one of the videos. CeCILE evaluates both, the maximum number of cell divisions and the number of vital daughter cells per mother cell, in a time period provided by the user. For this experiment, the first 28.3 h after irradiation were chosen as a time period. Only cells were taken into account that were in one of the vital cell states the first time they occurred. In Figure 3.50, the percentage of cells is given that either showed no cell division, one cell division, two cell divisions or three cell divisions in 28.3 h. Thereby, the maximum number of cell divisions one of the daughter cells of a mother cell has undergone is taken into account. The red bars indicates the results of the irradiated group and the black bars of the sham group. In both groups, most of the cells underwent 2 cell divisions, 71 % of the cells in the irradiated group and 63 % in the sham group. A maximum of three cell divisions was observed. 33 % of the sham group underwent three cell divisions and 4 % of the irradiated group. More irradiated cells than sham cells divided only once, 21 % of the irradiated cells and 4 % of the sham cells. 4 % of the irradiated cells did not divide and non of the sham cells. The irradiated cells underwent on average a maximum of 1.8 ± 0.6 cell divisions and the sham cells of 2.3 ± 0.6. The maximum numbers of cell divisions each cell underwent are statistically significantly different between the sham group and the irradiated group with a p-value < 0.05 (two-sample t-test, Origin 2021b).

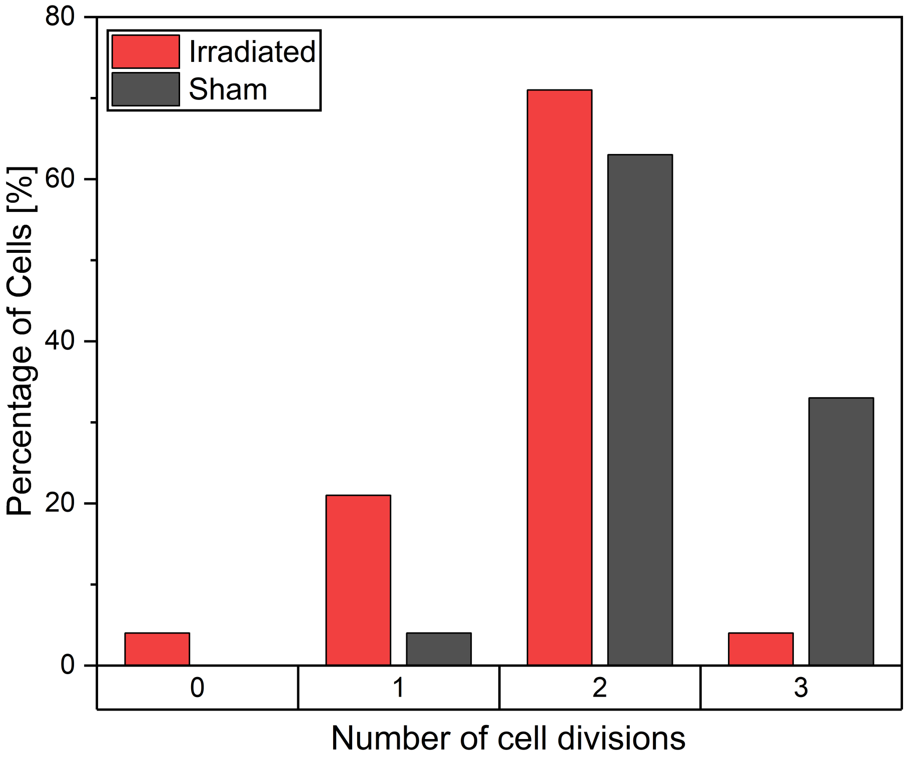

Figure 3.50: Maximum cell divisions per cell. The percentage of cells is displayed in a bar graph for the irradiated (red) and the sham sample (black) where one of the daughter cells has undergone a maximum number of cell divisions of 0, 1, 2 or 3 divisions.

The number of daughter cells per cell is presented in Figure 3.51. Cells that were not in a vital cell state at the beginning of their occurrence were excluded from evaluation. Here, the percentage of mother cells that produced 0 to 8 daughter cells are depicted in a bar graph with red bars for the irradiated sample and black bars for the sham sample. In both groups, the mother cells produced most often 4 daughter cells, namely 46 % (irradiated) and 60 % (sham). In the irradiated group, a maximum of five daughter cells was produced by 4 % of the mother cells. Also 4 % of the mother cells produced no vital daughter cells and one vital daughter cell. 25 % of mother cells resulted in two daughter cells and 17 % in three daughter cells. In the sham sample, only 4 % of mother cells produced three daughter cells that was also the minimum number of daughter cells. 4 % of mother cells produced 6 daughter cells, 7 % of mother cells seven daughter cells and 22 % of mother cells eight daughter cells that was also the maximum amount produced in the selected period of time. On average, the irradiated cells produced 3.1 ± 1.3 daughter cells and the sham cells 5.1 ± 1.9 daughter cells. The difference in the distributions of the number of vital daughter cells per mother cell is statistically highly significant with a p-value of 0.00003 (two-sample t-test, Origin 2021b). With a measured mean cell cycle duration of (11.6 ± 0.2) h, the cells can divide 2.5 times in 28.3 h. Therefore, for these cells four to eight daughter cells are expected, when the cells are healthy. In the sham sample, three daughter cells were only produced by cell 15 that showed a cell cycle abnormality (cf. Figure 3.43). In the irradiated sample, less than four daughter cells were produced by cell 0, cell 1, cell 9, cell 11, cell 12, cell 15, cell 17, cell 18, cell 21, cell 25, cell 27 and cell 30. Five reasons for these decreased amounts of daughter cells could be found in the lineages (cf. Figures 3.35-3.39). The cells started very late (> 15 h) with the first cell division: cell 1 and cell 9. Cell cycle abnormalities occurred: cell 0, cell 11 and cell 25. The cell divided once but was not able to divide a second time properly: cell 12, cell 15, cell 18 and cell 21. The cell died before the first division: cell 30. The cells were located at one edge of the video and a daughter cell left the video during cell division: cell 17 and cell 27.

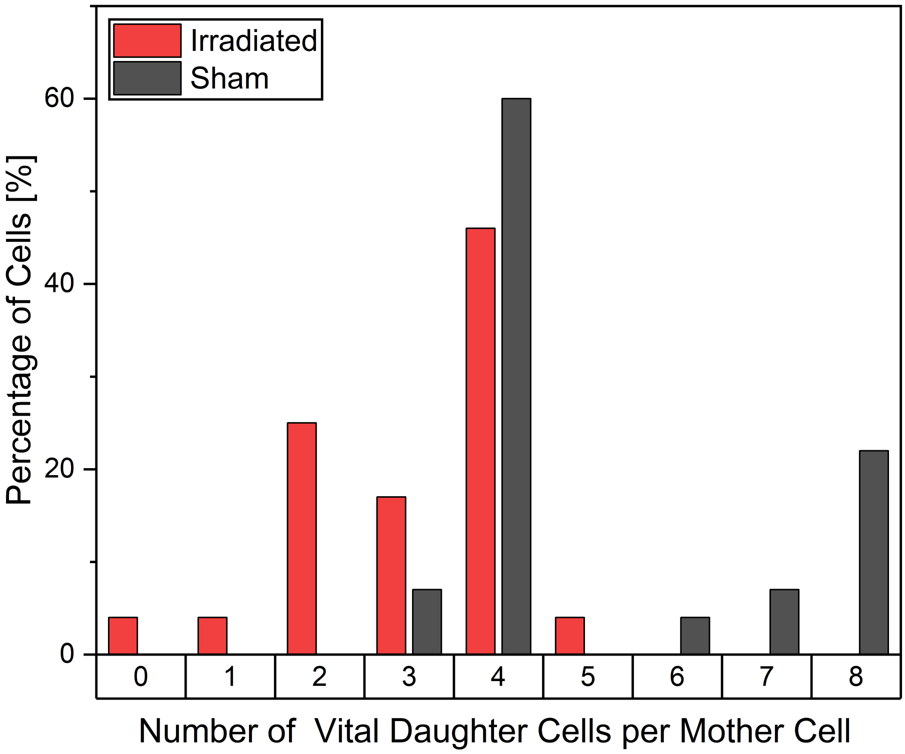

Figure 3.51: The number of vital daughter cells per mother cell. The percentage of mother cells that produced a given number of daughter cells is shown in a bar graph for the irradiated (red) and sham (black) samples.

The gold standard in radiobiology is the colony forming test that measures the cell survival. Here, the cells count as survived cells when a mother cell was able to form a colony with a minimum of 50 daughter cells within 5 days (when CHO cells were used as cell model). With a cell cycle duration of 11.5 h, the cells divide 10.4 times within 5 days and would produce under perfect healthy conditions between 1024 and 2048 daughter cells. In a real experiment these daughter cell numbers are typically not reached as the nutrition supply and space in a colony will not be enough for so many cells. Therefore, smaller number of daughter cells are expected here after 5 days and lead to the groundrule that colonies with more than 50 cells are counted as surviving. In the experiment presented here, the sham cells showed that all healthy cells were able to divide into four daughter cells within 28.3 h. The mother cell in the sham sample that was not able to reach that daughter cell number showed abnormalities in the cell cycle. This cell will most probably not be able to form a proper colony. The other cells in the sham sample were able to divide into four or more daughter cells and showed healthy normal cell cycles. Therefore, these cells will most probably be able to form colonies. Therefore, the survival fraction can be calculated by

$$SF = {}^{N_{\text{sample},\geq 4\ \text{DC}}}\!/_{N_{\text{sample,total}}} \Big/ {}^{N_{\text{sham},\geq 4\ \text{DC}}}\!/_{N_{\text{sham,total}}} \tag{3.20}$$

where $N_{\text{sample},\geq 4\ \text{DC}}$ is the number of mother cells in the evaluated sample that had divided into more than four daughter cells (DC) and $N_{\text{sample,total}}$ is the number of mother cells in the sample. $N_{\text{sham},\geq 4\ \text{DC}}$ and $N_{\text{sham,total}}$ are the number of mother cells with more than four daughter cells and the total number of mother cells in the sham sample, respectively. The SF results in $SF = 1$ for the sham sample and in $SF = 0.52$ for the sample irradiated with 3 Gy. These data can now be compared to the data of the colony forming assay presented in the second chapter of this thesis in Section 2.7.3. Here, the reference measurements on CHO cells performed with x-rays are presented. For 3 Gy, the measured SF was 0.55 ± 0.06 in the reference. Therefore, the SF measured with CeCILE stands in good agreement to the colony forming assay.

3.10 Discussion

In this chapter, I presented a novel method for investigating the effects of radiation on eukaryotic cells. This novel method is based on observing the cells for several days after irradiation via live-cell phase-contrast microscopy and analyzing the obtained data with the semi-automatic algorithm CeCILE (Cell classificaion and in-vitro life-cycle evaluation) based on artificial intelligence. The introduced algorithm can detect and track cells on microscopic videos and classify them into four cell states depending on their morphology. Furthermore, it is able to evaluate different cell cycle related endpoints like proliferation, cell cycle duration, cell cycle abnormalities and cell lineages. My first CeCILE paper in 2021 [143] was to my knowledge the first to present an artificial intelligence-based algorithm for analyzing cell response to radiation on live-cell phase-contrast videos. In this thesis, the whole process of developing such an algorithm was presented and its capabilities could be shown in a first irradiation experiment.

In the first step, I implemented an object detection based on artificial intelligence that is able to detect all cells on all frames of a live-cell phase-contrast video. As object detection algorithm, a pretrained faster RCNN was chosen. This algorithm is based on a deep learning neural network and needs to be trained with a dataset to perform an object detection task on custom data. Therefore, I set up a dataset of labeled cell images, which was used to train the algorithm. To enable an evaluation of the cell cycle, the cells were seperated into three vital cell classes due to their morphology and a class for dead cells. The vital cell classes were the living cell class (liv), which includes all cells that are attached to the surface and have an elongated shape with low contrast, the round cell class (round), which includes all cells with a round shape, and the dividing cell class (div), which includes all cells in cytokinesis. I labeled the cells by surrounding each cell with a rectangular bounding box and tagging the box with the label of the cell class. In the dataset, images of in total 20 videos of different experimental setups are included to increase the generalization and to widen the window of possible applications. I included here three cell lines, CHO-K1, LN229 and HeLa, which are often used in radiobiology. These cell lines have three important characteristics that are necessary for detection and tracking. They grow in an unchanged manner when seeded in small densities without clustering. They adhere on plane surfaces and grow there in a 2D like manner next to each and usually do not overlap. The cells of these cell lines can be easily distinguished from each other and can be followed throughout a video as long as the cell density is not too high. In principle, CeCILE can be applied to any cell line that meets these requirements, but it has to be tested if further training is necessary before application. The cells were seeded on three different containers that are used in our lab for various irradiation experiments. In 17 videos, the containers were coated before with either gelantine or CellTak. In 9 videos, cells were irradiated with proton doses of 4 Gy or were sham irradiated. In four videos, cells were irradiated with 1 Gy to 4 Gy of carbon ions or were sham irradiated. Four videos were recorded with a different imaging mode, by using phase stop 2 instead of phase stop 1. These used setups simulate typical irradiation experiments for which CeCILE will be used in the future. Furthermore, this high variety resulted in a high variety of images and ensures the generalization on videos of different experiments.

**

Before I trained CeCILE with the dataset, I tested whether my dataset was suitable for training a deep-learning based neuronal network using a simple CNN algorithm, which was trained to classify the cells. The quality was measured with the so-called F1-score, which combines the precision and the recall of the algorithm and has a maximum of 1.00. I achieved an F1-score of 0.93 with a precision of 0.93 and a recall of 0.94. The largest error was made in the class round, where the precision and recall were 0.87. This means that 13 % of the round cells were not classified as such. This problem occurs since there is a fluent transition between living, round and dividing cells. Therefore, it is difficult for the human expert as well as for the algorithm to sort a cell in the right class when it is directly at the transition step. To minimize the labeling error, the human expert takes the time information into account and looks at the cell morphology several frames before and after the labeled frame. The algorithm instead only gets the single frame image for classification. Therefore, a discrepancy between the human expert decision and the classification from the algorithm is expected. Nevertheless, the most common false predictions were round cells classified as living cells or the other way around. Since the transition between the two classes is very continuous, some cells can be classified for both classes and the occurring errors between these classes are negligible. The inaccuracy of the other classes was 5 % for dead cells and much below 5 % for cell divisions and living cells.

The results from classification looked promising so I went further and implemented object detection. CeCILE was developed based on a pretrained faster RCNN with ResNet-101 as a backbone CNN. This model was taken from the TensorFlow 2 Model Detection Zoo and was trained and finetuned on my dataset. The training and finetuning was in detail described in Section 3.6 and the optimized parameters are listed there. The performance of the object detection was scored on two videos of the test and tracking dataset, which were derived from an irradiation experiment. In the first video, CHO-K1 cells were irradiated with 3 Gy of x-rays and in the second video, cells were sham irradiated. For these two videos, I created a detection and tracking groundtruth that was used to score the performance of CeCILE on both tasks, the detection and the tracking. First, the object detection was scored due to its performance in localizing objects. This is the most important part of the object detection in CeCILE, as the tracking relies on a proper localization of the cells. Here, the F1-score was calculated. Correctly detected cells had, thereby, box overlaps with IoU-values > 0.5 of predicted boxes and groundtruth boxes. The video of irradiated cells achieved a mean F1-score of 0.90 with a mean precision of 0.88 and a mean recall of 0.93. In the video of sham cells, a mean F1-score of 0.92 was measured with a mean precision of 0.88 and a mean recall of 0.96. Therefore, the object detector performed slightly better on the sham video with a small difference of 0.02 in the F1-score and 0.03 in the recall. This means that over 90 % of the cells in both videos were accurately localized.

In addition to localization, an object detector also classifies the detected objects. For object detection, localization and classification are typically scored in a combined score, the mAP score. The mAP score is 1 for a perfectly correct detection and classification. The mAP can be calculated for each class individually and as a mean mAP over all classes. The object detector achieved the best results in the detection and classification of the class liv. In the irradiated video, this class had a mean mAP score of 0.95 and in the sham video of 0.97. In the irradiated video, 75.1 % of cells were in class liv and 85.6 % of cells in the sham video were in class liv. The second best results were achieved in the class dead with mean mAP scores of 0.82 (irradiated) and 0.69 (sham). More dead cells occurred with 17.0 % of the cells in the irradiated video than in the sham video with 9.8 % dead cells. The third highest mAP score was achieved in the class round with 0.72 in the irradiated video and 0.60 in the sham video. 7.6 % of cells were in the class round in the irradiated video and 4.2 % of cells in the sham video. The by far rarest occurring class was the class div. Only 0.3 % and 0.4 % of cells in the irradiated and sham video were in this class. Here, also the mean mAP scores were the lowest with 0.5 in both videos. This shows that the cell detection achieved better results for classes that contained more cells. However one has to be careful here, the mAP score is much more influenced by one missing bounding box or a false classification when there are fewer cells in the investigated class. This can be seen in the classes liv, round and dead, where higher mAP scores were achieved when more cells were in a class. Especially in the class liv, where the majority of cells were included, very high mAP scores of above 0.95 were obtained, indicating that the vast majority of cells were correctly detected and classified. The mAP score of a class was only below 0.8 when less than 10 % of the cells belonged to the class. As shown before in the classification with a simple CNN, the classification struggles for cells that transit from one to another class. In the cell cycle, the cells stay most of the time in the class liv. The class round as precursor for the cell division occurs only for about 30 min and the class div can be only observed for about 10 min. I recorded the cells every 5 minutes. Therefore, the probability that a cell is in a transition state is higher for the class round and div than for the class liv. Dead cells change their morphology after death. They can undergo a self-digestion, as for example this is the case for apoptosis or they can also be digested by other cells. In these processes, dead cells disappear after some time. Therefore, dead cells are difficult to detect and classify for an algorithm but also for a human expert annotator when the death was 1 h or more ago. False classifications in cell state transitions do not influence the outcome after tracking, as it is not important if a cell enters a specific cell state one frame earlier or later. Additionally, it is not important to track dead cells the whole observation time, as the only important information, namely that a cell is dead, is already received. Therefore, it can be concluded that the object detection provides all information that are needed for tracking and performed well enough to be forwarded to a tracking algorithm.

As tracking algorithm, I implemented the centroid tracker as proposed by A. Rosebrock [202] and adapted it for the special requirements of tracking cells in phase-contrast videos. The centroid tracker compares the bounding boxes of two frames by calculating the distances between all center-coordinates (centroids) of the bounding boxes and matches the boxes with the smallest distance between their centroids for a track. This tracker also has a feature to recover from a premature end of a track if bounding boxes are missed. Furthermore, I implemented the IoU as a second feature to take also the box overlap into account when matching bounding boxes. I could show that this feature increased the robustness of the tracking by 0.07 %. As the centroid tracker is a location based tracker it is well suited for cells on phase-contrast videos. Cells on phase-contrast videos hardly move between frames, when a frame to frame distance of 5 min was applied during recording. An appearance based tracker is less suited in the case of cell tracking, as cells change their morphology during the cell cycle. Also trackers that expect a directed movement of objects towards a certain destination cannot be applied, as cells in culture move in a more random walk like manner due to the homogeneous distribution of nutrients in culture. The centroid tracker is a hard-coded tracker that only takes into account the information of the previous and the current frame. It is made for accurate tracking of objects, where each object has one track, but provides no feature to track across cell divisions, when a track splits into two tracks. However, it can be used to track between cell divisions and manually assign the tracks of two daughter cells to a mother cell afterwards. The performance of the implemented tracker was tested, as the object detection before, on the two videos of the test and tracking dataset. Here, I tested the tracker on the bounding boxes of the groundtruth to test solely the performance of the tracker and not of the detector that was already tested before. As the centroid tracker cannot track across cell divisions, all ID assignments in between cell divisions predicted by the tracker and given by the groundtruth were compared to calculate a tracking accuracy. The tracking accuracy gives the percentage of right ID assignments out of all assignments. The centroid tracker achieved an accuracy of 97.77 % in the irradiated video and 98.51 % in the sham video. This shows that the proposed location-based tracker is well suited to track cells.

Detection and tracking implemented in CeCILE both achieved very good results when applied separately. In combination, however, the errors both make are amplified. Errors in the detection like missing bounding boxes lead to errors in the tracking, as the tracking relies on the bounding boxes of the object detection. For the evaluation of phase-contrast videos on a single cell basis, a 100 % accuracy is necessary and no errors can be accepted, as these would falsify the outcome. Especially, a switching of cell identities or a premature track ending leads to wrong results when evaluating the cell cycle and creating accurate cell lineages. Therefore, I implemented two manual correction steps. The first correction step was implemented after the object detection, to enable the user to add all missing bounding boxes. With these corrections, the tracking algorithm can be applied and leads to very accurate results. In the second correction step, the tracking IDs can be adjusted. Here, also tracks of mother and belonging daughter cells can be combined, as a tracking across cell divisions is not implemented in the tracker yet. In both correction steps, the class labels of the bounding boxes can be corrected if necessary. With this semiautomatic approach, the user can easily evaluate phase-contrast videos with a 100 % accuracy and receives precise information about each cell in the video.

Based on this semiautomatic approach and to demonstrate the potential of CeCILE, the two videos of the test and tracking video dataset, which were also used for the scoring of the performance of CeCILE, were evaluated by using CeCILE's evaluation tool. To create these videos, the cells were treated as in a typical irradiation experiment. Two parts of the same cell population were seeded in two dishes specially made for live-cell microscopy. The cells of one dish were irradiated with 3 Gy of x-rays, while the other dish was sham irradiated. Both dishes were moved to a microscope equipped with a stage-top incubator mounted on a motorized stage. The microscope took an image of both samples every 5 minutes in turn. With this method, both samples could be monitored simultaneously, allowing a direct comparison and eliminating systematic errors. In this experiment, I could show that a continuous recording for 4 days is possible with the proposed set-up. Extending the monitoring to more than 4 days is also possible, but the evaluation with CeCILE is limited by the density of the cells. A proper detection and tracking is only possible as long as the cells are still distinguishable from each other. CHO cells have a short cell cycle of only 11.5 h. When the cells are unirradiated as in the sham sample, the cells can be well distinguished up to 28.3 h. Irradiated cells show a decreased cell growth and could be evaluated almost 10 h longer for

38 h. The evaluation tool of CeCILE creates for every cell a cell lineage. Furthermore, it outputs the number of vital cells per frame and the number of cells in each class per frame and provides a table of all mother and daughter cells and the duration of occurrence in each generation. From these data, the duration of the cell cycles and the time points of the first cell divisions can be derived. Additionally, CeCILE outputs the number of daughter cells and the maximum number of cell divisions for each mother cell. Based on this evaluation, it could be shown that irradiated cells start later with cell division than the sham cells. In the sham sample, there were four cells that underwent cell division right after the start of the monitoring, whereas irradiated cells started dividing at earliest after 5.2 h. On average, the first cell divisions took place at (7.3 ± 0.8) h in the sham sample and at (12.0 ± 0.8) h in the irradiated sample, which is 4.7 h later. This difference was statistically highly significant with a p-value of < 0.00001 (two-sampe t-test, Origin 2021b). Interestingly, the cell cycles of sham cells and irradiated cells were the same. Also the first and second cell cycle took equally long in both groups. A mean cell cycle of (11.6 ± 0.2) h was measured. The cell lineages created by CeCILE provide deep inside in the evolution of each cell. For example, it can be seen here that some cells showed abnormalities in their cell cycles. In the evaluated videos, fusions of two daughter cells and divisions into three daughter cells were observed. Also combinations of both abnormalities were found. In total, 35 % of irradiated cells showed abnormalities in their cell cycle and only 4 % of the sham cells. The proliferation, the ability of a cell to divide, can be determined in two ways. The first method is to evaluate the maximum number of cell divisions one cell undergoes. This number is provided by CeCILE and was evaluated 28.3 h after irradiation in both samples. The irradiated cells underwent on average a maximum number of cell divisions of 1.8 ± 0.6 and the sham cells of 2.3 ± 0.6. These results were statistically significant with a p-value < 0.05 (two-sample t-test, Origin 2021b). The other method is to count the number of daughter cells that came from one mother cell at a certain time point. This number is also provided by CeCILE and was also evaluated at 28.3 h in both samples. The irradiated cells, which were vital at the beginning of the monitoring, produced on average 3.1 ± 1.3 daughter cells and the sham cells 5.1 ± 1.9 daughter cells. Also here, a high statistically significant difference with a p-value of 0.00003 (two-sample t-test, Origin 2021b) was found. Based on these data and by assuming that a healthy cell produces more than 4 daughter cells in 28.3 h, the clonogenic survival was calculated. As gold standard in radiobiologic research, the clonogenic survival is determined by the colony forming assay (CFA) [38]. Here, a clonogenic cell is a cell that was able to form a colony of more than 50 cells after 5 days in case of CHO-K1 cells. The survival fraction is the fraction of clonogenic cells out of all cells compared to control sample. The survival fraction can also be determined by assuming that a cell is clonogenic if it produces more than four daughter cells in 28.3 h. The survival fraction is calculated as for the CFA and resulted in 0.52. This result lies in good agreement with the SF of a reference measurement that was 0.55 ± 0.06 [136] and shows that the clonogenic survival can be determined with CeCILE in a shorter time range than in the CFA. This means that CeCILE can provide the information about clonogenic survival 3.8 days earlier than the CFA. By comparing the different results achieved, it can be concluded that the difference in cell growth of the irradiated and the sham cells did not come from different

cell cycle durations. It is a result of cell cycle arrests right after irradiation and therefore delayed cell divisions and of unsuccessful cell divisions, on the one hand, because more of the daughter cells died and, on the other hand, because of cell cycle abnormalities.

In this thesis, I could show that CeCILE can be used to accurately detect and track cells in phase-contrast videos in a semi-automatic mode. The results provided by CeCILE, give information about the cell growth, cell cycle durations, first cell divisions, proliferation, abnormalities of cell cycles and the relationships between cells in one assay. Therefore, CeCILE combines all important endpoints of radiobiologic research and provides more detailed information that cannot be derived by state of the art assays as, for example, the cell cycle abnormalities. Furthermore, CeCILE could achieve significant results by only evaluating 23 cells. Gold standard assays such as the colony forming assay require several thousand cells to get significant results [38]. No cell staining or any kind of specific treatment is necessary as this is the case in the CFA or for the Caspase3/7-Sytox assay, which evaluates the cell death. Possible influences caused by treatments can be prevented when using CeCILE. As the cells are monitored every 5 minutes, detailed information about the cells can be derived for every time point. Therefore, a detailed history of each cell is obtained. State of the art assays are typically evaluated at specific time points. The CFA is typically evaluated 5 days after irradiation and the Caspase3/7-Sytox assay after 24 h in case of CHO-K1 cells. If information at other time points are of interest, these assays have to be repeated.

At the moment, CeCILE is used in a semi-automatic mode. It is planned to improve CeCILE by including a more complex tracking algorithm based on MCMC (Monte Carlo Markov Chain) algorithms to achieve more automation. Here, I started a cooperation during my thesis and such an algorithm is currently under development. Nevertheless, manual correction steps will still be useful to ensure a 100 % accuracy.

In conclusion, I have presented here a method for monitoring cells on phase-contrast videos for more than 4 days. The proposed evaluation with the artificial intelligence based algorithm CeCILE provides detailed information about different radiobiologic endpoints combined in one assay. Furthermore, additional information about the cell cycle abnormalities, the evolution of each cell and relationships between cells can be derived. This makes CeCILE a powerful tool for radiobiologic research.

Chapter 4

Conclusion and Outlook

4.1 Conclusion

The aim of this work was to further investigate the proton-FLASH effect. In the first part of this thesis, a novel beamline design for investigating the FLASH effect on protons was presented and three in-vitro experiments and one in-vivo experiment were performed that addressed different important endpoints. As in-vitro experiments, a colony forming assay that investigates the cell survival, a Caspase3/7-Sytox assay that evaluates cell death and a micronuclei test that addresses genetic damage were performed. While the colony forming assay resulted in equal cell survival for the tested dose rates, a FLASH related sparing was observed in the Caspase3/7-Sytox assay for a dose rate of 310 Gy/s compared to a conventional dose rate of 0.06 Gy/s resulting in lower cell death. In the micronuclei test, less genetic damage was found in both FLASH dose rates 310 Gy/s and 9.3 Gy/s. Here, high dose rates seem to induce less genetic damage, but the damages seem to be more complex. In the mouse ear model, a sparing of the skin tissue in the ears could be observed. This sparing effect was visible in the ear swelling and the inflammation reaction for a dose of 33 Gy and dose rates of 930 Gy/s and 9.3 Gy/s. To my knowledge, this was the first time that a FLASH effect could be observed at dose rates as low as 9.3 Gy/s. The tested inflammatory blood markers showed no dose rate effects, but also no effects of the irradiation itself. Here, the irradiated blood volume seemed to be to small to induce an effect. However, an estimation of the irradiated blood volume, which could be easily conducted for the mouse ear model, could show that a 100 times higher blood volume was irradiated with a conventional dose rate when applying FLASH dose rates. This demonstrates that blood might play an important role in the FLASH effect. As state of the art models in radiobiology could not provide an explanation for the FLASH effect yet, new approaches are necessary to get new insights. In this work, I presented such a new approach, the artificial intelligence based detection and tracking of cells on live-cell phase-contrast videos. I presented the whole development process of the algorithm CeCILE that was trained on a custom dataset I created. The performance of CeCILE in the tasks cell detection and classification and cell tracking was scored on unseen test data. Accurate detection and tracking results were achieved. However, for the cell cycle evaluation a 100 % accuracy was needed. Therefore, manual correction steps were included into CeCILE's working pipeline. These correction steps could also supplement the tracking across cell divisions that has not been included yet. The potential of CeCILE could then be proven on two videos of an irradiation experiment. The cells in one video were irradiated while the cells in the other video not (sham). The following endpoints were evaluated: Number of cells at each time point in one of the four morphological classes living cell, round cell, cell division and dead cell, time after irradiation until the first cell division, cell cycle duration, cell cycle abnormalities and proliferation given by the maximum number of cell divisions per mother cell and the number of daughter cells per mother cell. The created cell lineages provided further insights into the evolution of each single cell. Irradiated cells needed more time to undergo the first cell cycle, they showed more often cell cycle abnormalities, the underwent fewer maximum cell divisions and they produced less daughter cells. These results were significantly different from the sham cells even though both videos started with only 23 cells. Similar cell cycle durations were found for both groups. This shows that the difference in cell growth is only caused by delayed first cell divisions, cell cycle abnormalities and the lack of ability to reproduce healthy cells. Therefore, CeCILE provides new insights into the cellular response to irradiation. It could open up new perspectives for finding the underlying mechanisms of the FLASH effect. Consequently, the next step is to evaluate cells irradiated with different dose rates with CeCILE.

4.2 Outlook

The results of the FLASH experiments showed that more investigations are needed to find the requirements for inducing a FLASH effect and that also new point of views are needed to understand the FLASH effect. Such a new point of view is on the one hand the irradiated blood volume estimation as performed for the mouse ears. Here, further investigations with novel approaches like the single-shot photoacoustic microscopy proposed by Liu et al. [166] could provide completely new information. With such a method, the hemoglobin concentration, the oxygen saturation and the blood flow can be measured. These endpoints might show how the amount of irradiated blood contributes to the FLASH effect. In this work, I could show that 9.3 Gy/s also induced a sparing effect. However, this finding was not significant as only three mice were in this irradiation group. In the future, it should be further tested whether such low dose rates of protons can induce a FLASH effect or not. In-vitro FLASH studies based on our CeCILE-method should be performed for various dose rates and conditions. Especially experiments under physoxic or hypoxic conditions are of interest as oxygen might play a role in the FLASH effect. CeCILE therefore needs to evolve towards a higher level of automation. This can be done by implementing a more complex tracking method like the MCMC based algorithms or by using an intelligent tracker containing some kind of memory, as for example LSTM based methods. From a radiobiologic point of view, the insertion of new classes like a class for senescence could provide new interesting results and completes the endpoint portfolio provided by CeCILE. A combined fluorescent and phase-contrast imaging can enable the creation of new classes, as for example senescence can be fluorescently stained. Then using fluorescent microscopy, also cells that include a fluorescently tagged DNA damage marker can be monitored and the DNA damage and the behavior of the cells could be compared. The obtained information could be used to find explanations of how the decreased DNA damage, the decreased cell death and the equal clonogenic survival are related when investigating FLASH. Therefore, CeCILE has great potential to help researchers to understand radiobiologic effects like the FLASH effect. The results of this work and the proposed methods have already provided, or have the potential to provide in the future, completely new insights to the FLASH effect. By improving the understanding of this effect, the presented results and proposed methods will contribute to improve the treatment of cancer by radiotherapy.

Appendix A

Appendix

A.1 Overview of dose rates inducing a FLASH effect in-vivo in literature

Data for Figure 2.2 were collected from in-vivo FLASH studies. The literature review was performed via PubMed to find all studies investigating the FLASH effect on different dose rates in-vivo. Only data of studies were included, where the investigated dose rate induced a FLASH effect (equals to a tissue sparing effect of healthy tissue) compared to a conventional dose rate in-vivo. For pulsed dose rates, the mean dose rate, which was applied during irradiation, was taken. For a better visualization, only dose rates < 1100 Gy/s were included. If more than one dose was investigated for a dose rate, just one dose was included, as data points with equal dose rate but different doses would overlap each other. The literature review was performed at the 21st of February 2023. Therefore, only studies are included, which were published before this date. The data extracted from the collected studies are listed in Table A.1 along with the references of these studies.

Particle Type	DR [Gy/s]	Dose [Gy]	Tissue	Species	Reference
electrons	40	17	lung	mouse	[6]
electrons	60	10	brain	mouse	[8]
electrons	100	10	brain	mouse	[8]
electrons	500	10	brain	mouse	[8]
electrons	160	31	skin	minipig	[10]
electrons	200	30	brain	mouse	[86]
electrons	300	30	brain	mouse	[86]
electrons	100	10	brain	mouse	[203]
electrons	100	17	lung	mouse	[12]
protons	100	15	whole body	zebrafish	[11]
protons	40	18	lung carcinoma	mouse	[204]
electrons	100	10	brain	mouse	[101]
electrons	216	16	abdomen	mouse	[9]
protons	63	18	abdomen	mouse	[205]
electrons	180	30	skin	mouse	[176]
electrons	270	20	flank,tumor	mouse	[206]
electrons	1100	11.2	abdomen	mouse	[98]
electrons	280	11.2	abdomen	mouse	[98]
electrons	310	12.5	abdomen	mouse	[98]
electrons	140	12.5	abdomen	mouse	[98]
protons	97	45	hint leg	mouse	[18]
protons	108	15	abdomen	mouse	[17]
electrons	352	14	lung carcinoma	mouse	[14]
protons	57	35	hint leg	mouse	[16]
protons	115	35	hint leg	mouse	[16]
protons	80	40	hint leg	mouse	[207]
electrons	287	32	whole body	zebrafish	[96]
electrons	177	32	whole body	zebrafish	[96]
protons	300	32	whole body	zebrafish	[96]

Table A.1: Literature review of dose rates inducing a FLASH effect in-vivo. Here, the underlying data for Figure 2.2 are listed along with the references these data were taken from. DR stands for dose rate.

A.2 Results of the CFA

Dose rate [Gy/s]	**Dose [Gy]**	**PE [%]**	**SF**	**Mean dose [Gy]**	**SEM dose [Gy]**	**Mean SF**	**SEM SF**
0.06	4.0	29	0.56	3.7	0.8	0.56	0.05
	4.2	31	0.59				
	4.2	30	0.57				
	3.8	33	0.62				
	2.3	26	0.49				
9.3	2.4	31	0.58	3.4	1.0	0.55	0.04
	4.8	26	0.49				
	3.8	28	0.53				
	2.3	31	0.59				
	3.9	30	0.57				
310	6.4	22	0.41	3.6	1.5	0.52	0.05
	3.2	30	0.56				
	3.0	30	0.56				
	2.1	32	0.61				
	3.2	24	0.46				
sham	0	62	1.00	0.0	0.0	1.0	0.1
	0	61	1.00				
	0	52	1.00				
	0	45	1.00				
	0	45	1.00				

Table A.2: The results of the CFA investigating a dose rate effect. The SEM SF was calculated by using equation 2.4.

Sample ID	Dose [Gy]	DR [Gy/s]	C+ [%]	S+ [%]	S+ and C- [%]	S+ and C+ [%]	S- and C- [%]	S- and C+ [%]
1	4.0	0.06	17.2	11.1	0.005	11.1	82.4	6.5
2	2.9	0.06	8.4	5.5	0.010	5.5	91.4	3.1
3	3.4	0.06	8.0	5.1	0.000	5.1	91.9	3.0
4	2.7	0.06	5.0	2.6	0.020	2.6	94.8	2.6
5	3.4	0.06	9.1	4.7	0.010	4.7	90.4	4.9
6	3.4	9.3	9.0	3.7	0.00	3.7	90.5	5.8
7	3.0	9.3	7.4	4.7	0.00	4.7	92.3	3.0
8	3.6	9.3	8.6	4.5	0.00	4.5	90.9	4.7
9	3.8	9.3	11.5	9.0	0.38	8.6	87.9	3.2
10	3.7	9.3	6.7	4.4	0.01	4.4	93.2	2.4
11	3.9	310	8.4	4.2	0.00	4.2	91.3	4.5
12	2.8	310	3.3	2.0	0.01	1.9	96.5	1.6
13	2.7	310	4.0	2.2	0.04	2.1	95.9	1.9
14	2.5	310	4.2	2.8	0.01	2.8	95.7	1.5
15	3.5	310	4.9	2.3	0.00	2.3	94.9	2.8
16	0.0	-	4.2	3.2	0.065	3.1	95.6	1.2
17	0.0	-	4.5	2.7	0.005	2.6	95.4	2.0
19	0.0	-	2.3	1.1	0.005	1.1	97.7	1.2
20	0.0	-	5.9	4.0	0.010	4.0	93.8	2.2
Conv	3.3 ± 0.2	0.06	9.5 ± 2.0	5.8 ± 1.3	0.009 ± 0.003	5.8 ± 1.3	90.2 ± 1.9	4.0 ± 0.7
Flash9	3.5 ± 0.2	9.3	8.6 ± 0.8	5.3 ± 0.9	0.08 ± 0.07	5.2 ± 0.8	91.0 ± 0.9	3.8 ± 0.6
Flash310	3.1 ± 0.3	310	4.9 ± 0.8	2.7 ± 0.4	0.01 ± 0.07	2.7 ± 0.4	94.9 ± 0.9	2.5 ± 0.6
Sham	0.0 ± 0.0	-	4.2 ± 0.7	2.7 ± 0.6	0.021 ± 0.013	2.7 ± 0.6	95.6 ± 0.7	1.6 ± 0.3

Table A.3: The results of the Caspase 3/7-Sytox assay. DR represents the dose rate, C+ Caspase 3/7 positive cells and S+ Sytox positive cells. C- and S- indicate cells without a Caspase 3/7 or a Sytox signal, respectively. In the last four rows of this table, the mean ± SEM is given for the four groups.

A.3 Results of the Caspase 3/7-Sytox assay

A.4 Results of the micronuclei test

Dose rate [Gy/s]	**Dose [Gy]**	**Percentage BN cells with MN [%]**				**Number of BN cells**
		1 MN	**2 MN**	**≥ 3 MN**	**total**	
0.06	2.27	27.1	1.5	1.5	30.2	199
0.06	3.28	22.9	5.0	0.9	28.9	537
0.06	2.57	25.0	3.7	1.9	30.6	108
0.06	2.66	26.5	3.0	1.8	31.3	336
0.06	2.61	18.8	4.1	2.9	25.8	414
9.3	3.79	25.3	6.6	0.0	31.9	91
9.3	3.68	29.1	9.3	1.3	39.7	151
9.3	3.32	21.2	5.3	1.2	27.7	321
9.3	3.71	26.4	1.4	0.0	27.8	72
9.3	3.71	24.8	4.4	3.9	33.0	206
310	3.11	21.1	4.3	0.6	26	322
310	3.56	13.0	4.6	0.8	18	131
310	3.23	21.7	9.7	3.4	35	175
310	2.90	23.2	6.3	1.4	31	142
0	0.00	5.8	0.53	0.0	6.3	190
0	0.00	3.9	0.78	0.0	4.7	255
0	0.00	4.1	0.46	0.0	4.6	218
0	0.00	4.1	0.29	0.0	4.4	340
0	0.00	2.7	0.00	0.0	2.7	259
Conv	2.68 ± 0.15	24.1 ± 1.4	3.4 ± 0.6	1.8 ± 0.4	29.3 ± 1.0	
Flash9	3.64 ± 0.08	25.3 ± 1.2	5.4 ± 1.2	1.3 ± 0.5	32.0 ± 2.0	
Flash310	3.20 ± 0.12	20.0 ± 2.0	6.2 ± 1.1	1.6 ± 0.7	28 ± 4	
Sham	0	4.1 ± 0.5	0.41 ± 0.12	0 ± 0	4.5 ± 0.6	

Table A.4: The results of the micronuclei test. BN stands for binucleated cells and MN for micronuclei.

A.5 Dose delivery to mouse ears

Mouse ID	**Dose rate [Gy/s]**	**Dose_{set} [Gy]**	**Dose_{irr} [Gy]**	**Δ Dose [Gy]**
1	Flash9	25	36.2	11.2
2	Flash9	35	47.4	12.4
3	Flash9	25	37.8	12.8
4	Conv	25	40.0	15.0
5	Flash930	35	28.6	6.4
6	Conv	35	42.6	7.6

7	Flash930	25	19.0	6.0
8	Conv	25	32.5	7.5
9	Flash930	35	35.6	0.6
10	Flash9	25	32.5	7.5
11	Flash9	35	42.3	7.3
12	Conv	35	47.2	12.2
13	Flash930	25	24.7	0.3
14	Sham	0	0.0	0.0
15	Sham	0	0.0	0.0
16	Flash9	35	7.0	28.0
17	Flash930	25	16.2	8.8
18	Conv	25	23.4	1.6
19	Flash930	35	36.5	1.5
20	Conv	35	33.2	1.8
21	Flash930	25	29.0	4.0
22	Conv	25	23.9	1.1
23	Flash930	35	32.3	2.7
24	Sham	0	0.0	0.0
25	Sham	0	0.0	0.0
26	Conv	35	33.1	1.9
28	Sham	0	0.0	0.0
29	Sham	0	0.0	0.0
30	Flash9	35	17.1	17.9
31	Flash9	25	22.8	2.2
32	Conv	25	23.8	1.2
33	Flash930	35	52.0	17.0
34	Conv	35	32.8	2.2
35	Flash930	25	28.3	3.3
36	Conv	25	22.1	2.9
37	Flash930	35	28.8	6.2
38	Flash9	25	25.2	0.2
39	Flash9	35	26.0	9.0
40	Conv	35	31.7	3.3
41	Flash930	25	35.9	10.9
42	Flash9	25	18.9	6.1
43	Flash9	25	21.4	3.6
44	Flash9	35	28.1	6.9
45	Sham	0	0.0	0.0
46	Conv	25	22.5	2.5
47	Flash930	35	31.0	4.0

48	Conv	35	34.4	0.6
49	Flash930	25	29.1	4.1
50	Conv	25	24.7	0.3
51	Flash930	35	44.7	9.7
52	Flash9	25	18.3	6.7
53	Flash9	35	23.1	11.9
54	Conv	35	30.9	4.1
55	Flash930	25	25.9	0.9
56	Flash9	35	26.5	8.5
57	Flash9	25	17.1	7.9
58	Flash9	35	30.1	4.9
59	Sham	0	0.0	0.0
60	Conv	25	23.6	1.4
61	Flash930	35	30.7	4.3
62	Conv	35	30.7	4.3
63	Flash930	25	34.0	9.0

Table A.5: The set doses $\mathrm{Dose}_{\mathrm{set}}$ and the actual irradiated doses $\mathrm{Dose}_{\mathrm{irr}}$ for every mouse. Mouse 27 is missing in this table, as this mouse was irradiated with a dose far too high ($>$ 60 Gy) due to a system failure and had to be euthanized immediately after irradiation.

Bibliography

[1] Benjamin Barnes, Enno Nowossadeck, Christoph Kowalski, and Sophie Schellack. Krebserkrankungen im erwerbsfähigen alter in deutschland, 2023. URL `https://www.krebsgesellschaft.de/files/dkg/deutsche-krebsgesellschaft/content/pdf/Zertifizierung/Publikationen/DKG_RKI_2023_20-64-J%C3%A4hrige.pdf`.

[2] 2023. URL `https://www.destatis.de/DE/Themen/Gesellschaft-Umwelt/Gesundheit/Todesursachen/_inhalt.html#235880`.

[3] Susan Magasi, Hilary K. Marshall, Cassandra Winters, and David Victorson. Cancer survivors' disability experiences and identities: A qualitative exploration to advance cancer equity. *International journal of environmental research and public health*, 19(5), 2022. doi: 10.3390/ijerph19053112.

[4] Mary C. White, Dawn M. Holman, Jennifer E. Boehm, Lucy A. Peipins, Melissa Grossman, and S. Jane Henley. Age and cancer risk: a potentially modifiable relationship. *American journal of preventive medicine*, 46(3 Suppl 1):S7–15, 2014. doi: 10.1016/j.amepre.2013.10.029.

[5] Geoff Delaney, Susannah Jacob, Carolyn Featherstone, and Michael Barton. The role of radiotherapy in cancer treatment: estimating optimal utilization from a review of evidence-based clinical guidelines. *Cancer*, 104(6):1129–1137, 2005. ISSN 0008-543X. doi: 10.1002/cncr.21324.

[6] Vincent Favaudon, Laura Caplier, Virginie Monceau, Frédéric Pouzoulet, Mano Sayarath, Charles Fouillade, Marie-France Poupon, Isabel Brito, Philippe Hupé, Jean Bourhis, Janet Hall, Jean-Jacques Fontaine, and Marie-Catherine Vozenin. Ultra-high dose-rate flash irradiation increases the differential response between normal and tumor tissue in mice. *Science translational medicine*, 6(245):245ra93, 2014. doi: 10.1126/scitranslmed.3008973.

[7] Yasaman Alaghband, Samantha N. Cheeks, Barrett D. Allen, Pierre Montay-Gruel, Ngoc-Lien Doan, Benoit Petit, Patrik Goncalves Jorge, Erich Giedzinski, Munjal M. Acharya, Marie-Catherine Vozenin, and Charles L. Limoli. Neuroprotection of radiosensitive juvenile mice by ultra-high dose rate flash irradiation. *Cancers*, 12(6), 2020. ISSN 2072-6694. doi: 10.3390/cancers12061671.

[8] Pierre Montay-Gruel, Kristoffer Petersson, Maud Jaccard, Gaël Boivin, Jean-François Germond, Benoit Petit, Raphaël Doenlen, Vincent Favaudon, François Bochud, Claude

Bailat, Jean Bourhis, and Marie-Catherine Vozenin. Irradiation in a flash: Unique sparing of memory in mice after whole brain irradiation with dose rates above 100gy/s. *Radiotherapy and oncology : journal of the European Society for Therapeutic Radiology and Oncology*, 124(3):365–369, 2017. doi: 10.1016/j.radonc.2017.05.003. URL `https://www.sciencedirect.com/science/article/pii/S0167814017303651`.

[9] Karen Levy, Suchitra Natarajan, Jinghui Wang, Stephanie Chow, Joshua T. Eggold, Phoebe E. Loo, Rakesh Manjappa, Stavros Melemenidis, Frederick M. Lartey, Emil Schüler, Lawrie Skinner, Marjan Rafat, Ryan Ko, Anna Kim, Duaa H Al-Rawi, Rie von Eyben, Oliver Dorigo, Kerriann M. Casey, Edward E. Graves, Karl Bush, Amy S. Yu, Albert C. Koong, Peter G. Maxim, Billy W. Loo, and Erinn B. Rankin. Abdominal flash irradiation reduces radiation-induced gastrointestinal toxicity for the treatment of ovarian cancer in mice. *Scientific reports*, 10(1):21600, 2020. doi: 10.1038/s41598-020-78017-7.

[10] Marie-Catherine Vozenin, Pauline de Fornel, Kristoffer Petersson, Vincent Favaudon, Maud Jaccard, Jean-François Germond, Benoit Petit, Marco Burki, Gisèle Ferrand, David Patin, Hanan Bouchaab, Mahmut Ozsahin, François Bochud, Claude Bailat, Patrick Devauchelle, and Jean Bourhis. The advantage of flash radiotherapy confirmed in mini-pig and cat-cancer patients. *Clinical cancer research : an official journal of the American Association for Cancer Research*, 25(1):35–42, 2019. doi: 10.1158/1078-0432.CCR-17-3375.

[11] Elke Beyreuther, Michael Brand, Stefan Hans, Katalin Hideghéty, Leonhard Karsch, Elisabeth Leßmann, Michael Schürer, Emília Rita Szabó, and Jörg Pawelke. Feasibility of proton flash effect tested by zebrafish embryo irradiation. *Radiotherapy and oncology : journal of the European Society for Therapeutic Radiology and Oncology*, 139:46–50, 2019. doi: 10.1016/j.radonc.2019.06.024.

[12] Charles Fouillade, Sandra Curras-Alonso, Lorena Giuranno, Eddy Quelennec, Sophie Heinrich, Sarah Bonnet-Boissinot, Arnaud Beddok, Sophie Leboucher, Hamza Umut Karakurt, Mylène Bohec, Sylvain Baulande, Marc Vooijs, Pierre Verrelle, Marie Dutreix, Arturo Londoño-Vallejo, and Vincent Favaudon. Flash irradiation spares lung progenitor cells and limits the incidence of radio-induced senescence. *Clinical cancer research : an official journal of the American Association for Cancer Research*, 26(6):1497–1506, 2020. doi: 10.1158/1078-0432.CCR-19-1440.

[13] Pierre Montay-Gruel, Munjal M. Acharya, Patrik Gonçalves Jorge, Benoît Petit, Ioannis G. Petridis, Philippe Fuchs, Ron Leavitt, Kristoffer Petersson, Maude Gondré, Jonathan Ollivier, Raphael Moeckli, François Bochud, Claude Bailat, Jean Bourhis, Jean-François Germond, Charles L. Limoli, and Marie-Catherine Vozenin. Hypofractionated flash-rt as an effective treatment against glioblastoma that reduces neurocognitive side effects in mice. *Clinical cancer research : an official journal of the American Association for Cancer Research*, 27(3):775–784, 2021. doi: 10.1158/1078-0432.CCR-20-0894.

[14] Young-Eun Kim, Seung-Hee Gwak, Beom-Ju Hong, Jung-Min Oh, Hyung-Seok Choi, Myeoung Su Kim, Dawit Oh, Frederik M. Lartey, Marjan Rafat, Emil Schüler, Hyo-Soo Kim, Rie von Eyben, Irving L. Weissman, Cameron J. Koch, Peter G. Maxim, Billy W. Loo, and G-One Ahn. Effects of ultra-high doserate flash irradiation on the tumor microenvironment in lewis lung carcinoma: Role of myosin light chain. *International journal of radiation oncology, biology, physics*, 109(5):1440–1453, 2021. doi: 10.1016/j.ijrobp.2020.11.012.

[15] Pierre Montay-Gruel, Audrey Bouchet, Maud Jaccard, David Patin, Raphael Serduc, Warren Aim, Kristoffer Petersson, Benoit Petit, Claude Bailat, Jean Bourhis, Elke Bräuer-Krisch, and Marie-Catherine Vozenin. X-rays can trigger the flash effect: Ultra-high dose-rate synchrotron light source prevents normal brain injury after whole brain irradiation in mice. *Radiotherapy and oncology : journal of the European Society for Therapeutic Radiology and Oncology*, 129(3):582–588, 2018. doi: 10.1016/j.radonc.2018.08.016.

[16] Shannon Cunningham, Shelby McCauley, Kanimozhi Vairamani, Joseph Speth, Swati Girdhani, Eric Abel, Ricky A. Sharma, John P. Perentesis, Susanne I. Wells, Anthony Mascia, and Mathieu Sertorio. Flash proton pencil beam scanning irradiation minimizes radiation-induced leg contracture and skin toxicity in mice. *Cancers*, 13(5), 2021. ISSN 2072-6694. doi: 10.3390/cancers13051012.

[17] Michele M. Kim, Ioannis I. Verginadis, Denisa Goia, Allison Haertter, Khayrullo Shoniyozov, Wei Zou, Amit Maity, Theresa M. Busch, James M. Metz, Keith A. Cengel, Lei Dong, Costas Koumenis, and Eric S. Diffenderfer. Comparison of flash proton entrance and the spread-out bragg peak dose regions in the sparing of mouse intestinal crypts and in a pancreatic tumor model. *Cancers*, 13(16), 2021. ISSN 2072-6694. doi: 10.3390/cancers13164244.

[18] Anastasia Velalopoulou, Ilias V. Karagounis, Gwendolyn M. Cramer, Michele M. Kim, Giorgos Skoufos, Denisa Goia, Sarah Hagan, Ioannis I. Verginadis, Khayrullo Shoniyozov, June Chiango, Michelle Cerullo, Kelley Varner, Lutian Yao, Ling Qin, Artemis G. Hatzigeorgiou, Andy J. Minn, Mary Putt, Matthew Lanza, Charles-Antoine Assenmacher, Enrico Radaelli, Jennifer Huck, Eric Diffenderfer, Lei Dong, James Metz, Constantinos Koumenis, Keith A. Cengel, Amit Maity, and Theresa M. Busch. Flash proton radiotherapy spares normal epithelial and mesenchymal tissues while preserving sarcoma response. *Cancer research*, 81(18):4808–4821, 2021. doi: 10.1158/0008-5472.CAN-21-1500.

[19] Walter Tinganelli, Olga Sokol, Martina Quartieri, Anggraeini Puspitasari, Ivana Dokic, Amir Abdollahi, Marco Durante, Thomas Haberer, Jürgen Debus, Daria Boscolo, Bernd Voss, Stephan Brons, Christoph Schuy, Felix Horst, and Ulrich Weber. Ultra-high dose rate (flash) carbon ion irradiation: Dosimetry and first cell experiments. *International journal of radiation oncology, biology, physics*, 112(4):1012–1022, 2022. doi: 10.1016/j.ijrobp.2021.11.020.

[20] Wolfgang Demtröder. *Atome, Moleküle und Festkörper*, volume 3 of *Springer-Lehrbuch*. Springer Spektrum, Berlin and Heidelberg, 5., neu bearbeitete und aktualisierte auflage edition, 2016. ISBN 978-3-662-49093-8. doi: 10.1007/978-3-662-49094-5.

[21] Gavin G. Poludniowski and Philip M. Evans. Calculation of x-ray spectra emerging from an x-ray tube. part i. electron penetration characteristics in x-ray targets. *Medical Physics*, 34(6):2164–2174, 2007. ISSN 2473-4209. doi: 10.1118/1.2734725.

[22] Gavin G. Poludniowski. Calculation of x-ray spectra emerging from an x-ray tube. part ii. x-ray production and filtration in x-ray targets. *Medical Physics*, 34(6):2175–2186, 2007. ISSN 2473-4209. doi: 10.1118/1.2734726.

[23] G. Poludniowski, G. Landry, F. DeBlois, P. M. Evans, and F. Verhaegen. Spekcalc: a program to calculate photon spectra from tungsten anode x-ray tubes. *Physics in medicine and biology*, 54(19):N433–8, 2009. doi: 10.1088/0031-9155/54/19/N01.

[24] Hanno Krieger. *Grundlagen der Strahlungsphysik und des Strahlenschutzes*. Springer eBook Collection. Vieweg+Teubner, Wiesbaden, 3., überarbeitete und erweiterte auflage edition, 2009. ISBN 9783834893482. doi: 10.1007/978-3-8348-9348-2.

[25] E.B. Podgorsak. *Radiation oncology physics: A Handbook for Teachers and Students*. International Atomic Energy Agency, Vienna, 2005. ISBN 92-0-107304-6.

[26] Paul Retif, Sophie Pinel, Magali Toussaint, Céline Frochot, Rima Chouikrat, Thierry Bastogne, and Muriel Barberi-Heyob. Nanoparticles for radiation therapy enhancement: the key parameters. *Theranostics*, 5(9):1030–1044, 2015. doi: 10.7150/thno.11642.

[27] Robin Hill, Brendan Healy, Lois Holloway, Zdenka Kuncic, David Thwaites, and Clive Baldock. Advances in kilovoltage x-ray beam dosimetry. *Physics in medicine and biology*, 59(6):R183–231, 2014. doi: 10.1088/0031-9155/59/6/R183.

[28] J. Perl, J. Shin, J. Schumann, B. Faddegon, and H. Paganetti. Topas: an innovative proton monte carlo platform for research and clinical applications. *Medical Physics*, 39 (11):6818–6837, 2012. ISSN 2473-4209. doi: 10.1118/1.4758060.

[29] James F. Ziegler, Jochen Biersack, and Matthias D. Ziegler. *SRIM - the stopping and range of ions in matter*. SRIM, Chester, Maryland, 2015. ISBN 9780965420716.

[30] J. F. Ziegler. Stopping of energetic light ions in elemental matter. *Journal of Applied Physics*, 85(3):1249–1272, 1999. ISSN 0021-8979. doi: 10.1063/1.369844.

[31] D. T. Goodhead. Spatial and temporal distribution of energy. *Health physics*, 55(2): 231–240, 1988. ISSN 0017-9078. doi: 10.1097/00004032-198808000-00015.

[32] Michael C. Joiner and Albert J. van der Kogel, editors. *Basic clinical radiobiology*. CRC Press Taylor & Francis Group, Boca Raton and London and New York, fifth edition edition, 2019. ISBN 9781444179637.

[33] H. H. Rossi. The role of microdosimetry in radiobiology. *Radiation and environmental biophysics*, 17(1):29–40, 1979. ISSN 0301-634X. doi: 10.1007/BF01323118.

[34] Jamshid Soltani-Nabipour, Abdollah Khorshidi, Faezeh Shojai, and Khazar Khorami. Evaluation of dose distribution from 12c ion in radiation therapy by fluka code. *Nuclear Engineering and Technology*, 52(10):2410–2414, 2020. ISSN 17385733. doi: 10.1016/j.net.2020.03.010.

[35] Barry Halliwell. *Free Radicals in Biology and Medicine.* OUP Oxford, Oxford, 2015. ISBN 9780198717485.

[36] Carlo M. Bergamini, Stefania Gambetti, Alessia Dondi, and Carlo Cervellati. Oxygen, reactive oxygen species and tissue damage. *Current pharmaceutical design*, 10(14):1611–1626, 2004. ISSN 1381-6128. doi: 10.2174/1381612043384664.

[37] Hongning Zhou, Mei Hong, Yunfei Chai, and Tom K. Hei. Consequences of cytoplasmic irradiation: studies from microbeam. *Journal of radiation research*, 50 Suppl A(0 0): A59–65, 2009. ISSN 0449-3060. doi: 10.1269/jrr.08120s.

[38] Nicolaas A. P. Franken, Hans M. Rodermond, Jan Stap, Jaap Haveman, and Chris van Bree. Clonogenic assay of cells in vitro. *Nature protocols*, 1(5):2315–2319, 2006. doi: 10.1038/nprot.2006.339.

[39] David S. Chang. *Basic Radiotherapy Physics and Biology.* Springer International Publishing AG, Cham, 2014. ISBN 9783319068411.

[40] Maarten Niemantsverdriet, Marc-Jan van Goethem, Reinier Bron, Wytse Hogewerf, Sytze Brandenburg, Johannes A. Langendijk, Peter van Luijk, and Robert P. Coppes. High and low let radiation differentially induce normal tissue damage signals. *International journal of radiation oncology, biology, physics*, 83(4):1291–1297, 2012. doi: 10.1016/j.ijrobp.2011.09.057.

[41] Anna Kirstein, Daniela Schilling, Stephanie E. Combs, and Thomas E. Schmid. Lomeguatrib increases the radiosensitivity of mgmt unmethylated human glioblastoma multiforme cell lines. *International journal of molecular sciences*, 22(13), 2021. doi: 10.3390/ijms22136781.

[42] Stephen Joseph McMahon. The linear quadratic model: usage, interpretation and challenges. *Physics in medicine and biology*, 64(1):01TR01, 2018. doi: 10.1088/1361-6560/aaf26a.

[43] Melvin Astrahan. Some implications of linear-quadratic-linear radiation dose-response with regard to hypofractionation. *Medical Physics*, 35(9):4161–4172, 2008. ISSN 2473-4209. doi: 10.1118/1.2969065.

[44] Katherina Munk. *Grundstudium Biologie - Biochemie, Zellbiologie,Ökologie, Evolution.* Spektrum Akademischer Verlag, Heidelberg and Berlin, 2000. ISBN 3827409101.

[45] Renate Huch. *Mensch Körper Krankheit.* Elsevier Health Sciences Germany, London, 6th ed (online-ausg.) edition, 2013. ISBN 9783437596391.

[46] J. A. Huberman and A. D. Riggs. On the mechanism of dna replication in mammalian chromosomes. *Journal of molecular biology*, 32(2):327–341, 1968. ISSN 0022-2836. doi: 10.1016/0022-2836(68)90013-2.

[47] Alberto Signore, editor. *Nuclear Medicine and Molecular Imaging.* Elsevier, San Diego, 2022. ISBN 9780128229804.

[48] Jonathan A. Ewald, Joshua A. Desotelle, George Wilding, and David F. Jarrard. Therapy-induced senescence in cancer. *Journal of the National Cancer Institute*, 102 (20):1536–1546, 2010. doi: 10.1093/jnci/djq364.

[49] P. Giglio and M. R. Gilbert. Glial tumors. In Michael J. Aminoff and Robert B. Daroff, editors, *Encyclopedia of the neurological sciences*, pages 438–447. Academic Press Elsevier, London and Waltham, MA and SanDiegeo, 2014. ISBN 9780123851581. doi: 10.1016/B978-0-12-385157-4.00485-1.

[50] W. K. Sinclair and R. A. Morton. X-ray and ultraviolet sensitivity of synchronized chinese hamster cells at various stages of the cell cycle. *Biophysical journal*, 5(1):1–25, 1965. ISSN 0006-3495. doi: 10.1016/s0006-3495(65)86700-5.

[51] Philip Hahnfeldt and Lynn Hlatky. Resensitization due to redistribution of cells in the phases of the cell cycle during arbitrary radiation protocols. *Radiation Research*, 145 (2):134, 1996. ISSN 00337587. doi: 10.2307/3579167.

[52] Henry Tat Kwong Tse, Westbrook McConnell Weaver, and Dino Di Carlo. Increased asymmetric and multi-daughter cell division in mechanically confined microenvironments. *PloS one*, 7(6):e38986, 2012. doi: 10.1371/journal.pone.0038986.

[53] Sophia Shaka, Nicolas Carpo, Victoria Tran, Carlos Cepeda, and Araceli Espinosa-Jeffrey. Space microgravity alters neural stem cell division: Implications for brain cancer research on earth and in space. *International journal of molecular sciences*, 23(22), 2022. doi: 10.3390/ijms232214320.

[54] K. Collins, T. Jacks, and N. P. Pavletich. The cell cycle and cancer. *Proceedings of the National Academy of Sciences of the United States of America*, 94(7):2776–2778, 1997. ISSN 0027-8424. doi: 10.1073/pnas.94.7.2776.

[55] M. C. Joiner, B. Marples, P. Lambin, S. C. Short, and I. Turesson. Low-dose hypersensitivity: current status and possible mechanisms. *International journal of radiation oncology, biology, physics*, 49(2):379–389, 2001. doi: 10.1016/s0360-3016(00)01471-1.

[56] Daniel J. Klionsky. Autophagy: from phenomenology to molecular understanding in less than a decade. *Nature reviews. Molecular cell biology*, 8(11):931–937, 2007. doi: 10.1038/nrm2245.

[57] Rasoul Yahyapour, Elahe Motevaseli, Abolhasan Rezaeyan, Hamid Abdollahi, Bagher Farhood, Mohsen Cheki, Masoud Najafi, and Vilmar Villa. Mechanisms of radiation bystander and non-targeted effects: Implications to radiation carcinogenesis and radiotherapy. *Current radiopharmaceuticals*, 11(1):34–45, 2018. doi: 10.2174/1874471011666171229123130.

[58] Ziqi Zhang, Kui Li, and Mei Hong. Radiation-induced bystander effect and cytoplasmic irradiation studies with microbeams. *Biology*, 11(7), 2022. ISSN 2079-7737. doi: 10.3390/biology11070945.

[59] Safura Jokar, Inês A. Marques, Saeedeh Khazaei, Tania Martins-Marques, Henrique Girao, Mafalda Laranjo, and Maria Filomena Botelho. The footprint of exosomes in the radiation-induced bystander effects. *Bioengineering (Basel, Switzerland)*, 9(6), 2022. ISSN 2306-5354. doi: 10.3390/bioengineering9060243.

[60] Nasir Jalal, Saba Haq, Namrah Anwar, Saadiya Nazeer, and Umar Saeed. Radiation induced bystander effect and dna damage. *Journal of cancer research and therapeutics*, 10(4):819–833, 2014. doi: 10.4103/0973-1482.144587.

[61] C. Mothersill and C. Seymour. Medium from irradiated human epithelial cells but not human fibroblasts reduces the clonogenic survival of unirradiated cells. *International journal of radiation biology*, 71(4):421–427, 1997. ISSN 0955-3002. doi: 10.1080/095530097144030.

[62] Nicole Matejka and Judith Reindl. Perspectives of cellular communication through tunneling nanotubes in cancer cells and the connection to radiation effects. *Radiation oncology (London, England)*, 14(1):218, 2019. doi: 10.1186/s13014-019-1416-8.

[63] Alicia Marín, Margarita Martín, Olga Liñán, Felipe Alvarenga, Mario López, Laura Fernández, David Büchser, and Laura Cerezo. Bystander effects and radiotherapy. *Reports of practical oncology and radiotherapy : journal of Greatpoland Cancer Center in Poznan and Polish Society of Radiation Oncology*, 20(1):12–21, 2015. ISSN 1507-1367. doi: 10.1016/j.rpor.2014.08.004.

[64] H. R. Withers, J. M. Taylor, and B. Maciejewski. Treatment volume and tissue tolerance. *International journal of radiation oncology, biology, physics*, 14(4):751–759, 1988. doi: 10.1016/0360-3016(88)90098-3.

[65] Narayanan Parameswaran and Sonika Patial. Tumor necrosis factor-α signaling in macrophages. *Critical reviews in eukaryotic gene expression*, 20(2):87–103, 2010. ISSN 1045-4403. doi: 10.1615/critreveukargeneexpr.v20.i2.10.

[66] Dan-In Jang, A-Hyeon Lee, Hye-Yoon Shin, Hyo-Ryeong Song, Jong-Hwi Park, Tae-Bong Kang, Sang-Ryong Lee, and Seung-Hoon Yang. The role of tumor necrosis factor alpha (tnf-α) in autoimmune disease and current tnf-α inhibitors in therapeutics. *International journal of molecular sciences*, 22(5), 2021. doi: 10.3390/ijms22052719.

[67] Sylwia Michlewska, Ian Dransfield, Ian L. Megson, and Adriano G. Rossi. Macrophage phagocytosis of apoptotic neutrophils is critically regulated by the opposing actions of pro-inflammatory and anti-inflammatory agents: key role for tnf-alpha. *FASEB journal : official publication of the Federation of American Societies for Experimental Biology*, 23(3):844–854, 2009. doi: 10.1096/fj.08-121228.

[68] Inès Zidi, Souhir Mestiri, Aghleb Bartegi, and Nidhal Ben Amor. Tnf-alpha and its inhibitors in cancer. *Medical oncology (Northwood, London, England)*, 27(2):185–198, 2010. doi: 10.1007/s12032-009-9190-3.

[69] Sang Heui Seo and Robert G. Webster. Tumor necrosis factor alpha exerts powerful anti-influenza virus effects in lung epithelial cells. *Journal of virology*, 76(3):1071–1076, 2002. ISSN 0022-538X. doi: 10.1128/jvi.76.3.1071-1076.2002.

[70] Claudia E. Rübe, Falk Wilfert, Daniela Uthe, Kurt W. Schmid, Reinhild Knoop, Norman Willich, Andreas Schuck, and Christian Rübe. Modulation of radiation-induced tumour necrosis factor alpha (tnf-alpha) expression in the lung tissue by pentoxifylline. *Radiotherapy and Oncology*, 64(2):177–187, 2002. ISSN 0167-8140. doi: 10.1016/s0167-8140(02)00077-4.

[71] Charles A. Dinarello. Overview of the il-1 family in innate inflammation and acquired immunity. *Immunological reviews*, 281(1):8–27, 2018. doi: 10.1111/imr.12621.

[72] Joost J. Oppenheim, editor. *Cytokine reference: A compendium of cytokines and other mediators of host defense.* Acad. Press, San Diego, 2001. ISBN 0122526708.

[73] Yun Yang, Wen-Long Ye, Ruo-Nan Zhang, Xiao-Shun He, Jing-Ru Wang, Yu-Xuan Liu, Yi Wang, Xue-Mei Yang, Yu-Juan Zhang, and Wen-Juan Gan. The role of tgf-β signaling pathways in cancer and its potential as a therapeutic target. *Evidence-based complementary and alternative medicine : eCAM*, 2021:6675208, 2021. ISSN 1741-427X. doi: 10.1155/2021/6675208.

[74] H. Kimura, T. Ishibashi, Y. Shikama, A. Okano, Y. Akiyama, T. Uchida, and Y. Maruyama. Interleukin-1 beta (il-1 beta) induces thrombocytosis in mice: possible implication of il-6. *Blood*, 76(12):2493–2500, 1990. ISSN 0006-4971. doi: 10.1182/blood.V76.12.2493.2493.

[75] Keunhee Oh, Ok-Young Lee, Yeonju Park, Myung Won Seo, and Dong-Sup Lee. Il-1β induces il-6 production and increases invasiveness and estrogen-independent growth in a tg2-dependent manner in human breast cancer cells. *BMC cancer*, 16(1):724, 2016. doi: 10.1186/s12885-016-2746-7.

[76] Weimin Liu, Ivan Ding, Keqiang Chen, John Olschowka, Jianhua Xu, Dongping Hu, Gary R. Morrow, and Paul Okunieff. Interleukin 1beta (il1b) signaling is a critical component of radiation-induced skin fibrosis. *Radiation Research*, 165(2):181–191, 2006. ISSN 00337587. doi: 10.1667/rr3478.1.

[77] Cristina M. DeCesaris, Stephanie R. Rice, Soren M. Bentzen, Jenna Jatczak, Mark V. Mishra, and Elizabeth M. Nichols. Quantification of acute skin toxicities in patients with breast cancer undergoing adjuvant proton versus photon radiation therapy: A single institutional experience. *International journal of radiation oncology, biology, physics*, 104(5):1084–1090, 2019. doi: 10.1016/j.ijrobp.2019.04.015.

[78] Hafsa Majeed and Vikas Gupta. *Adverse Effects Of Radiation Therapy.* Treasure Island (FL), 2022.

[79] Kerstin Müller and Viktor Meineke. Radiation-induced alterations in cytokine production by skin cells. *Experimental Hematology*, 35(4, Supplement):96–104, 2007. ISSN 0301-472X. doi: 10.1016/j.exphem.2007.01.017. URL `https://www.sciencedirect.com/science/article/pii/S0301472X07000203`.

[80] Esther Lutgens, Marion Gijbels, Marjan Smook, Peter Heeringa, Philip Gotwals, Victor E. Koteliansky, and Mat J. A. P. Daemen. Transforming growth factor-beta mediates balance between inflammation and fibrosis during plaque progression. *Arteriosclerosis, thrombosis, and vascular biology*, 22(6):975–982, 2002. doi: 10.1161/01.atv.0000019729.39500.2f.

[81] Walter Huda and Richard M. Slone. *Review of radiologic physics.* Lippincott Williams & Wilkins, Philadelphia, 2nd ed. edition, 2003. ISBN 9780781736756.

[82] Erica B. Collen and Monique N. Mayer. Acute effects of radiation treatment: skin reactions. *The Canadian veterinary journal = La revue veterinaire canadienne*, 47(9):931–2, 934–5, 2006. ISSN 0008-5286.

[83] David S. Chang, Foster D. Lasley, Indra J. Das, Marc S. Mendonca, and Joseph R. Dynlacht. Normal tissue radiation responses. In David S. Chang, Foster D. Lasley, Indra J. Das, Marc S. Mendonca, and Joseph R. Dynlacht, editors, *Basic Radiotherapy Physics and Biology*, pages 265–275. Springer International Publishing, Cham and s.l., 2014. ISBN 978-3-319-06840-4. doi: 10.1007/978-3-319-06841-1_26.

[84] Houda Kacem, Aymeric Almeida, Nicolas Cherbuin, and Marie-Catherine Vozenin. Understanding the flash effect to unravel the potential of ultra-high dose rate irradiation. *International journal of radiation biology*, 98(3):506–516, 2022. ISSN 0955-3002. doi: 10.1080/09553002.2021.2004328.

[85] M-C Vozenin, J. H. Hendry, and C. L. Limoli. Biological benefits of ultra-high dose rate flash radiotherapy: Sleeping beauty awoken. *Clinical oncology (Royal College of Radiologists (Great Britain))*, 31(7):407–415, 2019. doi: 10.1016/j.clon.2019.04.001.

[86] Danielle A. Simmons, Frederick M. Lartey, Emil Schüler, Marjan Rafat, Gregory King, Anna Kim, Ryan Ko, Sarah Semaan, Selena Gonzalez, Melissa Jenkins, Pooja Pradhan, Zion Shih, Jinghui Wang, Rie von Eyben, Edward E. Graves, Peter G. Maxim, Frank M. Longo, and Billy W. Loo. Reduced cognitive deficits after flash irradiation of whole mouse brain are associated with less hippocampal dendritic spine loss and

neuroinflammation. *Radiotherapy and oncology : journal of the European Society for Therapeutic Radiology and Oncology*, 139:4–10, 2019. doi: 10.1016/j.radonc.2019.06.006.

[87] Milos Pekny and Marcela Pekna. Astrocyte reactivity and reactive astrogliosis: costs and benefits. *Physiological reviews*, 94(4):1077–1098, 2014. doi: 10.1152/physrev.00041.2013.

[88] Elise Konradsson, Maja L. Arendt, Kristine Bastholm Jensen, Betina Børresen, Anders E. Hansen, Sven Bäck, Annemarie T. Kristensen, Per Munck Af Rosenschöld, Crister Ceberg, and Kristoffer Petersson. Establishment and initial experience of clinical flash radiotherapy in canine cancer patients. *Frontiers in oncology*, 11, 2021. ISSN 2234-943X.

[89] Jean Bourhis, Wendy Jeanneret Sozzi, Patrik Gonçalves Jorge, Olivier Gaide, Claude Bailat, Fréderic Duclos, David Patin, Mahmut Ozsahin, François Bochud, Jean-François Germond, Raphaël Moeckli, and Marie-Catherine Vozenin. Treatment of a first patient with flash-radiotherapy. *Radiotherapy and oncology : journal of the European Society for Therapeutic Radiology and Oncology*, 139:18–22, 2019. doi: 10.1016/j.radonc.2019.06.019.

[90] Michael Lempart, Börje Blad, Gabriel Adrian, Sven Bäck, Tommy Knöös, Crister Ceberg, and Kristoffer Petersson. Modifying a clinical linear accelerator for delivery of ultra-high dose rate irradiation. *Radiotherapy and oncology : journal of the European Society for Therapeutic Radiology and Oncology*, 139:40–45, 2019. doi: 10.1016/j.radonc.2019.01.031.

[91] Pierre Korysko, Joseph Bateman, Roberto Corsini, Luke Dyks, Wilfrid Farabolini, Vilde Rieker, and Cameron Robertson, editors. *Methods for VHEE/FLASH Radiotherapy Studies and High Dose Rate Dosimetry at the CLEAR User Facility: JACoW Publishing, Geneva, Switzerland*, 2022. doi: 10.18429/JACOW-LINAC2022-THPOPA06.

[92] Maria Grazia Ronga, Marco Cavallone, Annalisa Patriarca, Amelia Maia Leite, Pierre Loap, Vincent Favaudon, Gilles Créhange, and Ludovic de Marzi. Back to the future: Very high-energy electrons (vhees) and their potential application in radiation therapy. *Cancers*, 13(19), 2021. ISSN 2072-6694. doi: 10.3390/cancers13194942.

[93] Anthony E. Mascia, Emily C. Daugherty, Yongbin Zhang, Eunsin Lee, Zhiyan Xiao, Mathieu Sertorio, Jennifer Woo, Lori R. Backus, Julie M. McDonald, Claire McCann, Kenneth Russell, Lisa Levine, Ricky A. Sharma, Dee Khuntia, Jeffrey D. Bradley, Charles B. Simone, John P. Perentesis, and John C. Breneman. Proton flash radiotherapy for the treatment of symptomatic bone metastases: The fast-01 nonrandomized trial. *JAMA oncology*, 9(1):62–69, 2023. doi: 10.1001/jamaoncol.2022.5843.

[94] John C. Breneman. Flash radiotherapy for the treatment of symptomatic bone metastases in the thorax (fast-02): Clinical trial, 2022. URL `https://clinicaltrials.gov/ct2/show/study/NCT05524064`.

[95] Pierre Montay-Gruel, Stéphanie Corde, Jean A. Laissue, and Magdalena Bazalova-Carter. Flash radiotherapy with photon beams. *Medical Physics*, 49(3):2055–2067, 2022. ISSN 2473-4209. doi: 10.1002/mp.15222.

[96] Leonhard Karsch, Jörg Pawelke, Michael Brand, Stefan Hans, Katalin Hideghéty, Jeannette Jansen, Elisabeth Lessmann, Steffen Löck, Michael Schürer, Rico Schurig, Joao Seco, Emília Rita Szabó, and Elke Beyreuther. Beam pulse structure and dose rate as determinants for the flash effect observed in zebrafish embryo. *Radiotherapy and Oncology*, 173:49–54, 2022. ISSN 0167-8140. doi: 10.1016/j.radonc.2022.05.025. URL `https://www.sciencedirect.com/science/article/pii/S0167814022041317`.

[97] Jörg Pawelke, Michael Brand, Stefan Hans, Katalin Hideghéty, Leonhard Karsch, Elisabeth Lessmann, Steffen Löck, Michael Schürer, Emília Rita Szabó, and Elke Beyreuther. Electron dose rate and oxygen depletion protect zebrafish embryos from radiation damage. *Radiotherapy and oncology : journal of the European Society for Therapeutic Radiology and Oncology*, 158:7–12, 2021. doi: 10.1016/j.radonc.2021.02.003.

[98] Jia-Ling Ruan, Carl Lee, Shari Wouters, Iain D. C. Tullis, Mieke Verslegers, Mohamed Mysara, Chee Kin Then, Sean C. Smart, Mark A. Hill, Ruth J. Muschel, Amato J. Giaccia, Borivoj Vojnovic, Anne E. Kiltie, and Kristoffer Petersson. Irradiation at ultra-high (flash) dose rates reduces acute normal tissue toxicity in the mouse gastrointestinal system. *International journal of radiation oncology, biology, physics*, 111(5):1250–1261, 2021. doi: 10.1016/j.ijrobp.2021.08.004.

[99] O. Zlobinskaya, C. Siebenwirth, C. Greubel, V. Hable, R. Hertenberger, N. Humble, S. Reinhardt, D. Michalski, B. Röper, G. Multhoff, G. Dollinger, J. J. Wilkens, and T. E. Schmid. The effects of ultra-high dose rate proton irradiation on growth delay in the treatment of human tumor xenografts in nude mice. *Radiation Research*, 181(2): 177–183, 2014. ISSN 00337587. doi: 10.1667/RR13464.1.

[100] J. H. Hendry, J. V. Moore, B. W. Hodgson, and J. P. Keene. The constant low oxygen concentration in all the target cells for mouse tail radionecrosis. *Radiation Research*, 92 (1):172, 1982. ISSN 00337587. doi: 10.2307/3575852.

[101] Pierre Montay-Gruel, Munjal M. Acharya, Kristoffer Petersson, Leila Alikhani, Chakradhar Yakkala, Barrett D. Allen, Jonathan Ollivier, Benoit Petit, Patrik Gonçalves Jorge, Amber R. Syage, Thuan A. Nguyen, Al Anoud D. Baddour, Celine Lu, Paramvir Singh, Raphael Moeckli, François Bochud, Jean-François Germond, Pascal Froidevaux, Claude Bailat, Jean Bourhis, Marie-Catherine Vozenin, and Charles L. Limoli. Long-term neurocognitive benefits of flash radiotherapy driven by reduced reactive oxygen species. *Proceedings of the National Academy of Sciences of the United States of America*, 116(22):10943–10951, 2019. ISSN 0027-8424. doi: 10.1073/pnas.1901777116.

[102] Eline Hageman, Pei-Pei Che, Max Dahele, Ben J. Slotman, and Peter Sminia. Ra-

diobiological aspects of flash radiotherapy. *Biomolecules*, 12(10), 2022. doi: 10.3390/biom12101376.

[103] Marco Durante, Elke Bräuer-Krisch, and Mark Hill. Faster and safer? flash ultra-high dose rate in radiotherapy. *The British journal of radiology*, 91(1082):20170628, 2018. doi: 10.1259/bjr.20170628.

[104] Lloyd M. L. Smyth, Jacqueline F. Donoghue, Jessica A. Ventura, Jayde Livingstone, Tracy Bailey, Liam R. J. Day, Jeffrey C. Crosbie, and Peter A. W. Rogers. Comparative toxicity of synchrotron and conventional radiation therapy based on total and partial body irradiation in a murine model. *Scientific reports*, 8(1):12044, 2018. doi: 10.1038/s41598-018-30543-1.

[105] P. Wilson, B. Jones, T. Yokoi, M. Hill, and B. Vojnovic. Revisiting the ultra-high dose rate effect: implications for charged particle radiotherapy using protons and light ions. *The British journal of radiology*, 85(1018):e933–9, 2012. doi: 10.1259/bjr/17827549.

[106] Guillem Pratx and Daniel S. Kapp. A computational model of radiolytic oxygen depletion during flash irradiation and its effect on the oxygen enhancement ratio. *Physics in medicine and biology*, 64(18):185005, 2019. doi: 10.1088/1361-6560/ab3769.

[107] Joseph D. Wilson, Ester M. Hammond, Geoff S. Higgins, and Kristoffer Petersson. Ultra-high dose rate (flash) radiotherapy: Silver bullet or fool's gold? *Frontiers in oncology*, 9:1563, 2019. ISSN 2234-943X. doi: 10.3389/fonc.2019.01563.

[108] R. J. Berry and J. B. Stedeford. Reproductive survival of mammalian cells after irradiation at ultra-high dose-rates: further observations and their importance for radiotherapy. *The British journal of radiology*, 45(531):171–177, 1972. doi: 10.1259/0007-1285-45-531-171.

[109] Edward R. Epp, Herbert Weiss, and Ann Santomasso. The oxygen effect in bacterial cells irradiated with high-intensity pulsed electrons. *Radiation Research*, 34(2):320, 1968. ISSN 00337587. doi: 10.2307/3572557.

[110] T. L. Phillips and B. R. Worsnop. Ultra-high dose-rate effects in radiosensitive bacteria. *International journal of radiation biology and related studies in physics, chemistry, and medicine*, 14(6):573–575, 1969. ISSN 0020-7616. doi: 10.1080/09553006914551761.

[111] A. H. Nias, A. J. Swallow, J. P. Keene, and B. W. Hodgson. Effects of pulses of radiation on the survival of mammalian cells. *The British journal of radiology*, 42(499):553, 1969. doi: 10.1259/0007-1285-42-499-553-b.

[112] Gabriel Adrian, Elise Konradsson, Michael Lempart, Sven Bäck, Crister Ceberg, and Kristoffer Petersson. The flash effect depends on oxygen concentration. *The British journal of radiology*, 93(1106):20190702, 2020. doi: 10.1259/bjr.20190702.

[113] S. R. McKeown. Defining normoxia, physoxia and hypoxia in tumours-implications for treatment response. *The British journal of radiology*, 87(1035):20130676, 2014. doi: 10.1259/bjr.20130676.

[114] Jeannette Jansen, Jan Knoll, Elke Beyreuther, Jörg Pawelke, Raphael Skuza, Rachel Hanley, Stephan Brons, Francesca Pagliari, and Joao Seco. Does flash deplete oxygen? experimental evaluation for photons, protons, and carbon ions. *Medical Physics*, 48(7): 3982–3990, 2021. ISSN 2473-4209. doi: 10.1002/mp.14917.

[115] L. J. Wu, G. Randers-Pehrson, A. Xu, C. A. Waldren, C. R. Geard, Z. Yu, and T. K. Hei. Targeted cytoplasmic irradiation with alpha particles induces mutations in mammalian cells. *Proceedings of the National Academy of Sciences of the United States of America*, 96(9):4959–4964, 1999. ISSN 0027-8424. doi: 10.1073/pnas.96.9.4959.

[116] T. K. Hei, L. J. Wu, S. X. Liu, D. Vannais, C. A. Waldren, and G. Randers-Pehrson. Mutagenic effects of a single and an exact number of alpha particles in mammalian cells. *Proceedings of the National Academy of Sciences of the United States of America*, 94 (8):3765–3770, 1997. ISSN 0027-8424. doi: 10.1073/pnas.94.8.3765.

[117] Manuela Buonanno, Veljko Grilj, and David J. Brenner. Biological effects in normal cells exposed to flash dose rate protons. *Radiotherapy and oncology : journal of the European Society for Therapeutic Radiology and Oncology*, 139:51–55, 2019. doi: 10.1016/j.radonc.2019.02.009.

[118] Jennifer S. Dickey, Christophe E. Redon, Asako J. Nakamura, Brandon J. Baird, Olga A. Sedelnikova, and William M. Bonner. H2ax: functional roles and potential applications. *Chromosoma*, 118(6):683–692, 2009. doi: 10.1007/s00412-009-0234-4.

[119] Mohammad Mirza-Aghazadeh-Attari, Amir Mohammadzadeh, Bahman Yousefi, Ainaz Mihanfar, Ansar Karimian, and Maryam Majidinia. 53bp1: A key player of dna damage response with critical functions in cancer. *DNA repair*, 73:110–119, 2019. doi: 10.1016/j.dnarep.2018.11.008.

[120] O. Zlobinskaya, T. E. Schmid, G. Dollinger, V. Hable, C. Greubel, D. Michalski, J. Wilkens, G. Du, M. Molls, and B. Röper. Differences in gamma-h2ax foci formation after irradiation with continuous and pulsed proton beams. In Ratko Magjarevic, Olaf Dössel, and Wolfgang C. Schlegel, editors, *Radiation protection and dosimetry, biologcal effects of radiation*, volume 25/3 of *IFMBE Proceedings*, pages 142–145. Springer Berlin Heidelberg, Berlin, Heidelberg, 2009. ISBN 978-3-642-03901-0. doi: 10.1007/978-3-642-03902-7_41.

[121] Thomas E. Schmid, Günther Dollinger, Volker Hable, Christoph Greubel, Olga Zlobinskaya, Dörte Michalski, Michael Molls, and Barbara Röper. Relative biological effectiveness of pulsed and continuous 20 mev protons for micronucleus induction in 3d human reconstructed skin tissue. *Radiotherapy and oncology : journal of the European Society for Therapeutic Radiology and Oncology*, 95(1):66–72, 2010. doi: 10.1016/j.radonc.2010.03.010.

[122] T. E. Schmid, G. Dollinger, V. Hable, C. Greubel, O. Zlobinskaya, D. Michalski, S. Auer, A. A. Friedl, E. Schmid, M. Molls, and B. Röper. The effectiveness of 20 mev protons at nanosecond pulse lengths in producing chromosome aberrations in human-hamster hybrid cells. *Radiation Research*, 175(6):719–727, 2011. ISSN 00337587. doi: 10.1667/RR2465.1.

[123] Sylwester Sommer, Iwona Buraczewska, and Marcin Kruszewski. Micronucleus assay: The state of art, and future directions. *International journal of molecular sciences*, 21 (4), 2020. doi: 10.3390/ijms21041534.

[124] Marco Durante and Silvia C. Formenti. Radiation-induced chromosomal aberrations and immunotherapy: Micronuclei, cytosolic dna, and interferon-production pathway. *Frontiers in oncology*, 8:192, 2018. ISSN 2234-943X. doi: 10.3389/fonc.2018.00192.

[125] Guangming Zhou. Mechanisms underlying flash radiotherapy, a novel way to enlarge the differential responses to ionizing radiation between normal and tumor tissues. *Radiation Medicine and Protection*, 1(1):35–40, 2020. ISSN 2666-5557. doi: 10.1016/j.radmp.2020.02.002. URL `https://www.sciencedirect.com/science/article/pii/S2666555720300083`.

[126] Shiying Wu, Qian Zhang, Fei Zhang, Fansen Meng, Shengduo Liu, Ruyuan Zhou, Qingzhe Wu, Xinran Li, Li Shen, Jun Huang, Jun Qin, Songying Ouyang, Zongping Xia, Hai Song, Xin-Hua Feng, Jian Zou, and Pinglong Xu. Her2 recruits akt1 to disrupt sting signalling and suppress antiviral defence and antitumour immunity. *Nature cell biology*, 21(8):1027–1040, 2019. doi: 10.1038/s41556-019-0352-z.

[127] John Kwon and Samuel F. Bakhoum. The cytosolic dna-sensing cgas-sting pathway in cancer. *Cancer discovery*, 10(1):26–39, 2020. doi: 10.1158/2159-8290.CD-19-0761.

[128] Audrey Lasry and Yinon Ben-Neriah. Senescence-associated inflammatory responses: aging and cancer perspectives. *Trends in Immunology*, 36(4):217–228, 2015. ISSN 1471-4906. doi: 10.1016/j.it.2015.02.009. URL `https://www.sciencedirect.com/science/article/pii/S147149061500040X`.

[129] Claire Vanpouille-Box, Julie M. Diamond, Karsten A. Pilones, Jiri Zavadil, James S. Babb, Silvia C. Formenti, Mary Helen Barcellos-Hoff, and Sandra Demaria. Tgfβ is a master regulator of radiation therapy-induced antitumor immunity. *Cancer research*, 75 (11):2232–2242, 2015. doi: 10.1158/0008-5472.CAN-14-3511.

[130] Jonathan R. Hughes and Jason L. Parsons. Flash radiotherapy: Current knowledge and future insights using proton-beam therapy. *International journal of molecular sciences*, 21(18), 2020. doi: 10.3390/ijms21186492.

[131] A. Hauptner, S. Dietzel, G. A. Drexler, P. Reichart, R. Krücken, T. Cremer, A. A. Friedl, and G. Dollinger. Microirradiation of cells with energetic heavy ions. *Radiation and environmental biophysics*, 42(4):237–245, 2004. ISSN 0301-634X. doi: 10.1007/s00411-003-0222-7.

[132] Stefanie Girst, Christoph Greubel, Judith Reindl, Christian Siebenwirth, Olga Zlobinskaya, Dietrich W. M. Walsh, Katarina Ilicic, Michaela Aichler, Axel Walch, Jan J. Wilkens, Gabriele Multhoff, Günther Dollinger, and Thomas E. Schmid. Proton minibeam radiation therapy reduces side effects in an in vivo mouse ear model. *International journal of radiation oncology, biology, physics*, 95(1):234–241, 2016. doi: 10.1016/j.ijrobp.2015.10.020.

[133] Matthias Sammer, Annique C. Dombrowsky, Jannis Schauer, Kateryna Oleksenko, Sandra Bicher, Benjamin Schwarz, Sarah Rudigkeit, Nicole Matejka, Judith Reindl, Stefan Bartzsch, Andreas Blutke, Annette Feuchtinger, Stephanie E. Combs, Günther Dollinger, and Thomas E. Schmid. Normal tissue response of combined temporal and spatial fractionation in proton minibeam radiation therapy. *International journal of radiation oncology, biology, physics*, 109(1):76–83, 2021. doi: 10.1016/j.ijrobp.2020.08.027.

[134] Harry Scherthan, Stephanie-Quinta Wagner, Jan Grundhöfer, Nicole Matejka, Jessica Müller, Steffen Müller, Sarah Rudigkeit, Matthias Sammer, Sarah Schoof, Matthias Port, and Judith Reindl. Planar proton minibeam irradiation elicits spatially confined dna damage in a human epidermis model. *Cancers*, 14(6), 2022. ISSN 2072-6694. doi: 10.3390/cancers14061545.

[135] V. Hable, C. Greubel, A. Bergmaier, P. Reichart, A. Hauptner, R. Krücken, H. Strickfaden, S. Dietzel, T. Cremer, G. A. Drexler, A. A. Friedl, and G. Dollinger. The live cell irradiation and observation setup at snake. *Nuclear Instruments and Methods in Physics Research Section B: Beam Interactions with Materials and Atoms*, 267(12-13): 2090–2097, 2009. ISSN 0168583X. doi: 10.1016/j.nimb.2009.03.071.

[136] Thomas Friedrich, Katarina Ilicic, Christoph Greubel, Stefanie Girst, Judith Reindl, Matthias Sammer, Benjamin Schwarz, Christian Siebenwirth, Dietrich W. M. Walsh, Thomas E. Schmid, Michael Scholz, and Günther Dollinger. Dna damage interactions on both nanometer and micrometer scale determine overall cellular damage. *Scientific reports*, 8(1):16063, 2018. doi: 10.1038/s41598-018-34323-9.

[137] T. Vallentin, M. Moser, S. Eschbaumer, C. Greubel, T. Haase, P. Reichart, T. Rösch, and G. Dollinger. A microbeam slit system for high beam currents. *Nuclear Instruments and Methods in Physics Research Section B: Beam Interactions with Materials and Atoms*, 348:43–47, 2015. ISSN 0168583X. doi: 10.1016/j.nimb.2014.12.015. URL `https://www.sciencedirect.com/science/article/pii/S0168583X14010313`.

[138] Volker Hable. *Echtzeitbeobachtung schneller Reaktionskinetiken in lebenden Zellen nach Ionenmikrobestrahlung.* Dissertation, Universität der Bundeswehr, Neubiberg, 2011.

[139] S. Reinhardt, M. Würl, C. Greubel, N. Humble, J. J. Wilkens, M. Hillbrand, A. Mairani, W. Assmann, and K. Parodi. Investigation of ebt2 and ebt3 films for proton dosimetry in the 4-20 mev energy range. *Radiation and environmental biophysics*, 54(1):71–79, 2015. ISSN 0301-634X. doi: 10.1007/s00411-014-0581-2.

[140] Rebecca Moylan, Trent Aland, and Tanya Kairn. Dosimetric accuracy of gafchromic ebt2 and ebt3 film for in vivo dosimetry. *Australasian physical & engineering sciences in medicine*, 36(3):331–337, 2013. doi: 10.1007/s13246-013-0206-0.

[141] A. Bergmaier, G. Dollinger, and C. M. Frey. A compact Δe-eres detector for elastic recoil detection with high sensitivity. *Nuclear Instruments and Methods in Physics Research Section B: Beam Interactions with Materials and Atoms*, 136-138:638–643, 1998. ISSN 0168583X. doi: 10.1016/S0168-583X(97)00877-X.

[142] Daphnée Villoing, Charbel Koumeir, Arthur Bongrand, Arnaud Guertin, Ferid Haddad, Vincent Métivier, Freddy Poirier, Vincent Potiron, Noël Servagent, Stéphane Supiot, Grégory Delpon, and Sophie Chiavassa. Technical note: Proton beam dosimetry at ultra-high dose rates (flash): Evaluation of gafchromic™ (ebt3, ebt-xd) and orthochromic (oc-1) film performances. *Medical Physics*, 49(4):2732–2745, 2022. ISSN 2473-4209. doi: 10.1002/mp.15526.

[143] Sarah Rudigkeit, Julian B. Reindl, Nicole Matejka, Rika Ramson, Matthias Sammer, Günther Dollinger, and Judith Reindl. Cecile - an artificial intelligence based cell-detection for the evaluation of radiation effects in eucaryotic cells. *Frontiers in oncology*, 11:688333, 2021. ISSN 2234-943X. doi: 10.3389/fonc.2021.688333.

[144] Sonia Soloneski, Maciej Kujawski, Anna Scuto, and Marcelo L. Larramendy. Carbamates: A study on genotoxic, cytotoxic, and apoptotic effects induced in chinese hamster ovary (cho-k1) cells. *Toxicology in Vitro*, 29(5):834–844, 2015. ISSN 0887-2333. doi: 10.1016/j.tiv.2015.03.011. URL `https://www.sciencedirect.com/science/article/pii/S0887233315000521`.

[145] Dolores Diaz, Andrew Scott, Paul Carmichael, Wei Shi, and Chester Costales. Evaluation of an automated in vitro micronucleus assay in cho-k1 cells. *Mutation Research/Genetic Toxicology and Environmental Mutagenesis*, 630(1):1–13, 2007. ISSN 1383-5718. doi: 10.1016/j.mrgentox.2007.02.006. URL `https://www.sciencedirect.com/science/article/pii/S1383571807000496`.

[146] Xun Xu, Harish Nagarajan, Nathan E. Lewis, Shengkai Pan, Zhiming Cai, Xin Liu, Wenbin Chen, Min Xie, Wenliang Wang, Stephanie Hammond, Mikael R. Andersen, Norma Neff, Benedetto Passarelli, Winston Koh, H. Christina Fan, Jianbin Wang, Yaoting Gui, Kelvin H. Lee, Michael J. Betenbaugh, Stephen R. Quake, Iman Famili, Bernhard O. Palsson, and Jun Wang. The genomic sequence of the chinese hamster ovary (cho)-k1 cell line. *Nature biotechnology*, 29(8):735–741, 2011. doi: 10.1038/nbt.1932.

[147] Bárbara A. Pérez-Fernández, Jorge Fernandez-de Cossio-Diaz, Tammy Boggiano, Kalet León, and Roberto Mulet. In-silico media optimization for continuous cultures using genome scale metabolic networks: The case of cho-k1. *Biotechnology and bioengineering*, 118(5):1884–1897, 2021. doi: 10.1002/bit.27704.

[148] Kritika Gupta, Deepak Modi, Ratnesh Jain, and Prajakta Dandekar. A stable cho k1 cell line for producing recombinant monoclonal antibody against tnf-α. *Molecular biotechnology*, 63(9):828–839, 2021. doi: 10.1007/s12033-021-00329-4.

[149] Eisuke Sato, Alexander Zaboronok, Tetsuya Yamamoto, Kei Nakai, Sergey Taskaev, Olga Volkova, Ludmila Mechetina, Alexander Taranin, Vladimir Kanygin, Tomonori Isobe, Bryan J. Mathis, and Akira Matsumura. Radiobiological response of u251mg, cho-k1 and v79 cell lines to accelerator-based boron neutron capture therapy. *Journal of radiation research*, 59(2):101–107, 2018. ISSN 0449-3060. doi: 10.1093/jrr/rrx071.

[150] Urszula Kaźmierczak, Dariusz Banaś, Janusz Braziewicz, Iwona Buraczewska, Joanna Czub, Marian Jaskóła, Łukasz Kaźmierczak, Andrzej Korman, Marcin Kruszewski, Anna Lankoff, Halina Lisowska, Marta Nesteruk, Zygmunt Szefliński, and Maria Wojewódzka. Investigation of the bystander effect in cho-k1 cells. *Reports of practical oncology and radiotherapy : journal of Greatpoland Cancer Center in Poznan and Polish Society of Radiation Oncology*, 19(Suppl):S37–S41, 2014. ISSN 1507-1367. doi: 10.1016/j.rpor.2014.04.015.

[151] Christoph Greubel, Katarina Ilicic, Thomas Rösch, Judith Reindl, Christian Siebenwirth, Marcus Moser, Stefanie Girst, Dietrich W.M. Walsh, Thomas E. Schmid, and Günther Dollinger. Low let proton microbeam to understand high-let rbe by shaping spatial dose distribution. *Nuclear Instruments and Methods in Physics Research Section B: Beam Interactions with Materials and Atoms*, 404:155–161, 2017. ISSN 0168583X. doi: 10.1016/j.nimb.2016.11.032.

[152] Herbert Braselmann, Agata Michna, Julia Heß, and Kristian Unger. Cfassay: statistical analysis of the colony formation assay. *Radiation oncology (London, England)*, 10:223, 2015. doi: 10.1186/s13014-015-0529-y.

[153] Katarina Ilicic. *The Cellular Responses to Focused Low LET Proton Irradiation in Comparison to High LET Irradiation.* Dissertation, TUM, München, 2018. URL `https://mediatum.ub.tum.de/1419733`.

[154] Donald Wlodkowic, Joanna Skommer, and Zbigniew Darzynkiewicz. Flow cytometry-based apoptosis detection. *Methods in molecular biology (Clifton, N.J.)*, 559:19–32, 2009. ISSN 1064-3745. doi: 10.1007/978-1-60327-017-5_2.

[155] Emma M. Creagh. Caspase crosstalk: integration of apoptotic and innate immune signalling pathways. *Trends in Immunology*, 35(12):631–640, 2014. ISSN 1471-4906. doi: 10.1016/j.it.2014.10.004. URL `https://www.sciencedirect.com/science/article/pii/S1471490614001896`.

[156] Thermo Fisher Scientific. Sytox™ aadvanced™ totzellen-farbstoff-kit: Katalognummer: S10349, invitrogen™. URL `https://www.thermofisher.com/order/catalog/product/de/de/S10349`.

[157] Katherine M. McKinnon. Flow cytometry: An overview. *Current protocols in immunology*, 120:5.1.1–5.1.11, 2018. doi: 10.1002/cpim.40.

[158] BD Biosciences. Bd facscalibur instructions for use: User manual. URL `https://www.bdbiosciences.com/content/dam/bdb/marketing-documents/BD_FACSCalibur_instructions.pdf`.

[159] *Test No. 474: Mammalian Erythrocyte Micronucleus Test.* OECD Guidelines for the Testing of Chemicals, Section 4. OECD Publishing, Paris, 2016. ISBN 9789264264762. doi: 10.1787/9789264264762-en.

[160] John A. Heddle, Michael Fenech, Makoto Hayashi, and James T. MacGregor. Reflections on the development of micronucleus assays. *Mutagenesis*, 26(1):3–10, 2011. doi: 10.1093/mutage/geq085.

[161] E. A. Ainsbury, E. Bakhanova, J. F. Barquinero, M. Brai, V. Chumak, V. Correcher, F. Darroudi, P. Fattibene, G. Gruel, I. Guclu, S. Horn, A. Jaworska, U. Kulka, C. Lindholm, D. Lloyd, A. Longo, M. Marrale, O. Monteiro Gil, U. Oestreicher, J. Pajic, B. Rakic, H. Romm, F. Trompier, I. Veronese, P. Voisin, A. Vral, C. A. Whitehouse, A. Wieser, C. Woda, A. Wojcik, and K. Rothkamm. Review of retrospective dosimetry techniques for external ionising radiation exposures. *Radiation protection dosimetry*, 147(4):573–592, 2011. ISSN 0144-8420. doi: 10.1093/rpd/ncq499.

[162] Susan MacLean-Fletcher and Thomas D. Pollard. Mechanism of action of cytochalasin b on actin. *Cell*, 20(2):329–341, 1980. ISSN 0092-8674. doi: 10.1016/0092-8674(80)90619-4. URL `https://www.sciencedirect.com/science/article/pii/0092867480906194`.

[163] M. Fenech, M. Kirsch-Volders, A. T. Natarajan, J. Surralles, J. W. Crott, J. Parry, H. Norppa, D. A. Eastmond, J. D. Tucker, and P. Thomas. Molecular mechanisms of micronucleus, nucleoplasmic bridge and nuclear bud formation in mammalian and human cells. *Mutagenesis*, 26(1):125–132, 2011. doi: 10.1093/mutage/geq052.

[164] Matthias Sammer, Katharina Teiluf, Stefanie Girst, Christoph Greubel, Judith Reindl, Katarina Ilicic, Dietrich W. M. Walsh, Michaela Aichler, Axel Walch, Stephanie E. Combs, Jan J. Wilkens, Günther Dollinger, and Thomas E. Schmid. Beam size limit for pencil minibeam radiotherapy determined from side effects in an in-vivo mouse ear model. *PloS one*, 14(9):e0221454, 2019. doi: 10.1371/journal.pone.0221454.

[165] Matthias Sammer, Esther Zahnbrecher, Sophie Dobiasch, Stefanie Girst, Christoph Greubel, Katarina Ilicic, Judith Reindl, Benjamin Schwarz, Christian Siebenwirth, Dietrich W. M. Walsh, Stephanie E. Combs, Günther Dollinger, and Thomas E. Schmid. Proton pencil minibeam irradiation of an in-vivo mouse ear model spares healthy tissue dependent on beam size. *PloS one*, 14(11):e0224873, 2019. doi: 10.1371/journal.pone.0224873.

[166] Chao Liu, Yizhi Liang, and Lidai Wang. Single-shot photoacoustic microscopy of hemoglobin concentration, oxygen saturation, and blood flow in sub-microseconds. *Photoacoustics*, 17:100156, 2020. ISSN 2213-5979. doi: 10.1016/j.pacs.2019.100156. URL `https://www.sciencedirect.com/science/article/pii/s2213597919300795`.

[167] Mosby. *Mosby's Medical Dictionary - E-Book*. Mosby, 11th edition, 2021. ISBN 9780323831628.

[168] M. W. Pfaffl. A new mathematical model for relative quantification in real-time rt-pcr. *Nucleic acids research*, 29(9):e45, 2001. doi: 10.1093/nar/29.9.e45.

[169] A. Giulietti, L. Overbergh, D. Valckx, B. Decallonne, R. Bouillon, and C. Mathieu. An overview of real-time quantitative pcr: applications to quantify cytokine gene expression. *Methods (San Diego, Calif.)*, 25(4):386–401, 2001. ISSN 1046-2023. doi: 10.1006/meth.2001.1261.

[170] J. Vácha. Blood volume in inbred strain balb/c, cba/j and c57bl/10 mice determined by means of 59fe-labelled red cells and 59fe bound to transferrin. *Physiologia Bohemoslovaca*, 24(5):413–419, 1975.

[171] Simon Jolly, Hywel Owen, Marco Schippers, and Carsten Welsch. Technical challenges for flash proton therapy. *Physica Medica*, 78:71–82, 2020. ISSN 1120-1797. doi: 10.1016/j.ejmp.2020.08.005. URL `https://www.sciencedirect.com/science/article/pii/S1120179720301964`.

[172] Yinghao Lv, Yue Lv, Zhen Wang, Tian Lan, Xuping Feng, Hao Chen, Jiang Zhu, Xiao Ma, Jinpeng Du, Guimin Hou, Wenwei Liao, Kefei Yuan, and Hong Wu. Flash radiotherapy: A promising new method for radiotherapy. *Oncology letters*, 24(6):419, 2022. doi: 10.3892/ol.2022.13539.

[173] Bethany Rothwell, Matthew Lowe, Erik Traneus, Miriam Krieger, and Jan Schuemann. Treatment planning considerations for the development of flash proton therapy. *Radiotherapy and oncology : journal of the European Society for Therapeutic Radiology and Oncology*, 175:222–230, 2022. doi: 10.1016/j.radonc.2022.08.003.

[174] Jintao Han, Zhusong Mei, Chunyang Lu, Jing Qian, Yulan Liang, Xiaoyi Sun, Zhuo Pan, Defeng Kong, Shirui Xu, Zhipeng Liu, Ying Gao, Guijun Qi, Yinren Shou, Shiyou Chen, Zhengxuan Cao, Ye Zhao, Chen Lin, Yanying Zhao, Yixing Geng, Jiaer Chen, Xueqing Yan, Wenjun Ma, and Gen Yang. Ultra-high dose rate flash irradiation induced radio-resistance of normal fibroblast cells can be enhanced by hypoxia and mitochondrial dysfunction resulting from loss of cytochrome c. *Frontiers in cell and developmental biology*, 9:672929, 2021. ISSN 2296-634X. doi: 10.3389/fcell.2021.672929.

[175] Annique C. Dombrowsky, Jannis Schauer, Matthias Sammer, Andreas Blutke, Dietrich W. M. Walsh, Benjamin Schwarz, Stefan Bartzsch, Annette Feuchtinger, Judith Reindl, Stephanie E. Combs, Günther Dollinger, and Thomas E. Schmid. Acute skin damage

and late radiation-induced fibrosis and inflammation in murine ears after high-dose irradiation. *Cancers*, 11(5), 2019. ISSN 2072-6694. doi: 10.3390/cancers11050727.

[176] Luis A. Soto, Kerriann M. Casey, Jinghui Wang, Alexandra Blaney, Rakesh Manjappa, Dylan Breitkreutz, Lawrie Skinner, Suparna Dutt, Ryan B. Ko, Karl Bush, Amy S. Yu, Stavros Melemenidis, Samuel Strober, Edgar Englemann, Peter G. Maxim, Edward E. Graves, and Billy W. Loo. Flash irradiation results in reduced severe skin toxicity compared to conventional-dose-rate irradiation. *Radiation Research*, 194(6):618–624, 2020. ISSN 00337587. doi: 10.1667/RADE-20-00090.

[177] M. E. Masterson and R. Febo. Pretransfusion blood irradiation: clinical rationale and dosimetric considerations. *Medical Physics*, 19(3):649–657, 1992. ISSN 2473-4209. doi: 10.1118/1.596809.

[178] M. F. Fenech, V. Dunaiski, Y. Osborne, and A. A. Morley. The cytokinesis-block micronucleus assay as a biological dosimeter in spleen and peripheral blood lymphocytes of the mouse following acute whole-body irradiation. *Mutation research*, 263(2):119–126, 1991. ISSN 0027-5107. doi: 10.1016/0165-7992(91)90069-g.

[179] Ian Goodfellow, Aaron Courville, and Yoshua Bengio. *Deep learning*. Adaptive computation and machine learning. The MIT Press, Cambridge, Massachusetts, 2016. ISBN 0262337371. URL `https://search.ebscohost.com/login.aspx?direct=true&scope=site&db=nlebk&db=nlabk&AN=2565107`.

[180] Keiron O'Shea and Ryan Nash. An introduction to convolutional neural networks. URL `https://arxiv.org/pdf/1511.08458`.

[181] Y. Lecun, L. Bottou, Y. Bengio, and P. Haffner. Gradient-based learning applied to document recognition. *Proceedings of the IEEE*, 86(11):2278–2324, 1998. ISSN 00189219. doi: 10.1109/5.726791.

[182] Xiaowei Huang, Gaojie Jin, and Wenjie Ruan. Loss function and gradient descent. In Xiaowei Huang, Gaojie Jin, and Wenjie Ruan, editors, *Machine Learning Safety*, Artificial Intelligence, pages 103–107. Springer Nature Singapore and Imprint Springer, Singapore, 2023. ISBN 978-981-19-6813-6. doi: 10.1007/978-981-19-6814-3_9.

[183] Kaiming He, Xiangyu Zhang, Shaoqing Ren, and Jian Sun. Deep residual learning for image recognition. URL `https://arxiv.org/pdf/1512.03385`.

[184] Zhengxia Zou, Keyan Chen, Zhenwei Shi, Yuhong Guo, and Jieping Ye. Object detection in 20 years: A survey. URL `https://arxiv.org/pdf/1905.05055`.

[185] Tsung-Yi Lin, Michael Maire, Serge Belongie, James Hays, Pietro Perona, Deva Ramanan, Piotr Dollár, and C. Lawrence Zitnick. Microsoft coco: Common objects in context. In David Fleet, Tomas Pajdla, Bernt Schiele, and Tinne Tuytelaars, editors, *Computer vision - ECCV 2014*, volume 8693 of *Lecture Notes in Computer Science*, pages 740–755. Springer, Cham, 2014. ISBN 978-3-319-10601-4. doi: 10.1007/978-3-319-10602-1_48.

[186] Jordi Pont-Tuset and Luc van Gool. Boosting object proposals: From pascal to coco. In *Proceedings of the IEEE International Conference on Computer Vision (ICCV)*, 2015.

[187] Mayu Otani, Riku Togashi, Yuta Nakashima, Esa Rahtu, Janne Heikkilä, and Shin'ichi Satoh. Optimal correction cost for object detection evaluation. In *Proceedings of the IEEE/CVF Conference on Computer Vision and Pattern Recognition (CVPR)*, pages 21107–21115, 2022.

[188] Shaoqing Ren, Kaiming He, Ross Girshick, and Jian Sun. Faster r-cnn: Towards real-time object detection with region proposal networks. URL `https://arxiv.org/pdf/1506.01497`.

[189] Lyudmil Vladimirov. Tensorflow 2 object detection api tutorial: Training custom object detector, 2021. URL `https://tensorflow-object-detection-api-tutorial.readthedocs.io/en/latest/training.html`.

[190] Banat Gul, Sumara Ashraf, Shamim Khan, Hasan Nisar, and Iftikhar Ahmad. Cell refractive index: Models, insights, applications and future perspectives. *Photodiagnosis and photodynamic therapy*, 33:102096, 2021. doi: 10.1016/j.pdpdt.2020.102096.

[191] August Köhler. New method of illumination for photomicrographical purposes. *Journal of the Royal Microscopical Society*, (14):261–262, 1894.

[192] Rudi Rottenfusser, Erin E. Wilson, and Michael W. Davidson. Enhancing contrast in optical microscopy: Phase contrast. URL `https://zeiss-campus.magnet.fsu.edu/articles/basics/contrast.html`.

[193] Eljen Technology. Fast timing ej-228, ej-230. URL `https://eljentechnology.com/products/plastic-scintillators/ej-228-ej-230`.

[194] Sarah Rudigkeit. *The Response of Mitochondria to Ionizing Radiation and their Role in Cell Survival.* Master thesis, Technische Universität München, München, 2018.

[195] Sarah Rudigkeit, Nicole Matejka, Matthias Sammer, Dietrich W. M. Walsh, Günther Dollinger, and Judith Reindl. Beam optimization of a heavy ion microbeam for targeted irradiation of mitochondria in human cells. *Nuclear Instruments and Methods in Physics Research Section B: Beam Interactions with Materials and Atoms*, 542:195–205, 2023. ISSN 0168583X. doi: 10.1016/j.nimb.2023.07.004. URL `https://www.sciencedirect.com/science/article/pii/S0168583X23003129`.

[196] Abhishek Dutta and Andrew Zisserman. The via annotation software for images, audio and video. In Laurent Amsaleg, editor, *Proceedings of the 27th ACM International Conference on Multimedia*, ACM Digital Library, pages 2276–2279, New York,NY,United States, 2019. Association for Computing Machinery. ISBN 9781450368896. doi: 10.1145/3343031.3350535.

[197] Juan Du. Understanding of object detection based on cnn family and yolo. *Journal of Physics: Conference Series*, 1004:012029, 2018. ISSN 1742-6588. doi: 10.1088/1742-6596/1004/1/012029.

[198] Hongkun Yu, Chen Chen, Xianzhi Du, Yeqing Li, Abdullah Rashwan, Le Hou, Pengchong Jin, Fan Yang, Frederick Liu, Jaeyoun Kim and Jing Li. Tensorflow model garden, 2020.

[199] Adrian Rosebrock. *Deep Learning for Computer Vision with Python.* PyImageSearch, vol. iii, 3rd edition edition, Nov 2019.

[200] Ilya Loshchilov and Frank Hutter. Sgdr: Stochastic gradient descent with warm restarts. URL `https://arxiv.org/pdf/1608.03983`.

[201] Lucas Villaverde Zimmermann. *Optimierung der Detektionsgenauigkeit des KI-basierten Objekterkennungsalgorithmus CeCILE.* Masterarbeit, Universität der Bundeswehr München, Neubiberg, 2022.

[202] Adrian Rosebrock. Simple object tracking with opencv, 2018. URL `https://pyimagesearch.com/2018/07/23/simple-object-tracking-with-opencv/`.

[203] Pierre Montay-Gruel, Mineh Markarian, Barrett D. Allen, Jabra D. Baddour, Erich Giedzinski, Patrik Goncalves Jorge, Benoît Petit, Claude Bailat, Marie-Catherine Vozenin, Charles Limoli, and Munjal M. Acharya. Ultra-high-dose-rate flash irradiation limits reactive gliosis in the brain. *Radiation Research*, 194(6):636–645, 2020. ISSN 00337587. doi: 10.1667/RADE-20-00067.1.

[204] N. Rama, T. Saha, S. Shukla, C. Goda, D. Milewski, A. E. Mascia, R. E. Vatner, D. Sengupta, A. Katsis, E. Abel, S. Girdhani, M. Miyazaki, A. Rodriguez, A. Ku, R. Dua, R. Parry, and T. V. Kalin. Improved tumor control through t-cell infiltration modulated by ultra-high dose rate proton flash using a clinical pencil beam scanning proton system. *International Journal of Radiation Oncology*Biology*Physics*, 105(1): S164–S165, 2019. ISSN 03603016. doi: 10.1016/j.ijrobp.2019.06.187.

[205] Eric S. Diffenderfer, Ioannis I. Verginadis, Michele M. Kim, Khayrullo Shoniyozov, Anastasia Velalopoulou, Denisa Goia, Mary Putt, Sarah Hagan, Stephen Avery, Kevin Teo, Wei Zou, Alexander Lin, Samuel Swisher-McClure, Cameron Koch, Ann R. Kennedy, Andy Minn, Amit Maity, Theresa M. Busch, Lei Dong, Costas Koumenis, James Metz, and Keith A. Cengel. Design, implementation, and in vivo validation of a novel proton flash radiation therapy system. *International journal of radiation oncology, biology, physics*, 106(2):440–448, 2020. doi: 10.1016/j.ijrobp.2019.10.049.

[206] Xu Cao, Rongxiao Zhang, Tatiana V. Esipova, Srinivasa Rao Allu, Ramish Ashraf, Mahbubur Rahman, Jason R. Gunn, Petr Bruza, David J. Gladstone, Benjamin B. Williams, Harold M. Swartz, P. Jack Hoopes, Sergei A. Vinogradov, and Brian W. Pogue. Quantification of oxygen depletion during flash irradiation in vitro and in vivo.

International journal of radiation oncology, biology, physics, 111(1):240–248, 2021. doi: 10.1016/j.ijrobp.2021.03.056.

[207] Brita Singers Sørensen, Mateusz Krzysztof Sitarz, Christina Ankjærgaard, Jacob Johansen, Claus E. Andersen, Eleni Kanouta, Cathrine Overgaard, Cai Grau, and Per Poulsen. In vivo validation and tissue sparing factor for acute damage of pencil beam scanning proton flash. *Radiotherapy and oncology : journal of the European Society for Therapeutic Radiology and Oncology*, 167:109–115, 2022. doi: 10.1016/j.radonc.2021.12.022.

List of Publications

2017

1. Heidsieck A., **Rudigkeit S.**, Rümenapp C., Gleich B., *"Simple optical measurement of the magnetic moment of magnetically labeled objects"*. Journal of Magnetism and Magnetic Materials, Volume 427, 2017, Pages 2-6, doi: 10.1016/j.jmmm.2016.10.057.

2021

2. Sammer M., Dombrowsky A.C., Schauer J., Oleksenko K., Bicher S., Schwarz B., **Rudigkeit S.**, Matejka N., Reindl J., Bartzsch S., Blutke A., Feuchtinger A., Combs S.E., Dollinger G., Schmid T.E., *"Normal Tissue Response of Combined Temporal and Spatial Fractionation in Proton Minibeam Radiation Therapy"*. Int J Radiat Oncol Biol Phys. 2021 Jan 1;109(1):76-83. doi: 10.1016/j.ijrobp.2020.08.027
3. **Rudigkeit S.**, Reindl J. B., Matejka N., Ramson R., Sammer M., Dollinger G., Reindl J., *"CeCILE - An Artificial Intelligence Based Cell-Detection for the Evaluation of Radiation Effects in Eucaryotic Cells"*. Frontiers in Oncology 11., doi: 10.3389/fonc.2021.688333

2022

4. Scherthan H., Wagner S.-Q., Grundhöfer J., Matejka N., Müller J., Müller S., **Rudigkeit S.**, Sammer M., Schoof S., Port M., Reindl J., *"Planar Proton Minibeam Irradiation Elicits Spatially Confined DNA Damage in a Human Epidermis Model"*. Cancers 2022, 14, 1545. doi: 10.3390/cancers14061545

2023

5. **Rudigkeit S.**, Matejka N., Sammer M., Walsh D.W.M., Dollinger G., Reindl J., *"Beam optimization of a heavy ion microbeam for targeted irradiation of mitochondria in human cells"*. Nuclear Instruments and Methods in Physics Research Section B: Beam Interactions with Materials and Atoms, Volume 542, 2023, Pages 195-205, doi: 10.1016/j.nimb.2023.07.004.

6. Schwarz B., Sammer M., Matejka N., **Rudigkeit S.**, Reindl J., *”HighLET targeted microbeam irradiation induces local chromatin reorganization in living cells showing active basal mechanisms at highly complex DNA damage sites”.* J Radiat Res Imaging. 2023;2(1):1-8.

7. **Rudigkeit S.**, Reindl J., *”Single-Cell Radiation Response Scoring with the Deep Learning Algorithm CeCILE 2.0”.* Cells 2023, 12, 2782. doi:10.3390/cells12242782

2024

8. **Rudigkeit S.**, Schmid T. E., Dombrowsky A. C., Stolz J., Bartzsch S., Chen C., Matejka N., Sammer M., Bergmaier A., Dollinger G., Reindl J., *”Proton-Flash – effects of ultra-high dose rate irradiation on an in-vivo mouse ear model”.* Sci Rep 14, 1418. doi: 10.1038/s41598-024-51951-6

9. Schwarz B., Matejka N., **Rudigkeit S.**, Sammer M., Reindl J., *”Chromatin Organization after High-LET Irradiation Revealed by Super-Resolution STED Microscopy”.* Int. J. Mol. Sci. 2024, 25, 628. doi: 10.3390/ijms25010628

10. Matejka N., Amarlou A., Neubauer J., **Rudigkeit S.**, Reindl J., *”High-Resolution Microscopic Characterization of Tunneling Nanotubes in Living U87 MG and LN229 Glioblastoma Cells”.* Cells 2024, 13, 464. doi:10.3390/cells13050464

Acknowledgments

First of all, I want to thank Professor Dr. Judith Reindl, who makes this work possible, for the supervision and the support I received starting from my master's thesis to the completion of this Ph.D. project. Furthermore, I want to thank her for many fruitful discussions and that she always had an open ear and a helping hand also in difficult times of this project. I also need to mention that she always helped me out during experimental periods, with the supervision of students, the writing of publications and than I had an argument with the old Observer microscope. She gave not only useful advises, but also lent a hand herself to fix a problem in an experimental setup. I would also like to thank her for allowing me to attend several conferences and for introducing me to the art of networking. Then, I want to thank Professor Dr. Günther Dollinger for not only providing financial support, but also for supporting me and helping me out, especially, when setting up the beam line for FLASH experiments. Special thanks go to Julian Reindl, who helped me to set up the object detection of CeCILE and the git environment and provided support whenever I needed it. I also want to thank Prof. Thomas Schmid and his biology team, especially Annique Dombrowsky (off-duty), Sandra Bicher and Jessica Stolz for their invaluable help in the FLASH experiments. They organized the mice, were able to prevent their killing during the corona crisis, collected and analyzed the blood, provided the protocols for the in-vitro experiments, allowed me to use their labs, and helped during beam time to anesthetize and fix the mice for irradiation. Without their help, such interdisciplinary experiments would not have been possible. Next, I want to thank PD Dr. Hai Huang for the discussions and for sharing his ideas with me how to implement an MCMC tracking in CeCILE. I also want to thank Dr. Andreas Bergmaier for setting up the detector for the dosimetry at the FLASH beam line. Special appreciation goes to my colleague Stefanie Girst for her help with the mouse experiments and her neat corrections of my writings. I also want to thank my "roommates" Nicole Matejka and Jessica Neubauer. Nicole Matejka has been a reliable and motivating companion and friend since the third semester of my bachelor's degree, always helping me out in difficult situations. Jessica Neubauer brought to our small SNAKEbio team not only a lot of motivational energy but also a completely new sight of how a cell culture lab should be organized and biological experiments should be performed. Nicole and Jessica gave me an extraordinary comfortable working environment and we shared a lot of great moments not only at work. Furthermore, I want to thank my colleagues Marcel Dickmann, Johannes Mitteneder, Ricardo Helm, Michael Mayerhofer, Guanzhong Wang, Jannis Schauer, Katherina Rousseti, Patrick Reichart, Heinrich Ruser, Werner Egger and Peter Sperr and my former colleagues Matthias Sammer and Dietrich Walsh for all the discussions, advice, and all the support I got during this work and

for giving me such a nice time at the LRT2 institute. I will definitely miss our “Laborbesprechungen”.

Finally, I want to thank all my friends and my family. Especially, I want to thank my partner Jan Buitkamp for always being there for me and cheering me up, when I was frustrated. Also for helping me out whenever I had problems with a computer or with the code. Special thanks go also to my parents, Jan Rudigkeit and Karin Rudigkeit, who always supported me in everything I did and made my entire education and studies possible. Furthermore, I want to thank my sister Nadine Rudigkeit and her partner Lukas Gorisch and my brother Fabian Rudigkeit as well as the parents of my partner, Maria Gomolka and Johannes Buitkamp, for all the emotional support.